Doctoral Dissertation

OBSERVATIONS AND NUMERICAL SIMULATIONS OF MIXING PROCESSES IN SHALLOW COASTAL REGIONS

March 2015

Graduate School of Marine Science and Technology
Tokyo University of Marine Science and Technology
Doctoral Course of Applied Marine Environmental Studies

Eiji Masunaga

Abstract

Internal waves are ubiquitous and one of the energetic phenomena in stratified oceans and lakes. Large-scale internal waves (e.g., internal tides and internal seiches) increase their nonlinearity when they propagate into shallower areas. Nonlinear internal waves enhance turbulent mixing and transport water, sediments, nutrients, iron and organic materials within oceans and lakes. In particular, shallow coastal areas and continental shelves are known as “hot spots” of internal wave breaking sites. Internal waves contribute to water exchange between coastal waters and open ocean waters, which play a significant role in ocean circulations and ocean ecosystems. However, due to the lack of field surveys, detailed processes of internal waves and mixing processes in coastal areas are not well understood. To further understanding these phenomena, this study investigated mixing processes associated with river plumes and internal waves using two approaches: (1) in situ field surveys and (2) numerical simulations.

In order to observe detailed features of physical structures in shallow coastal regions, I have developed a new, portable tow-yo instrument, Yoing Ocean Data Acquisition Profiler (YODA Profiler, *Masunaga and Yamazaki,* 2014). Using the YODA Profiler, I was able to rapidly obtain high-resolution data in a shallow estuary. The results showed fine-scale complicated internal wave features, upslope propagating fronts and a patchy distribution of phytoplankton. These observations are consistent with recent numerical models and acoustic surveys as well as with the critical angle theory for internal wave reflections along bottom slopes. I have also developed a statistical technique to estimate the rate of turbulent kinetic energy dissipation, ε, from conductivity data. Using this technique I was able to estimate the turbulent kinetic energy dissipation rate associated with river outflow and internal waves in shallow coastal regions.

Observed results in Otsuchi Bay showed fine features of river plumes and internal waves. A shallow river plume was generally present in the bay. Rapid river plume mixing events were observed during summer campaigns with a time scale of *O* (1 hour). These events coincided with tidally induced internal bores (***1**) propagating on a slope. The isothermal displacement due to internal bores reached 20 m vertically at a depth of 40 m in the water column. The combined effects of the wind stress and the baroclinic flow due to the internal bore generated a shear layer near the sea surface and enhanced river plume mixing. The vertical eddy diffusivity in the river plume during the mixing event reached 3.0×10^{-4} $m^2 s^{-1}$. In addition to field surveys, a fully non–hydrostatic numerical model SUNTANS, developed by *Fringer et al.* (2006), was used to investigate mixing processes in the bay. The numerical simulations revealed that three forcing factors (barotropic tide, baroclinic internal tide and wind) are equally important for river plume mixing in the bay.

The YODA Profiler and mooring surveys also showed details in nonlinear internal bores propagating into the bay. The high-resolution mooring observation revealed a high-frequency wave feature in the interface of the bore wave, likely induced by shear instability, and a vortex structure at the head of the bore wave. The vortex was accompanied by strong vertical currents, which induced strong vertical sediment resuspension and intensified turbulent mixing. The rate of turbulent energy dissipation was approximately 10^{-6} W kg^{-1} at the bore head. The vertical current reached 0.03 m s^{-1} in the vortex, which induced strong vertical resuspension of sediments. Suspended particles detached from the sloping bottom and intruded into offshore above the thermocline, forming an intermediate nepheloid layer (INL).

Astrong turbulent mixing event was also observed when a receding bore ran into the next run-up bore, which causes a collision of the receding bore and the run-up bore. This strong turbulent mixing event due to the collision (crashing) of non-linear bores has never been observed before; I named this phenomenon "*crash mixing*". The highest turbulent kinetic energy dissipation rate near the crashing site reached 10^{-6} – 10^{-5} W kg^{-1}.

The high-resolution mooring observation showed high-frequency waves and shear instability motion during the crashing period. The observed results also showed the high dissipation area appearing not only in the bottom boundary layer but also near the sea surface above the crashing site that leads to a strong mixing of the river plume.

In order to investigate physical mechanisms involved in internal bores, we conducted numerical simulations using SUNTANS. The numerical simulation reproduced internal bores, crash mixing and details of the vortex motion at the head of the bore, which all showed excellent agreement with field observation results. I have found that the Iribarren number (***2**) is a key parameter for mixing processes associated with internal bores. Numerical results indicated that a low Iribarren number condition leads to strong turbulent mixing along the slope. The vortex motion and the crash mixing due to internal bores were enhanced in the low Iribarren number condition. This study also investigated sediment resuspension and sediment transport processes using SUNTANS. Numerical simulations forced by first-mode internal waves reproduced sediment resuspension and intermediate nepheloid layers (INLs). The results indicated that repeated internal bores contribute to the tertiary circulation, which transports mixed high turbidity water into the interior of the water column. This circulation leads to the growth of INLs into the offshore area. Therefore, strong turbulent mixing in the low Iribarren number condition contributes to strong sediment resuspension and the growth of INLs.

As the results of this study show, nonlinear internal bores and high-frequency internal waves dramatically alter physical processes and are the key to understanding mixing processes in shallow coastal regions.

(*1) A bore refers to a high tidal wave propagating into the upstream of a river or estuary. In the internal wave field, an internal bore refers to an internal wave (dense water) advancing on a sloping bottom with a steep isopycnal displacement.

(*2) The Iribarren number is the ratio of the wave slope to the topographic slope for classifying wave breaking types. The details of this number are described in Chapter 4 of this thesis.

Acknowledgements

I would like to thank and express my sincere appreciation to my advisor, Prof. Hidekatsu Yamazaki, who guided my thesis research and provided valuable supports. I would also like to thank co-advisors Prof. Yujiro Kitade and Prof. Takeyoshi Nagai for their helpful and thoughtful advice. I am grateful to Prof. Oliver Fringer (Stanford Univ.) and his group members, who supported my numerical simulations.

I gratefully acknowledge the Tohoku-Ecosystem-Associated Marine Science (TEAMS) project members associated with this thesis work, Prof. Akio Okayasu, Prof. Chiaki Imada, Prof. Takeshi Terahara, Hikaru Homma, Yuka Saito, Nagisa Tachikawa, Prof. Kiyoshi Tanaka, Prof. Hideki Fukuda and Prof. Yuichiro Nishibe, for their assistance and for coordinating observations. We thank *Shin-Otsuchi* fishery and *Kamaishi-Tobu* fishery for their kind support during observations in Otsuchi Bay.

I thank crews of the R/V Hiyodori (Tokyo University of Marine Science and Technology), R/V Grand-maillet (the University of Tokyo), the fishing boat Senshu-maru (Shin-Otsuchi fishery) the fishing-boat Daimutsu-maru (Shin-Otsuchi fishery) for their time and help. I am indebted to Masahide Wakita (JAMSTEC), who provided observation data off the Sanriku Coast, shown in Chapter 6. I also thank Hirokazu Imura, who developed a special computer program (FOT) that helped facilitate YODA Profiler field surveys.

I am indebted to the laboratory members for their assistance with the deployment of instruments during field observations and with numerical simulations.

Finally, I want to thank my wife, Hiroko, and my parents for their support and encouragement.

This study was supported by a fund from the Tohoku Ecosystem-Associated Marine Science Project (Ministry of Education, Culture, Sports, Science and Technology of Japan).

Contents

Chapter 1 Introduction

Chapter 2 Developing a new tow-yo profiler to observe high-resolution coastal phenomena

Chapter 3 An observational and numerical study of river plume dynamics in Otsuchi Bay, Japan

Chapter 4 Observations and numerical simulations of internal bores induced by the internal tides

Chapter 5 Crash mixing induced by internal bores

Chapter 6 The generation mechanism of intermediate nepheloid layers

Chapter 7 Conclusion and outlook

Chapter 1

Introduction

1.1Background and motivation

Physical processes in coastal oceans are the key to understand the global ocean circulation (*Munk and Wunsch,* 1998; *St. Laurent and Thurnherr,* 2007; *Lumpkin and Speer,* 2007) and the global carbon flux (*Walsh,* 1991; *Sharples et al.,* 2009; *Nakatsuka et al.,* 2004). Vertical exchanges of materials and buoyancy are essentials to maintaining global ocean circulation, and such exchanges are mainly generated by turbulent mixing (*Munk and Wunsch,* 1998; *St. Laurent and Thurnherr,* 2007; *Lumpkin and Speer,* 2007). Nutrient and gas exchanges due to turbulent mixing have been recognized as important contributors to ocean ecosystems and the global carbon cycles (*Sharples et al.,* 2009; *Nakatsuska et al.,* 2004; *Walsh,* 1991)

Internal waves are frequently found in stratified atmosphere, ocean and lakes. Tidally generated internal waves are one of several major energetic phenomenon in the ocean (e.g., *Ostrovsky and Stepanyants,* 1989; *Helfrich and Melville,* 2006). Internal waves appearing near seas surfaces associated with river plumes (fresh water discharge) are common features in coastal areas (e.g., *Moum et al.,* 2003; *Nash and Moum.,* 2005; *Masunaga and Yamazaki,* 2014). Tidal flows generate internal solitary wave packets released from river mouths. It is known that internal waves in coastal areas show highly non-linear motions that lead to turbulent mixing in the ocean (*Moum et al.,* 2003). Linear internal tides reflect on the sloping ocean floor, which leads to energy convergence along slopes and enhances the amplitude of internal waves (e.g., *Cacchione et al.,* 2002; *Van Gastel et al.,* 2009). Such internal waves propagate to shore areas from deeper offshore sites, and they finally run-up, break or reflect on shallow slopes. Satellite images indicate that shoreward internal waves appear in most coastal ocean areas (*Fu and Holt*, 1982). Run-up of internal waves on slopes was initially studied by *Wallace and Wilkinson* (1988) and *Helfrich* (1992) through tank experiments. Surges of such internal waves have been described as "boluses" or "bores." Internal bores generate strong currents and turbulent mixing along slopes (*Cacchione et al.,* 2002; *Klymak and Moum,* 2003). The strong current induced by bores causes sediment resuspension and material transport between onshore and offshore sites (*McPhee-Shaw,* 2006).

Although the appearance of internal waves in shallow coastal areas has been well demonstrated by previous studies, details of the physical processes behind internal waves have not been well understood due to lack of suitable methods to observe these waves. This dissertation attempts to reveal fine scale processes of internal waves through the three aspects listed below:

1) Developing a new profiler to observe fine scale physical processes in coastal areas.
2) In situ field surveys using a new profiler and high-resolution mooring arrays.
3) Reproducing the observed internal waves from numerical simulations.

Various techniques to observe oceanic internal waves have been studied for over half a century. Studies in the 1960s have found the large internal waves in the ocean using vertical thermistor arrays for the first time (*Helfrich and Melville,* 2006); which is a method now commonly employed to observe internal waves in the ocean. Recently developed high resolution thermistor arrays can observe fine scale density inversions and shear instability (e.g., *van Haren,* 2009). However, thermistor arrays do not observe spatial patterns of physical structures.

In addition to the mooring method, a method, vertical profiling with a CTD (Conductivity, Temperature and Depth) sensor is another method used to observe oceanic structures. Spatial physical structures can be observed by obtaining vertical CTD profiles at several locations. Although a conventional CTD survey allows us to observe large scale spatial fields, this method requires a stop and go operation mode and does not allow us to observe fine scale internal wave structures. Therefore, a new method to observe small-scale structures is needed. A towed observation is a useful method for observing spatial structures in the ocean. A few towed profiling systems have been developed (e.g., *Herman et al.,* 1998); however, these systems are not suited to observing internal waves in shallow coastal areas. In order to observe fine scale structures of internal waves, I have developed a new tow-yo instrument, Yoing Ocean Data Acquisition Profiler (YODA Profiler).

I carried out field surveys in two locations using the YODA Profiler: (1) Arakawa River mouth (located north of Tokyo Bay) and (2) Otsuchi Bay (located on the Sanriku Coast, Iwate Prefecture). Mooring systems, a microstructure profiler TurboMAP-L (*Wolk et al.,* 2002) and an Underway CTD (UCTD, *Rudnick and Klinke,* 2007) were also used for the field surveys.

In addition to observations, recent numerical approaches have revealed fine features and breaking processes of internal waves in coastal seas. *Venayagamoothy and Fringer* (2006) showed run-up of internal bores and a vortex core from a non-hydrostatic high-resolution Large Eddy Simulation (LES). *Vlasenko and Hutter* (2002) revealed breaking processes of internal solitary waves on a shallow slope. *Fringer et al.* (2006) suggested that reproducing internal waves in coastal areas require non-hydrostatic model to generate high frequency motion, so they developed a numerical simulation model, Stanford Unstructured Nonhydrostatic Terrain-following Adaptive Navier-Stokes Simulator (SUNTANS). Although numerical methods have drastically improved with the advancement of computer technologies, few studies have been successfully compared the numerical results against field surveys. I combined SUNTANS and field surveys to reveal fine scale physical processes associated with internal waves and river plumes.

1.2 Layout of the thesis

This dissertation consists of six chapters.

The second chapter describes a development of a newly developed tow-yo instrument (the YODA Profiler) and also new findings obtained from this instrument. Technical descriptions of the YODA Profiler and several observed fine scale phenomena are described in this chapter. A new statistical method to infer the rate of turbulent kinetic energy dissipation is also presented. This chapter has been published in a peer-reviewed journal, Journal of Marine Systems (*Masunaga and Yamazaki,* 2014).

The third chapter presents river plume dynamics and mixing processes in a shallow bay investigated by both field surveys and numerical simulations. This chapter describes river plume mixing enhanced by barotropic tides, baroclinic internal tides and the wind stress.

The fourth chapter shows run-up of non-linear internal bores on a shallow slope. This chapter focuses on the fine features of internal bores observed using the YODA Profiler and high-resolution mooring systems. This chapter also investigates non-linear internal bores using numerical simulations.

The fifth chapter introduces the “crash mixing” induced by the collision of the receding internal bore and run-up of the next internal bore. This chapter also focuses on the Iribarren number (ratio of the wave slope to the topographic slope) controlling the mixing intensity of crash mixing.

The sixth chapter presents the generation mechanism of intermediate nepheloid layers (INLs) due to internal bores by making use of numerical simulations. In this chapter, numerical simulations in variable slope conditions show that the low Iribarren number condition tends to induce INLs.

The final chapter summarizes this dissertation with major conclusions and describes recommendations for future works.

Chapter 2

A new tow-yo instrument to observe high resolution coastal phenomena

2.1 Introduction

Understanding the small-scale physical and biological processes in coastal and estuarine areas is a pressing issue in oceanography. Recent observations have captured small-scale physical processes in these areas (e.g., *Moum et al.,* 2003; *Van Haren,* 2009). Numerical studies have also shown small and complex density structures caused by internal waves in near shore areas (e.g., *Venayagamoorthy and Fringer,* 2006; *Vlasenko and Hutter,* 2002). However, no previous study has shown the complex physical structure data from in situ field CTD observations since a conventional CTD survey requires positioning a research vessel from one place to another.

A useful method for observing oceanic processes is a towed observation. With this method, high spatial resolution data can be obtained rapidly and continuously. Examples of towed profiling systems are SeaSoar (*Pollard,* 1986), AQUAshuttle (Chelsea Instruments, Ltd), the Moving Vessel Profiler (MVP; *Herman et al.,* 1998) and the Underway CTD (UCTD; *Rudnick and Klinke, 2007*). SeaSoar and AQUAshuttle are towed and winged instruments. While being deployed the instruments move up and down in the ocean changing their wing angle, allowing for rapid towed observation. This type of observation provides a saw-tow mode data, but the instrument does not produce vertical profiles. MVP and UCTD are tow-yo instruments that succeed in providing many vertical profiles during a transect. Since both instruments descend at a high speed in order to obtain free-fall profiles from a fast moving ship, they are difficult to operate in shallow waters without hitting the bottom. Furthermore, their deployments require a dedicated winch, and most of them are difficult to use with a small vessel, like a fishing boat. In order to address these issues, I have designed a portable free-fall tow-yo instrument Yoing Ocean Data Acquisition Profiler (YODA Profiler, Fig. 2-1), to capture high spatial resolution data of physical features in a shallow coastal area. The YODA Profiler is deployed using a procedure similar to that of the MVP and UCTD. Inspired from free-fall microstructure profilers, such as TurboMAP (*Wolk et al.,* 2002), a brush is mounted at the top of the profiler. The brush promotes a stable, uniform sinking velocity in a free-fall mode. I was able to observe detailed fine-scale physical features in shallow coastal areas quickly and efficiently using this new small profiler and a small, inexpensive winch.

I have also developed a statistical technique to estimate the turbulent kinetic energy dissipation rate, ε, from the vertical gradient of conductivity (dC/dz) that is the surrogate of the temperature gradient. This method permits us to infer detailed turbulent phenomena in shallow coastal areas.

In this chapter, I describe the design of the YODA Profiler and some results from observations made near a river mouth. Functional descriptions are presented in section 2.2. The instrumentation and locations of observations are described in section 2.3. Results from observations near a river mouth are discussed in section 2.4. A statistical technique to estimate the turbulent kinetic energy dissipation rate is described in section 2.5. Section 2.6 concludes this chapter.

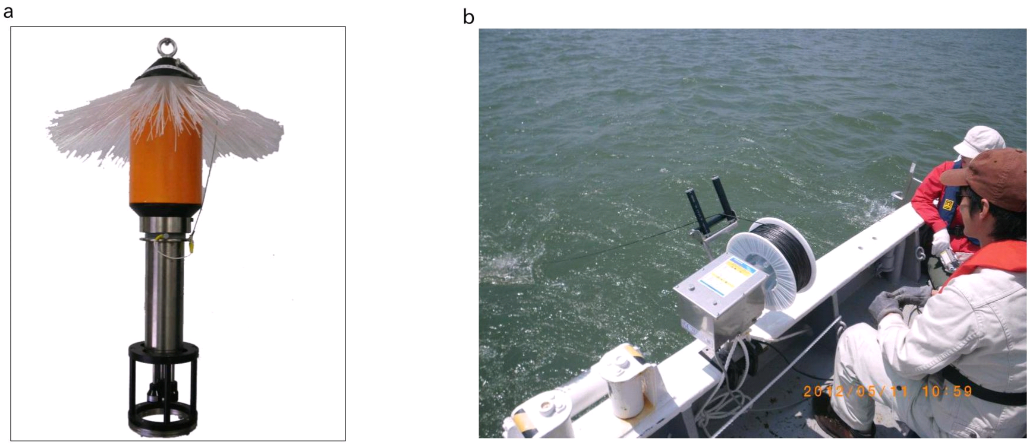

Fig. 2-1. (a) The YODA Profiler and (b) the winch mounted on the R/V *Hiyodori*.

2.2 YODA Profiler design

The most important consideration for the design of the YODA Profiler is portability. Observations in shallow coastal areas require small research vessels or small fishing boats, which have limited space, so a small and simple profiling system is desired. Therefore, I selected a small memory-type CTD sensor, a small fishing winch and a strong, thin cable for the YODA Profiler system. Another aspect that must be considered when developing and using high speed profiling systems is the drag of the sensor and the cable. However, the drag of these parts is very small for the YODA Profiler and can almost be neglected, as mentioned in following subsections.

Sensors

A small memory-type CTD, RINKO-Profiler (JFE Advantech Co., Ltd.), was selected as the main sensor for the YODA Profiler. The RINKO-Profiler carries temperature, conductivity, pressure, fluorescence, turbidity and oxygen sensors mounted at the bottom of the profiler. The response time of the RINKO oxygen sensor is 0.4 s and 0.2 s for the other sensors.

Brush and weight

The brush mounted on the top of the profiler acts the same way as those on free-fall microstructure profilers, providing a stable free-fall mode. The difference from general microstructure profilers is that the sloping brush is mounted on the YODA Profiler at approximately 45 degrees (Fig. 2-2a). The flexible brush expands while sinking to promote a stable free-fall mode (Fig. 2-2b). During the recovery phase, it contracts to reduce drag, which allows for a smooth recovery with reduced drag (Fig. 2-2c).

An accurate sinking velocity is necessary to set the profiling time duration for the target depth. The sinking velocity of the profiler varies sensitively depending on the density of water in the observation area and the condition of the brush. The sinking speed can be adjusted by altering the ring weight at the bottom of the profiler. The sinking speed is adjusted to 0.2 ms^{-1} in this study (Fig. 2-3).

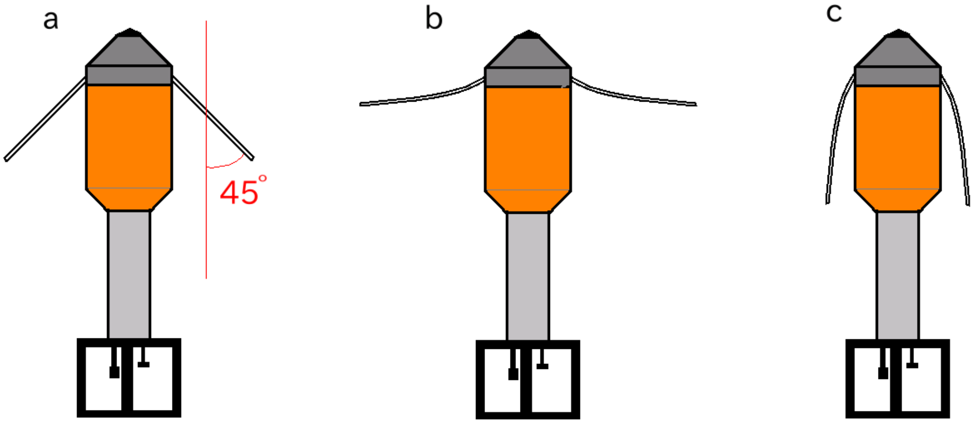

Fig. 2-2. Schematic images of the YODA Profiler brush: (a) before deployment, (b) during descent and (c) at recovery.

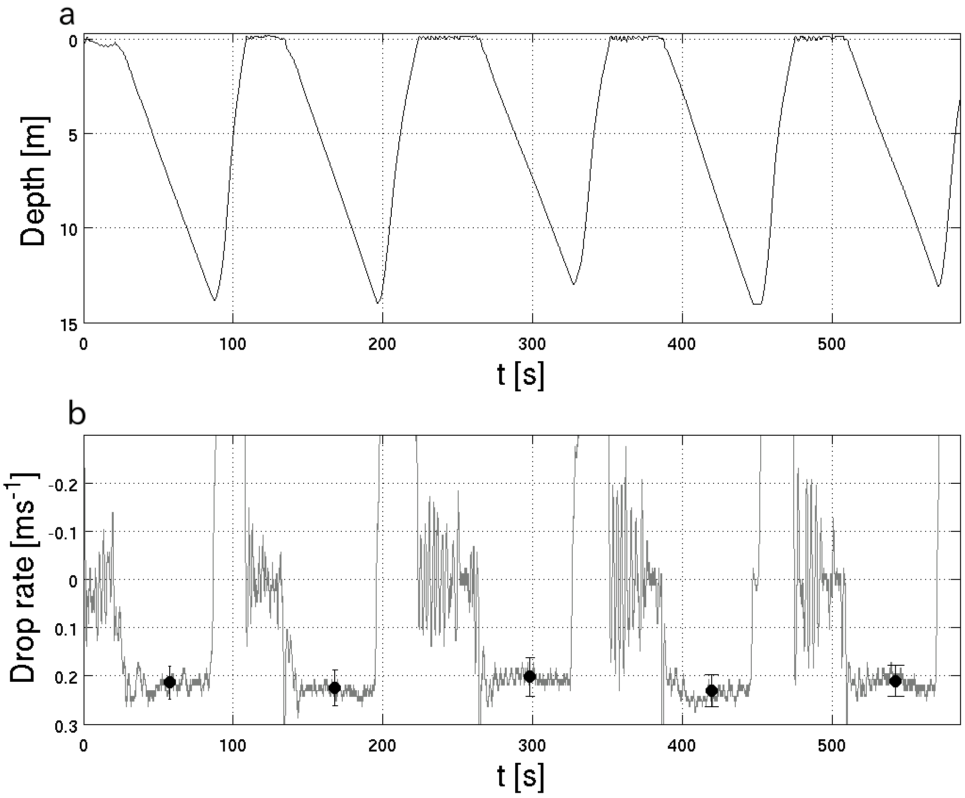

Fig. 2-3. (a) Depth and (b) drop rate of the YODA Profiler as a function of time during the tow-yo observations. Black solid circles and error bars in (b) indicate mean and standard deviation of the drop rate in each cast.

Winch and line

The recovery winch is a small portable ‘Light Weight Fisher 4th (*Inoue-kikai*)’ powered by a 24 volt DC power supply (Fig. 2-1b). The weight of the winch is 11 kg. In this study, I used a lead storage battery, which allowed us to set up the winch system on a small vessel without onboard power. I have chosen a 3 mm diameter ‘Dyneema Rope’ (Falcon, Ltd) made from high molecular weight polyethylene, because this material is 1.4 times stronger than aramid fiber. The breaking strength of the Dyneema line is 900 kg, and the relative specific gravity is 0.97 in the water. The slow sinking velocity and the thin recovery line permit us to operate the YODA Profiler without drag, which would prevent a stable free-fall mode.

2.3 Instrumentation and observations

Observations were repeated numerous times between 2010 and 2012 from the 16.5-m, 19-t R/V *Hiyodori* (Tokyo University of Marine Science and Technology) near the Arakawa River mouth located in the northern area of Tokyo Bay, Japan (Fig. 2-4). The minimum and maximum depths of this area are approximately 3 and 15 m respectively. In recent studies, such as *Okada et al*. (2008), river plumes and a thin phytoplankton layer were reported in the same area.

The YODA Profiler observation transects of approximately 6–10 km were set up north to south from the river mouth. The sinking speed of the profiler was adjusted to approximately 0.2 ms^{-1}, which corresponds to a vertical resolution of 0.04 m. The sampling interval for data was set to 10 Hz, and the data were recorded internally. The speed of the ship was kept at approximately 2 kts in order to obtain high spatial resolution data. Several times, microstructure data were collected by TurboMAP (*Wolk et al.,* 2002) to compare with the data from the YODA Profiler. YODA Profiler and TurboMAP deployments were also carried out in the middle of Sagami Bay, Japan (35°02.5’N, 139°20.9’E), to compare turbulent intensity data from each instrument.

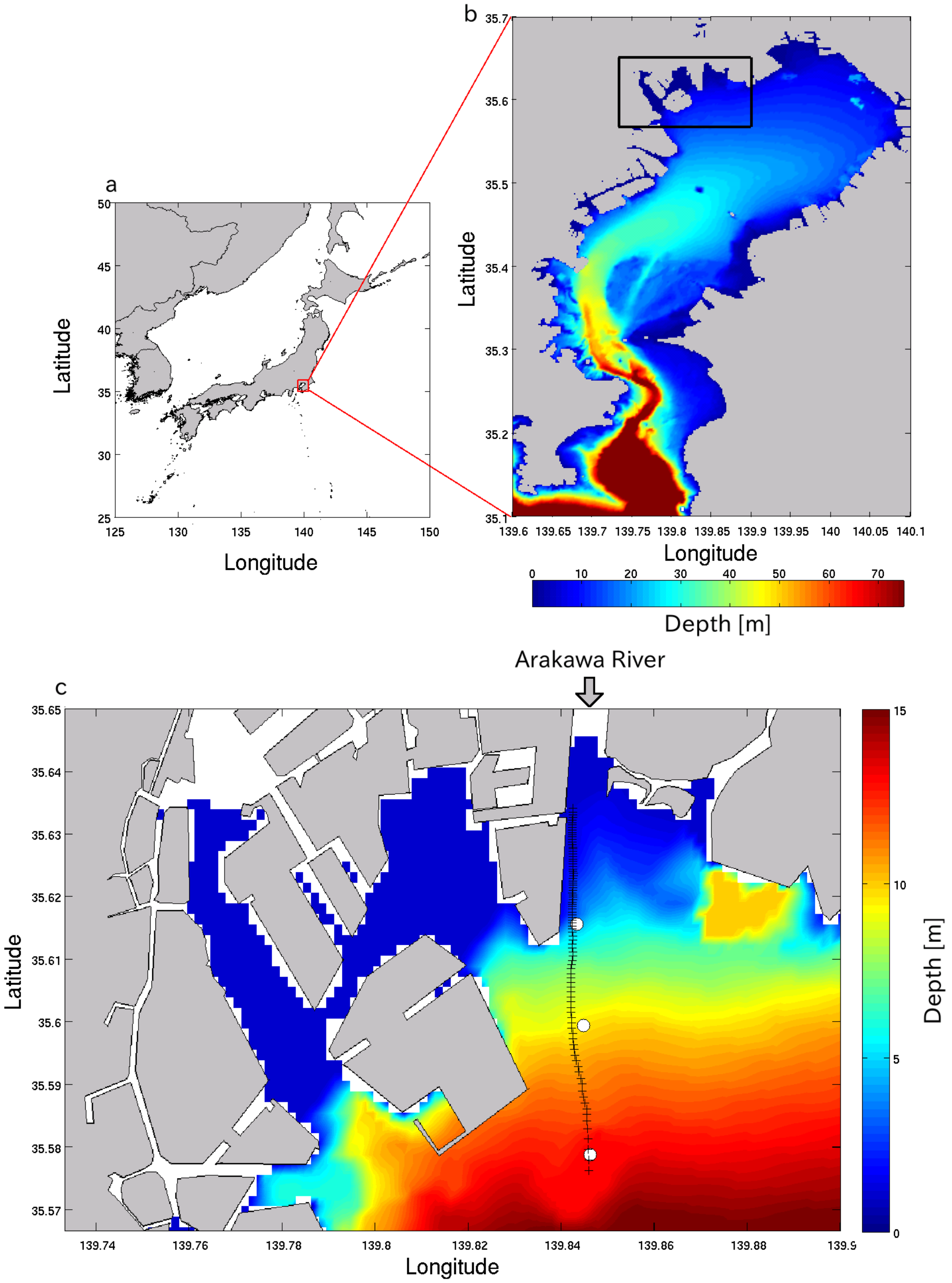

Fig. 2-4. The coastline around Japan (a), study area in Tokyo Bay (b) and around the Arakawa River mouth (c). The black rectangle in (b) is expanded in (c). The bottom panel shows the observation area and observation points of the YODA Profiler (+) and TurboMAP (solid white circles) on September 1, 2010.

2.4 Results

High-resolution data from the YODA Profiler

My efforts to obtain high-resolution data from the Arakawa River mouth using the YODA Profiler proved to be successful. Fig. 2-5 shows an example of the observed data. The data set consisted of 105 profiles in a transect (approximately 6 km). The lengths of the horizontal intervals varied between 50 and 200 m, and were largely affected by tidal currents and profiling depth. The horizontal intervals increased (decreased) as depth and ground speed increased (decreased). Each transect observation took approximately 1–2.5 hours, with the short observation intervals giving detailed snap shots of the river mouth in each tidal phase.

To compare the high-resolution data from the YODA Profiler with the conventional CTD surveys conducted by Okada et al. (2008), I converted the original high-resolution data to lower-resolution data by sub-sampling to mimic Okada et al. (2008). The low-resolution data were made from 11 of the original 105 profiles. Horizontal intervals of profiling points in the sub-sampled data set are equivalent to the results presented by *Okada et al*. (2008). The high-resolution data show small wave-like features in salinity under the river plume (Fig. 2-5a) which are not resolved in the low-resolution data (Fig. 2-5c). In Fig. 2-5b the high-resolution data show a pronounced patchy and wave-like distribution of phytoplankton below the river plume, while the low-resolution fluorescence data appear a thin layer-like feature that is a biased structure (Fig. 2-5d).

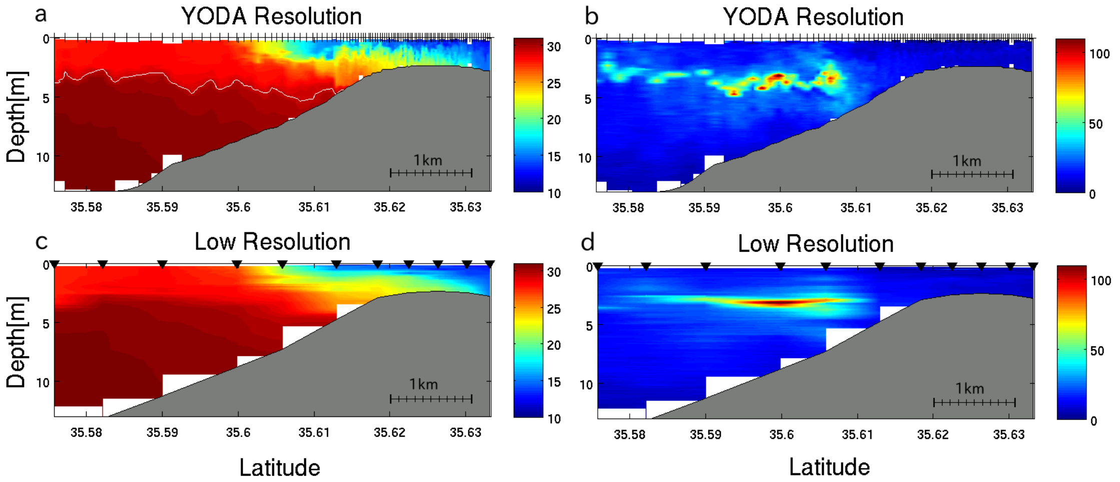

Fig. 2-5. High-resolution (upper panels) and low-resolution (lower panels) observation data of salinity [psu] (left) and fluorescence [a.u.] (right) from YODA Profiler. Tick marks and black inverted triangles on the top of panels represent profiling points. The thin white line in (a) indicates halocline of 29.5 psu.

Small-scale internal waves near the river plume

My observations found small-complicated internal wave features between low salinity water at the river mouth with more saline water underneath the river plume (Fig. 2-5 and Fig. 2-6a and b). Fig. 2-5a shows small-scale internal waves in water with salinity between 15 and 25 psu (0–3 m). Fig. 2-6a presents a detailed close-up of other features near the surface and detailed wave structures under the river plume. The R/V *Hiyodori*'s wake may have created the waves, but they appear restricted to a certain area. If the ship's wake had induced the waves at the surface, the waves should have appeared in the whole observation area as long as stratification was horizontally homogeneous. The horizontal scale of these waves is approximately 50–100 m. This scale is considerably larger than the size of the R/V *Hiyodori* (16.5 m length); thus the observed waves were unlikely to have been caused by the ship. The small waves near the surface layer could have been generated by shear instability from the river outflow. *Li et al.* (2008) identified such a phenomenon in the surface area during ebb tide by making use of a high-resolution numerical model. Small waves also appear in the sub-surface layer (Fig.

2-5a; 3–5 m, salinity between 29 and 30 psu), but the wavelengths and shapes are different from those in the surface layer. The thin white line between the two layers indicates the 29.5 psu isohaline and shows the wave features. The horizontal wavelengths in the sub-surface layer are approximately 200–500 m. Fig. 2-6b shows a sharp salinity front in the middle of the transect. The horizontal salinity gradient in the front reaches 10 psu km^{-1}, and the horizontal scale is approximately 1 km. A typical internal solitary wave was also observed near the river plume (Fig. 2-6c; latitude = 35.59). Small-scale internal solitary waves (several hundred meters) have frequently been observed by acoustic surveys (e.g., *Moum et al.,* 2003; *Nash and Moum,* 2005). The YODA Profiler was able to capture similar small-scale wave events. Combining acoustic surveys with YODA Profiler operations should improve understanding of coastal dynamics.

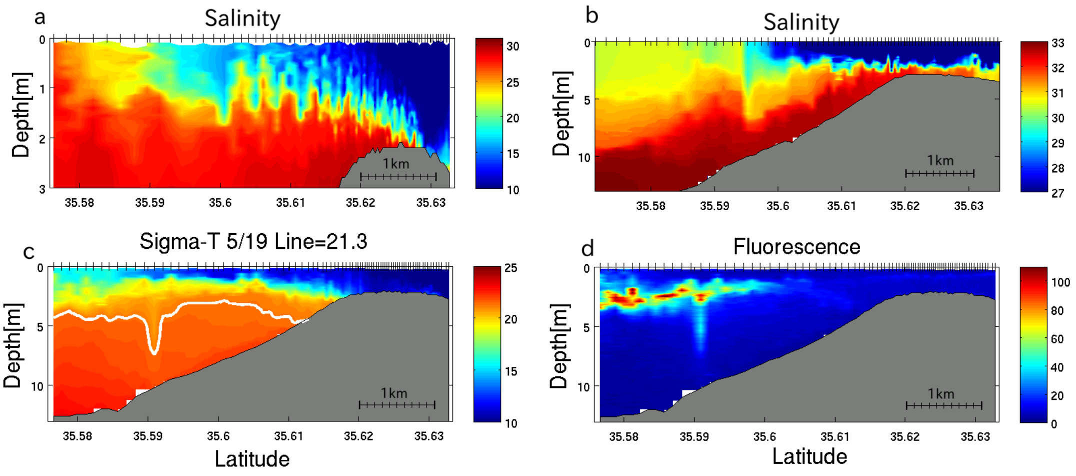

Fig. 2-6. (a) Salinity distribution near the surface (0–3m) on May 20, 2011, (b)salinity [psu] distribution on January 7, 2012 and (c) sigma-T and (d) fluorescence [a.u.] distributions on May 19, 2011. The thick white line in (c) indicates the isopycnal line of 21.3 (sigma-T).

Phytoplankton thin layer

Recent advances in phytoplankton research have revealed thin phytoplankton layers in coastal areas (e.g., Dekshenieks et al., 2001; Sullivan et al., 2010). These thin layers play a major role in production and temporal evolution of harmful algal blooms (*GEOHAB,* 2013). I have observed a typical thin phytoplankton layer in May 2011 (Fig. 2-7). A structure must meet the following four requirements in order to be considered a thin phytoplankton layer (*Dekshenieks et al.,* 2001; GEOHAB, 2013; *Sullivan et al.,* 2010):

1) The maximum concentration must exceed three times that of background values.
2) The thin layer must be present in two or more sequent profiles.
3) The full-width half-maximum (FWHM) peak must not exceed 3 m.
4) The thin layer must contain more than six data points.

The results shown in Fig. 2-7 satisfy all four requirements. The peak value of the fluorescence in Fig. 2-7a is more than 10 times larger than the background value, and the thickness and horizontal length of the layer is 1.5–2.5 m and over 3.5 km respectively in the observation area. In addition, the layer appeared in a strongly stratified layer, which was immediately below the interface between low salinity water and saline water.

Fig. 2-6d shows the thin phytoplankton layer stretched by an internal solitary wave. The thin layer is related to physical conditions, stratification, flow, shear, turbulence and buoyancy (e.g., *Dekshenieks et al.,* 2001; *Durham and Stocker,* 2012). *Dekshenieks et al.* (2001) observed a thin, highly concentrated phytoplankton layer below the pycnocline similar to the results shown in Fig. 2-7. They concluded that the increase in the stratification influences the steepness and thinness of the layer. On the other hand, a patchy phytoplankton distribution was observed during another observation (Fig. 2-5b) in which the patchy distribution appears contained within the internal wave structure (Fig. 2-5a). This feature could have been considered a thin layer if the observation had been made with a conventional CTD, as discussed in the previous section. The horizontal scale of the patches is approximately 50–200 m.

Previous studies have focused on an interaction between plankton distribution and the dynamics of internal waves. High concentrations of fluorescence patches have been found in high-frequency internal waves (*Lennert-Cody and Franks*, 1999), and plankton convergences have been observed in coastal frontal zones (*Pineda,* 1999). The observed data from the YODA Profiler reveal the detailed spatial distribution of the thin phytoplankton layer structure as well as phytoplankton patches in small-scale internal waves.

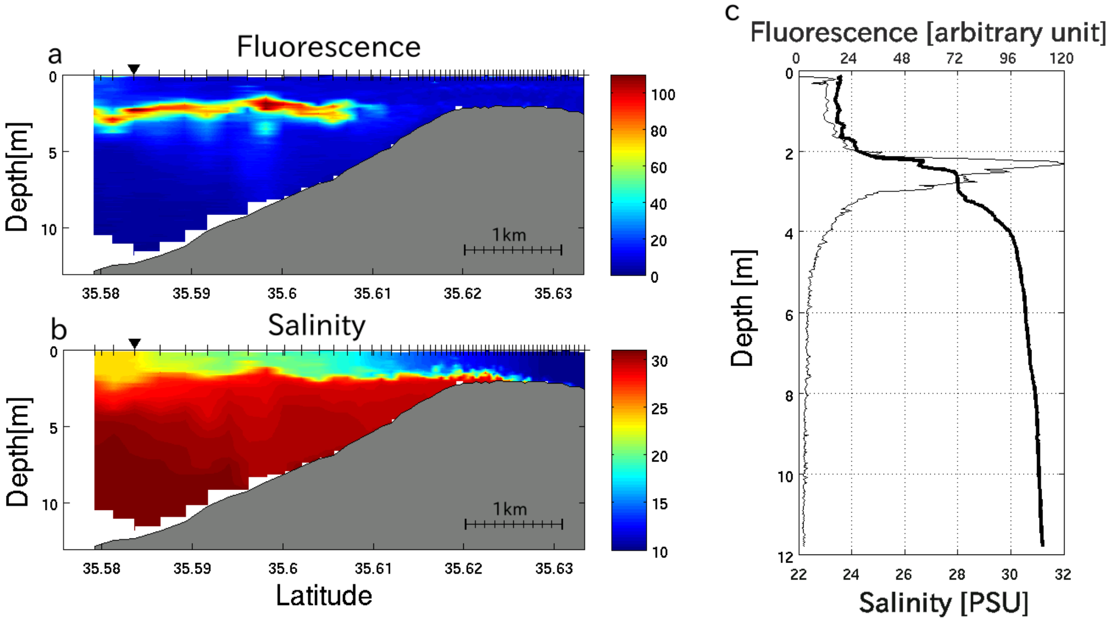

Fig. 2-7. (a) Fluorescence [a.u.] and (b) salinity [psu] observed on May 19, 2011. Panel (c) shows fluorescence (thin line) and salinity (thick line) profiles obtained at black inverted triangle points in (a) and (b).

Bottom boundary layer

The YODA Profiler sinks slowly (0.2 ms^{-1}) and stably in the water column. This property permitted us to obtain a complete set of profiling data from the sea surface to near the sea floor. Fig. 2-8a shows a sloping bottom boundary layer between 5 and 10 m depth. Low temperature water appears as the run-up on the slope, accompanied by low dissolved oxygen (Fig. 2-8c) and high turbidity water (Fig. 2-8b). Such a run-up of internal waves on a slope is described as a “bolus” or “bore” (*Helfrich,* 1992; *Wallace and Wilkinson,* 1988). The vertical displacement of the isothermal depth associated with the bore wave reaches 5 m along the slope (Fig. 2-8a). Bore waves accompanied by sediment resuspension frequently have been observed in sloping areas (e.g., *Cacchione* *and Drake,* 1986; *Hosegood et al.,* 2004; *McPhee-Shaw and Kunze,* 2002; *Van Haren,* 2005; *Yanagi et al.,* 1995). The turbidity distribution shown in Fig. 2-8b suggests resuspension due to the propagation of the bore wave and suspended sediments spreading away from the head of the bore wave toward the intermediate depth of the offshore direction (latitude = 35.61). Lateral intrusions of suspended sediments from the bottom boundary layer into the interior have been pointed out by previous observations (*Moum et al.,* 2002) and tank experiments (*McPhee-Shaw and Kunze,* 2002). Such events are important processes for the horizontal nutrient and sediment transports in the ocean. Hypoxic water (dissolved oxygen less than 3 mg/L; Nakayama et al., 2010) is also associated with bore wave and propagates into the shallow area (Fig. 2-8c). The lack of understanding of the distribution and transport processes of the bottom boundary layer associated with the hypoxic water in enclosed bays and lakes is a pressing problem (e.g., *Keister et al.,* 2000; *Nakayama et al.,* 2010). Observations with the YODA Profiler may advance the understanding of these processes.

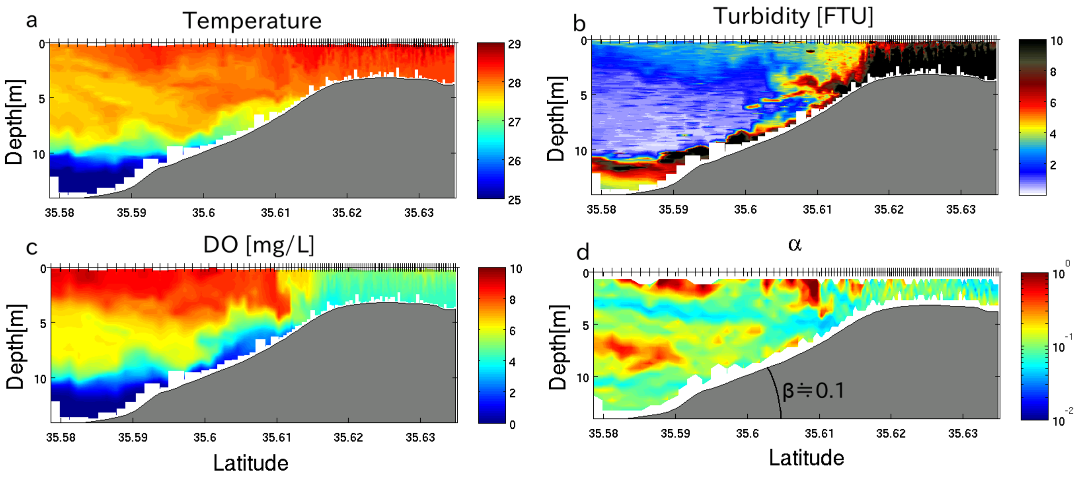

Fig. 2-8. (a) Temperature [℃], (b) turbidity [FTU], (c) dissolved oxygen [mgL^{-1}] and (d) internal wave beam angle [degrees] distributions obtained on September 18, 2012.

Internal wave reflections on the bottom slope induce a strong energy convergence in the bottom boundary layer, and the intensity depends on the relationship between the incident wave angle (α) and the slope angle (β) of the sea floor. The internal tides travel at an angle α , represented as

$$\alpha = \sin^{-1}\sqrt{\frac{\sigma^2 - f^2}{N^2 - f^2}} \tag{1}$$

where σ is the semidiurnal tidal frequency, f is the local inertial frequency and N is the buoyancy frequency. The local inertial frequency is expressed as $2\,\Omega \sin\phi$, where Ω is the Earth's rotational vector and ϕ is the latitude. The buoyancy frequency for a shallow water condition is a function of the vertical density gradient and is defined as

$$N^2 = -\frac{g}{\rho_0}\frac{d\rho}{dz} \tag{2}$$

where g is the gravitational acceleration, z is the vertical coordinate with positive upward, ρ is the local density and ρ_0 is the mean density. When the incident internal wave beam angle matches the bottom slope ($\alpha = \beta$), the wave reflection is in the critical condition, which means that reflected waves travel parallel to the slope and induce strong energy convergence along the bottom. Remarkable physical features induced by internal wave reflections in the critical angle condition were shown in recent numerical studies and tank experiments. *Venayagamoorthy and Fringer* (2006) showed complex density structures and upslope propagating fronts along the critical slope ($\alpha = \beta$). *Gayen and Sarker* (2011) noted strong energy convergence in the bottom boundary layer from a numerical model forced by barotropic tide. Tank experiments by *McPhee-Shaw and Kunze* (2002) produced sediment intrusions from a sloping bottom boundary due to internal wave reflections in the critical condition. In the northern area of Tokyo Bay, the bottom slope angle is approximately 0.1 degrees. Internal wave beam angles are approximately 0.1 degrees along the slope. Thus, the internal wave beam angles satisfied the critical angle condition for strong energy convergence induced by internal wave reflections in this period. Although bore waves along sloping areas associated with sediment resuspension and internal wave reflections were discussed by previous studies (e.g., *Cacchione and Drake,* 1986; *Cacchione et al.,* 2002; *McPhee-Shaw and Kunze,* 2002), the YODA Profiler data showed the detailed spatial structure of a bore wave in a shallow area with useful parameters, such as fluorescence, turbidity and oxygen.

Fig. 2-9a shows ray-like sediment resuspension shooting from the sloping bottom upwards toward the river mouth in the shallower area (latitude between 35.62 and 35.63). During the observation period, internal wave beam angles above the sloping bottom satisfied the critical angle condition (Fig. 2-9b) and the angle of the shooting resuspension is consistent with the internal wave beam angles and the bottom slope angle. *Gayen and Sarker* (2011) also showed a ray-like strong energy convergence off the slope induced by internal wave interaction with the bottom slope in the critical condition, which is consistent with our finding. A combination of these numerical studies and the YODA Profiler observation should provide insight into the bottom boundary processes in coastal water

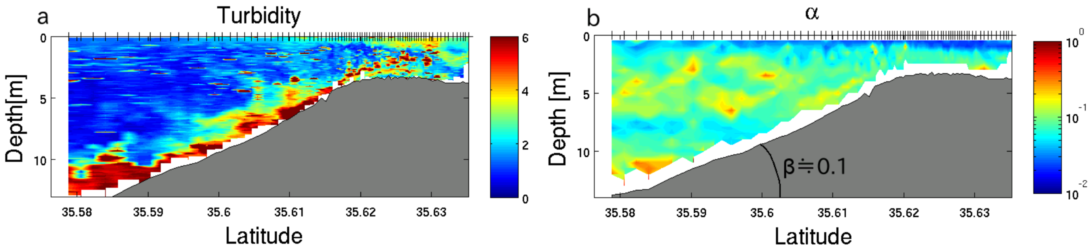

Fig. 2-9. (a) Turbidity [FTU] and (b) internal wave beam angle [degrees] distributions observed on September 1, 2010.

Temporal variation in the tidal phase

In this study, the YODA Profiler observations were done in short time-intervals of approximately 1–2.5 hours for each transect. The quickness of the transect observations allowed us to conduct several observations during available ship time. Fig. 2-10 shows three transect observations from the middle of ebb tide to the beginning of flood tide. The salinity and temperature distributions in transects (**A**) and (**B**) show a fine scale feature of low salinity and high temperature water outflowing from the river mouth and spreading over the offshore surface during ebb tide (Fig. 2-10a, b, d, e). The salinity distribution at the beginning of the flood tide (**C**) shows that high salinity water intrudes to the shallower area (generally known as a salt wedge), and the low salinity surface layer becomes thinner than during the previous observations (Fig. 2-10c). The fluorescence distribution in transect (**A**) shows a patchy and high concentration of phytoplankton around 4 m depth (Fig. 2-10j). In transects (**B**) and (**C**), the phytoplankton layer spreads out and becomes less concentrated during ebb and the beginning of flood tide (Fig. 2-10j, k, l). The distribution of the dissolved oxygen is also changed with river outflow and the phytoplankton distribution (Fig. 2-10g, h, i). The turbidity distributions show high turbidity water outflowing from the river mouth and sediment resuspension in the river mouth area (Fig. 2-10m, n, o). In contrast to the results shown in Fig. 2-8b and Fig. 2-9a, the turbidity resuspensions do not appear along the slope, since the internal wave beam angles do not satisfy the critical angle condition. The internal wave angle is steeper than the slope angle due to weaker stratification in these periods ($\alpha > \beta$, super-critical condition). The beam angle is approximately 0.3 degrees along the slope. Thus, this condition does not lead to strong energy convergence along the slope. Physical and biological features tend to change rapidly in coastal areas that are strongly affected by tidal elevation, as shown in Fig. 2-10.

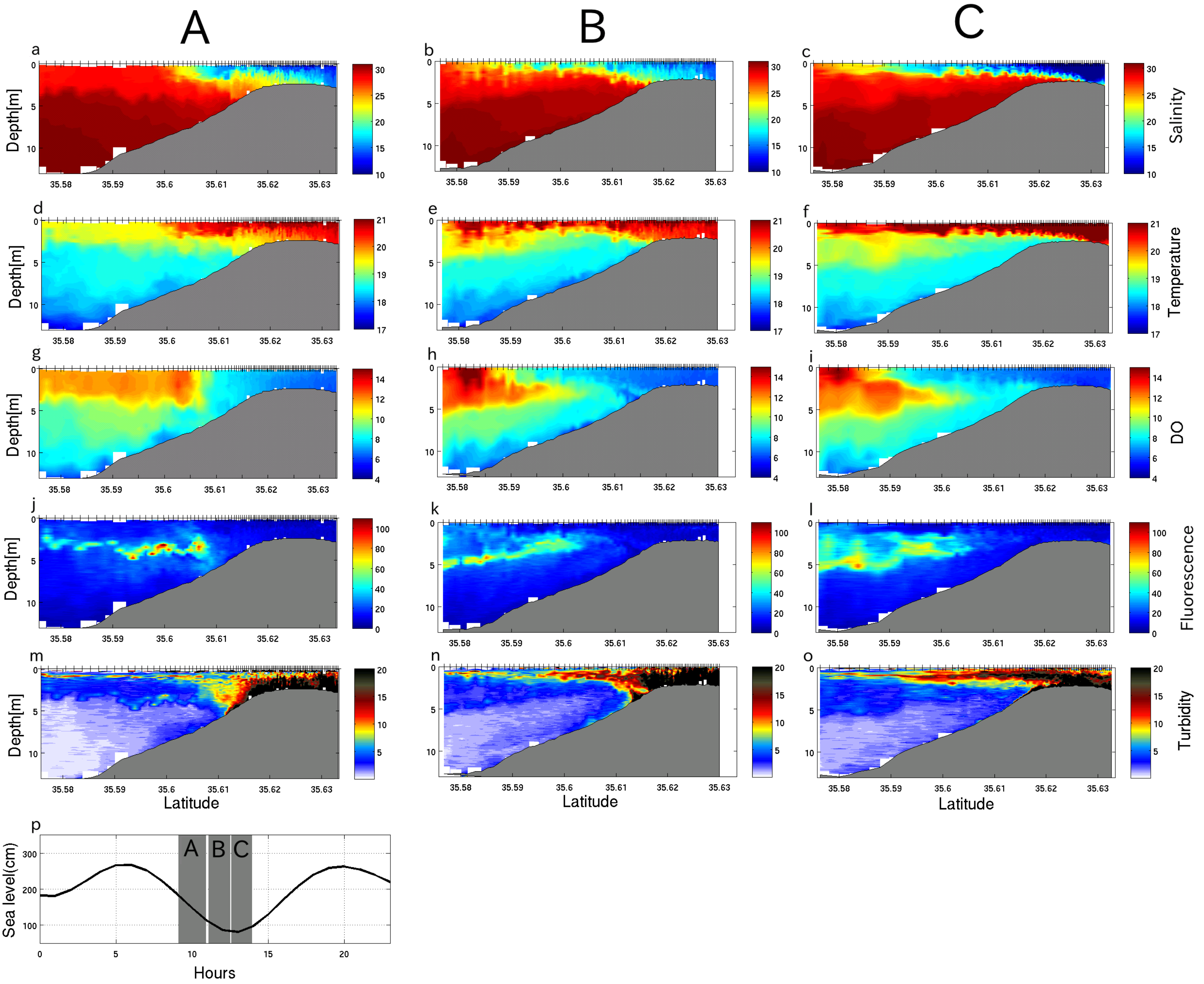

Fig. 2-10. Salinity [psu] (a, b, c), temperature [℃] (d, e, f), dissolved oxygen [mgL^{-1}] (g, h, i), fluorescence [a.u.] (j, k, l), turbidity [FTU] (m, n, l) and tidal level (p) on May 20, 2011. Shaded areas in (p) indicate observation periods: the middle of ebb (A), the end of the ebb (B) and the beginning of the flood tide (C).

2. 5 Turbulent intensity inferred from the YODA Profiler

Measurement of ocean turbulence is necessary to estimate energy flux and mass transport in the ocean. Estimating turbulent mixing is an important part of revealing diffusive processes of fresh water from rivers and sediment transport in coastal areas. Generally, the turbulent kinetic energy dissipation rate, ε, is estimated by two methods: (1) a direct turbulent shear measurement using an air-foil shear probe (*Osborn,* 1974) and (2) an indirect measurement made from a fast response thermistor probe. The first method is based on small-scale shear fluctuations, $\mathrm{d}u'/\mathrm{d}z$, and the turbulent energy dissipation rate is estimated from the isotropic formula, $\varepsilon = 7.5\,\nu\,\langle(\mathrm{d}u'/\mathrm{d}z)^2\rangle$ (*Osborn,* 1980), where ν is the kinematic viscosity of water. The second method is based on microstructure temperature fluctuations, $\mathrm{d}T'/\mathrm{d}z$, and the dissipation is determined by fitting the power spectrum to the Batchelor spectrum (*Dillon and Caldwell,* 1980; *Gibson and Schwarz,* 1963). These two methods require high-resolution data in micro scales. The spatial resolution is much smaller than the vertical resolution of the data obtained from the YODA Profiler (0.04 m). Therefore, I have developed a statistical technique to infer turbulent intensity from conductivity data.

Vertical gradient of conductivity

The conductivity probe mounted on the YODA Profiler may act as a surrogate of a fast response thermistor (*Nash and Moum,* 1999; *Washburn et al.,* 1996). The probability density function (PDF) of the turbulent energy dissipation rate, ε, follows a lognormal distribution in the ocean (*Baker and Gibson,* 1987; *Monin and Yaglom,* 1971; *Yamazaki and Lueck,* 1990). ε and the variance of the temperature gradient, χ, may hold a joint lognormal PDF (*Antonia and Van Atta,* 1975). Thus, one may relate χ with ε in terms of the joint PDF. I attempted to compare $\mathrm{d}C/\mathrm{d}z$ with turbulent velocity shear data obtained from the microstructure profiler TurboMAP operated in the middle of Sagami Bay. The turbulent velocity shear ($\mathrm{d}u'/\mathrm{d}z$) and the temperature gradient ($\mathrm{d}T'/\mathrm{d}z$) from TurboMAP show the surface mixing layer and the mixing layer around 40 m depth

(Fig. 2-11). The profile of dC/dz also shows strong fluctuations in the surface layer (0–20m) and the layer around 40 m depth, which are consistent with mixing layers observed by the microstructure profiler. Thus, I may be able to relate the dC/dz to the turbulent kinetic energy dissipation rate by making use of the following logic:

1) The rate of dissipation of turbulent kinetic energy and temperature gradient follows a joint lognormal pdf;
2) Conductivity signals follow temperature signals;
3) The rate of dissipation of turbulent kinetic energy and conductivity gradient follows a joint lognormal pdf.

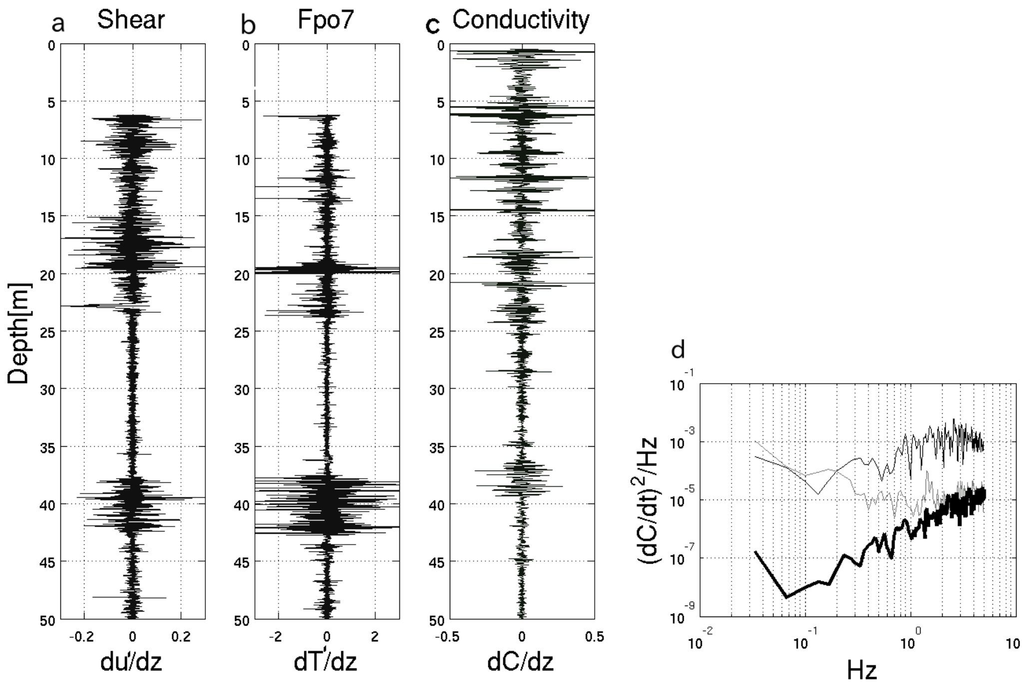

Fig. 2-11. (a) The microstructure velocity shear and the temperature gradient from (b) TurboMAP, and (c) dC/dz from the YODA Profiler in the middle of the Sagami Bay. (d) the power spectrum of dC/dt obtained in an ocean experiment (two thin lines) and in a water tank (thick line).

Estimation of ε

Nash and Moum (1999) and Washburn et al. (1996) developed methods to estimate the turbulent energy dissipation rate using high-resolution conductivity probes. Since the vertical resolution of the data from the YODA Profiler is too low to apply their methods, I developed a statistical method to estimate ε from the variance of dC/dz having assumed these two quantiles follow a joint PDF. I attempted to estimate ε from the YODA Profiler through a comparison of the PDF of ε from the microstructure profiler and the variance of dC/dz. The variance of dC/dz was estimated at every 0.5 m depth. No filtering was made before the computation for the variance estimation, since no apparent noise signals were detected (Fig. 2-11d). The PDF of the variance of the dC/dz shown in Fig. 2-12 is larger than the noise level estimated in a still water tank experiment, which was approximately 1.8×10^{-3}. The PDF of the variance of dC/dz was a bi-modal mixture lognormal distribution in the Arakawa River mouth area on September 1, 2010 (Fig. 2-12a). The turbulent kinetic energy dissipation rate obtained by TurboMAP also followed a bi-modal mixture log-normal distribution (Fig. 2-12b). The TurboMAP observation was carried out at three points in the transect (see Fig. 2-4c). Both PDFs in Fig. 2-12 have a large peak at lower intensity and a small peak at higher intensity. The QQ plot (quantile versus quantile; Fig. 2-12c) for the variance of dC/dz with ε shows a linear relationship in a log-log space. With a linear relationship of the QQ plot and a least squares method, I estimated the coefficients a and b for the following relationship:

$$\varepsilon = a \times \left[\overline{(dC/dz)^2}\right]^b \qquad (3).$$

These coefficients changed in each observation period (Table 2-1), depending on temperature and salinity conditions. The distributions of ε_C were not significantly different from ε obtained from TurboMAP across all observations (Kolmogorov-Smirnov test, $p < 0.05$). Vertical profiles of ε_C from the variance of dC/dz showed good agreement with ε obtained from TurboMAP (Fig. 2-13). The estimated ε_C from the YODA Profiler were compared with those from TurboMAP. The coefficient of determination, R^2, in the two cases shown in Fig. 2-13c are statistically significant values at 0.30 and 0.42 ($p<0.01$), from September 2010 and September 2011 respectively.

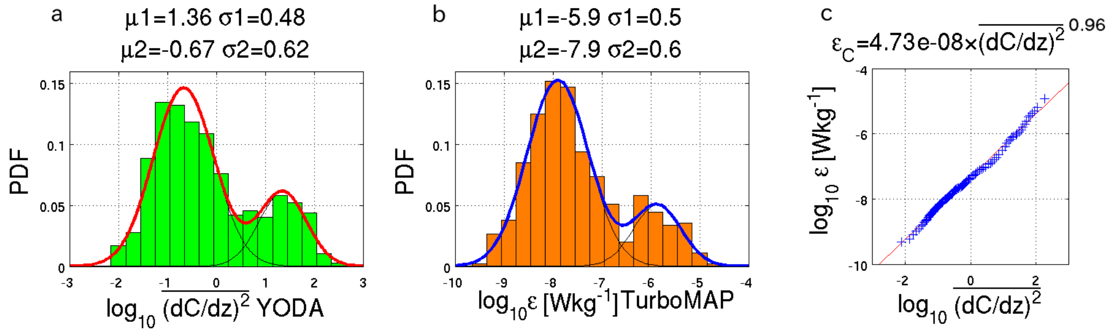

Fig. 2-12. Probability Density Function (PDF) of the variance of dC/dz from (a) YODA Profiler and ε [Wkg^{-1}] from (b) TurboMAP and (c) quantile versus quantile (QQ) plot between dC/dz and ε [Wkg^{-1}] in summer 2010.

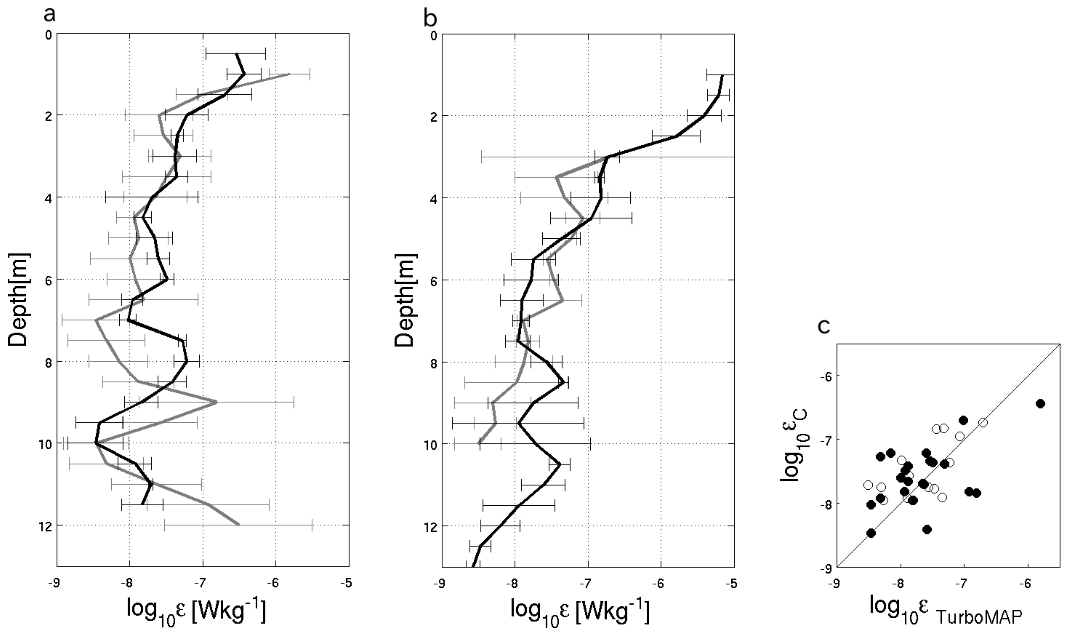

Fig. 2-13. ε [Wkg^{-1}] profiles from the YODA Profiler (black line) and TurboMAP (gray line) near the Arakawa River mouth on September 1, 2010 (a) and September 6, 2011 (b). Scatter plot (c) shows a relationship between ε [Wkg^{-1}] from TurboMAP and variance of dC/dz from the YODA Profiler in September 2010 (black solid circles) and September 2011 (white circles).

Table 2-1

Empirical coefficients *a* and *b* calculated from five separate observation periods around the Arakawa River mouth.

	a	b
September 1, 2010	4.7×10^{-8}	0.96
May 20, 2011	4.6×10^{-8}	0.71
September 6, 2011	1.7×10^{-8}	0.61
September 9, 2011	5.6×10^{-8}	0.74
June 1, 2012	1.1×10^{-7}	1.4

Turbulent mixing in the river plume and the bottom boundary layer

The statistical technique developed by this study allows us to obtain a detailed structure of the turbulent kinetic energy dissipation rate near river mouth areas. The turbulent kinetic energy dissipation rate, ε_C, and the salinity distribution in the Arakawa River mouth area on May 20, 2011, are shown in Fig. 2-14 (The salinity distribution in this Figure is the same data as in Fig. 2-10a, but the salinity color range has been changed to highlight between 28 and 30 psu). It is known that strong turbulent mixing, generated by shear instability, occurs near river mouth areas (e.g., *Goodman and Sastre-Córdova,* 2011; *MacDonald and Geyer,* 2004; *Nash et al.,* 2009). *Nash et al.* (2009) showed a high turbulent kinetic energy dissipation rate in a river mouth that reached 10^{-3} Wkg^{-1}, and *Goodman and Sastre-Córdova* (2011) showed a rate reaching 10^{-4} Wkg^{-1}. Fig. 2-14 shows the strong turbulent mixing ($\varepsilon \fallingdotseq 10^{-5}$ Wkg^{-1}) in the river plume; ε_C is weak near the surface in the offshore area (latitude < 35.6°N), while ε_C in the sub-surface layer (3–5 m) is higher than near the surface ($\varepsilon > 10^{-7}$). A sub-surface layer in the salinity interface between 29 and 30 psu is an internal wave feature associated with the high dissipation rate (Fig. 2-14). The turbulence in the sub-surface layer could be caused by the internal wave breaking in the layer. Also worth noting is that the patchy phytoplankton distribution is located in this sub-surface layer (Fig. 2-10j). This feature may indicate that internal waves and turbulent mixing can influence phytoplankton distributions.

I was able to observe a strong turbulent mixing event in a bolus-like structure (Fig. 2-15) when internal wave beam angles satisfied the critical angle condition. The temperature distribution in Fig. 2-15a shows an upslope front, a rotor-like structure and small-scale internal waves (a schematic image of the rotor is depicted in Fig. 2-15c). The scale of the rotor is approximately 1.5 km and 3 m horizontally and vertically, respectively. The aspect ratio of the rotor (turbulent patch) is restricted by the stratification in the ocean, and the typical value of the ratio is approximately 0.01 (*Rosenblum and Marmorino,* 1990). Since the rotor shown in Fig. 2-15 indicates a very small aspect ratio (0.002), the true feature of the rotor structure may consist of more than one overturn structure. The ε_C shows the strong turbulent mixing in the rotor, reaching 3×10^{-6} Wkg^{-1} (Fig. 2-15b). Rotor structures above sloping areas generated by internal waves have been reported from tank experiments (*Helfrich,* 1992; *Wallace and Wilkinson,* 1988), from numerical models (*Venayagamoorthy and Fringer,* 2006; *Vlasenko and Hutter,* 2002) and from high-resolution mooring thermistor arrays (*Van Haren,* 2009). Shoreward propagating internal waves along sloping areas generate energetic turbulent mixing due to breaking internal waves in bottom boundary layers (e.g., *Boegman and Ivey,* 2009; *Hosegood et al.,* 2004; *Ivey et al.,* 2000; *Klymak and Moum,* 2003). The turbulent mixing is enhanced by internal wave reflection near the critical angle condition. *Ivey et al.* (2000) showed the strong turbulent mixing, $\varepsilon = 10^{-6}$ Wkg^{-1}, in the critical sloping boundary using a tank experiment. This value is equivalent to our results (Fig. 2-15b). Therefore, the critical internal wave reflection may enhance the turbulent mixing in the bottom boundary layer in the Arakawa River mouth.

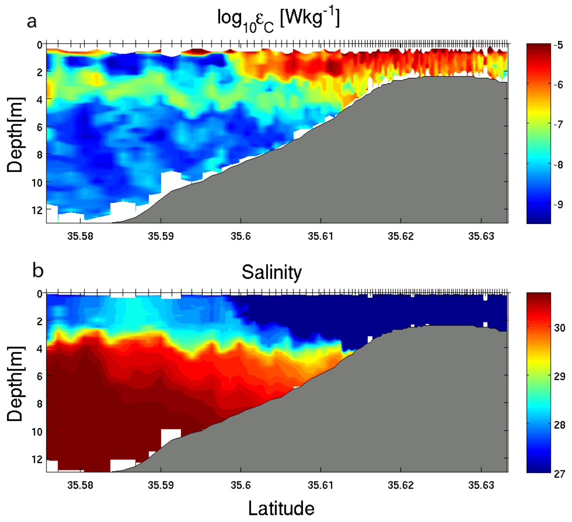

Fig. 2-14. (a) dissipation rate ε_C [Wkg^{-1}] and (b) salinity [psu] in the Arakawa River mouth on May 20, 2011.

The generating process of vortex structures is hypothesized to result from a localized intensification in the shoreward sweep flow along the slope and vertical ejections (*Boegman and Ivey,* 2009; a schematic image of a sweep and an ejection is depicted in Fig. 2-15c). The sweep and the ejection flow in the vortex structure have been reproduced by a high-resolution numerical model (*Venayagamoorthy and Fringer,* 2006) and a mooring observation (*Van Haren,* 2009). The rotor shown in Fig. 2-15 appears to be associated with the sweep and the ejection flow.

The rotor flow generates localized patches of sediment resuspension as well as the strong turbulent mixing (*Boegman and Ivey,* 2009). The turbidity distribution in Fig. 2-16 shows sediment resuspension along the slope and suspended sediments following the ring of the vortex core. The rotor structure is also associated with low dissolved oxygen water that appears to be moving toward shallow onshore (Fig. 2-16b).

The vertical turbulent diffusivity, $K\rho$, was estimated using the Osborn (1980) formula:

$$K\rho = 0.2\frac{\varepsilon}{N^2} \qquad (4).$$

The vertical turbulent diffusivity is high around the vortex structure. The diffusivity, $K\rho$, reaches 3×10^{-4} m^{2}s^{-1} (Fig. 2-16c). Boluses and breaking of internal waves contribute to the vertical mixing in the river mouth, which implies that they are important factors in the diffusive processes between the bay water and the low salinity water from the river.

Several hypotheses, observations and numerical model results concerning shoreward internal waves associated with the rotor structure and internal wave breaking have been presented in previous studies (e.g., *van Haren,* 2009; *Vlasenko and Hutter,* 2002). However, high spatial resolution in situ observation data, as presented in this study, have not been presented. This study shows that the YODA Profiler provides *in situ* data for a multiple parameter set such as this simultaneously.

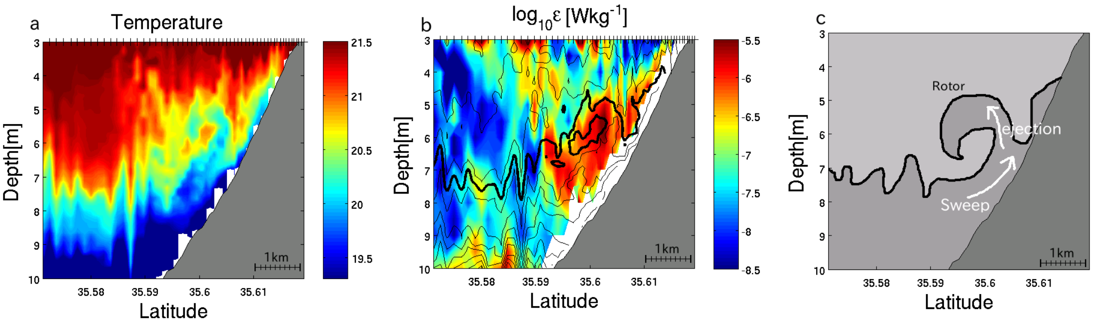

Fig. 2-15. (a) Temperature, (b) ε_C [Wkg^{-1}] distributions and (c) a schematic image of the rotor wave on June 1, 2012. The black lines in (b) indicate isothermal lines.

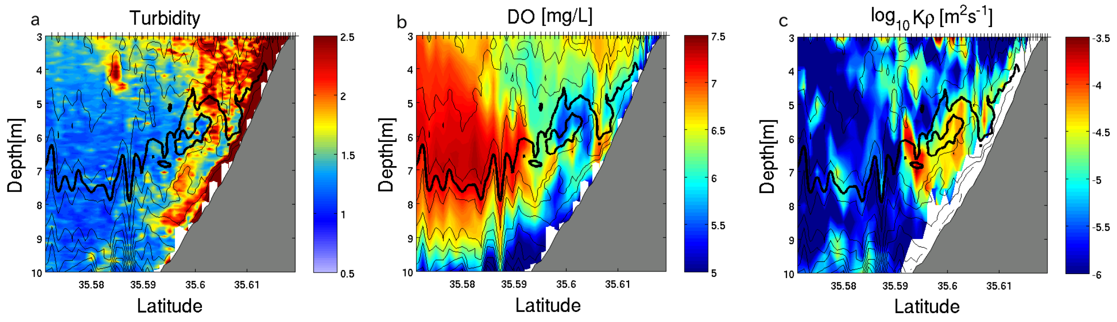

Fig. 2-16. (a) Turbidity [FTU], (b) dissolved oxygen [mg/L] and (c) K_ρ [m^{2}s^{-1}] distributions on June 1, 2012. The black lines indicate isothermal lines.

2.6 Conclusions

I have developed a new tow-yo CTD instrument, the YODA Profiler, for shallow coastal areas. This instrument allows observation of high-resolution physical and biological data in shallow coastal areas from a small vessel.

Observations in the Arakawa River mouth showed complex wave-like features and patchy distributions of phytoplankton layer as well as a thin phytoplankton layer. The bore wave and turbidity resuspension observed along the bottom slope were likely induced by internal wave reflection and interaction under the critical angle condition.

I have also developed a statistical method to estimate the turbulent energy dissipation rate, ε_C, from the variance of dC/dz. The estimated dissipation rate, ε_C, was consistent with ε from TurboMAP data in the same area. The estimated ε_C from the YODA Profiler showed detailed features of turbulent mixing in the Arakawa River mouth caused by shear instability from river outflow and internal waves. The data also showed patchy distributions of phytoplankton located in the internal wave layer, which are associated with strong turbulent mixing. The phytoplankton distribution followed the same pattern as the small waves in the layer, indicating that internal waves and turbulent mixing may affect the distribution of phytoplankton. Perhaps this feature indicates an important role in the ecosystem of the relationship between turbulence and phytoplankton distributions.

Recently developed high-performance numerical models designed for shallow coastal areas are useful (e.g., *Fringer et al.,* 2006; *Li et al.,* 2008; *Wang et al.,* 2009). However, few studies have compared detailed oceanic phenomena from numerical models against high-resolution *in situ* observation data. Detailed ocean processes should be studied by combining both numerical models and high-resolution *in situ* observations.

Chapter 3

An observational and numerical study of river plume dynamic in Otsuchi Bay, Japan

3.1 Introduction

River plumes are formed by buoyant spreading of low salinity water from rivers and are found worldwide in coastal areas (e.g, *MacDonald and Geyer,* 2004; *Nash and Moum,* 2005; *Simpson,* 1997). River discharge is known as a significant source of nutrients and sediments in coastal oceans (e.g., *Mayer et al.,* 1998; *Yin et al.,* 1997). Moreover, river plumes and their mixing mechanisms are important for coastal ecosystems (e.g., *Wang and Goodman,* 2009; *Yin et al.,* 1997). The low salinity water of river plumes is mixed vertically by the shear stress due to river outflows (*Klicher and Nash,* 2010; *MacDonald and Geyer,* 2004), tidal flows (*Kokubu et al.,* 2013), internal waves (*MacKinnon and Gregg,* 2003) and wind stress (*Moum and Smyth,* 2001).

It is well known that tidal flows largely influence river plume mixing in estuaries. Strong tidal flows cause strong shear stress in estuaries, which results in strong vertical diffusion of fresh water (e.g., *Kay and Jay,* 2003; *Simpson et al.,* 2005). Currents in tidal flows in shallow estuaries frequently exceed $O(1)$ m s^{-1} (e.g., *Kay and Jay,* 2003; *Nash et al.,* 2009). The intensity of river plume mixing due to tidal flows depends on the tidal range, the stratification and the river discharge (*Nash et al.,* 2009). The wind effect is one of the major factors in river plume mixing. Diurnal sea breeze and land breeze are ubiquitous phenomena in coastal areas (*Gille et al.,* 2003). The wind stress strongly influences turbulent mixing in the sea surface layer. *Orton et al.,* (2010) observed strong wind-induced turbulent mixing in a shallow estuary, the rate of turbulent kinetic energy dissipation reaching 10^{-5} W kg^{-1}. They also suggested that wind-induced mixing contributes to gas exchanges between the sea surface and the atmosphere. In addition, wind-induced currents enhance or restrict horizontal spreading of buoyant plumes (*Kourafalou et al.,* 1996; *Möller Jr. et al.,* 2008).

River plumes are not completely mixed at river mouths; low salinity layers spread from a river mouth to coastal areas and create a vertical salinity gradient over continental shelves far from river mouths (*Kourafalou et al.,* 1996). These low salinity layers are frequently associated with high-frequency internal waves and internal solitary waves (*Lien et al.,* 2014; *Nash and Moum,* 2005). High-frequency internal solitary waves have been found in coastal areas worldwide (*Fu and Holt,* 1982; *Moum et al.,* 2003). The breaking of solitary waves induces strong turbulent mixing near shore areas (*Bourgault et al.,* 2014; *Richard et al.,* 2013; *Vlasenko and Hutter,* 2002,). *Richard et al.* (2013) showed breaking of shoreward solitary wave packets generates mixing events in shallow areas. *Masunaga and Yamazaki* (2014) measured turbulent mixing associated with high-frequency internal waves below a low salinity layer. *Vlasenko and Hutter* (2002) reproduced breaking of solitary waves using a high-resolution numerical model. According to these previous studies, an understanding of river plume dynamics requires consideration of numerous processes (e.g., density currents, winds, tides, internal waves) and large-scale physical processes far from estuaries.

Rivers are the main source of nutrients and organic materials in the ocean. Therefore, understanding the behavior of fresh water discharge is essential to understanding ocean ecosystems in the off-Sanriku area. However, river plume mixing processes have not been studied in bays located on the Sanriku Coast. Here, I present river plume mixing processes associated with tides, internal tides and winds in Otsuchi Bay. In order to observe fine features in river plumes, the YODA Profiler (*Masunaga and Yamazaki,* 2014) was employed to use in field surveys. This profiler allows us to observe high-resolution physical structure in river plumes, internal waves and sediment resuspension in shallow coastal areas. In addition to the field surveys, I used the non-hydrostatic numerical simulator SUNTANS (*Fringer et al.,* 2006).

The next section summarizes the instrumentation used in the field surveys in Otsuchi Bay. The third section presents observed phenomena in Otsuchi Bay. The fourth section discusses river plume mixing in the bay and presents numerical simulations. The last section summarizes this study with conclusions.

3. 2 Field campaigns

Otsuchi Bay is located on the Sanriku Coast of northeast mainland Japan (Fig. 3-1). The bay mouth opens to the North Pacific Ocean. The length and the width of the bay are approximately 8 km and 3 km, respectively, while the depth at the bay mouth reaches 80 m. Three rivers, the Unosumai River, the Otsuchi River and the Kotsuchi River, flow into the bay, and the total discharge from the rivers ranges from 3 to 35 m^3 s^{-1} (*Anbo et al.,* 2005). The Sanriku Coast has steep narrow bays formed by the partial submersion river valleys; this type of coastline is called a “ria”. *Otobe et al*. (2009) reported that an estuarine gravitational forcing dominates during the winter season and an anti-clockwise current dominates during the spring and summer seasons in Otsuchi Bay. They also pointed out that wind and tidal residual currents largely influence the bay circulation. *Okazaki* (1994) showed intrusion of cold-water masses related to internal tides propagating into Toni Bay (located near Otsuchi Bay).

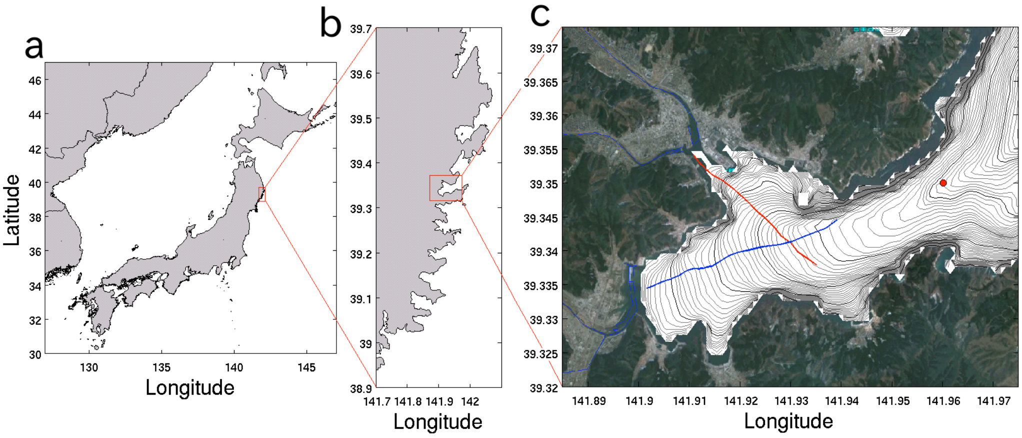

Fig. 3-1 Observation area. (a), (b) and (c) show coastlines around Japan and the Sanriku Coast and the bathymetry in Otsuchi Bay. The blue and red lines in (c) are transect observation lines on September 27, 2012. The red circle is the location of the mooring observation.

Observations were repeated numerous times between 2012 and 2014 using the YODA Profiler (*Masunaga and Yamazaki,* 2014). Table 3-1 shows a list of all field campaigns described in this chapter. The YODA Profiler is a tow-yo portable instrument and is suited for obtaining high-resolution physical structures in coastal areas. The profiler carries a conductivity-temperature-depth (CTD) and also fluorescence, turbidity and oxygen probes. The YODA Profiler can be used to estimate the rate of turbulent kinetic energy dissipation from conductivity data using a new statistical method developed by Masunaga and Yamazaki (2014). I refer to the dissipation rate estimated from the YODA Profiler as the pseudo dissipation rate, ε_P, in this chapter, since this dissipation is not estimated from a direct turbulent measurement. The sinking velocity of the profiler was set to 0.2 – 0.5 m s^{-1} during the observations. In order to obtain high-resolution data in the horizontal, the towing speed was set to approximately 2 knots. I used several fishing boats, the Senshu-maru (Shin-Otsuchi Fishery), the Daimutsu-maru (Shin-Otsuchi Fishery) and the R/V Grand-maillet (the University of Tokyo), for the YODA Profiler observations. Transect observations were carried out along two lines (Fig. 3-1c): (1) an along-bay transect from the west head of the bay (near the mouth of the Unosumai River) to the bay mouth (off-Nanamodori-misaki) and (2) a cross-bay transect from the mouth of the Otsuchi River to Shirohama-port. The depth in the observation area ranges from 5 to 45 m. The River Ray ADCP (RD instrument) was also deployed during transect surveys to obtain background current data.

In addition to the transect surveys, a mooring system was deployed at the mouth of the bay between June 10, 2013 and September 13, 2013 (96 days). The location of the mooring site is shown in Fig. 3-1. The mooring system consisted of a thermistor chain and a 600 kHz Acoustic Doppler Current Profiler (ADCP, Teledyne RD instruments). Twenty-four Tidbit v2 (Onset Computer Corporation) temperature sensors were selected to use for the thermistor chain and were mounted between 2.5 m above the bottom and 33.5 m above the bottom (vertical interval was 1 m). The sampling interval of the temperature sensors was set to 5 minutes. The ADCP was mounted near the bottom in upward looking mode and was set to record 5-minute averaged data using 50 pings and 1-m vertical bins.

Table 3-1 List of field campaigns.

Period (date)	Method	Figure
September 27,2012	Transect survey	Fig. 3-3, Fig. 3-9
January 21, 2013	Transect survey	Fig. 3-4
June 10, 2013	Transect survey	Fig. 3-2
September 11, 2013	Transect survey	Fig. 3-10
March 10, 2014	Transect survey	Fig. 3-5
June 10, 2013–September 13, 2013	Mooring survey	Fig. 3-6, Fig. 3-7, Fig. 3-8

“Figure” refers to the number of the Figure(s) showing the results from the respective survey.

3. 3 Observed data

River plumes in Otsuchi Bay

The bay water in Otsuchi Bay was covered with a thin low salinity layer during all observation periods (2012/9, 2013/1, 2013/6, 2013/9, and 2014/3); several examples are shown in Fig. 3-2 – 3.5. Water temperature in the river plume was lower than that in the bay water, except during the coldest month of March 2014. In July 2013, the river plume spread from the Unosumai river mouth to the mouth of the bay (Fig. 3-2). The thickness of the low salinity layer decreased (5–2 m) with distance from the river mouth. In addition, high turbidity water appeared in the river plume, indicating that river plumes may transport sediments and organic materials into the bay mouth from the upper stream of the river. In the summer case (September 27, 2012, Fig. 3-3), a thin low-salinity layer spread into the bay (approximately 3 m) with high fluorescence water (high concentrated phytoplankton). The river plumes generated strong stratification even in the cold winter season (Fig. 3-4 and 3-5). During the coldest month (March 2014), the cold Oyashio water flowed into the bay and the warmer river water covered the cold bay water (Fig. 3-5). Due to the Coriolis effect, observations along the cross-bay transect show the Unosumai river plume flowing along the southern coast of the Bay (Simpson 1997; Fig. 3-4).

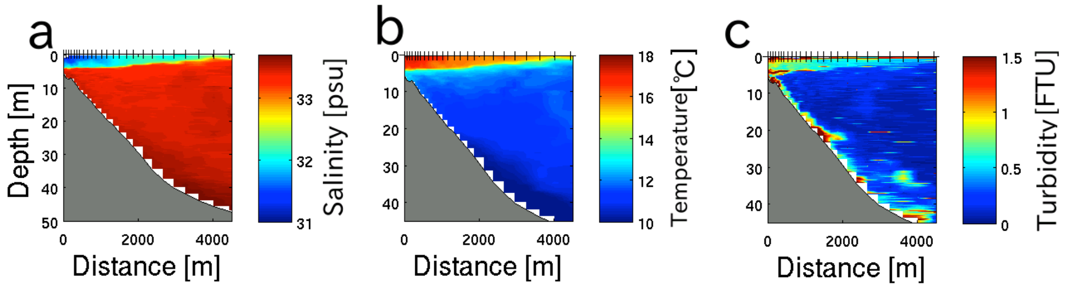

Fig. 3-2 (a) Salinity, (b) temperature and (c) turbidity distributions observed in the along-transect in the bay on June 10, 2013.

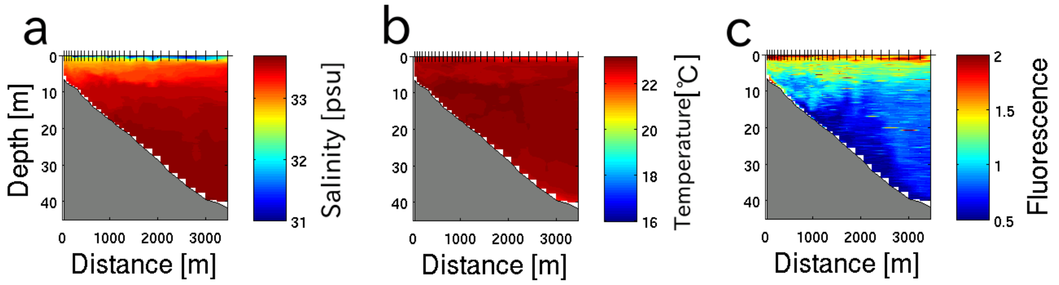

Fig. 3-3 (a) Salinity, (b) temperature and (c) fluorescence distributions observed in the along-transect in the bay on September 10, 2013.

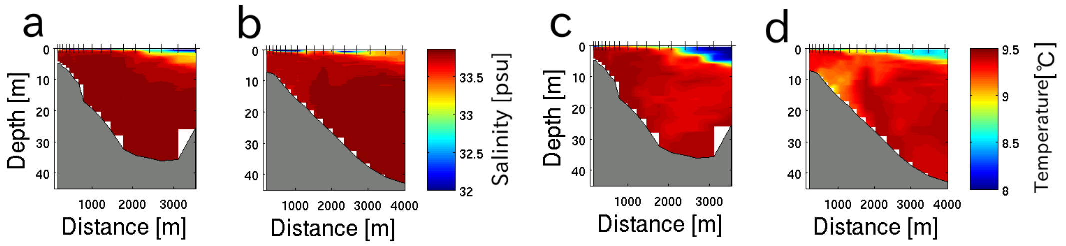

Fig. 3-4 (a, b) Salinity and (c, d) temperature distributions observed in the (a, c) cross-bay transect and (b, d) along-bay transect on January 21, 2013.

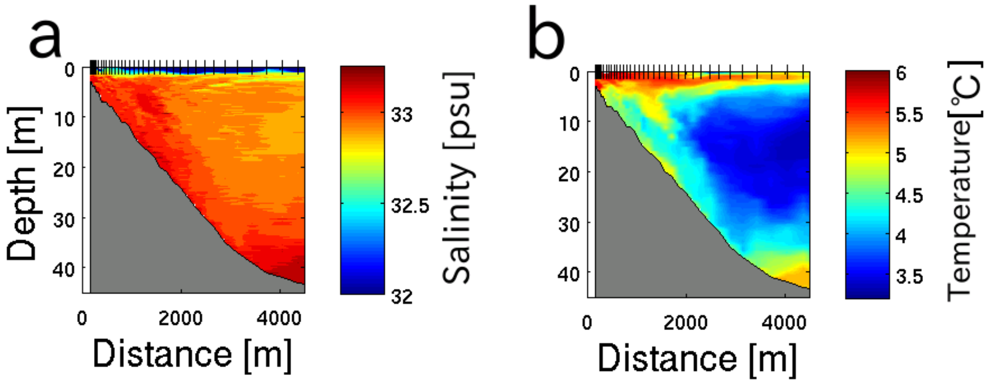

Fig. 3-5 Along-bay transect distributions of (a) Salinity and (b) temperature observed in the bay on March 10, 2014.

Background physical processes in Otsuchi Bay

Mooring data obtained in the bay show weak currents between June and the middle of the July (Julian date 160–195, Fig. 3-6c) and highly fluctuating strong currents during the summer season (Julian date 195–255, the middle of July–September, Fig. 3-6c). Like the currents, bottom temperature also fluctuated during the summer season (Fig. 3-6b). The bottom temperature dropped over 10°C within a few hour on September 9, 2013 (Julian date = 252). The maximum horizontal flow exceeded 0.5 m s^{-1} several times during the summer season. The spectra computed from the bottom current during the summer season indicated two peaks at the semidiurnal and diurnal tidal frequencies (Fig. 3-7). This indicates that the fluctuating currents and temperatures were due to internal tides propagated from the off-Sanriku Coast, although the intensity of currents and the temperature fluctuation were not related to spring-neap tidal cycle. Cold-water intrusions induced by internal tides have frequently been found in coastal areas (e.g., *Leichter et al.,* 1996; *Pineda,* 1994; *Walter et al.,* 2012). *Okazaki* (1994) also found internal tides propagating into Toni Bay during the summer season.

The internal tides induced strong baroclinic flow in Otsuchi Bay (Fig. 3-8). When the cold water intruded (receded) into the bay, it generated onshore (offshore) currents in the lower layer and offshore (onshore) currents in the upper layer (Fig. 3-8), indicative of first-mode internal wave behavior. Such flow variability with depth is referred to as “sakashio (inverse flow)” by local fishermen and is frequently found in bays along the

Sanriku Coast (*Okazaki,* 1990). The internal wave-driven vertical isothermal displacement exceeded 30 m on August 23 (Fig. 3-8a, Julian date = 235). To compare the strength of the baroclinic currents to the barotropic currents, the barotropic tidal currents induced by tides at the bay mouth can be estimated from the volume conservation formula (*Petruncio et al.,* 1998),

$$u_{barotropic} = \frac{\eta A}{T_P H W} \qquad (3\text{-}1)$$

where η is tidal range (1 m), A is the surface area of the bay (approx. $1.0 \times 10^7\,\mathrm{m}^2$), T_P is duration of flood or ebb tide (6.2 h), H is the average depth across the bay mouth (approx. 50 m), and W is the width of the bay at the mouth (approx. 2000 m). This formula gives an estimate of the barotropic current at the Otsuchi Bay mouth of $4.5 \times 10^{-3}\ \mathrm{m\ s^{-1}}$, which is 100 times smaller than the baroclinic currents. Thus, the baroclinic flow induced by internal tides dominates the flows in the bay during the summer season.

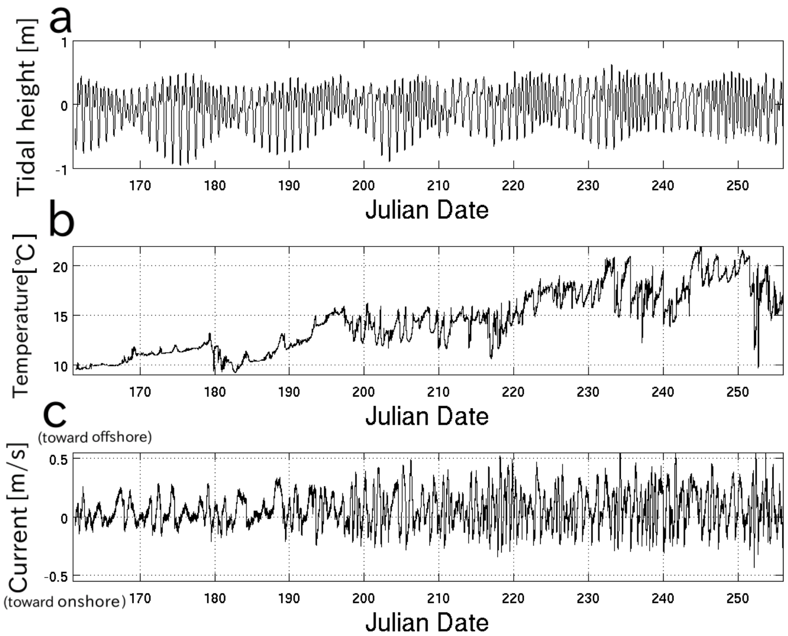

Fig. 3-6 Background physical data observed in Otsuchi Bay from the mooring system in 2013. (a) The tidal height, (b) temperature at 4 m above the bottom and (c) the along-channel current speed at 5.5 m above the bottom.

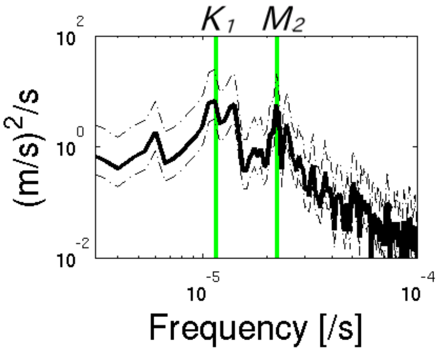

Fig. 3-7 Current spectra observed near the bottom at the mooring station. Dash-dotted lines show the 95% confidence interval. The vertical green lines indicate the diurnal frequency (*K1*) and the semidiurnal frequency (*M2*).

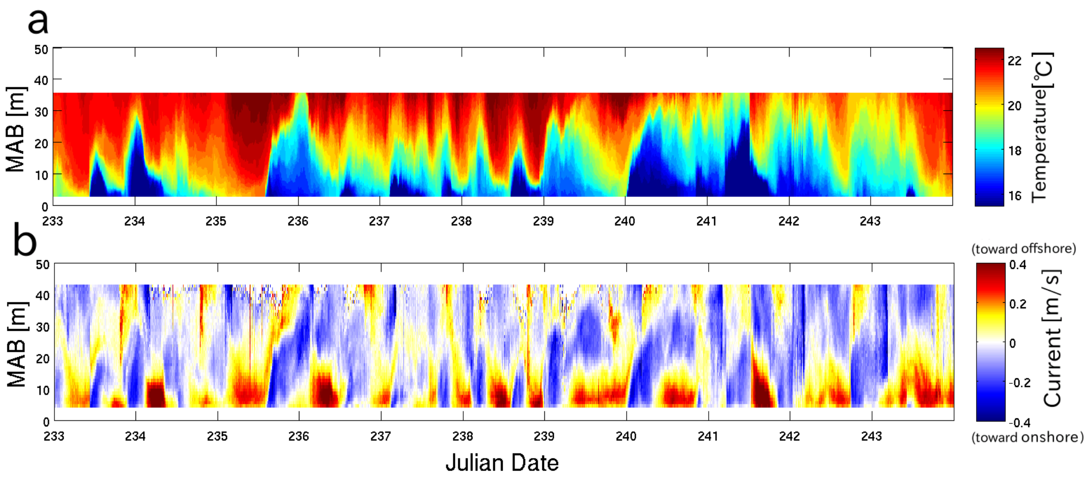

Fig. 3-8 (a) Temperature time series data from thermistor chain and (b) the along-channel current from the ADCP at the mooring station between August 21 and September 1, 2013.

River plumes and internal tides

Transect observations capture fine features related to the physical structure of the internal tides in the bay. The results clearly show a cold-water intrusion into Otsuchi Bay during the flood tide on September 27, 2012 (Fig. 3-9). The vertical isotherm displacement of the internal tide exceeds 20 m at a depth of 40 m. As the salinity did not change significantly in the cold-water mass, density changes were determined primarily by the temperature. A thin river plume layer of approximately 3 m thickness covered the observation area before the cold-water intrusion event (Fig. 3-9d, observed between 9:13–10:15, period A). The river plume appeared to be spreading vertically, and the salinity gradient decreased during the cold-water intrusion event (Fig. 3-9e, observed between 13:16–14:22, period B). In addition, the surface low-salinity layer (river plume) did not spread uniformly in the horizontal and was associated with the small-scale internal waves (Fig. 3-9e, distance = 0 – 2000). The thickness of the river plume was 3–9 m during period B. The low salinity layer was thinner above the front of cold water than other areas (Fig. 3-9ce distance ~1500 m) and appeared to be pushed upward due to the cold-water intrusion. The time interval between the two observations was approximately 4 hours; thus, the observed change in the low salinity layer was accomplished within 4 hours.

Current data obtained from the RiverRay ADCP show the onshore current (0.1–0.15 m s^{-1}) below the thermocline (20–30 m) and the offshore current (0.05–0.15 m s^{-1}) in the upper layer (5–20 m) during the cold-water intrusion event (Fig. 3-9g). The upper layer flow was opposite the lower cold layer flow, which is indicative of a baroclinic current induced by internal tides. Although the current near the sea surface (0–5 m) flows in an opposite direction from the subsurface flow (5–20 m), this shear layer may be caused by the wind stress (Fig. 3-9fg).

I also observed a change in the river plume structure likely associated with internal tides on September 11, 2013 (Fig. 3-10). Fig. 3-10 shows the salinity and temperature distributions when the cold water propagates on the slope (periods A and B) and when the cold water recedes offshore (periods C and D). The low salinity layer spread vertically after the cold-water intrusion events (Fig. 3-10 cd). In the September 2013 case, the timing of the cold-water intrusion did not coincide with the flood tide because there is a lag between the surface tidal elevation and the internal tides

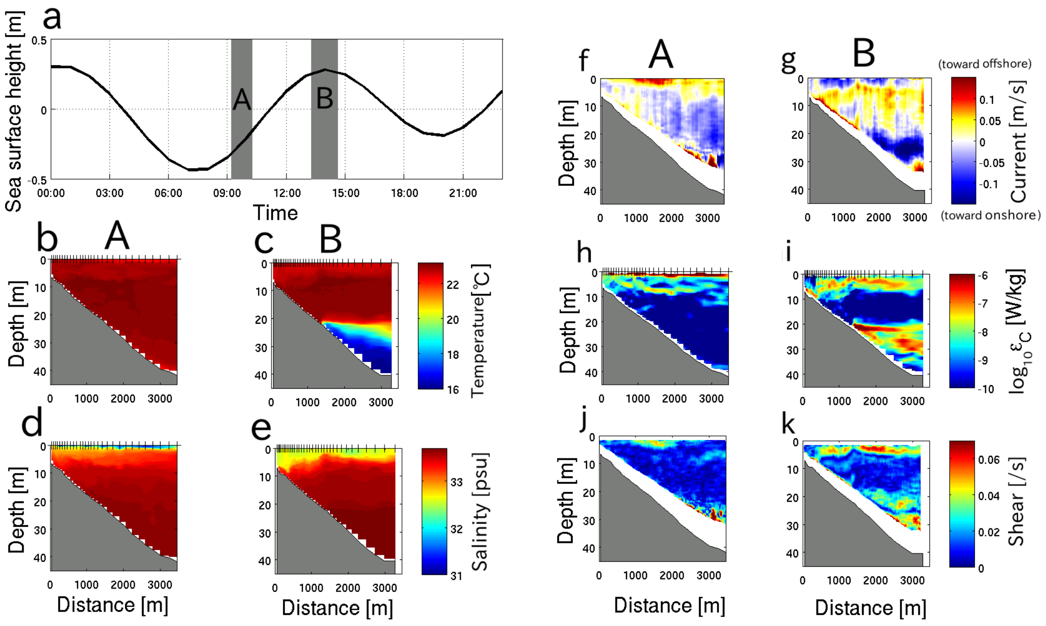

Fig. 3-9 (a) The tidal elevation, (b, c) temperature, (d, c) salinity, (f, g) along-bay current, (h, i) the pseudo dissipation rate and (j, k) current shear on September 27, 2012. Gray shaded areas in (a) indicate two observation periods, (A) before the cold-water intrusion event and (B) during the cold-water intrusion event.

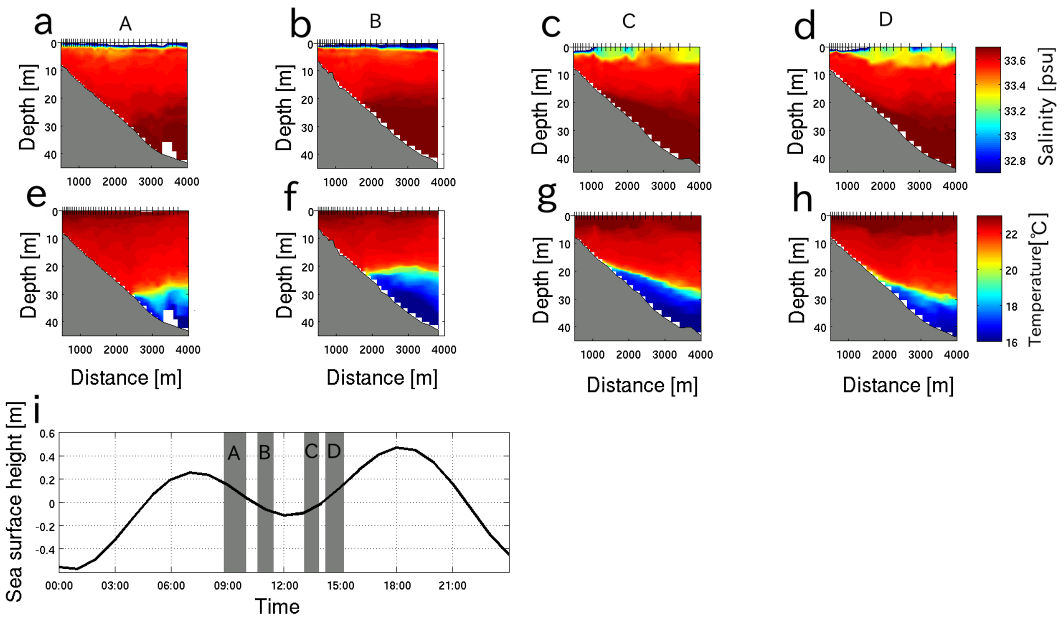

Fig. 3-10 Four snapshots of (a, b, c, d) salinity and (e, f, g, h) temperature distributions during the cold water intrusion event on September 11, 2013. Panel (i) shows the tidal elevation and four observation periods, (A), (B), (C) and (D).

3. 4 Discussion

River plume mixing induced by internal tides

In order to evaluate the mixing intensity in the river plume during the cold-water intrusion event, I estimated the vertical eddy diffusivity, K_Z, from the salinity distribution. Assuming that the lateral diffusion and the advection are weak, the rate of change in salinity is expressed as the following one-dimensional diffusive equation,

$$\frac{\partial S}{\partial t} = K_Z \frac{\partial^2 S}{\partial z^2} \qquad \text{(3-2)}$$

where S is the salinity, t is time and z is the vertical coordinate. The solution for an initial condition given by a point source with total salinity mass per unit length M (or the salinity integrated over the water column) at $z=0$ is given by

$$S = \frac{M}{\sqrt{4\pi K_Z t}} \exp\left(-\frac{z^2}{4K_Z t}\right) \qquad \text{(3-3)}$$

This formula is equivalent to the Gaussian probability density function with a mean ,0 ,and a standard deviation, $\sqrt{2K_z t}$. Then, the relationship between the standard deviation, σ, and the vertical diffusivity, K_Z, can be expressed as (*Hasegawa et al.,* 2008; *Ledwell et al.,* 2000)

$$\sigma^2 = 2K_Z t \rightarrow K_Z = \frac{1}{2}\frac{\Delta\sigma^2}{\Delta t} \qquad \text{(3-4).}$$

In this study, the salinity in the surface layer is lower than background value. Therefore, we estimated σ using salinity data with

$$-\int_0^{\sigma} S(z) - S(D_{base}) dz = \text{ 68\% of } -\int_0^{D_{base}} S(z) - S(D_{base}) dz \qquad \text{(3-5)}$$

where D_{base} is the lower limit of the depth integration. According to the observed data set, the river plume does not influence the salinity field deeper than a depth of 10 m . Therefore, I assumed that D_{base} is 10 m. I computed the change of the standard deviation, $\Delta\sigma$, between two transect surveys (between periods A and B on September 27, 2012 shown in Fig. 3-9de and between periods B and C on September 11, 2013 shown in Fig. 3-10cd) to estimate the vertical diffusivity. The standard deviation σ was estimated from horizontally-averaged salinity profiles in each transect survey. Fig. 3-11 shows the change of the salinity gradient and σ during each period. $\Delta\sigma$ is approximately 1.0 m and 2.3 m for the 2012 and 2013 cases, respectively, while the time interval is approximately 4 hours and 2.5 hours in the 2012 and 2013 cases, respectively. These values provide an estimated K_Z of 3.5×10^{-5} m^2 s^{-1} and 3.0×10^{-4} m^2 s^{-1} for the 2012 and 2013 cases, respectively. In general, the relationship between the rate of turbulent kinetic energy dissipation rate, ε, and the vertical eddy-diffusivity is expressed as followed (*Osborn,* 1980)

$$K_\rho = \gamma_{mix} \frac{\varepsilon}{N^2} \qquad (6)$$

where γ_{mix} is the efficiency factor (often referred to as mixing efficiency) and N is the buoyancy frequency. Making use of the estimated K_Z from the river plume data, this formula provides the rate of turbulent kinetic energy dissipation as

$$\varepsilon = \frac{N^2 K_Z}{\gamma_{mix}} \qquad (7).$$

where N^2 in the surface layer (0–10m depth) was 5.8×10^{-4} s^{-2} and 4.1×10^{-4} s^{-2} in September 2012 and 2013 respectively. I assumed the maximum efficiency factor of $\gamma = 0.2$ (*Osborn,* 1980) to estimate a conservative dissipation rate from the salinity distributions. The estimated ε from K_Z and N^2 are 1.0×10^{-7} W kg^{-1} and 6.0×10^{-7} W kg^{-1} in September 2012 and 2013, respectively.

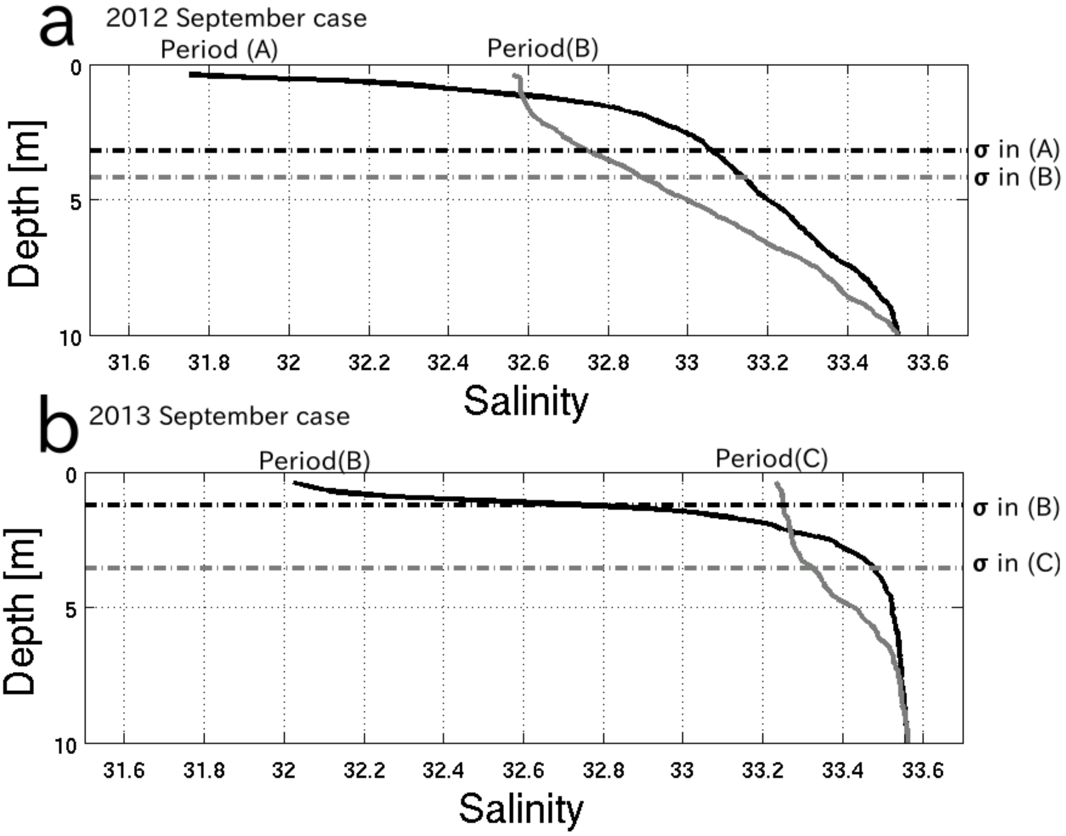

Fig. 3-11 Average salinity profiles during period (A) and period (B) on September 27, 2012 (Fig. 9), and period (B) and period (C) on September 11, 2013 (Fig. 10). Dash-dotted lines indicate the standard deviation in each period.

The YODA Profiler allows me to estimate the pseudo dissipation, ε_P, by making use of the variance of vertical conductivity gradients (*Masunaga and Yamazaki,* 2014). The estimation of ε_P from the profiler needs a background probability density function (PDF) of ε from a separate direct microstructure measurement to estimate coefficients, *a* and *b* in the following formula,

$$\varepsilon_P = a\left[\overline{(dC/dz)^2}\right]^b \qquad (3\text{-}8).$$

In order to estimate background PDF of ε, I conducted a TurboMAP-Glider (*Foloni-Neto et al.,* 2014) survey in Otsuchi Bay on September 27, 2012. The estimated coefficients, *a* and *b*, are 1.42×10^{-7} and 1.37, respectively, for the September 2012 case. *Masunaga and Yamazaki* (2014) describe the details of the estimation method of ε_P

using conductivity data. The pseudo dissipation, ε_P, inferred from the YODA profiler showed a subsurface turbulent layer (2-m–10-m depth) during the cold-water intrusion (Fig. 3-9i). The order of ε_P in the subsurface layer is 10^{-7} W kg^{-1}, which is consistent wth ε estimated from the salinity distributions. The turbulent intensity is also high at the front of the cold-water mass and reaches $\varepsilon_P = 10^{-6}$ W kg^{-1}.

The current shear computed from the RiverRay survey shows a strong shear layer in the subsurface between the onshore surface flow and the offshore subsurface flow (Fig. 3-9k). According to weather data obtained by AMEDAS Miyako Station (Japan Metrological Agency), a typical diurnal land-sea breeze occurred along the Sanriku Coast in September 2012. The wind direction was onshore in the morning and offshore in the afternoon. The maximum wind speed reached approximately 10 m s^{-1}. The wind condition between Otsuchi Bay and Miyako Station can be expected to be similar, since AMEDAS Miyako Station is located approximately 30 km north of Otsuchi Bay. Assuming that the diurnal breeze occurred in Otsuchi Bay, the offshore (onshore) surface flow in the morning (afternoon), shown in Fig. 3-9fg, was probably due to the diurnal sea-land breeze. The strong shear layer was caused by wind-induced onshore flow and offshore flow due to internal tides. Therefore, the combined effects of internal tides (cold-water intrusion) and winds have the potential to generate strong turbulent mixing in the river plume.

Numerical simulation of river plume mixing in the bay

In order to understand the observed features, I employed the nonhydrostatic SUNTANS model of *Fringer et al.* (2006). I used a two-dimensional (x-z) numerical domain with a length of 30 km. The bathymetry consisted of a 10 km long river region with a depth of 1.5 m, a 10 km long slope region, and a 10 km long region with a depth of 80 m (Fig. 3-12). The slope in the domain is similar to the along-channel slope in Otsuchi Bay. The horizontal grid resolution, Δx, is 100 m, and the number of vertical grid cells is 41 in the deepest portion in the domain. To refine the grid in the surface river plume, the cell size is stretched in the vertical direction; the minimum and the maximum vertical cell sizes are 0.14 m and 7.1 m, respectively. The time step is set to

10 s. The shallow river boundary is forced by a constant river discharge of an inflow velocity of 0.06 m s^{-1}, and the inflow salinity is set to 0. Assuming that the width of the river mouth is 100 m, the river discharge is 9.0 m^3 s^{-1} in the numerical simulation. The initial salinity is constant throughout the domain and is set to 33.6. The initial temperature distribution is constant in the horizontal but the vertical profile is initialized with field surveys on September 27, 2012. No heat flux model is employed, as the timescale of the simulations is too short to be affected by thermally-driven stratification.

To investigate the combined effects of the barotropic tide, the baroclinic internal tide and the wind stress, I employed six forcing scenarios in the numerical simulations. All scenarios included the river inflow as the purpose of this study was to investigate the impact of the forcing on the river plume stratification:

(1) *No forcing (only river discharge).*

(2) *Barotropic tidal forcing*. The frequency and the amplitude of the sea-surface elevation were set to the *M2* tidal frequency and 1 m, respectively, which reproduces the observed sea-surface heights in Otsuchi Bay.

(3) *Baroclinic internal tidal forcing*. In order to reproduce observed internal tides in Otsuchi Bay, the numerical domain was forced by imposing the first-mode internal wave horizontal velocity profile at the ocean boundary. The frequency and the velocity amplitude were set to the semidiurnal *M2* tidal frequency and 0.2 m s^{-1}, respectively. This velocity amplitude is selected to reproduce the internal tide and the cold-water intrusion observed in September 2012 and 2013.

(4) *Combined forcing of the barotropic tide and the baroclinic internal tide.*

(5) *Wind forcing*. The wind at 10 m above the surface was idealized as a diurnal sea-land breeze in the x-direction with $U_{10}=u_w \times sin(2\pi t/T_{\mathrm{day}})$, where T_{day}=24 hr and u_w is the maximum wind speed. Two wind speeds were simulated, namely a weak breeze of 5 m s^{-1} and a strong breeze 10 m s^{-1}. The wind stress on the surface was then given by $\tau_w=\rho_{air}\ C_d\ U_{10}\ |\ U_{10}|$, where the air density was ρ_{air}= 1.2×10^{-3} kg m^{-3} and the drag coefficient as C_d= 1.5×10^{-3}.

(6) *Combined forcing of the barotropic tide, the baroclinic internal tide and diurnal winds.*

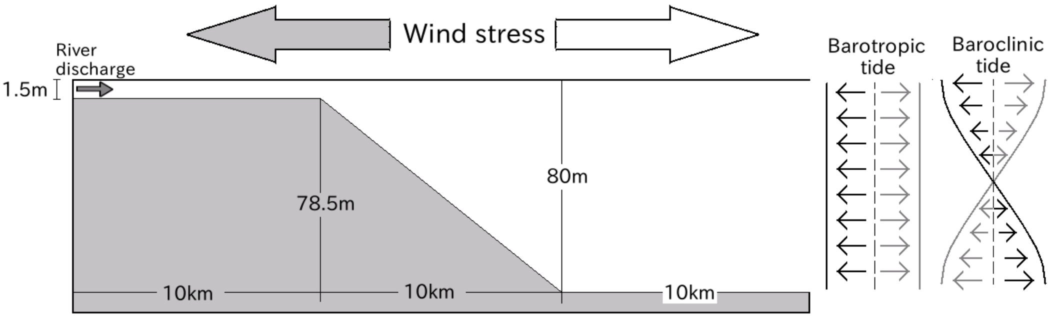

Fig. 3-12 Schematic of the model domain. The right side is the shallow river boundary and the left side is the velocity-specified ocean boundary.

(1) *No forcing (only river discharge)*

Fresh water outflowed into the bay and caused a thin fresh water layer in the no forcing condition (only river discharge). The river plume induced a weak offshore flow (approx. 0.06 ms^{-1}) near the surface and drove an onshore flow below the river plume (Fig. 3-13i). The thickness of the layer was less than 2 m (Fig. 3-13a). A strong stratification due to the river discharge restricted river plume mixing. The average Richardson number, $Ri = N^2/(du/dz)^2$, between the river plume and the ambient bay water was approximately 100, which is far above the critical value, 0.25, for shear-induced turbulent mixing. Therefore, the buoyant river plume did not generate significant mixing.

(2) *Barotropic tidal forcing*

Sea surface elevations due to the barotropic tide caused strong currents at the river mouth and generated saline water intrusions into the river (salt wedge) during the flood tide (Fig. 3-15b, distance between 6000 and 10000 m). The tidally-driven currents reached 0.6 m s^{-1} at the edge of the river mouth (not shown) and approximately 0.1 m s^{-1} at a depth of 10 m (Fig. 3-13j). The combined effects of the river discharge and the barotropic flow generated baroclinic flows during ebb tides, and the flow speed reached 0.2 m s^{-1} near the sea surface (Fig. 3-13j). These strong currents induced mixing between the river plume water and bay water (Fig. 3-15bj). In addition, a series of internal solitary waves was generated at the river mouth and released into the offshore (Fig. 3-13bj, 3-15bj). On the other hand, the barotropic tide did not cause much mixing of the river plume far from the river mouth; the current speed was less than 0.03 m s^{-1} at a depth of 50 m (Fig. 3-14j).

(3) *Baroclinic tidal forcing*

Numerical simulations forced by the first-mode internal tide reproduced the cold-water intrusion event along the slope, as depicted in Fig. 3-16, which shows a good agreement with the observations shown in Fig. 3-9bc. The baroclinic tide caused strong currents far from the river mouth (middle of the bay, Fig. 3-14k). The flow speed due to the baroclinic internal tide reached 0.3 m s^{-1} near the surface and 0.6 m s^{-1} in the bottom boundary layer at a depth of 50 m. The strong current in the bottom boundary layer due the internal tide is consistent with the mooring data in Otsuchi Bay (Fig. 3-8b). Meanwhile, the baroclinic tide did not induce a strong current near the river mouth, since the internal tide did not propagate into the shallow river mouth area (Fig. 3-13k). Because the flow speed at 10 m depth was less than 0.05 m s^{-1}, the fresh-water plume spread over the bay without strong mixing near the river mouth, although the baroclinic currents induced river plume mixing in the middle of the bay.

(4) *Combined forcing of the barotropic tide and the baroclinic tide*

Numerical results forced by both barotropic and baroclinic tides showed strong currents in both shallow and deep areas which resulted in enhanced river plume mixing in both the shallow river mouth and in the middle of the bay. In addition to large-scale motions, the internal tide caused small-scale high-frequency onshore internal solitary waves (Fig. 3-15cdkl). The high-frequency solitary waves were generated far from the river mouth, and the direction of the waves was opposite to those in the barotropic forcing case. Therefore, solitary waves caused by the baroclinic tidal forcing are completely different phenomena from those caused by the barotropic forcing. It is well known that internal solitary waves enhance turbulent mixing (e.g., *Moum et al.,* 2003;

Vlasenko and Hutter, 2002), and my results indicate that internal solitary waves driven by the shoaling internal tide may be important contributors to river plume mixing in the bay.

(5) *Wind forcing*

Numerical results from a weak and strong sea-breeze case showed the development of wind-driven recirculation due to the wind stress. The intensity of the current speed caused by winds was approximately 0.05 m s^{-1} and 0.1 m s^{-1} for the weak and strong breeze case, respectively (Fig. 3-13mn). The weak breeze (5 m s^{-1}) did not significantly contribute to river plume mixing (Fig. 3-15em), although the strong breeze (10 m s^{-1}) enhanced river plume mixing in the bay (Fig. 3-15fn). Fig. 3-17 shows the location of the plume front changed by wind forcing. The strong land breeze drove the river plume offshore and back onshore during the sea breeze phase (Fig. 3-17) by a distance of approximately 5 km (Fig. 3-17).

(6) *The combined forcing (the barotropic tide, the baroclinic tide and the wind forcing)*

Fig. 3-18 shows the surface salinity at 10 km from the river mouth for all 8 simulations. For the no-forcing condition, the salinity rapidly decreases to zero (Fig. 3-18 time = 90 – 100) and fresh water flowed from the bay with little mixing because the vertical mixing in the river plume is extremely low. These results indicated that, in the absence of forcing, the river plume flows out into the open ocean. The 5 m s^{-1} diurnal wind case also shows weak mixing and there is little difference between cases "Barotropic + Baroclinic tide" and "Barotropic + Baroclinic tide + 5 m s^{-1} wind" (Fig. 3-18). Therefore, river plume mixing due to the weak diurnal breeze (5 m s^{-1}) was much weaker than other effects. In other cases, surface salinity gradually decreased with fluctuations due to tides and winds.

In order to evaluate river plume mixing in the numerical simulations, I defined the ratio of river plume mixing as follows,

$$R_{MIX} = \frac{S_{Surf}}{S_0} \qquad (3\text{-}9)$$

where S_{Surf} is the surface salinity and S_0 is the mean salinity in the water column. R_{MIX} = 1 when complete vertical mixing occurs in the water column. Fig. 3-18b shows the river plume mixing ratio, R_{MIX}, averaged between 110 and 158 hours (48 hours, approx. 4 tidal cycle and 2 diurnal cycle) at 10 km from the river mouth. The ratio in the "Barotropic tide", "Baroclinic tide" and "10 m s^{-1} wind" cases ranges from 0.35 to 0.56. Therefore, these three forcings are equally important for river plume mixing in the bay. Numerical simulations using the three combined forcings (the barotropic tide, the baroclinic tide and 10 m s^{-1} wind forcing) show strong shear flows near the surface and strongly mixed river plume water (Fig. 3-13hp, 3-14hp, 3-15hp). Surface currents were enhanced when the direction of the tidal flow matched the wind direction. The mixing ratio is 0.80 in the combined forcing case with 10 m s^{-1} winds. In addition, salinity and the thickness of the river plume rapidly changed over a time scale of $O(1)$ hour, which is consistent with the field observations. Therefore, the combined wind, barotropic and baroclinic effects play an important role in mixing processes and dynamics of the river plume in Otsuchi Bay.

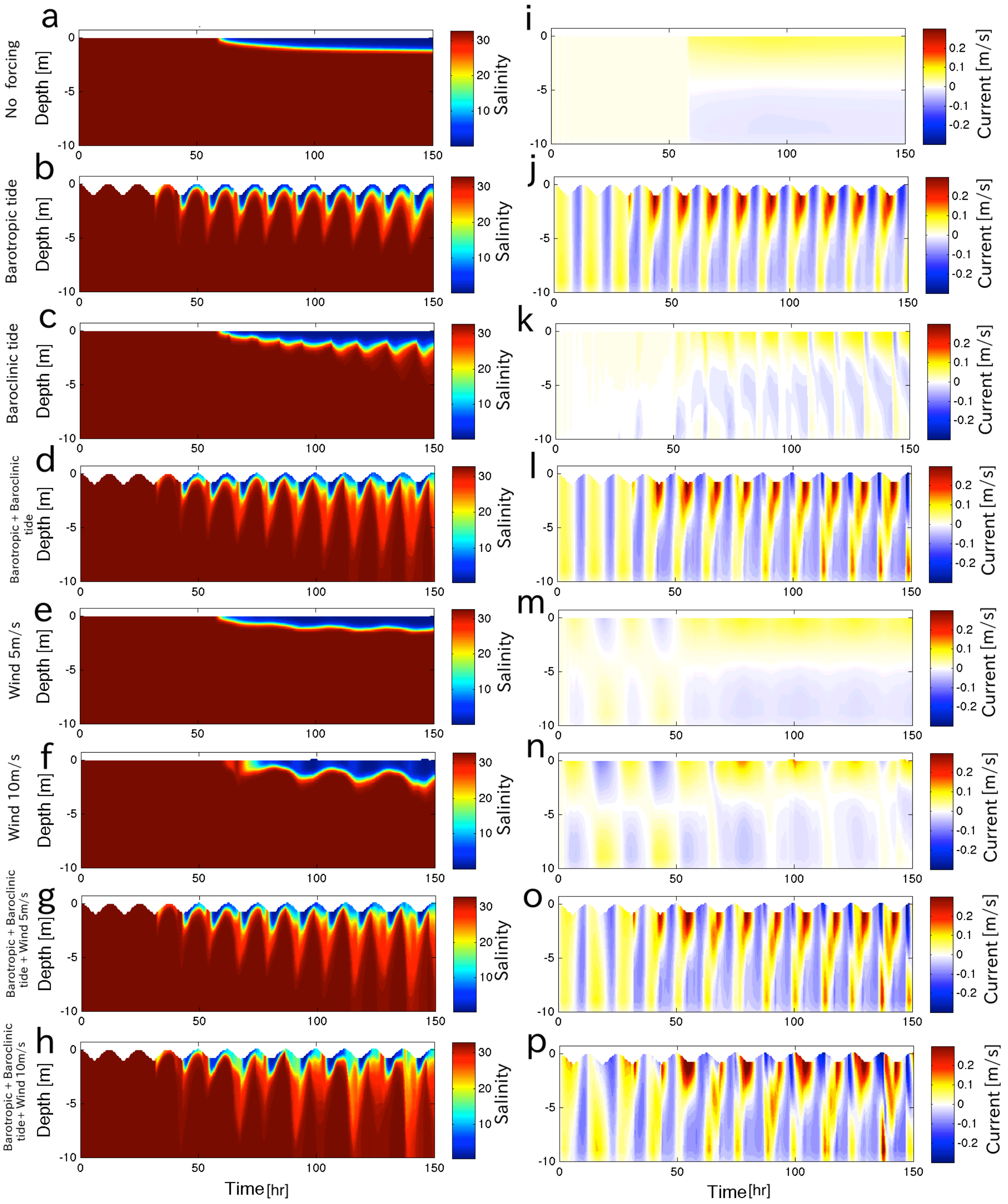

Fig. 3-13 (a–h) salinity and (i–p) horizontal current time series at 10-m depth from numerical simulations forced by (a, i) the only river discharge, (b, j) barotropic tides, (c, k) baroclinic (internal) tides, (d, l) barotropic and baroclinic tides, (e, m) 5 m s^{-1} diurnal winds, (f, n) 10 m s^{-1} diurnal winds, (g, o) barotropic and baroclinic tides with 5 m s^{-1} diurnal winds, and (h, p) barotropic and baroclinic tides with 10 m s^{-1} diurnal winds.

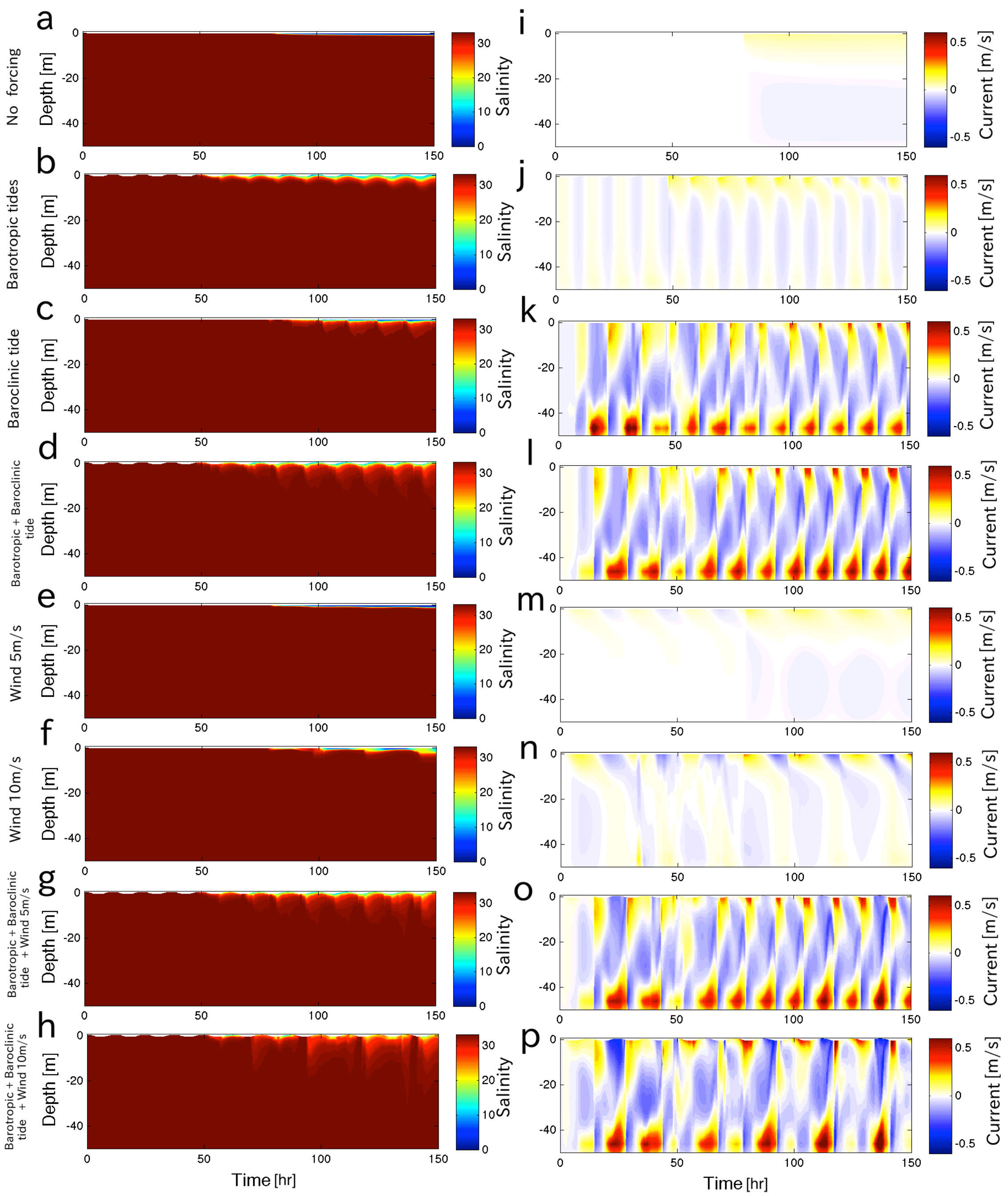

Fig. 3-14 (a–h) salinity and (i–p) horizontal current time series at 50-m depth from numerical simulations.

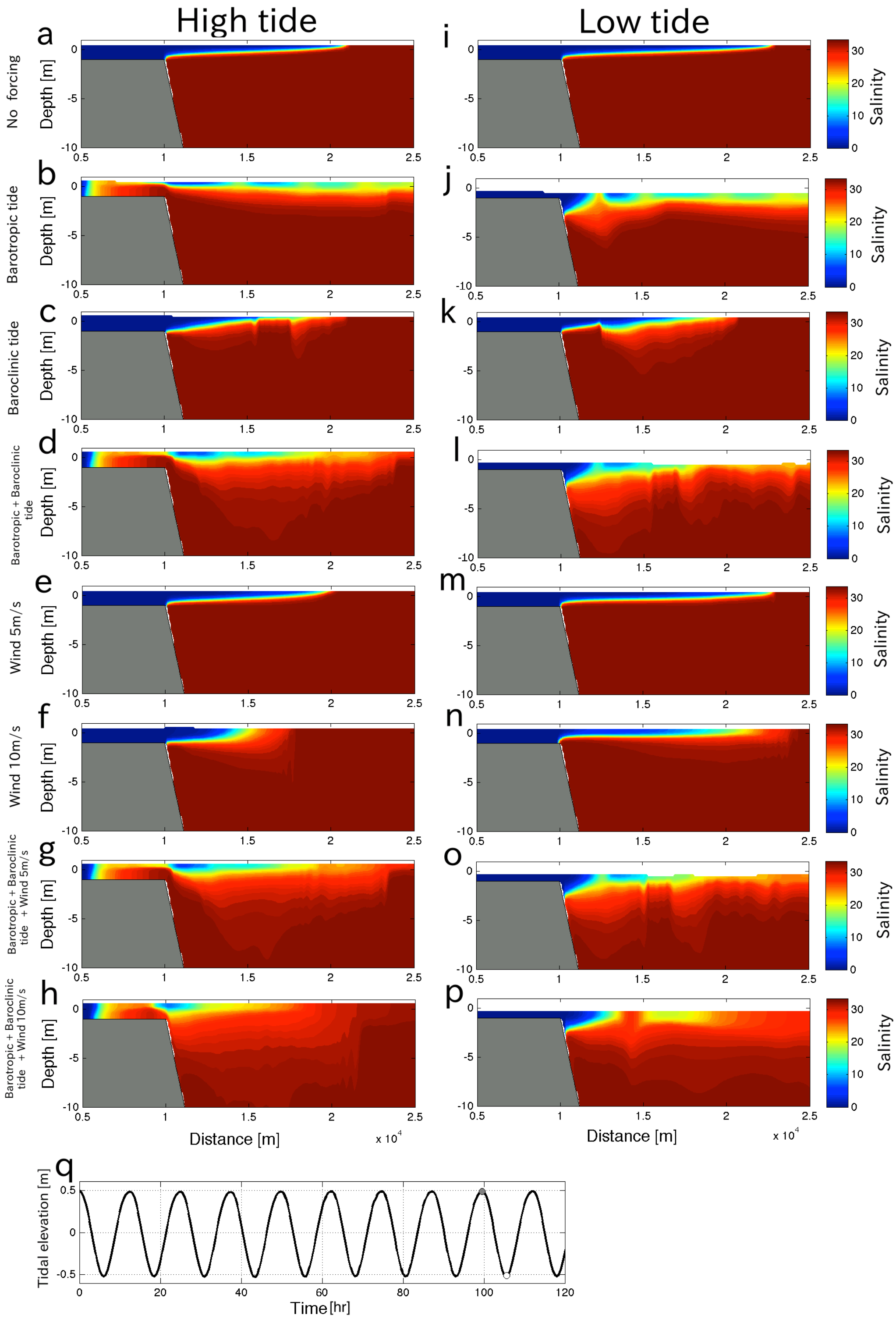

Fig. 3-15 Snapshots of salinity distributions in the bay at (a–h) the high tide and (i–p) the low tide from numerical simulations. Panel (q) shows the tidal elevation (the tide essentially co-oscillates in the bay) and timings of the high tide (gray circle, roughly at 100 hr) and the low tide (white circle, roughly 6 hr later).

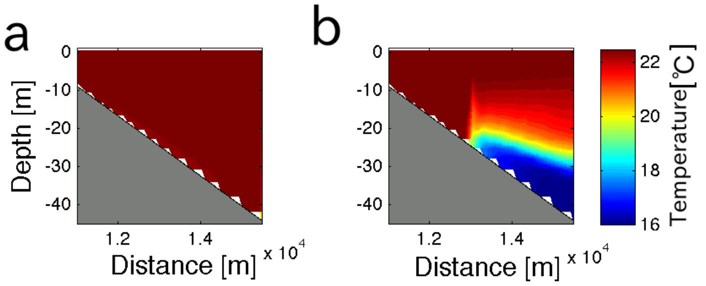

Fig. 3-16 Modeled temperature distributions before (a) and during (b) a cold-water intrusion event.

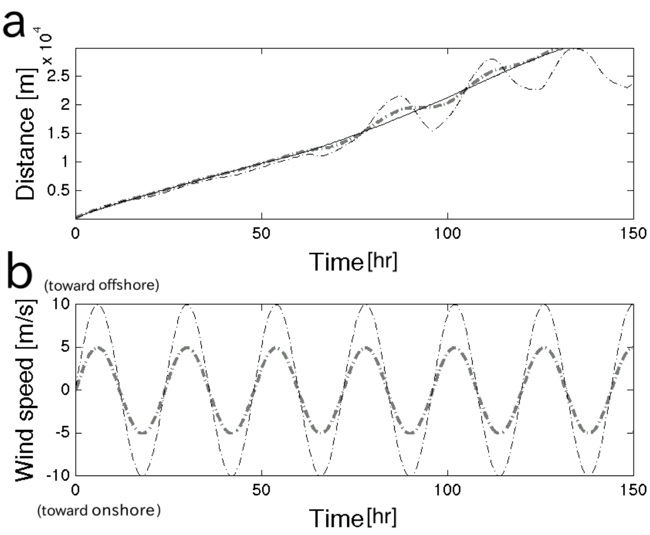

Fig. 3-17 (a) Location of the river plume front simulated in the no forcing condition (thin black line), the 5 m s^{-1} diurnal wind condition (thick gray chain dot line) and the 10 m s^{-1} diurnal wind condition (thin black dash-dotted line). The location of the river plume front in the panel (a) is defined by the surface salinity = 30.0. The vertical axis in panel (a) indicates the distance from the shallow river boundary. Panel (b) shows the wind forcing in numerical simulations.

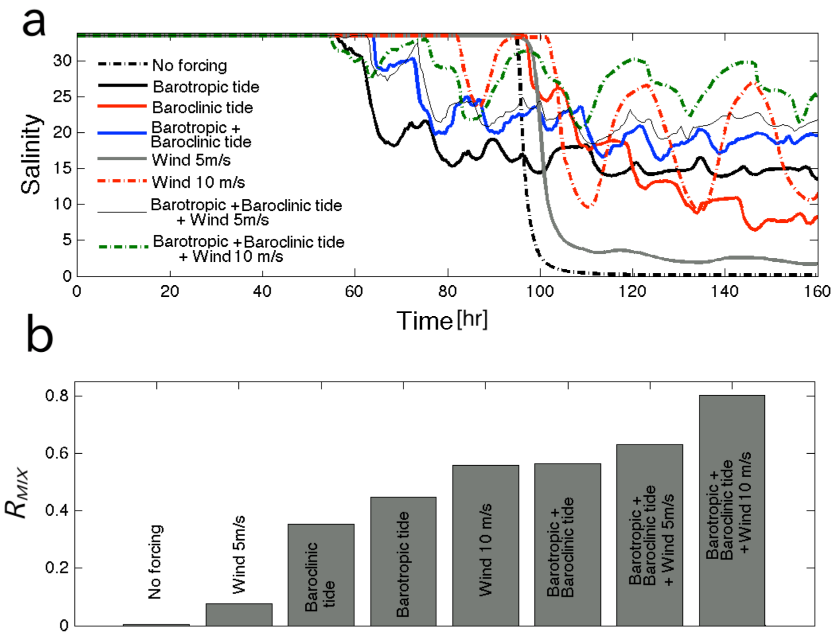

Fig. 3-18 (a) Time series of surface salinity 10 km from the river mouth and (b) the ratio of river plume mixing (averaged between 110 and 158 hr) 10 km from the river mouth for all 8 simulation cases.

3. 5 Conclusion

Field observations using the YODA Profiler revealed details of the river plume structure in Otsuchi Bay. River plumes covered the ambient bay water and caused strong stratification in the surface layer in all observation periods. River plumes contained a high concentration of phytoplankton and high turbidity water, which indicated that river plumes contribute to the transport processes of sediments and organic materials into the bay. The current and temperature field are strongly influenced by cold-water intrusion events caused by internal tides. The cold-water intrusion induced strong shear stress not only in the bottom boundary layer but also in the surface layer. The combined effect of the wind stress and internal tides generated strong turbulent mixing in the river plume, and the vertical eddy-diffusivity reached 3.0×10^{-4} $m^2 s^{-1}$.

In addition to the field surveys, I made use of the nonhydrostatic SUNTANS model to investigate the river plume dynamics in the bay. I investigated the effects of the barotrophic tide, the baroclinic tide (internal tide) and the wind stress separately the in numerical simulations. The barotrophic tide caused strong mixing between fresh water and bay water near the river mouth. On the other hand, the baroclinic tide (internal tide) contributed to river plume mixing in the middle area of the bay and generated high-frequency internal solitary waves. The wind stress also played a major role in river plume mixing and the location of the plume front. This study has clearly shows that these three elements (the barotrophic tide, the baroclinic internal tide and the wind stress) are equally important to mix river plume in Otsuchi Bay.

Chapter 4

Observations and numerical simulations of internal bores induced by the internal tides

4. 1 Introduction

Shoreward propagating internal waves are ubiquitous features of the coastal ocean (e.g., *Fu and Holt*, 1982; *Helfrich and Melville*, 2006; *Bourgault et al.*, 2007; *Nam and Send*, 2011; *Walter et al.*, 2012). These waves run-up on a slope unbroken or broken as surging waves, described as "boluses" or "bores" (*Wallace and Wilkinson*, 1988; *Helfrich*, 1992). Shoreward propagating internal bores have been investigated in both numerical simulations (e.g., *Venayagamoorthy and Fringer*, 2006) and observations (e.g., *Walter et al.*, 2012). Shoreward propagating internal bores are important processes for the cross-shelf transport of nutrients (e.g., *Leichter et al.*, 1996), sediment (e.g., *McPhee-Shaw*, 2006), and zooplankton and larvae (e.g., *Pineda*, 1994). The internal bore generates the vortex core accompanied by strong vertical motion at the front of the bore (*Venayagamoorthy and Fringer*, 2006). The vortex structure has also been observed by high-resolution thermistor arrays on a sloping continental shelf (*Van Haren*, 2009; *Hosegood et al.*, 2004).

Isopycnal displacements induced by internal tides are 20–80 m in continental shelves (*Huthnance*, 1989; *Petruncio et al.*, 1998). In particular, in submarine canyons, previous studies pointed out large isopycnal displacements of 60–120 m due to internal tides (*Broenkow and McKain*, 1972; *Shea and Broenkow*, 1982; *Wang et al.*, 2008). *Broenkow and McKain* (1972) observed the internal tide with an isopycnal displacement of 80 m in water depth of 120 m. Strong horizontal currents in bottom boundary layers are also generated by internal waves (e.g., *Wang et al.*, 2008; *Van Gastel et al.*, 2009). *Van Gastel et al.* (2009) observed internal bores accompanied by strong currents reaching 1.0 ms^{-1}. Such internal waves are generated at critical points where the topographic slope matches the internal wave beam angle (*Vlasenko et al.*, 2005; *Van Gastel et al.*, 2009). At the critical angle condition, internal wave reflections lead to strong energy convergence over continental shelves (e.g., *Thorpe*, 1998; *Cacchione et al.*, 2002). The appearance of internal bore waves is intermittent, and the frequency of the appearance is not consistent with tidal cycles (*Hosegood et al.*, 2004; *Van Haren*, 2009). *Vlasenko et al.* (2012) showed a few days of lag between the appearance of internal waves and the semidiurnal barotropic tide due to the distance between the wave generation site and the observation site. *Walter et al.* (2012) found that the propagation speed of internal bores is related to the local stratification condition.

Klymak and Moum (2003) and *Carter et al.* (2005) observed strong turbulent mixing in internal solitary waves (boluses) advancing on a sloping shelf. *Venayagamoorthy and Fringer* (2006) and *Vlasenko and Hutter* (2002) produced fine-scale breaking processes of boluses using numerical models. The passage of internal bore waves provides a burst of strong turbulent kinetic energy along slope (*Boegman and Ivey*, 2009; *Venayagamoorthy and Fringer*, 2006). *Walter et al.* (2012) showed that high-frequency temperature fluctuations are generated by bore waves. Such high-frequency temperature fluctuations in large-scale internal waves have been pointed out by *Antenucci and Imberger* (2001) and *Boegman et al.* (2003), who hypothesized that these high-frequency waves resulted from shear instability. *Ivey et al.* (2000) estimated that when internal waves reflect on the slope in the critical angle condition, the turbulent kinetic energy dissipation rate reaches an order of 10^{-6} Wkg^{-1}.

In addition to strong turbulent mixing, internal bore waves induce strong sediment resuspension (e.g., *Cacchione et al.*, 2002; *McPhee-Shaw and Kunze*, 2002). *Hosegood et al.* (2004) and *Bonnin et al.* (2006) observed sediment resuspension associated with the passage of bore waves. *McPhee-Shaw and Kunze* (2002) investigated sediment resuspension and slope angle conditions from tank experiments. They showed that resuspension and the growth of turbidity intrusions into the ocean interior are enhanced near the critical reflection condition. These turbid waters, which become detached from boundaries and intrude into the ocean interior, have frequently been observed in coastal areas (*Dickson and McCave*, 1986; *McPhee-Shaw et al*., 2004; *Nakatsuka et al*., 2004) and are called intermediate nepheloid layers (INLs). Lateral dispersal of sediments, nutrients, irons, and organic matters from sloping bottoms is much greater than that caused by vertical settling from the ocean surface (*Van Weering et al*., 2001; *Nakatsuka et al*., 2004, *McPhee-Shaw*, 2006). Cross-shelf transport of such materials from nearshore areas due to internal waves is vital for biological production in offshore sites (*Nakatsuka et al*., 2004; *McPhee-Shaw*, 2006). *Cacchione et al*. (2002) and *Puig et al*. (2004) reported that the erosion and resuspension of sediments are enhanced in the critical angle condition. The vortex motion induced by internal waves is the key to understanding sediment resuspension and mixing processes (*Boegman and Ivey*, 2009; *Van Haren*, 2009; *Richards et al*., 2013; *Masunaga and Yamzaki*, 2014).

Although previous studies have shown internal bore waves propagating along slopes, few studies have revealed detailed structure of run-up internal waves on sloping areas using in situ surveys. I have attempted to observe the detailed features of the run-up of internal waves using the newly developed YODA Profiler (*Masunaga and Yamazaki*, 2014), which captures data in high spatial and horizontal resolution. I also deployed a high-resolution temperature mooring array during the YODA Profiler survey. *Masunaga and Yamazaki* (2014) used the YODA Profiler to reveal the detailed structure of river plumes, small-scale internal waves and sediment resuspension. In addition to the field observation, I used a fully nonhydrostatic model, Stanford Unstructured Nonhydrostatic Terrain-following Adaptive Navier-Stokes Simulator (SUNTANS) (*Fringer et al*., 2006), to investigate further details of the internal wave propagating along a slope numerically.

In this chapter, I present internal bore waves propagating on a slope observed in Otsuchi Bay. Section 4.2 outlines the location and instrumentation. Section 4.3 presents fine features and an overview of physical structure in the bay. Section 4.4 discusses sediment resuspension, turbulent mixing due to internal waves in the bay, the generation internal bore waves, and numerical simulation results. Section 4.5 is a summarization of our study.

4. 2 Field campaigns

Location

Field campaigns were carried out in Otsuchi Bay, located on the Sanriku Coast, Iwate Prefecture, Japan (Fig. 4-1), in September 2012 and 2013. The Sanriku Coast has steep narrow bays formed by the partial submergence of river valleys; this type of coastline is called a “ria” (Fig. 4-1). Otsuchi Bay is a long narrow bay; the length and the width of the bay are 8 km and 3.5 km, respectively. The maximum depth of the observation area is approximately 50 m. The bay has a gently sloping bottom with a slope angle of approximately 0.6 degrees. Three rivers flow into the bay: the Unosumai River, the Otsuchi River, and the Kotsuchi River. The Unosumai River mouth is located at the innermost west part of the bay, and the mouths of the Otsuchi River and the Kotsuchi River are located at the northwest area of the bay (Fig. 4-1). The total discharge from the rivers ranges between 3 and 35 m^3s^{-1} (*Anbo et al*., 2005; *Otobe et al*., 2009). *Okazaki* (1990) observed the intermittent appearance of internal bores in Toni Bay, that locates near Otsuchi Bay (17 km south of Otsuchi Bay). The off-Sanriku area is in the Kuroshio-Oyashio transition zone where the cold nutrient-rich Oyashio water and the warm nutrient-depleted Kuroshio water are alternatively occupy the region(e.g., *Hanawa and Mistudera*, 1986), and is known as a highly productive fishery ground.

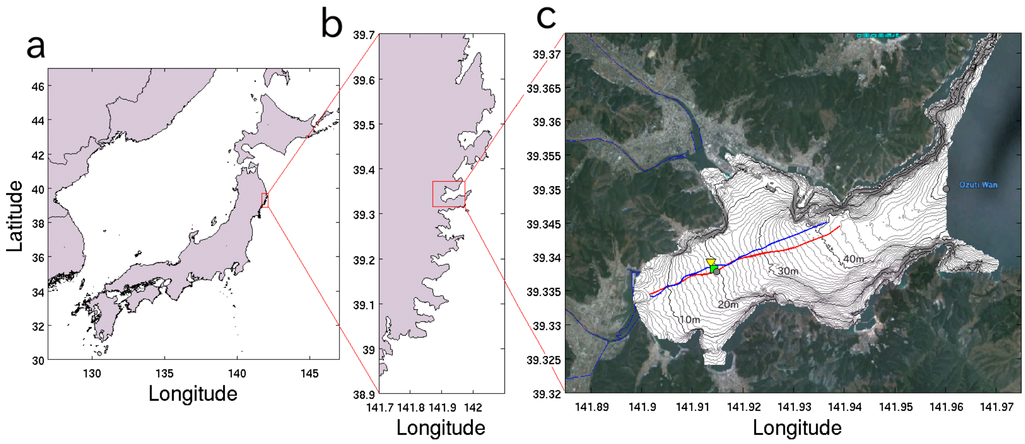

Fig. 4-1. Observation area. (a), (b), and (c) show coastlines around Japan, the Sanriku Coast, and

Otsuchi Bay, respectively. The blue and red lines in (c) are transect observation lines on 27 September 2012. The ADCP and the thermistor array mooring sites in 2012 are indicated by the yellow inverted triangle and the light green square. The two mooring sites in 2013 are represented by the gray circles. Black and gray contour lines in (c) indicate isobaths.

Transect Observations

Transect observations were carried out to survey physical structures using the YODA Profiler (*Masunaga and Yamazaki*, 2014) and the RiverRay ADCP (Teledyne RD Instruments) on September 27, 2012 and September 11, 2013. The YODA Profiler is a free-fall tow-yo instrument and provides high-resolution of physical structures in coastal shallow areas. To deploy these instruments, we used two fishing boats belong to the Shin-Otsuchi Fishery: the Senshu-maru in 2012 and the Daimutsu-maru in 2013. The transect observation line extends from the Unosumai River mouth (bay head) to the bay mouth, and the distance of observation lines was approximately 3.5 km (Fig. 4-1). In order to observe high-resolution data horizontally, the ship speed and the sinking speed of the YODA Profiler were adjusted to 2 kts and 0.3 ms^{-1}, respectively. The YODA Profiler carries conductivity-temperature-depth (CTD), fluorescence, turbidity, and dissolved oxygen sensors, and data were collected at 10 Hz. I used data obtained during a stable free-fall descending phase. The horizontal intervals of tow-yo profiling points increase as the depth increases. The intervals vary between 24 m and 364 m. The YODA Profiler also allows us to estimate the turbulent kinetic energy dissipation rate, ε , from vertical fluctuations of conductivity, dC/dz, making use of the method described in *Masunaga and Yamazaki* (2014). The RiverRay ADCP collects the data at 1 Hz, and current data were run-mean averaged over 1-minute intervals in this study.

Microstructure Observation

Since the YODA Profiler does not carry a microstructure sensor, I can not measure the intensity of turbulence directly using this instrument. *Masunaga and Yamazaki* (2014) developed a statistical method to estimate a proxy of the dissipation rate by making use of conductivity signals. The proxy dissipation rate can be inferred from the variance of the conductivity by the following asumptions (*Masunaga and Yamazaki*, 2014):

1. The rate of dissipation of turbulent kinetic energy and temperature gradient follows a joint log normal the probability density function (PDF);
2. Conductivity signals follow temperature signals;
3. The rate of dissipation of turbulent kinetic energy and conductivity gradient follows a joint log normal PDF.

I call the proxy dissipation inferred from the YODA Profiler as a pseudo dissipation rate, ε_P, in this chapter. The estimation of ε_P from the YODA Profiler requires the background PDF of ε from a separate microstructure survey in the same area. Therefore, I collected microstructure data using a glider-type microstructure profiler, TurboMAP-Glider (*Foloni et al*., 2014), at numerous points in Otsuchi Bay 26–27 September, 2012. The TurboMAP-Glider was deployed from the R/V Grand-maillet (the University of Tokyo). In order to infer ε_P from the YODA Profiler, I estimated coefficients *a* and *b* for the following empirical formula,

$$\varepsilon = a\left[\overline{(dC/dz)^2}\right]^b \tag{4-1}$$

with the QQ plot (quantile versus quantile) between ε from TurboMAP-Glider and ε_P from the variance of *dC/dz* from the YODA Profiler (Fig. 4-2b). Making use of the least square method, the estimated coefficients are 1.42×10^{-7} and 1.37 for *a* and *b*, respectively. The PDFs of the dissipation from the two instruments are consistent with each other (Fig. 4-2a). Vertical profiles of the dissipation estimated from the YODA Profiler are in reasonable agreement with TurboMAP-Glider data (Fig. 4-2c and 2d).

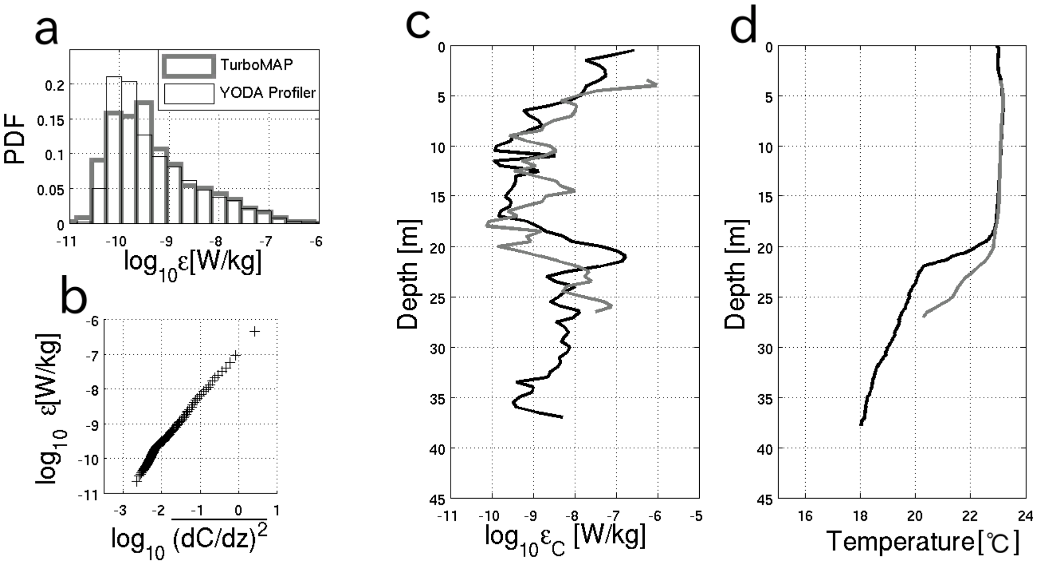

Fig. 4- 2. (a) PDFs of ε, (b) QQ plot between ε obtained by TurboMAP (thick gray bar), and the variance of the dC/dz obtained by the YODA Profiler (thin black bar), (c) vertical profiles of ε, and (d) temperature. Black and gray lines in (a), (c), and (d) represent data from the YODA Profiler and TurboMAP, respectively.

Mooring Observations

A thermistor mooring array and an Acoustic Doppler Current Profiler (ADCP) were mounted at the middle of the transect observation line, at approximately 20-m depth (Fig. 4-1) September 25-27, 2012. Table 4-1 shows the locations of the two mooring sites and the deployment-recovery time. The distance between these two mooring sites was approximately 120 m. HOBO U24 sensors (Onset Computer Corporation) were used as a thermistor array and were arranged from near the bottom to approximately 10 m above the bottom at 0.4-m intervals. The data sampling frequency for HOBO U24 sensors was set at 0.1 Hz. The MicroCAT C-T sensor (Sea-Bird Electronics, Inc.) and the Compact-CTD (JFE Advantech, Ltd.) were also mounted at 2 m and 1 m above the bottom, respectively. Sampling intervals of the MicroCAT and the Compact-CTD were set to 10 seconds and 1 minute, respectively. The Compact-CTD also carries fluorescence and turbidity sensors. I deployed a 600 kHz four-beam ADCP (Teledyne RD Instruments) mounted on the bottom using a bottom-landing frame. The ADCP was set to resolve 0.5-m vertical intervals and 2-second sampling intervals (each sampling includes 8 pings). The ADCP also carries a pressure sensor and a temperature sensor.

For the 2013 campaign, a thermistor mooring array was deployed with a 600 kHz four-beam ADCP (Teledyne RD Instruments) at a deeper site (54-m depth), and an electromagnetic current meter (INFINITY-EM, JFE Advantech Ltd.) was deployed near the bottom at a shallower site (21-m depth) from June to September 2013 (Fig. 4-1, Table 4-1). Twenty-three HOBO Tidbit v2 (Onset Computer Corporation) temperature sensors were mounted between 2.5 m above the bottom and 35.5 m above the bottom. The sampling interval of the Tidbit temperature sensors was set to 5 minutes. The ADCP was set to resolve 1-m vertical bins and 5-minute sampling intervals (each sampling includes 50 pings). The electromagnetic current meter collected data every 10 minutes, and the observation mode was set to a burst mode (10 data were collected every 10 minutes).

Table 1. Instrument deployments and recovery by location and time

Instrument	Location		Deployment time (JST)	Recovery time (JST)	Depth
Thermistor array	39°20.352' N	141°52.824' E	25 September 2012 13:44	27 September 2012 14:40	20 m
ADCP	39°20.293' N	141°52.855' E	25 September 2012 13:31	27 September 2012 14:45	20 m
Thermistor array and ADCP	39°21.007' N	141°57.610' E	10 June 2013 8:08	13 September 2013 8:03	54 m
Electromagnetic current meter	39°20.270' N	141°54.889' E	10 June 2013 10:06	13 September 2013 8:37	20 m

Tidal Data and Climatological Data

Tidal elevations were not recorded in Otsuchi Bay; therefore, we made use of the tidal elevation data estimated from the Oregon State University Tidal Inversion Software (OTIS) (*Egbert and Erofeeva*, 2002). The phase of the pressure data observed at our mooring site is almost identical to the tidal elevation estimated by OTIS (Fig. 4-3). According to the cross-correlation analysis, the phase of the mooring pressure data is 3 minutes behind the phase estimated by OTIS.

In order to investigate the background hydrographic condition the off-Sanriku area, I used the monthly climatological temperature and salinity data from the World Ocean Atlas 2009 (WOA 2009), produced by the National Oceanographic Data Center (NODC). The seasonal climatological data were only used for investigating the hydrographic condition below 1750-m depth.

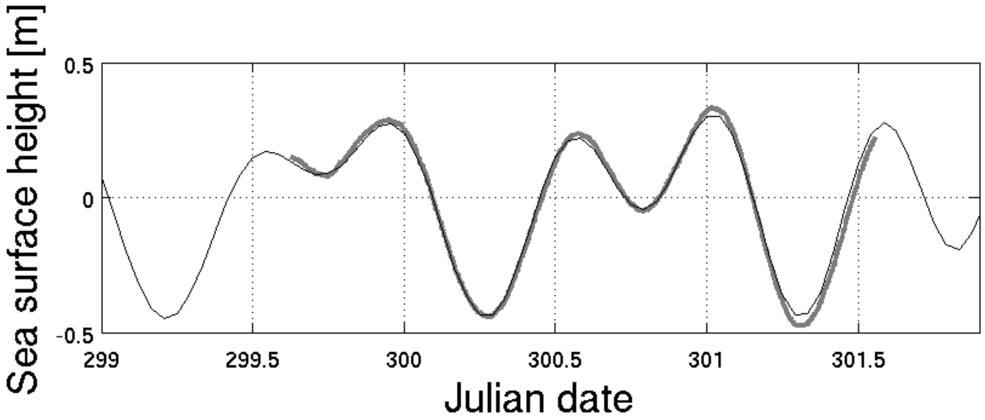

Fig. 4- 3. The sea surface height observed at the mooring site (thick gray line) and estimated by OTIS during the observation period in September 2012.

Sediments samplings

I collected bottom sediment samples in the bay using a Smith-MacIntyre Bottom Sampler in September 2012. I used a laser diffraction particle size analyzer, LS-200 (Beckman Coulter, Inc.), to measure the particle size of the samples. LS-200 measures particle density in the size range between 0.375 and 1822 μm. Fig. 4-4 shows the locations of the bottom sampling points.

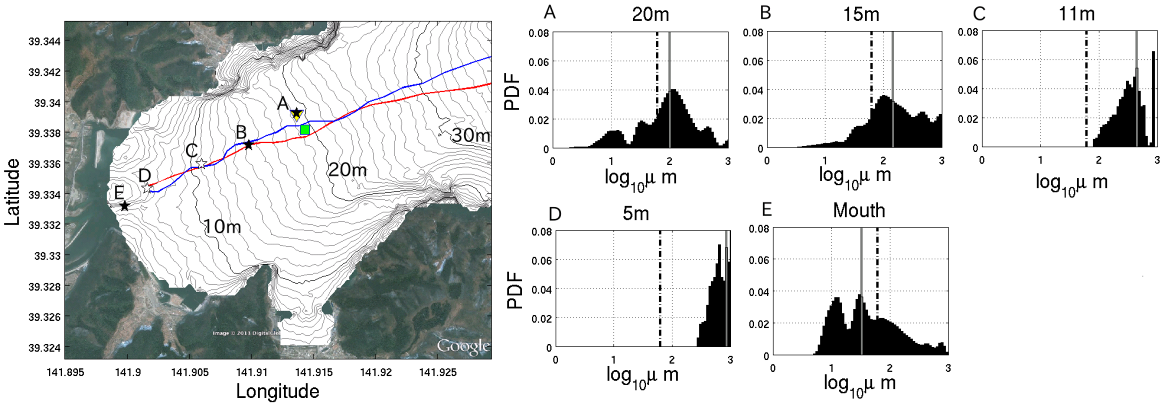

Fig. 4- 4. Bottom sampling locations and histograms of the sediment particle size. Stars indicate sampling points (A, B, C, D, E). Histograms (A, B, C, D, E) show the particle size at each sampling point in the left panel. The black chain-dotted line is the threshold between the silt and the sand (62.5 μm), and the gray line marks the median particle size.

4. 3 Results

Cold Water Incursion Events

The observed temperature time series at the bottom of the mooring station (Fig. 4-1c) show that temperature dropped three times during the 2012 campaign (Fig. 4-5a). The mooring observation was terminated during the last low-temperature incursion period. Thus, observed data did not reveal the complete phase for the last low-temperature event. The temperature dropped approximately 1.0, 2.5, and 4.5 °C on 25, 26, and 27 September, respectively. These events occurred after large amplitude flood tides. Low-temperature incursions appear to be related to the barotropic tide. However, the time intervals between the beginning of the temperature decrease and the lowest tide (beginning of the flood) were different for each event; the intervals were 8.97, 8.68, and 6.45 hours on 25, 26 and 27 September, respectively.

According to *Walter et al.* (2012), shoreward propagating internal bores are classified into two types:

1) a canonical bore, in which the bore takes the form of a sudden decrease in

temperature during the run-up phase and a gradual increase in temperature during the relaxation phase (“sawtooth” shape).

2) a noncanonical bore, in which the temperature rapidly changes during both the run-up and relaxation phases, or the temperature gradually changes during the run-up and rapidly changes during the relaxation.

The observed temperature indicates that a canonical bore appeared on 25 September while a noncanonical bore appeared on 26 September (Fig. 4-5a). *Walter et al.* (2012) found that a noncanonical bore occurs when the bottom slope γ is larger than the square root of the internal wave slope (a/L), where a and L are the amplitude and the wavelength of the internal wave.

Temperature observed by the thermistor array shows a high-frequency wave feature (Fig. 4-6a) and a vortex-like structure (Fig. 4-6d) appearing in the data set. A spectrum of the isothermal depth fluctuation shows a significant peak between 10^{-3} and 10^{-2} Hz (Fig. 4-6b); this peak frequency is near the buoyancy frequency, N in the observed internal bore. Inside the internal bore, N was approximately 5×10^{-3} s^{-1}. I estimated the buoyancy frequency, N, from the following shallow water formula,

$$N = \sqrt{-\frac{g}{\rho_0}\frac{d\rho}{dz}} \quad , \qquad (4\text{-}2)$$

where g is the gravitational acceleration, z is the vertical coordinate with positive upward, ρ is the local density, and ρ_0 is the mean density. *Antenucci and Imberger* (2001) and *Boegman et al.* (2003) observed high-frequency waves near the buoyancy frequency in large-scale internal waves. They suggested that these waves resulted from shear instability in large-scale internal waves. Using a high-resolution numerical model, *Walter et al.* (2012) showed a vortex structure accompanied by a steep isothermal displacement at the head of the bore waves, which is consistent with the steep displacement that appeared in our field data (Fig. 4- 6c).

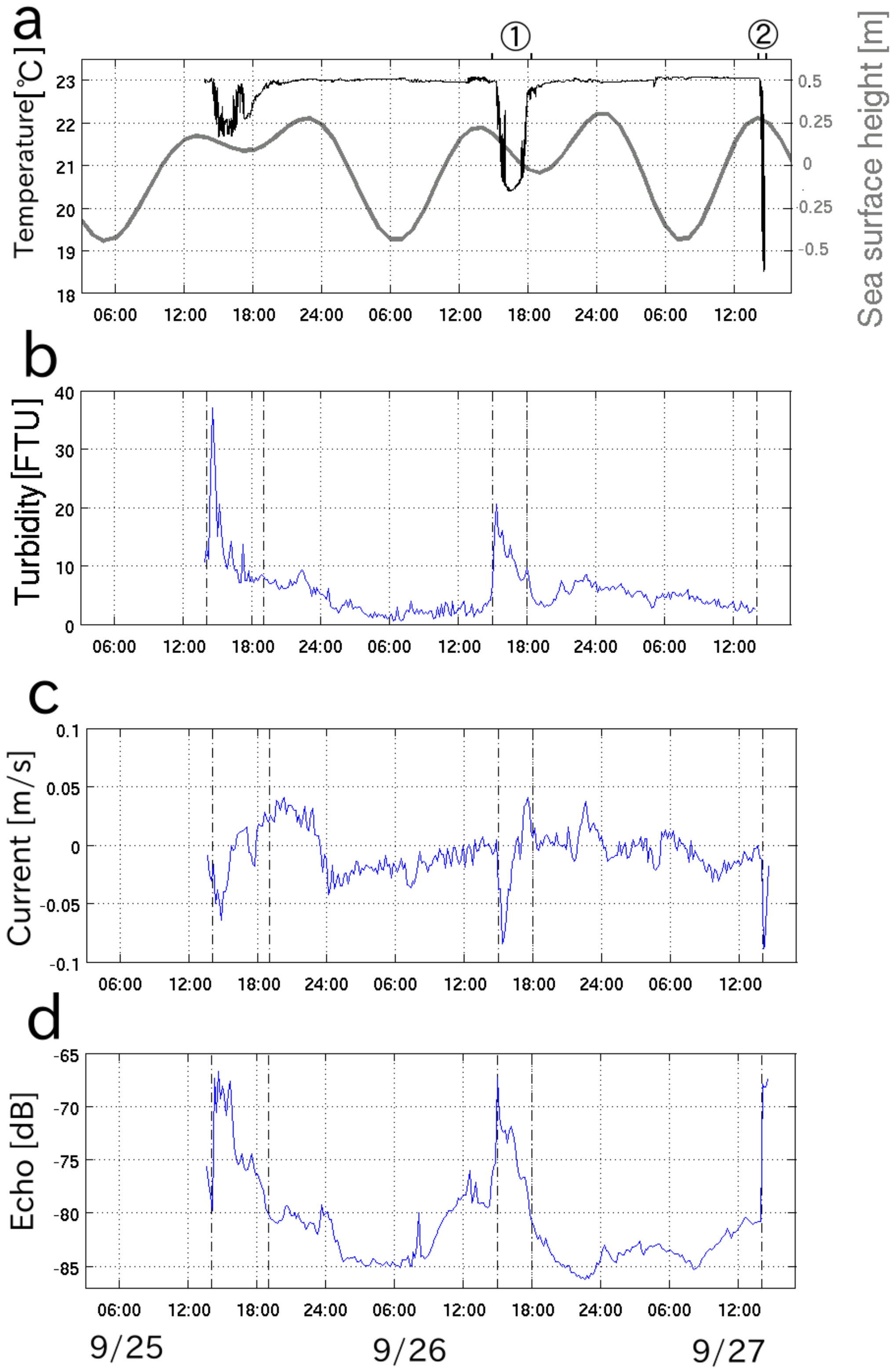

Fig. 4- 5. **(a) Bottom water temperature (thin black line) and the sea surface height (thick gray line), (b) turbidity obtained by the Compact-CTD, (c) the along channel current data, and (d) the echo intensity [dB] at 2 m above the bottom obtained by ADCP observed at the mooring site in**

September 2012. The chain-dotted lines indicate the beginning and the end of the internal wave period. The positive (negative) value in the panel (c) indicates the offshore (onshore) ward flow.

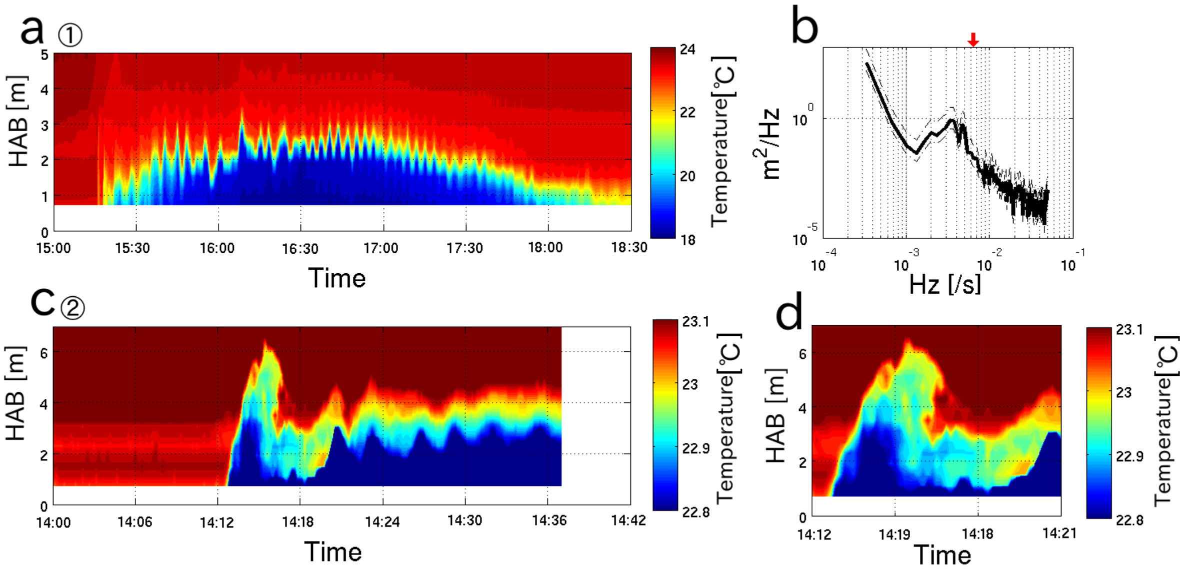

Fig. 4- 6 (a, c) Temperature distributions during bore wave periods on 26 (①) and 27 (②) September, and (b) the spectra of the 22-degree isothermal depth fluctuation shown in (a). (d) is the close-up of the head of the wave shown in (c). The red arrow in (b) indicates the buoyancy frequency in the internal bore wave on September 26, 2013. The chain dot lines in the panel (b) indicate a 95% confidence interval of the spectra. Periods of panels (a) and (c) are represented as ① and ② in Fig. 4- 7a, respectively.

Temperature data from the YODA Profiler show a fine feature in the internal bore wave accompanied by a low-temperature water mass propagating along the bottom slope into the shallow area (Fig. 4-7b and 7c). Observed data shown in Fig. 4- 7 were obtained 9:13–10:15 (phase A in Fig. 4-7a) and 13:16–14:22 (phase B in Fig. 4-7a) on 27 September 2012. The isothermal displacement was caused by the bore reaching 20 m vertically (Fig. 4-7b and 7c). Assuming that the bore front was located at the deepest right edge of the transect line in the phase A and that the bore front propagated approximately 2000 m across the slope between phases A and B (4 hours), the average propagation speed of the bore and the average displacement speed of the thermocline were at least 0.14 ms^{-1} and 1.4×10^{-3} ms^{-1}, respectively.

The RiverRay ADCP data show the shoreward current (0.1–0.15 ms^{-1}) below the interface of the internal wave (20–30 m) and the offshoreward current (0.05–0.15 ms^{-1}) in the upper layer (5–20 m); the upper layer flow was opposite from the lower cold layer flow (Fig. 4-7g). This phenomenon is common for first mode internal waves. Such inverse flow is called “sakashio (inverse flow)” by local fishermen and is frequently found in bays along the Sanriku Coast (*Okazaki*, 1990). Although the current near the sea surface (0–5 m) flows in an opposite direction from the subsurface flow, this layer may be induced by the wind stress (Fig. 4-7f and 7g). Ten minutes averaged moored ADCP data show shoreward flow near the bottom at the beginning of the wave events (Fig. 4-5c, 9/25 15:00, 9/26 15:00, 9/27 14:00) and offshoreward flow during the receding phases (Fig. 4-5c, 9/25 16:00, 9/26 17:00). Assuming that the volume flow rate at the bay mouth during flood (or low) tide is equivalent to the volume change between low and high tide, the temporally averaged barotropic current in the bay is calculated from a simple volume conservation equation (*Petruncio et al.*, 1998):

$$u_{barotropic} = \frac{\eta A}{T_P H W} \qquad (4\text{-}3)$$

where for the *M2* semidiurnal component, η is tidal range (1 m), A is the surface area of the bay (1.105×10^7 m^2), T_P is duration of flood or ebb tide (6.2 h), H is the average depth across the bay mouth (40 m), and W is the width of the bay at the mouth (2400 m). With this formula, the average semidiurnal barotropic current is approximately 5.2×10^{-3} ms^{-1} in Otsuchi Bay. This barotropic current is considerably weak and negligible, and thus, the current is largely dominated by the baroclinic tidal current in Otsuchi Bay.

According to a study of the water classification based on the temperature-salinity relationship (*Hanawa and Mitsudera*, 1987), the low-temperature water mass in internal waves is identified as Tsugaru Warm Current water (Fig. 4-8). This water mass is from the northern region of Sanriku Coast. *Okazaki* (1990) found the same water mass in internal waves observed in Toni Bay located near Otsuchi Bay.

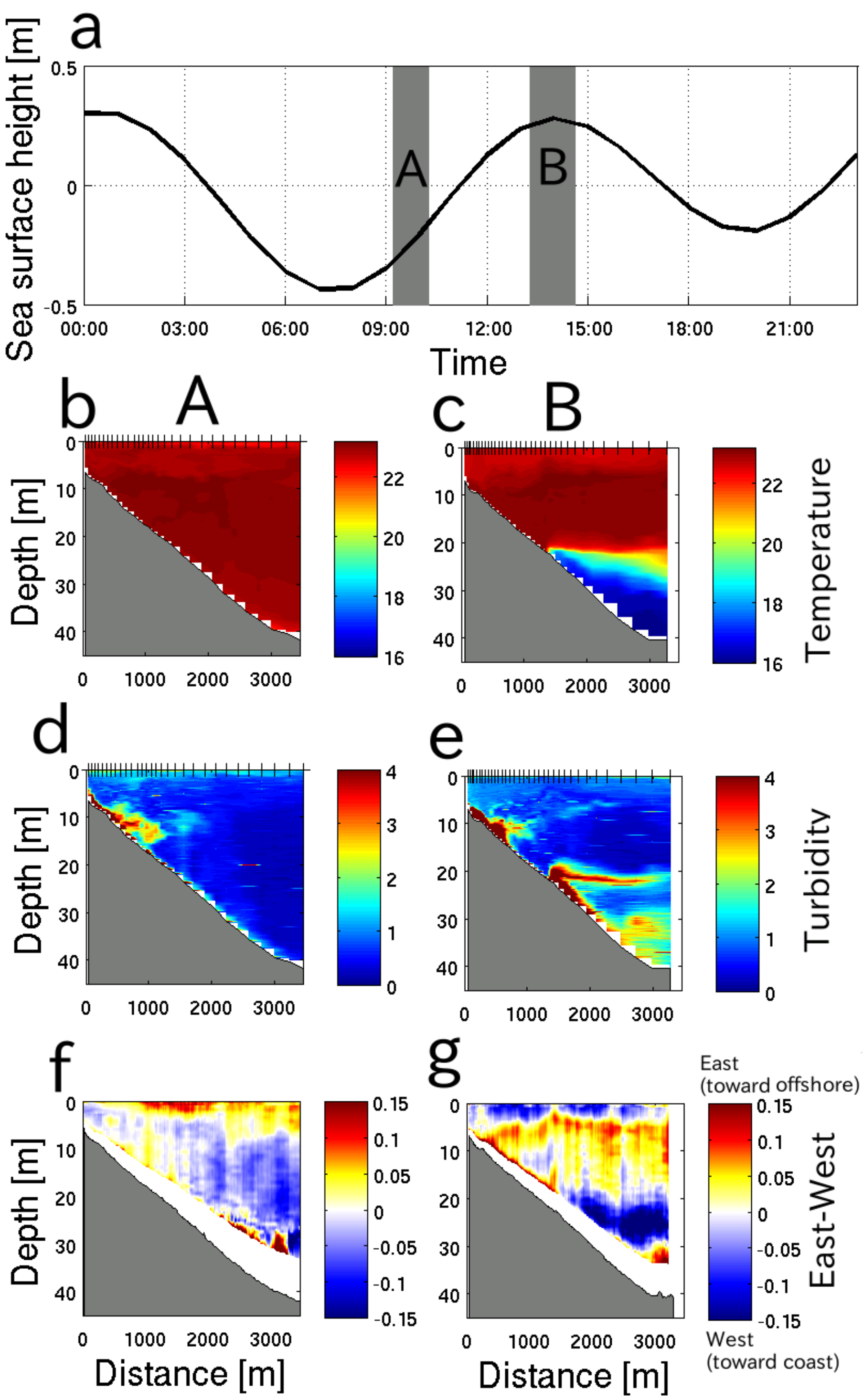

Fig. 4-7. (a) The tidal elevation, observation results obtained by the (b, c, d, e) YODA Profiler and (f, g) the RiverRay ADCP on 27 September 2012. Shaded areas in (a) indicate transect observation period: (A) the beginning of the flood tide and (B) the high tide. Observation results show (b, c) temperature, (d, e) turbidity [FTU], and (f, g) east-west current [ms^{-1}] distributions observed (b, d,

f) before the bore wave period and (c, e, g) during the bore wave period. Tick marks on *x* axis in panels (b), (c), (d), and (e) indicate the points at which the YODA Profiler collected data.

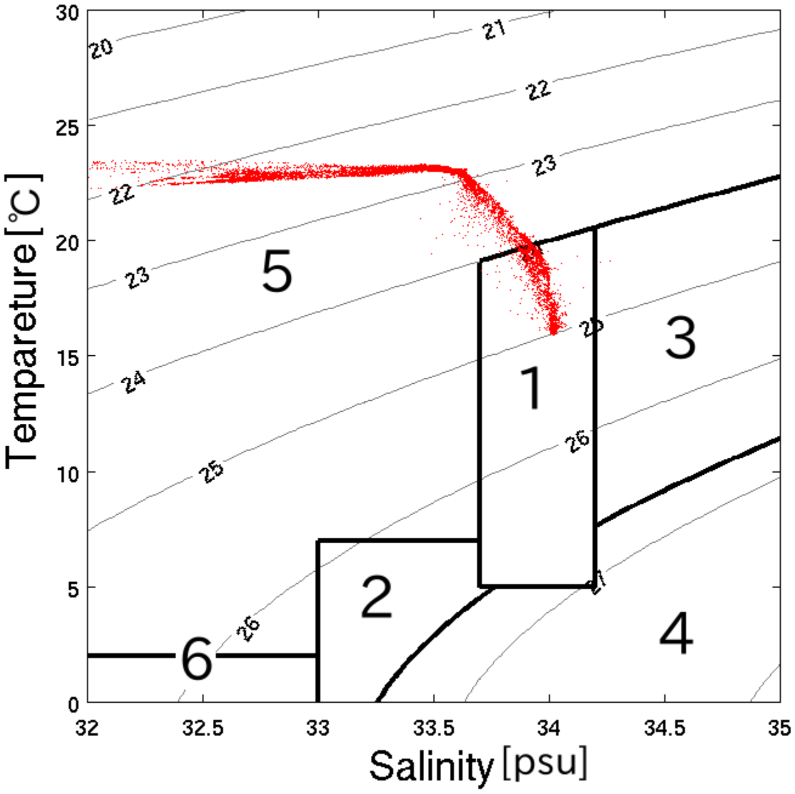

Fig. 4-8 Temperature-Salinity (TS) diagram for water observed in Otsuchi Bay and classification of six water systems from Hanawa and Mitsudera (1987). The six areas indicate water masses off the Sanriku Coast: 1. the Tsugaru Warm Current water system; 2. the Oyashio water system; 3. the Kuroshio water system; 4. the cold lower-layer system; 5. the surface water system; 6. the Coastal Oyashio water system.

Sediment Resuspension

High turbidity water was observed at two locations: in the internal wave (20–40 m depth) and in the shallow area (5–15 m depth, Fig. 4-7d and 7e). The internal bore wave propagates along the slope accompanied by strong sediment resuspension at the head of the bore wave (Fig. 4-7e). In addition, suspended sediments become detached from the sloping bottom and intrude into the ocean interior above the interface of the wave. This feature is frequently observed over continental shelves and is called an intermediate nepheloid layer (INL) (e.g., *Thorpe*, 1998; *McPhee-Shaw*, 2006). On the other hand, the strong sediment suspension was not observed before the bore wave period below 20 m depth. The turbidity data observed by the Compact-CTD mounted near the bottom (1 m above the bottom) at the mooring site show burst-like strong sediment resuspension at the beginning of bore wave periods, and high turbidity signals gradually decrease after the burst events (Fig. 4-5b). Unfortunately, the Compact-CTD power supply failed at 14:00 on 27 September; thus, turbidity data from the Compact-CTD were not obtained from the last bore wave period. Backscatter echo intensity data observed by the moored ADCP also show high echo intensity in bore wave periods (Fig. 4-5d).

The surveyed particle size distribution shows that the sediments consist of silts and sands below 15 m depth (Fig. 4-4A and B) and near the river mouth (Fig. 4-4E). In contrast, sediments consist of only larger particles, sand, between 5 m depth (Fig. 4-4D) and 11 m depth (Fig. 4-4C). A sandbar located at the Unosumai River mouth was completely flushed out by the tsunami on March 11, 2011, and sand spread out from the sandbar (*Okayasu et al.*, 2013). The sandy area between 5 and 11 m depths is probably covered with sand from the lost sandbar. Therefore, internal bore waves propagated on the sloping bottom consisting of mixture sediments of silts and sands.

4. 4 Discussion

The Vortex Motion at the Head of the Bore

Internal bores accompanied by strong currents induce a vortex motion at the head of the wave (*Van Haren*, 2009; *Boegman and Ivey*, 2009; *Masunaga and Yamazaki*, 2014). The vortex is generated by a localized intensification in the shoreward sweep flow along the bottom and the vertical ejection flow at the head of the bore (*Boegman and Ivey*, 2009; *Masunaga and Yamazaki*, 2014). *Van Haren* (2009) observed the vortex structure accompanied by the strong vertical resuspension, reaching 40 m above the deep sloping bottom. In shallow areas, *Richards et al.* (2013) observed vortex wave packets accompanied by vertical sediment resuspension, reaching 10 m above the bottom.

One-minute-averaged ADCP current data, observed on September 27, 2012, show horizontal shoreward flow (0.1 ms^{-1}) near the bottom, a strong upward ejection flow (0.02–0.03 ms^{-1}) at the head of the bore, and a downward flow behind the head (Fig. 4-9a and 9b). These motions indicate that the vortex motion was induced by the shoaling internal bores (a schematic image of the vortex is depicted in Fig. 4-9e). High-frequency upward and downward currents remain after the burst-like vortex event (Time = 14:00 – 14:30). This high-frequency motion may result from shear instability (*Antenucci and Imberger*, 2001; *Boegman et al.*, 2003). The echo intensity shows that suspended sediments follow a ring-like vortex motion and are lifted up to 8 m above the bottom (Fig. 4-9c). In addition, the temperature distribution shows the vortex structure and the upward motion at the head of the wave (Fig. 4-9d). The beginning of the bore event recorded by the ADCP was approximately 7 minutes ahead of that recorded by the thermistor array (Fig. 4-9d). This lag is due to the distance (120 m) between the two mooring sites (Fig. 4-1c). Although the high-resolution mooring data show the vortex motion accompanied by the strong current and vertical sediment resuspension, the YODA Profiler observation did not capture the vortex structure (Fig. 4-5d). The horizontal scale of the vortex may be estimated from observed time scale of vortex (360 s, Fig. 4-9) and the horizontal current in the vortex (0.1 ms^{-1}, Fig. 4-9a), which suggests that the scale is approximately 36 m. Since the propagatimg direction of the vortex is unknown and the propagation speed of the vortex is less than the average horizontal current speed (*Hosegood et al.*, 2004), the actual vortex scale should be less than 36 m. The horizontal resolution of the YODA Profiler observations was approximately 100 m near the head of the bore; this scale is larger than the vortex structure scale. Therefore, the small vortex structure was not identified from the YODA Profiler survey.

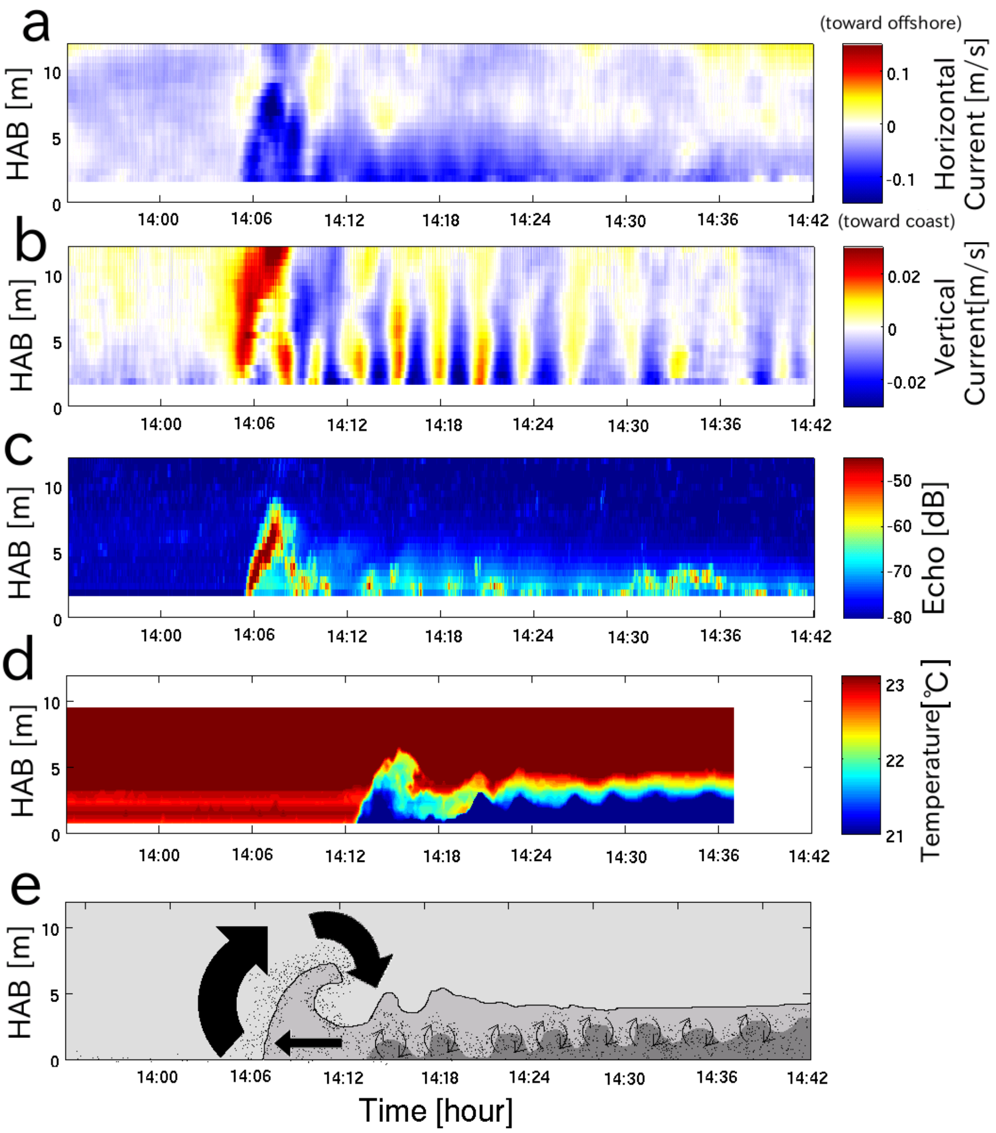

Fig. 4-9. (a) East-west current [ms^{-1}], (b) vertical current [ms^{-1}] and (c) echo intensity [dB] from the moored ADCP, and (d) temperature from the thermistor array during the bore wave period on 27 September 2012. Panel (e) depicts the schematic image of the vortex motion at the head of the bore wave. The time lag (approximately 7 minutes) between the ADCP data and the thermistor chain data is due to distance between two mooring sites (120 m).

Sediment Resuspension and Bottom Friction

In order to remove the sea surface gravity wave effect, the current data shown in Fig. 4-10 was filtered by the low-pass filter with a cutoff frequency at 0.05 Hz. The current time series near the bottom shows weak current before the bore period, less than 0.06 ms^{-1} (Fig. 4-10a). On the other hand, the current speed is high when the cold water intruded into the observation site (Fig. 4-10a, Time > 14:06). The current due to the internal wave reaches 0.22 ms^{-1} at the first burst-like event (Fig. 4-10a). To verify the bed shear stress, I estimated the bed shear stress, τ, as following

$$\tau = \rho C_D U^2 \quad , \qquad (4\text{-}4)$$

where ρ is the water density 1.024 gcm^{-3}, C_D is the empirical drag coefficient 2.5×10^{-3}, and U is the current above the bottom. The bed shear stress, τ, estimated from the observed currents shows highly fluctuated values during the bore period and varies between 0.05 and 1.2 dyne cm^{-2}. The average shear stress at the head of the bore is approximately 0.35 dyne cm^{-2} (time between 14:06 and 14:12). The critical value of the bed shear stress for resuspension of fine sediments is roughly 0.3–1.0 dyne cm^{-2} , according to previous studies previous studies (e.g., *Ross et al.*, 2009; *Cacchione et al.*, 2002; *Gardner*, 1989). Sediments consist of fine particles (silts and sands) at 20 m depth (Fig. 4-4). Thus, the estimated shear stress due to the internal bore is strong enough to suspend sediments. Previous studies reported burst-like currents inducing resuspension above the sloping bottom (*Gloor et al.*, 1994; *Boegman and Ivey*, 2009; *Bonin et al.*, 2006). The first burst-like strong current coincides with strong sediment resuspension revealed from the echo intensity (Fig. 4-10).

According to Stokes' law, the terminal velocity of fine suspended particles is approximately 0.3–8 mh^{-1} ($8.9 \times 10^{-5} – 2.2 \times 10^{-3}\ ms^{-1}$) when the particle size and density are 10–50 μm and 2.65 gcm^{-3} (typical value for wet silts), respectively. The terminal velocity of suspended particles ($8.9 \times 10^{-5} – 2.2 \times 10^{-3}\ ms^{-1}$) is much lower than the upward motion in the vortex (Fig. 4-9b); suspended particles can be lifted up to 8 m above the bottom within a few minutes by the vortex as shown in Fig. 4-10e. In addition, the displacement speed of the thermocline during the run-up ($1.4 \times 10^{-3}\ ms^{-1}$) is faster than the terminal velocity for small sediments. Small sediments maybe lifted up along the interface of the bore, and then the high turbidity water may be stretched by the inverse flow (Fig. 4-7f and 7g). During the receding phase, suspended particles reached the bottom within the duration of flood or ebb (6.2 h). Also during the receding phase, the intruded turbidity layer moved to the offshore with the receding water. Consequently, no suspended particles appeared below 20 m before the bore event (Fig. 4-5e).

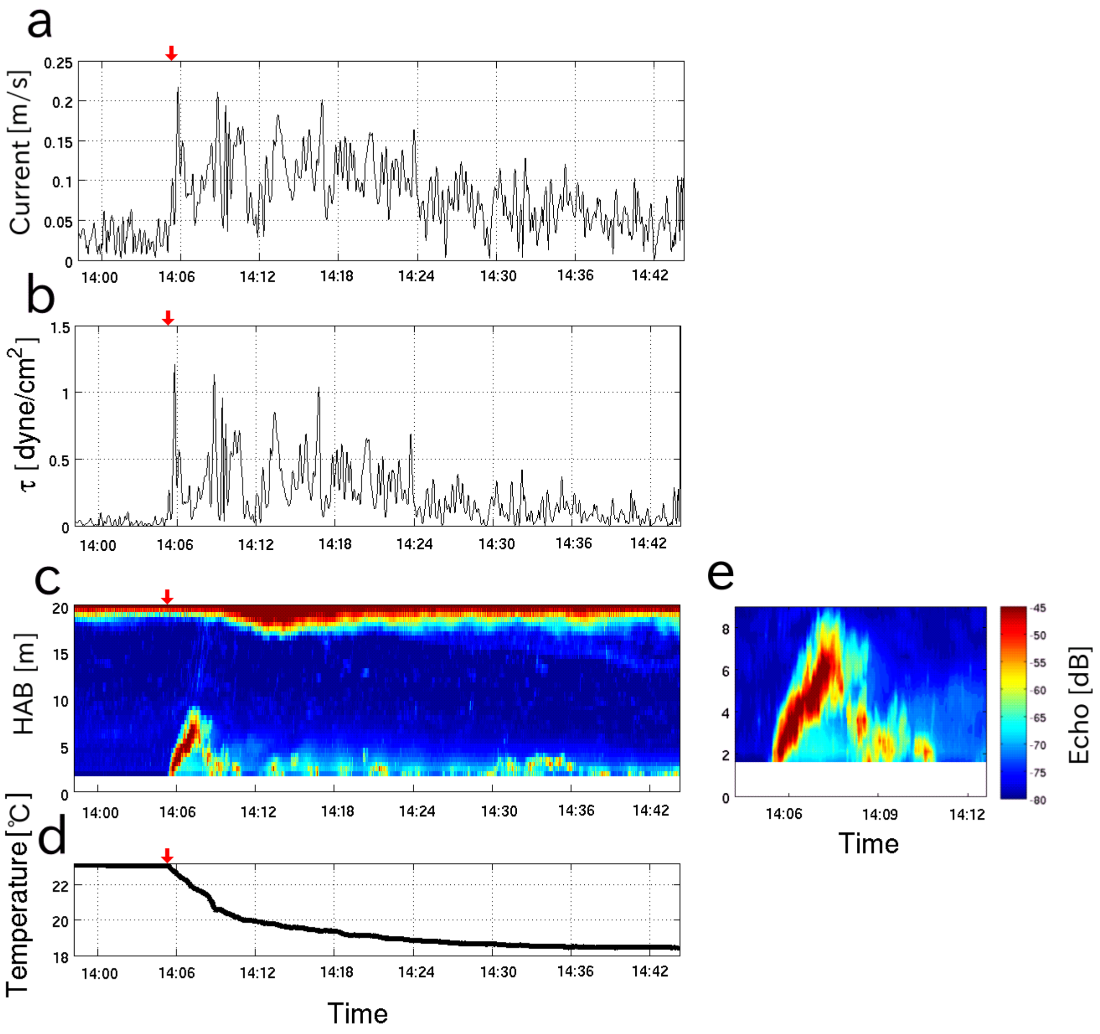

Fig. 4- 10. (a) Velocity due to the internal wave at 2 m above the bottom, (b) the bottom shear stress *τ* dyne cm^{-2}, (c, e) the echo amplitude, and (d) the temperature time series from the moored ADCP. Panel (e) is a close-up of the echo amplitude in the beginning of the bore wave period. Red arrows on panels (a), (b), (c), and (d) indicate the beginning of the internal bore wave period.

The observed data from the mooring at the deeper site (54-m depth) in 2013 show the strong shoreward current near the bottom and the bed shear stress, reaching 0.25 ms^{-1} and 1.6 dyne cm^{-2}, respectively, during the wave surging period (Fig. 4- 13b). The current speed and the bed shear stress are higher during the receding phase than those during the run-up, exceeding 0.4 ms^{-1} and 4.1 dyne cm^{-2}, respectively. If sediments contain silts at the deeper site that are the same as those at the shallower site (Fig. 4- 2 A and 2B), the strong shear stress due to the internal waves in the deeper site is sufficient to suspend sediments. The speed of the current due to the internal waves decreased with the decrease in the depth of the bottom, since the flow has to fight against gravity. The shoreward current speed at the shallower site was approximately 3 times slower than that at deeper site, 0.07 ms^{-1} (Fig. 4-11c and 11d).

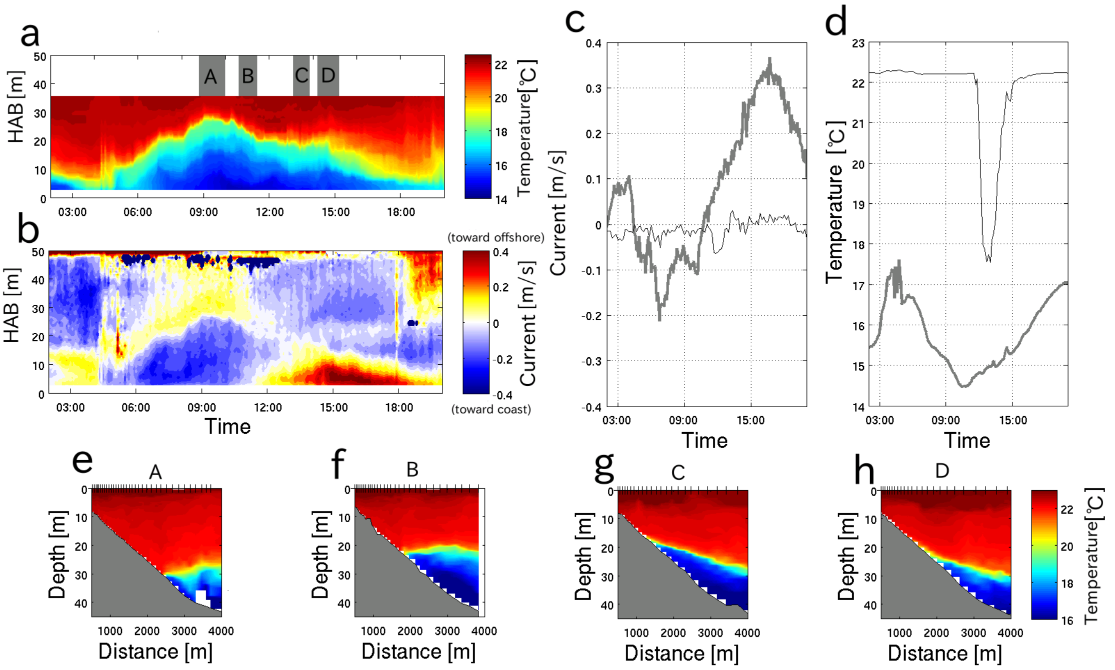

Fig. 4- 11. (a) Temperature and (b) east-west current observed from the mooring array, (c) current, and (d) temperature observed near the bottom at the deep mooring site (54 m, thick gray line) and the shallow site (21 m, thin black line), and (e, f, g, h) temperature distributions observed from the transect survey on 11 September 2013. Shaded areas in (a) indicate transect observation periods: (A), (B), (C), and (D). The data shown in (c) and (d) were obtained at 2.5 m above the bottom (deeper site) and at 1 m above the bottom (shallower site).

High turbidity water was also observed near the shore area, 5–10-m depth (Fig. 4-7de). However, the sediment particle size is too large to sustain resuspension between 5 and 10 m depths (Fig. 4-4C and D); the sediment consists mainly of sands. The terminal sinking velocity is approximately 32–288 mh^{-1} (8.9×10^{-3} – 8.0×10^{-2} ms^{-1}) when particle size is 100–300 μm (Fig. 4-2C and 2D). Therefore, the high-turbidity water in the shallow area was not due to sediment resuspension, but it was probably due to fine sediments transported from the Unosumai River. The mouth of the Unosumai River is located at the west bay head. The high turbidity water from rivers is transported to the offshore area as a downslope turbidity current near river mouth areas (*Kineke et al.*, 1996; *Wright and Nittrouer*, 1995).

Turbulent Mixing in the internal bore

Breaking of internal waves and the vortex motion induce strong turbulent mixing as well as sediment resuspension (e.g., *Thorpe*, 1998; *Cacchione et al.*, 2002; *McPhee-Shaw and Kunze*, 2002). *Ivey et al.* (2000) identified a strong kinetic turbulent dissipation rate, 10^{-6} Wkg^{-1}, from a tank experiment at the critical angle condition. *Richards et al.* [2013] measured a high dissipation rate exceeding 10^{-5} Wkg^{-1} in shoaling vortex waves along a shallow slope. The turbulent kinetic energy dissipation rate, ε, estimated from the YODA Profiler indicates strong turbulent mixing in the internal bore wave (Fig. 4-12). The turbulent intensity was also strong near the surface layer (0–10 m), likely due to the wind stress, 10^{-8} - 10^{-7} Wkg^{-1} (see chapter 3). The dissipation rate ε reached 10^{-6} Wkg^{-1} at the head of the wave on 27 September, which is consistent with that estimated from the law of the wall theory (*Dewey and Crawford*, 1988),

$$\varepsilon = \frac{{C_D}^{3/2} u^3}{\kappa z} , \qquad (4\text{-}5)$$

where κ is the von Kármán constant 0.41, z is the height above the bed, and u is the velocity above the bottom. The estimated ε is 2.4×10^{-6} – 8.2×10^{-6} Wkg^{-1} at 1 m above the bottom, when u is 0.2 – 0.3 ms^{-1}. The high dissipation rate appeared not only at the head of the wave, but also along an isopycnal interface (Fig. 4-12b). Vertical turbulent diffusivity, $K\rho$, was estimated from the following formula (*Osborn*, 1980),

$$K\rho = 0.2 \frac{\varepsilon}{N^2} \qquad (4\text{-}6).$$

The vertical turbulent diffusivity was high at the head of the bore wave, reaching 10^{-4} m^2s^{-1} (Fig. 4-12b). On the other hand, the background value of $K\rho$ was low, 10^{-7} m^2s^{-1}, which is almost equivalent to the molecular diffusivity of heat. Therefore, the internal waves play a significant role in mixing processes and the heat fluxes in the bay water.

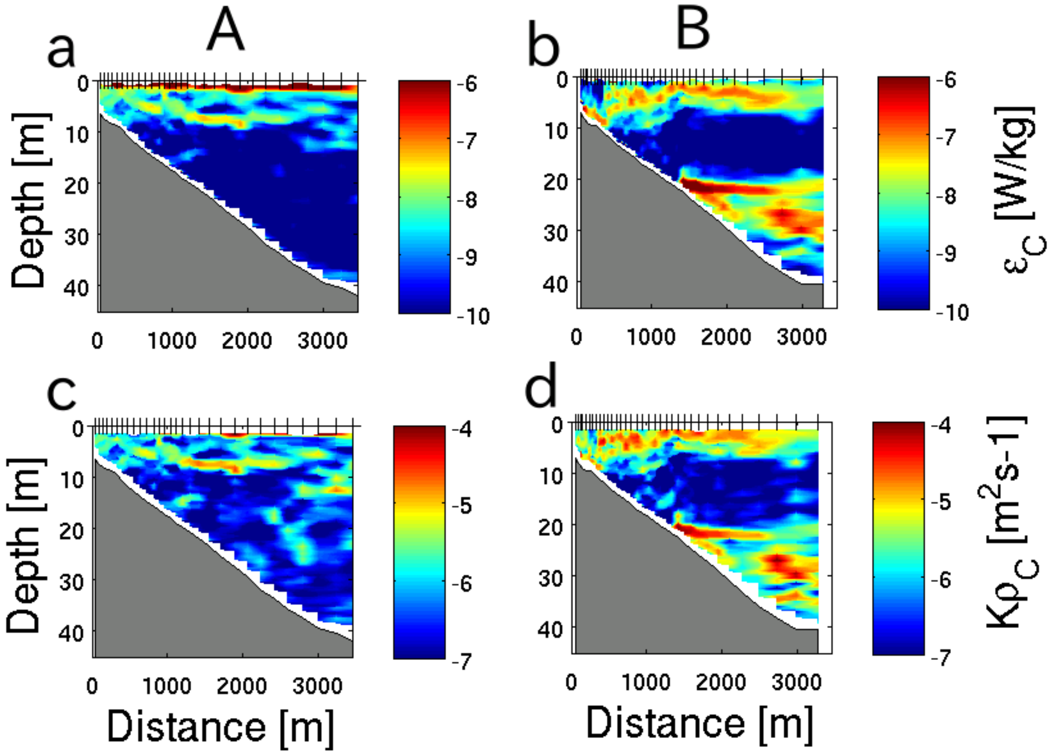

Fig. 4-12. (a, b) ε_P Wkg^{-1} and (c, d) $K\rho$ m^2s^{-1} distributions (a, c) before the bore wave period and (b, d) during the bore wave period estimated from the YODA Profiler observations on 27 September 2013.

The Intermittent Appearance and the Generation of Bore Waves

Run-up of internal waves was observed three times in the observation period (Fig. 4-5). Although the bore waves appeared after high amplitude flood tides, intervals between low tides and the timing of the temperature decrease are not consistent in each case (Fig. 4-5a). The periodicity of the internal wave incursion event does not agree with the tidal frequency. *Hosegood et al.* (2004) and *Van Haren* (2006, 2009) also mentioned a similar difference. The theoretical propagation speed of a linear internal wave is directly proportional to the density stratification and the depth (*Kundu*, 1990). The difference between the tide and the appearance of internal waves may be affected by the propagation speed of the internal wave. In order to compare the propagation speed of the waves, the density differences, $\Delta\rho$, between the upper layer and the lower layer on 26 and 27 September were estimated from the YODA Profiler observation data. The interface between the lower layer and the upper layer was assumed to be at a 22°C isothermal depth, since this corresponds to the interface of the internal wave. Fig. 4-13 shows density distributions and the 22°C isothermal depth in internal wave periods on 26 and 27 September 2012. The density differences, $\Delta\rho$, are approximately 1.34 and 1.85 kgm^{-3} for 26 and 27 September, respectively. According to the two-layer long wave theory, the propagation speed of internal waves is expressed as

$$C = \sqrt{\frac{(\Delta\rho/\rho_0)gh_1h_2}{h_1+h_2}} \quad , \qquad (4\text{-}7)$$

where h_1 and h_2 are the layer thicknesses. Assuming h_1 and h_2 are the same for both dates (Fig. 4-13), the ratio between the propagating speeds of the internal wave on 26 and 27 September can be expressed as

$$C_{Ratio} = \frac{C_{27}}{C_{26}} = \sqrt{\frac{\Delta\rho_{27}}{\Delta\rho_{26}}} \quad , \qquad (4\text{-}8)$$

where subscripts 26 and 27 denote the date. The C_{Ratio} is approximately 1.38, and therefore, the wave propagation speed on 27 September was approximately 1.38 times faster than that on 26 September. This ratio is consistent with the lags between the low tide and the beginning of the decrease in temperature. The lag on 27 September was shorter than that on 26 September. This difference is consistent with the propagation speed of bores. Thus, the propagation speed of each internal wave is proportional to the strength of the stratification. Consequently, the variation of the stratification causes variable lags between the barotropic tide and the appearance of internal waves. *Walter et al.* (2012) showed a similar consistency between the stratification condition and the appearance of bore waves. However, observed data were not enough to verify a clear relationship between stratification conditions and the periodicity of internal bore waves, because the observation period was too short and the amount of observed data was not sufficient. Also, the nonlinear motion accelerates the propagation speed of internal bores (*Vlasenko et al*., 2012). To address these issues, longer period and larger area observations are required.

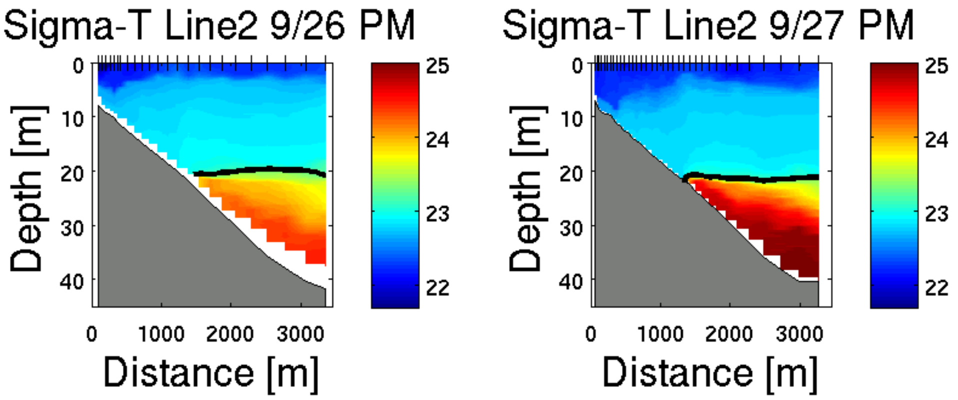

Fig. 4-13 Density (sigma-T) distributions during internal bore wave periods on 26 and 27 September 2013. Black lines indicate isothermal lines of 22 degrees.

The source of the internal bore energy is a linear barotropic internal tide in a deeper site (e.g., *Vlasenko et al*., 2005; *Van Gastel et al*., 2009). The reflection of the internal tide along a slope induces energy convergence, internal bore waves, and sediment resuspension over the continental shelves and slopes (e.g., *Cacchione et al*., 2002; *Puig et al*., 2004). The direction of the ray of internal waves after the reflection on the slope is determined by the ratio γ/s, where γ is the topographic slope and s is the internal wave beam slope. The beam of internal tide, s, is given by

$$s = \tan\alpha = \sqrt{\frac{\sigma^2 - f^2}{N^2 - \sigma^2}} \quad , \qquad (4\text{-}9)$$

where α is the internal wave beam angle, σ is the semidiurnal tidal frequency, f is the local inertial frequency, and N is the buoyancy frequency. The local inertial frequency is expressed as $2\ \Omega\ \sin\phi$, where Ω is the Earth's rotational vector and ϕ is the latitude. When the topographic slope angle γ is smaller than the internal wave slope angle ($\gamma/s < 1$, Fig. 4-14a), the wave can propagate into the shallow area after the reflection (the subcritical topography/transmissive condition). When the topographic slope is steeper than the wave slope angle ($\gamma/s > 1$, Fig. 4-14b), the wave reflects back to offshore and cannot propagate into the shallow area after the reflection (the super critical topography/reflective condition). When the topographic slope angle matches the wave slope ($\gamma/s = 1$), the reflected waves travel parallel to the slope and lead to strong energy convergence along the slope (the critical condition, Fig. 4-14c). To investigate the reflection condition over the shelf and the slope, I compared the slope gradient and the angle of the internal tide in the off-Sanriku area in September. The buoyancy frequency, N, for estimating the beam angle of the internal tide was computed from the monthly (September) and the seasonal (summer) climatological temperature and salinity data of the World Ocean Atlas 2009 (WOA 2009), produced by National Oceanographic Data Center (NODC). The ratio of the topographic slope to the internal wave slope, γ/s (Fig. 4-14d), indicates that the continental shelf break is critical with respect to the $M2$ internal tide in depths ranging from 300-m to 700-m where $\gamma/s \sim 1$. These depth are thus likely the site of the generation of the internal tides that propagate on shore over the subcritical topography, which is transmissive ($\gamma/s < 1$). Upon reaching the shore, the tides encounter critical topography, which leads to energy convergence, bottom intensification and the large-amplitude bores that observed in Otsuchi Bay. In addition to the critical reflection, the characteristic coastline, the “ria” (Fig. 4-1), may enhance the amplitude of bore waves. Also worth noting is that all of the Sanriku Coast is bounded by the critical slope. Thus, the large run-up internal bores are probably common in other bays along the Sanriku Coast.

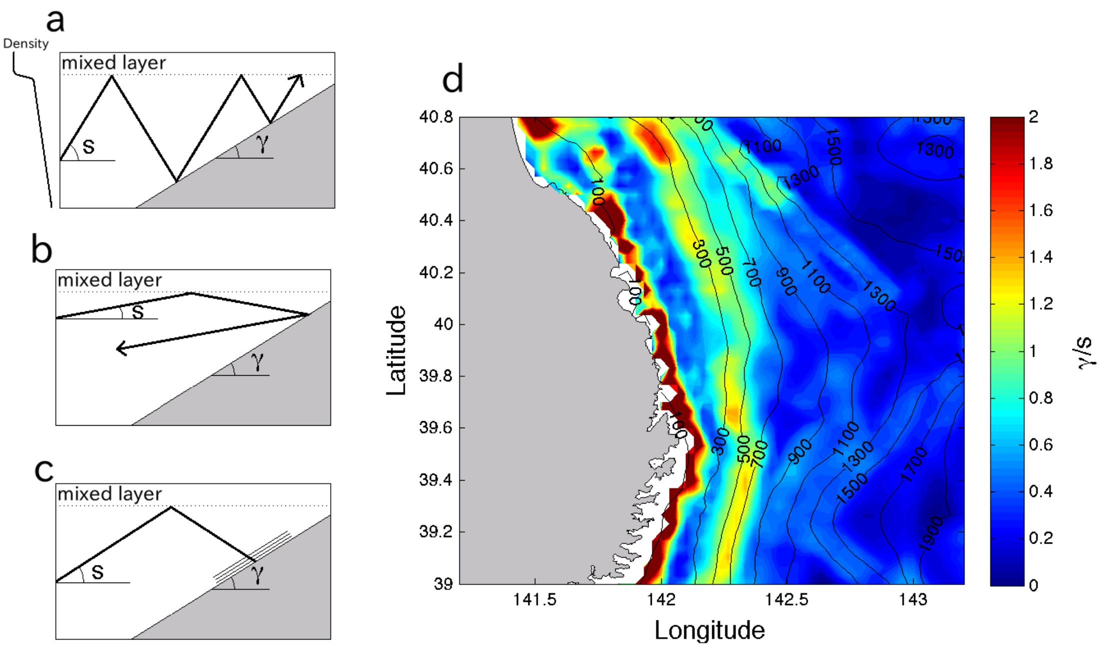

Fig. 4-14. (a, b, c) Schematic images of internal wave reflection on a slope and (d) the reflection condition (*γ*/*s*) off-Sanriku coast. Contour lines in panel (d) indicate the depth.

Numerical Simulations

In order to reproduce the observed bore waves numerically, I used a fully nonlinear, nonhydrostatic model, SUNTANS (*Fringer et al.*, 2006), in a two-dimensional domain. The size of the domain is 10 km long and 80 m deep. The horizontal grid spacing, the vertical grid spacing, and the time step are 20 m, 0.56 m, and 1 s, respectively. The Mellor-Yamada 2.5 level turbulent closure model (*Mellor and Yamada*, 1982) is used with the two-dimensional SUNTANS. The initial conditions for the temperature and the salinity are taken from the transect observation with the initial main thermocline depth of 40 m (interface of the internal wave). The model was forced by the first mode internal wave at the velocity specified ocean boundary. The frequency of the internal waves is set to M_2 tidal frequency. In order to reproduce 20 m of the isothermal displacement as observed in the bay, the velocity amplitude of internal waves is set at 0.2 ms^{-1}. The shallow coast boundary is closed in the domain.

The results from Otsuchi Bay simulations show internal bore waves propagating into the bay and are in good agreement with the in situ observations (Fig. 4-15). When the bore wave propagates into the bay (surging period), the bore head is accompanied by a sharp cold front and a vortex (Fig. 4-15de). A steep isothermal displacement at the head of the wave represents the vortex. The horizontal flow field indicates the shoreward flow in the lower layer and the offshoreward flow in the upper layer during the surging period (Fig. 4-15bjk), which are consistent with field surveys (Fig. 4-7hi). The offshoreward current in the bottom boundary layer shown in Fig. 4- 15i is due to the receding of the previous bore wave. During the receding phase, the cold bore propagates back to the offshore as a downslope gravity current. The current direction switches during the receding phase. In contrast to the receding cold water in the deeper area, the head of the bore continues to propagate into the shallow area (Fig. 4- 15l and 15m). The bore is stretched along the sloping bottom by the downslope current and the upslope motion of the bore head during the receding phase, and the bore becomes thinner in the vertical direction than that in the surging period. The shoreward flow is enhanced at the head of the bore (Fig. 4- 15j, 15k, and 15l). The maximum shoreward flow appears when the bore head passes through the initial thermocline depth (40 m), and the maximum speed reaches 0.36 ms^{-1}. Above the thermocline depth, the shoreward current decreases as it shallows (Fig. 4- 15j, 15k, and 15l).

The results indicate that the run-up of internal waves enhances the bottom current located near the initial thermocline depth. The horizontal scale of the vortex resolved by the model is approximately 100 m (Fig. 4- 15d, 15e, and 16a). However, this scale is approximately three times larger than the observed scale (36 m) estimated from the mooring survey. The large-scale vortex motion in the model is probably due to the numerical diffusion and the limitation of the resolution, since the horizontal grid spacing ($\Delta x = 20$ m) is too large to capture such a small vortex motion.

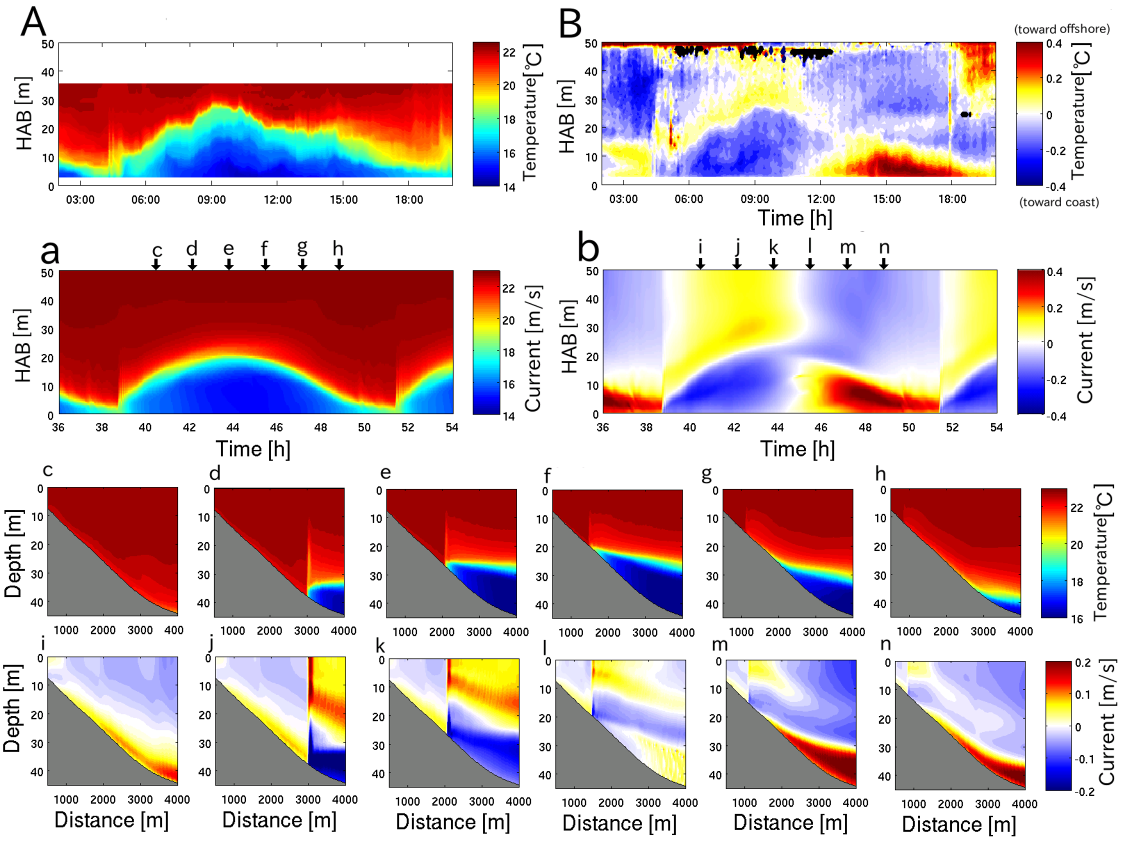

Fig. 4- 15. (A, B) Observation results and (a–n) numerical simulation results from SUNTANS. Time series of (A) temperature and (B) east-west current from the mooring survey in September 2013. Time series of (a) the temperature and (b) the horizontal current at 50-m depth, and snapshots of (c–h) temperature distributions and (i–j) horizontal current distributions in the transect line from SUNTANS. Arrows at upper *x* axis in panels (a) and (b) indicate the timing of snapshots shown in (c–n). The red (blue) color in panels (a), (b) and (i - n) indicates the onshore (offshore) ward flow.

To resolve the small vortex motion, I used a small and finer resolution domain, with a length of 320 m, a horizontal grid spacing of 0.64 m, and a vertical grid spacing of 0.22 m. The finer resolution model was forced by a cold-water intrusion from the deeper boundary (0.1 ms^{-1}) and a weak outflow was set above the cold water intrusion layer to maintain the total volume flux = 0. The shallower boundary was set as open boundary. The finer model result shows a detail structure of the vortex motion (Fig. 4-16b and 16c). The horizontal scale is approximately 20 m and is five times smaller than that from the coarser original model. The vertical ejection current and the downward current at the head of the wave reach 0.03 ms^{-1}, which is consistent with the observed result shown in Fig. 4- 12a and 12b. The time series of the vortex from the model was compared with the observed feature from the mooring survey (Fig. 4- 16f and 16g) and shows an excellent agreement between the model and the observation.

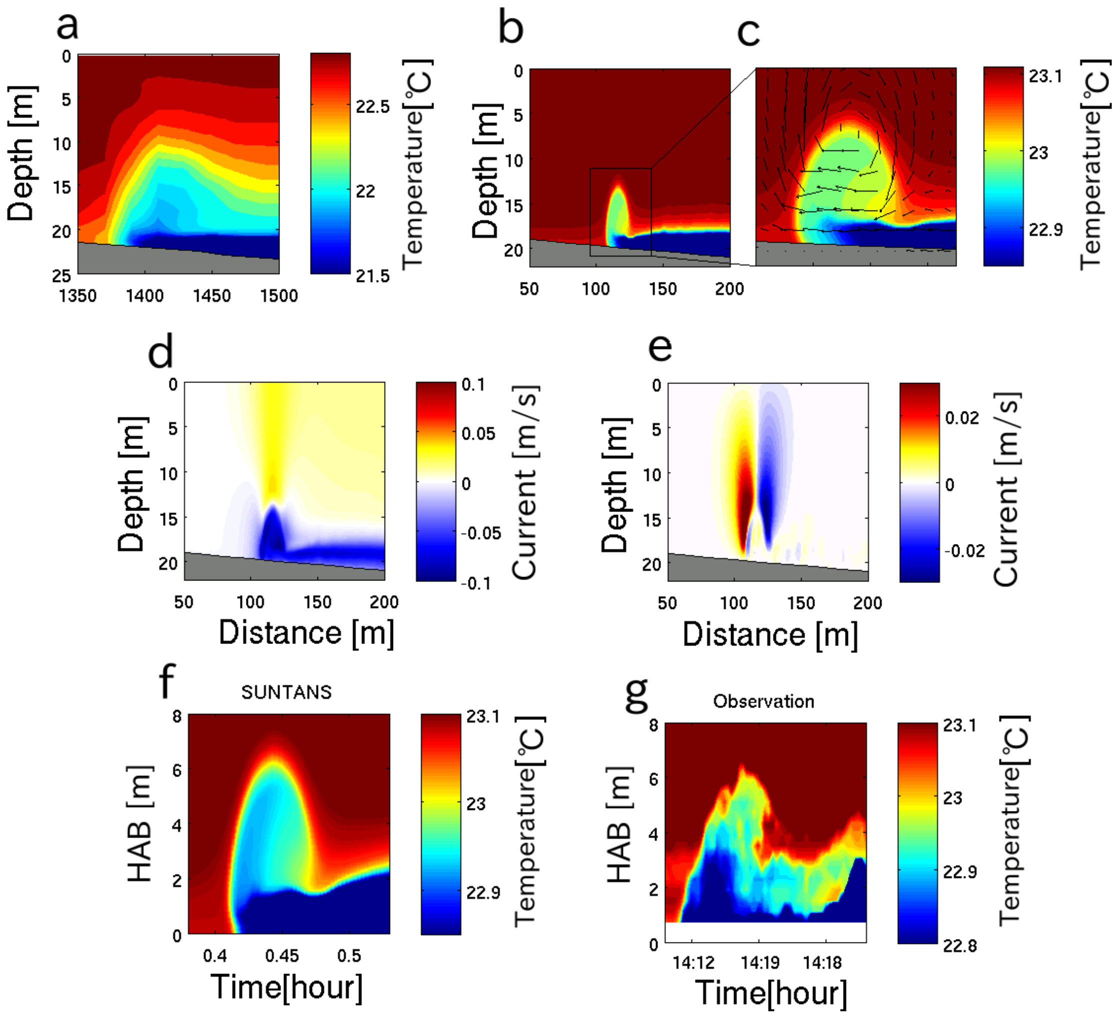

Fig. 4- 16. Numerical results of temperature at the bore head from (a) the coarser domain and (b, c) the finer domain. (d) The horizontal current and (e) the vertical current from the finer domain. Bottom two panels show the time series of the temperature at the bore head from (f) the numerical model and (g) the observation. The rage of the horizontal axis in panels (f) and (g) are same as each other.

4. 5 Conclusions

I have observed fine features of the physical structures in Otsuchi Bay using mooring systems and the YODA Profiler. The YODA Profiler observations have shown large amplitude run-up of internal bores. The sharp intermediate nepheloid layers (INLs) detached from the slope were also observed above the interface of the internal waves. The high-resolution thermistor array observation has revealed the high-frequency wave feature in the interface of the bore wave, likely induced by shear instability, and the vortex structure at the head of the bore wave. Strong turbulent mixing was observed in bore waves. The turbulent kinetic energy dissipation rate reached 10^{-6} Wkg^{-1} at the head of the bore wave. The internal bore generated the vortex accompanied by the strong vertical motion at the head of the bore. The vertical current reached 0.03 ms^{-1} in the vortex and induced the ring-like strong vertical resuspension of sediments. The topographic slope off-Sanriku shelf satisfied the critical condition, leading to the strong energy convergence. SUNTANS reproduced observed internal bores propagating into the bay well. The model results showed the thick bore front during the surging periods and the thin stretched downslope flow during the receding phase as observed results in this study. However, the resolution of the domain for the bay area was too low to reproduce the vortex motion. A simplified high-resolution simulation showed the detailed structure of the vortex motion. The numerical results are in good agreement with the observed feature. This study clearly indicates that internal bore waves generate locally intensified strong currents (a vortex) at the head of the wave, turbulent mixing and sediment resuspension in a shallow bay.

4. 6 Appendix

The orbital velocity due to sea surface waves

In shallow area, the near-bottom current is largely affected by surface waves (*Noble and Xu*, 2003; *Trowbridge*, 1998). *Noble and Xu* (2003) showed that the bed shear stress due to surface waves is larger than that due to the mean currents in a coastal area.

Fig. 3-17a presents a spectrum of current data obtained by the ADCP in September 2012 at 2 m above the bottom at a 20-m depth. A steep peak appears in this data at approximately 0.09 Hz. This peak agrees with the surface gravity wave frequency obtained from the pressure data (Fig. 3-17a). The heights of sea surface waves were 0.25–0.4 m in the observation period. In order to differentiate current from the internal bores, the current data have to be separated into two parts: (1) the surface gravity wave part and (2) the internal bore part. I assumed that the current lower than 0.05 Hz (20 s period) is the current due to the internal waves. This threshold is between the peak frequency of surface waves (approx. 10 s) and the maximum buoyancy period ($2\pi/N$) in the internal bore (approx. 30 s). The low-frequency current, U_{low}, is estimated from a low-pass filter data processing. The high-frequency current due to the surface wave, U_{high}, is assumed to be $U_{High} = U_{Total} - U_{Low}$, where U_{Total} is nonfiltered data. The spectra of U_{Total}, U_{Low}, and U_{High} are shown in Fig. 3-17b. Although the high-frequency component may contain turbulence, the current due to turbulence is much smaller than the current due to surface waves and can be negligible (*Trowbridge*, 1998). The maximum orbital velocity due to surface waves 2 m above the bottom is 0.05–0.11 ms^{-1}. The maximum orbital velocity is estimated from the variance of the high-frequency current component and is defined as

$$Usw_{OBS} = \sqrt{2(\mathrm{var}(U_{high}) + \mathrm{var}(V_{high}) - 2\,\mathrm{var}(U_{noise}))} \quad , \qquad (10)$$

where $var(U_{noise})$ is the variance of the noise velocity estimated by the RDI's software, 0.00023 m^2s^{-2}. On the other hand, the maximum orbital velocity can be parameterized by the sea surface elevation using the *Soulsby* (1997) formula,

$$Usw_{PAR} = \frac{\pi H_{1/3}}{T \sinh(kh)} \cosh(kd) \quad , \qquad (11)$$

where $H_{1/3}$ is the significant height of surface waves, $H_{1/3} = 4.004\ \eta_{rms}$ (η_{rms} is the root mean square of the observed sea surface height), T is the period of the surface wave, k is the wave number estimated from a method described in *Wiberg and Sherwood* (2008), h is the depth, and d is the distance from the bottom, 2 m. Usw_{PAR} and Usw_{OBS}, estimated every hour, are consistent with each other (Fig. 3-17cd). The determination coefficient, R^2, between Usw_{PAR} and Usw_{OBS} is 0.86 ($p < 0.01$). The observed high-frequency current component was mostly generated by surface gravity waves. Therefore, I assumed that the current data filtered by the low-pass filter (cutoff frequency at 0.05 Hz) is the current caused by internal bores.

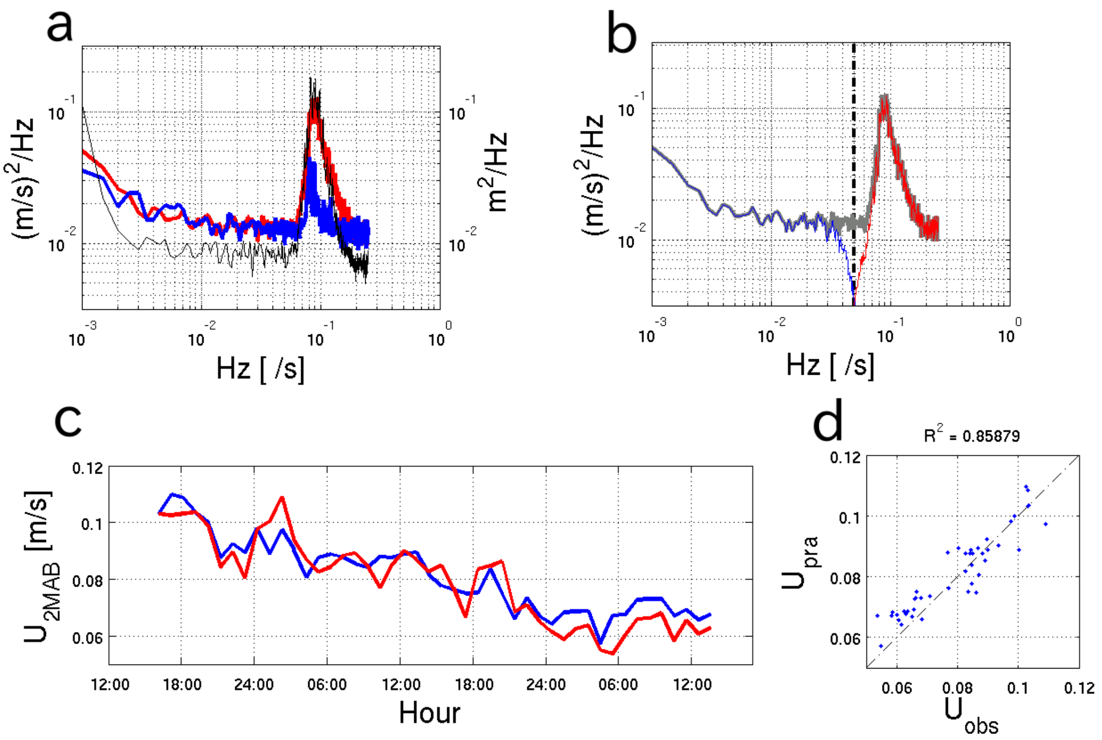

Fig. 3-17. (a) Spectrum of east-west (red line) and north-south (blue line) current component and the depth fluctuation (black line). (b) East-west current spectrum of the low frequency (thin blue line), the high frequency (thin red line), and the total current components (thick gray line). (c) The maximum orbital velocity due to the surface wave estimated by the ADCP (blue) and the *Soulsby* (1997) parameterization (red). (d) Relationship between the maximum orbital velocity induced by surface waves from the ADCP and the *Soulsby* (1997) parameterization.

Chapter 5

Crash mixing induced by internal bores

5. 1 Introduction

Vertical exchanges of materials and buoyancy play a significant role in global ocean circulation and such exchanges are mainly generated by turbulent mixing (*Munk and Wunsch*, 1998; *St. Laurent and Thurnherr,* 2007; *Lumpkin and Speer,* 2007). Nutrients and gas exchanges due to turbulent mixing have been recognized as important contributor to ocean ecosystems and the global carbon cycles (*Sharples et al.,* 2009; *Nakatsuka et al.,* 2004; *Walsh, 1991*).

One major phenomenon that generates turbulent events in the ocean is the interaction between the current and the topography (e.g., *Ledwell et al.,* 2000; *Klymak and Gregg, 2004; Hasegawa et al.,* 2004). Tidally driven turbulent mixing has been frequently found in channels and estuaries (e.g., *MacDonald and Geyer,* 2004; *Nash et al.,* 2009; *Kokubu et al.,* 2013). Geostrophic or tidal flows flowing over sills or near islands induce intensified turbulent mixing and vertical diffusive transports (e.g., *Klymark and Gregg,* 2003; *Hasegawa et al.,* 2004). *Heywood et al.* (2002) and *Ledwell et al.* (2000) revealed that the intensity of turbulent mixing is also high in deep abyssal oceans due to rough topographies.

Internal waves and internal tides are energetic, ubiquitous phenomena in the ocean; internal waves and their breaking events are also major generator of turbulent mixing (e.g., *Cacchione et al.,* 2002; *Mackinnon and Gregg,* 2003; *Venayagamoorthy and Fringer*, 2006). Reflections of linear internal tide on continental slopes induce energy convergence along slopes and intensified bottom currents, which results in non-linear shoaling internal waves (e.g., *Cacchione et al.,* 2002; *Vlasenko et al.,* 2005; *Van Gastel* *et al.,* 2009). Internal waves have frequently been observed in coastal areas, and they are important for the cross-shelf transport of nutrients (e.g., *Leichter et al.,* 1996), sediment (e.g., *McPhee-Shaw,* 2006), and zooplankton and larvae (e.g., *Pineda,* 1994). Internal tides induce large isopycnal displacements and strong currents (*Huthnance,* 1989; *Petruncio et al.,* 1998; *Broenkow and McKain,* 1972; *Van Gastel et al.,* 2009; *Wang et al.,* 2008). *Broenkow and McKain* (1972) observed an 80 m isopycnal displacement due to internal tides. *Van Gastel et al.* (2009) observed strong horizontal currents, reaching 1.0 ms^{-1}, induced by internal tides. Shoaling internal waves finally run-up on shallow slopes and break as highly non-liner waves and are called as “boluses” or “bores” (*Wallace and Wilkinson,* 1988; *Helfrich,* 1992). After run-up, they recede back to offshore areas, receding and run-up events are repeated by tidal cycles (e.g., *Walter et al.,* 2012). Breaking of run-up internal bores leads to strong turbulent mixing events in coastal areas (e.g., *Vlasenko and Hutter,* 2002). Although the cycle of internal bore events is influenced by tidal cycles, the appearance of internal bores is intermittent and is not consistent with tidal cycles (*Hosegood et al.,* 2004; *Walter et al.,* 2012). There are time lags between tidal cycles and internal wave cycles, because of the distance between the wave generation site and the observation site (*Vlasenko et al.,* 2012). *Walter et al.* (2012) pointed out that the speed of an internal bore is controlled by the local stratification.

Recent studies found that a vortex core accompanied by strong vertical motion is formed at the head of bore waves (*Venayagamoorthy and Fringer,* 2006; *Masunaga and Yamazaki,* 2014). Vortex cores contribute to vertical mixing, mass transports and sediment resuspension (*Venayagamoorthy and Fringer,* 2006; *Masunaga and Yamazaki,* 2014; *Richard et al.,* 2013). *Richard et al.* (2013) showed strong turbulent mixing in vortex packets and the rate of turbulent kinetic energy reached 3×10^{-5} Wkg^{-1}.

Although, it is well known that internal waves are important for mixing and vertical fluxes in the ocean, details of internal waves and the whole picture of breaking processes have not been well understoo due to the lack of field survey data. I attempted to reveal behaviors of internal waves repeatedly propagating into a shallow area by combining field surveys and numerical simulations. In the field surveys, I used the

Yoing Data Acquisition Profiler (YODA Profiler, *Masunaga and Yamazaki*, 2014), the Underway CTD (UCTD, *Rudnick and Klinke,* 2007) and a microstructure profiler TurboMAP-L (*Wolk et al.,* 2002). The YODA Profiler and the UCTD are tow-yo instruments and allow us to obtain high-resolution data in horizontally. The YODA Profiler sinks in a stable free fall mode in water columns using a brush and also provides high-resolution data in vertically. Therefore, I can infer the rate of turbulent kinetic energy dissipation, ε, from the vertical fluctuation of conductivity. Although the YODA Profiler is suitable for observing high-resolution physical data in shallow areas, it is not suitable for observing deeper areas. In order to obtain high-resolution data in deep areas, I used the UCTD. The free-fall microstructure profiler TurboMAP-L (*Wolk et al.,* 2002) was also used to estimate the rate of turbulent kinetic energy dissipation. In addition to the field surveys, I employed a fully non-hydrostatic numerical simulator, Stanford Unstructured Nonhydrostatic Terrain-following Adaptive Navier-Stokes Simulator (SUNTANS, *Fringer et al.,* 2006), which has an ability to reproduce details of shoaling internal bore waves, as presented in Chapter 4.

This chapter presents internal bore waves investigated by both field and numerical surveys. Section 2 describes the filed survey location and instrumentation. Section 3 presents observed results in Otsuchi Bay. Section 4 presents numerical simulation results and the criteria for crash mixing. Section 5 discusses reflected and dissipated internal wave energy on the slope. Section 6 describes intensified river plume mixing coinciding with crash mixing. The last section summarizes this chapter with conclusions.

5. 2 Instrumentations and numerical setups

Transect observations

Two types of instruments were deployed for transect observations, the YODA Profiler (*Masunaga and Yamazaki,* 2014) and the UCTD (*Rudnick and Klinke,* 2007) in Otsuchi Bay on September 10, 2013. The YODA Profiler was used to observe the near shore area (Depth < 60 m), and the UCTD was used to observe deeper area (Depth >50 m). I deployed the YODA Profiler from the R/V *Grand-maillet* (the University of Tokyo), and the UCTD was deployed from the fishing-boat *Daini-wakashio-maru* (*Kamaishi-Toubu* fishery). The transect line was set up from the western head to the bay mouth, and the total observation line length from two instruments was approximately 12 km (Fig. 5-1). The sinking velocity of the YODA Profiler was adjusted to 0.5 ms^{-1} to obtain high-resolution data horizontally. The UCTD carries Conductivity, Temperature and Depth (CTD) sensors and records data at 16 Hz. In order to prevent the UCTD sensor hitting the bottom, the line was not rewound on the tail spool, which reduced the sinking velocity of the sensor. The sinking velocity of the UCTD sensor was approximately 3 ms^{-1} without the tail winding.

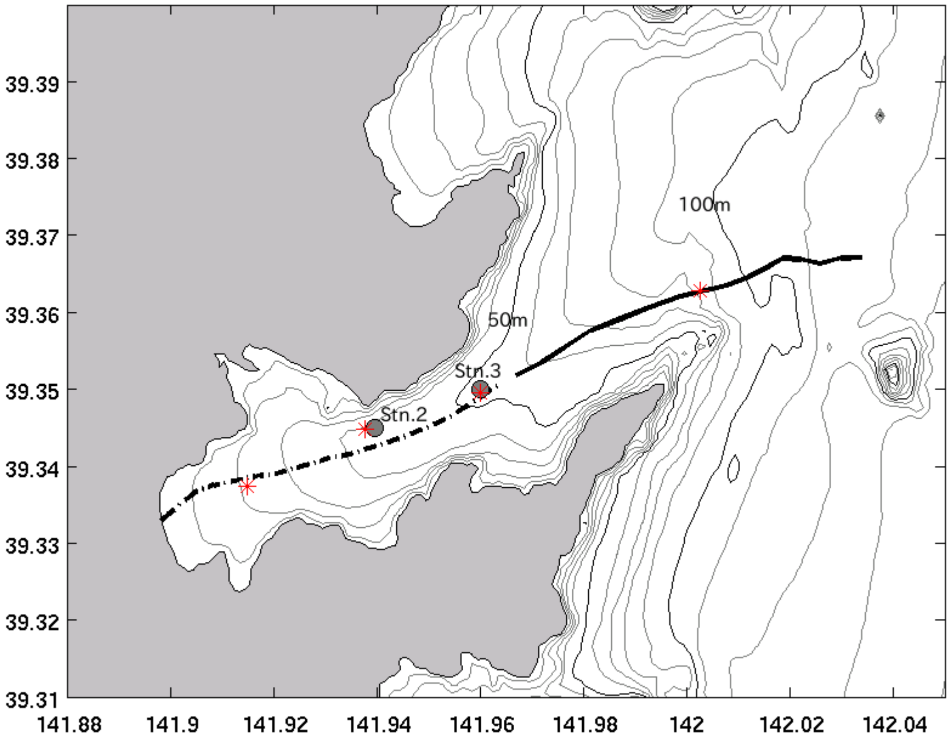

Fig. 5-1 The observation area. A black chain dot line and a black line indicate the YODA Profiler and the UCTD observation lines, respectively. Gray circles show two mooring stations, Stn. 2 and Stn. 3. Red stars (*) show TurboMAP-L observation points.

Microstructure observations

I made use of a free-fall microstructure profiler, TurboMAP-L (*Wolk et al.,* 2002), to estimate the rate of turbulent kinetic energy dissipation, ε, in the bay (Fig. 5-1). TurboMAP-L carries two microstructure shear probes, a fast response thermistor FP07, CTD, fluorescence and turbidity sensors. The observed data were recorded between 64 and 512 Hz depending on the sensor. The dissipation rate is estimated by using the following isotropic formula (*Osborn,* 1980),

$$\varepsilon = 7.5\nu\overline{\left(\frac{du'}{dz}\right)^2} \qquad (5\text{-}1)$$

where u' is the horizontal component of turbulent velocity, and ν is the kinetic viscosity of water. TurboMAP-L was deployed from *Daini-wakashio-maru* (*Kamaishi-Toubu* fishery). I obtained microstructure data at four points and made three profiles at each location in the bay on September 10, 2013.

The YODA Profiler allows us to infer the rate of turbulent kinetic energy dissipation using vertical fluctuations of conductivity, *dC/dz*, and the background PDF of ε (*Masunaga and Yamazaki,* 2014). The background PDF was obtained from TurboMAP-L observations in the bay. In order to infer the dissipation from the YODA Profiler, I estimated coefficients *a* and *b* for the following formula

$$\varepsilon = a\left[\overline{(dC/dz)^2}\right]^b \qquad (5\text{-}2)$$

with the QQ plot (quantile versus quantile) between PDFs of ε from TurboMAP-L and the variance of dC/dz from the YODA Profiler (Fig. 5-2b). Estimated coefficients, *a* and *b,* were 6.5×10^{-7} and 1.26 respectively. The profile of dC/dz from the YODA Profiler shows similar signals to the shear from TurboMAP-L near Stn. 3 in the bay. The distance between the two profiles observed by the YODA Profiler and TurboMAP-L was approximately 250 m. Data from TurboMAP and YODA Profiler shown in Fig. 5-2cde were obtained at 9:06 and 10:14 on September 10 respectively. The estimated ε from the YODA Profiler showed a good agreement with ε obtained from TurboMAP-L (Fig. 5-2e).

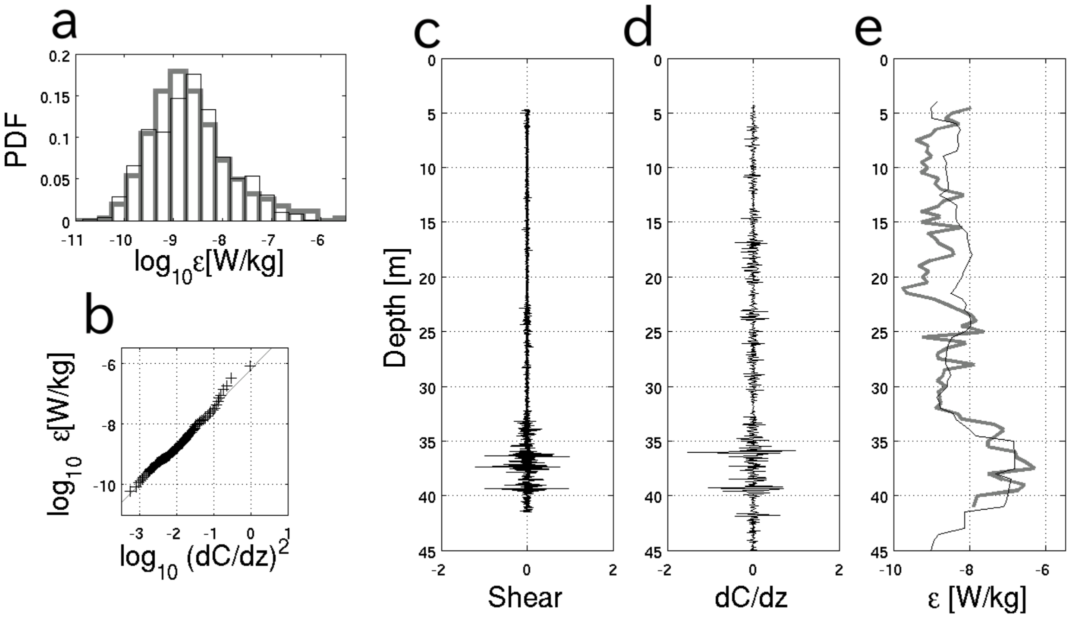

Fig. 5-2 (a) PDF of ε from the YODA Profiler (thin black outlined bars) and TurboMAP-L (thick gray outlined bars), (b) QQ plot between ε from TurboMAP-L and the variance of dC/dz from the YODA Profiler, (c) shear from TurboMAP-L, (d) dC/dz from the YODA Profiler and (e) ε profiles estimated from the YODA Profiler (thin black line) and TurboMAP-L (thick gray line) in Otsuchi Bay on September 10, 2013.

Mooring observation

Two mooring systems were deployed at 40 m (Stn. 2) and 54 m (Stn. 3) depth in Ostuchi Bay (Fig. 5-1) between July 10 and September 13, 2013. At the deeper mooring site (Stn. 3), an upward-looking four-beam ADCP (Teledyne RD instrument) was mounted at near the bottom. An upward-looking 600 kHz Aquadopp (JFE Advantech Co., Ltd.) was mounted at the Stn. 2. The vertical bin size and sampling interval of the ADCP was set to 1 m and 5 minutes (each sampling included 50 pings) respectively. The Aquadopp was set to resolve 1 m vertical bins and 10-minute sampling intervals (each sampling included 50 pings). Fifteen and twenty-three HOBO Tidbit v2 (Onset Computer Corporation) temperature sensors were mounted at Stn. 2 and Stn .3 respectively. These temperature sensors were arranged at 1.5 m vertical intervals.

In addition to these long-term mooring arrays, a high resolution mooring array was deployed near Stn. 3 during September 11 – 12, 2013. The distance between the high-resolution thermistor array and Stn. 3 was approximately 40 m. HOBO U24 (Onset Computer Corporation) sensors, the Compact-CTD (JFE Advantech Co., Ltd.) and an electro-magnetic current meter (INFINITY-EM, JFE Advantech Co., Ltd.) were mounted on the high resolution mooring system. Twenty-four HOBO U24 sensors were arranged between 0.7 m and 23.7 m at 1 m intervals and recorded data every 6 seconds. The electro-magnetic flow meter and the Compact-CTD were mounted at 0.7 m and 1.7 m above the bottom, respectively. Sampling intervals of the electro-magnetic flow meter and the Compact -CTD were 0.1 and 60 seconds (20 sample burst mode), respectively. The density field was dominated by temperature, and the relationship between the density (σ_T) and the temperature showed a nearby linear relationship on September 11, 2013 (Fig. 5-3). Therefore, I estimated the density making use of observed temperature from the high-resolution thermistor array.

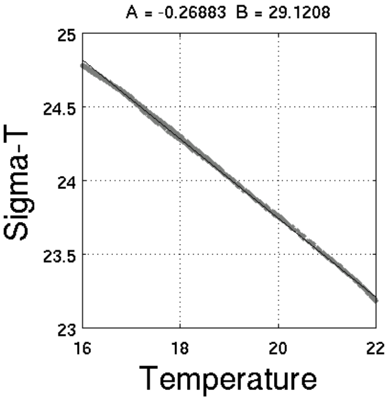

Fig. 5-3. The relationship between temperature and density (σ_T) on September 11, 2013. The black line is the regression line computed from the relation.

Numerical setups

I used two domains to simulate observed internal waves on September 10 (run#4-1) and 11 (run#4-2), 2013; density differences between the upper layer and lower layer were set to 0.81 and 2.2 kgm^{-3} in run#4-1 and run#4-2 respectively. Numerical setups in run#4-1 were the same as those described in the chapter 4. In order to resolve larger area in the numerical model, a large area domain was used in run#4-2. The numerical domain was 20 km long and 120 m deep with a horizontal grid spacing of 20 m and a vertical grid spacing of 0.8 m. A time step was set at 1s. The Mellor-Yamada 2.5 turbulent closure model (*Mellor and Yamada,* 1982) was used in numerical simulations. The initial stratification condition was taken from observed CTD data in Otsuchi Bay. The offshore boundary forcing was the semidiurnal internal tide. The interface of the forcing wave was set at the 40 m depth, the same depth as the thermocline. The velocity magnitude of the forcing internal wave was 0.20 ms^{-1} and 0.085 ms^{-1} in the upper layer and the lower layer respectively (the mean flux is zero at the boundary). Fig. 5-4 depicts a schematic image of the numerical domain.

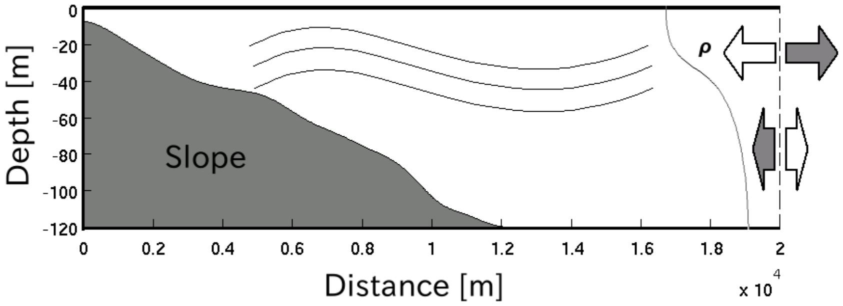

Fig. 5-4 A schematic image of the numerical domain for run#4-2.

5. 3 Observation results

Run-up and receding bores in Otsuchi Bay

Observed temperature data from the thermistor chain at Stn. 3 showed 87 bore waves between July 15 and September 12, 2013. In order to detect bore waves, I set the following two requirements: (1) the period of each bore wave is determined by one sinusoidal wave cycle near the bottom (4.5 m above the bottom) observed from the ADCP at Stn. 3 and (2) temperature must change at least 0.5 degrees during the wave period. The temperature time series gradually increased from 12 to 20℃ on a long time scale during the observation period, while the temperature fluctuated on a short time scale (less than one day) due to internal bore waves. The average temperature change during bore wave events is approximately 2.8℃, and the temperature dropped by more than 10℃ near the bottom on September 9. The east-west current speed varied -0.45 – 0.55 ms^{-1} (negative is shoreward flow, Fig. 5-5c). The flow speed during receding phases was higher than that during run-up phases in 80% of the cases. The flow speed during receding phases was linearly related to that during run-up phases, and the determination coefficient, R^2, was 0.44 (Fig. 5-5d). The flow speed during receding phases was approximately 1.5 times larger than that during run-up phases (Fig. 5-5d). Since the run-up bore has to fight against gravity on the slope, and the speed of the bore decreases as the depth decreased (as described in the last chapter). On the other hand, the gravity may accelerate the speed of the bore during the receding phase as a downslope gravity flow. Therefore, the mean flow over the bore wave period shows the asymmetry flow field in the vertical direction (Fig. 5-6). The mean flow was offshoreward from the bottom to 10 m above the bottom and was shoreward upper than 10 m from the bottom (Fig. 5-6c). The mean offshore flow was approximately 0.07 ms^{-1}. Thus, internal bore waves probably have the potential to transport sediment and materials to offshore areas from shallow areas along the bottom layer. The numerical simulation result also showed a similar asymmetrical mean flow field (Fig. 5-7). The mean flow field from the numerical survey was not consistent with observed results above 25 m depth. This difference may be due to the wind stress and background flows in the bay.

The periodicity of internal bores was intermittent, and the cycle (period) of internal bores ranged 2.5 – 34.6 hours. An example of the periodicity of bores is shown in Fig. 5-8. The current spectrum indicates two significant peaks, near the semidiurnal and the diurnal frequencies (Fig. 5-8a). Fig. 5-8b shows a histogram of the internal bore period. The semidiurnal (~12 h) and the diurnal (~24 h) peaks appear in the histogram. Means of the two components computed from theoretical fitting were estimated to be 12.0 and 22.9 hours. The weight of the semidiurnal components was 1.8 times larger than that of the diurnal component. Although the periodicity of bores was intermittent and unpredictable as shown in Fig. 5-8, the appearance of bores was largely dominated by the semidiurnal tide. Therefore, internal bores repeatedly run-up and recede on the slope in Otsuchi Bay near the semidiurnal tidal cycle. The intensity of currents due to internal bores was not related to a neap-spring cycle.

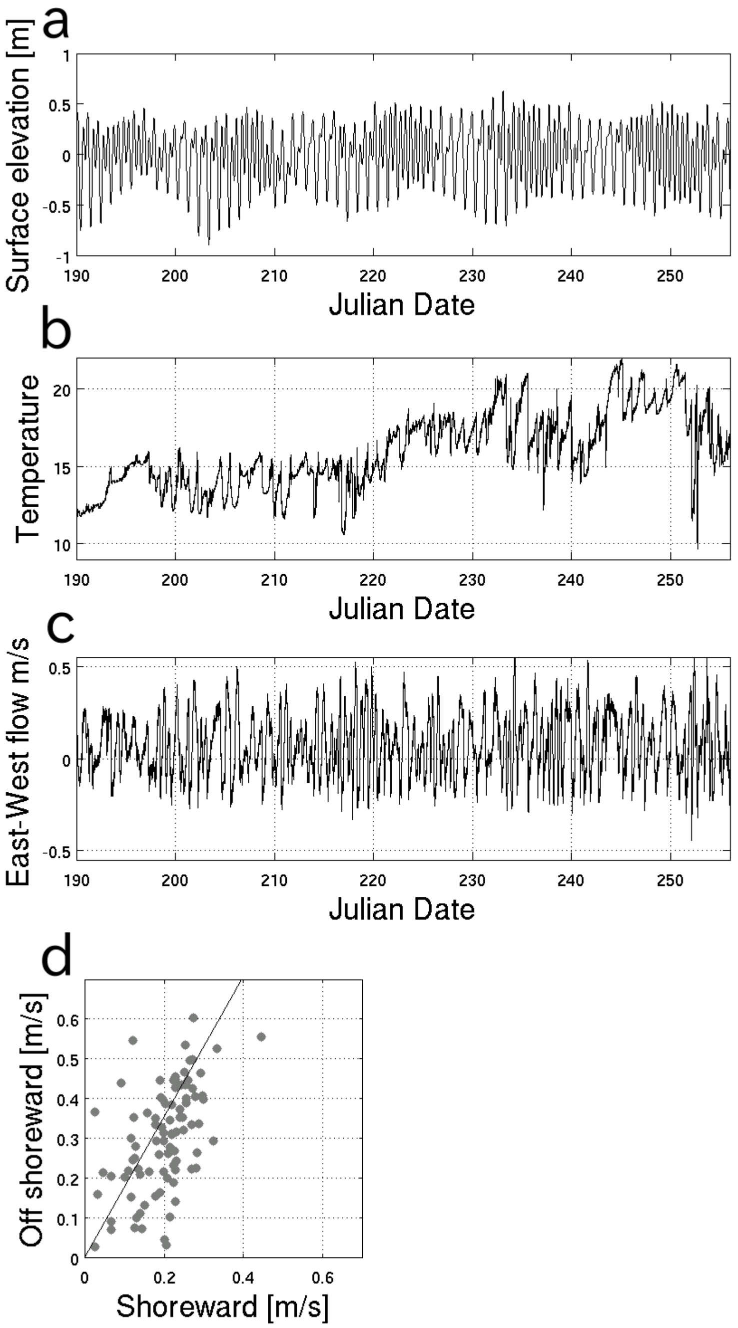

Fig. 5-5 Observed results at the Stn. 3 mooring station. (a) The sea surface tidal height, (b) temperature at 4 m above the bottom, east-west current speed at 5.5 m above the bottom and (d) the scatter plot between the offshoreward flow speed and shoreward flow speed for each bore wave event. The slope of the black regression line shown in panel (d) is 1.77.

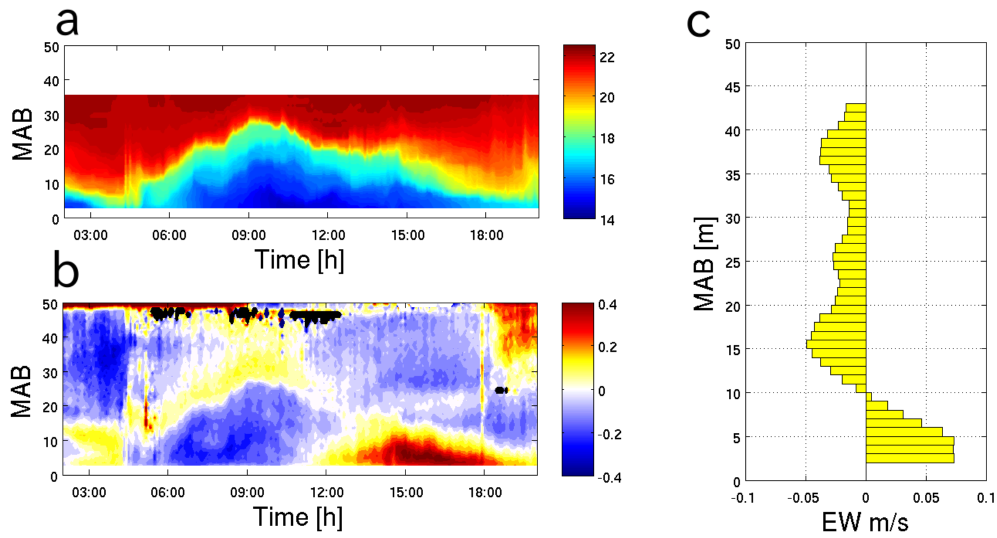

Fig. 5-6 (a) Temperature and (b) east-west current speed observed from the mooring system at Stn.3 on September 11, 2013. (c) The mean current speed over the bore wave period.

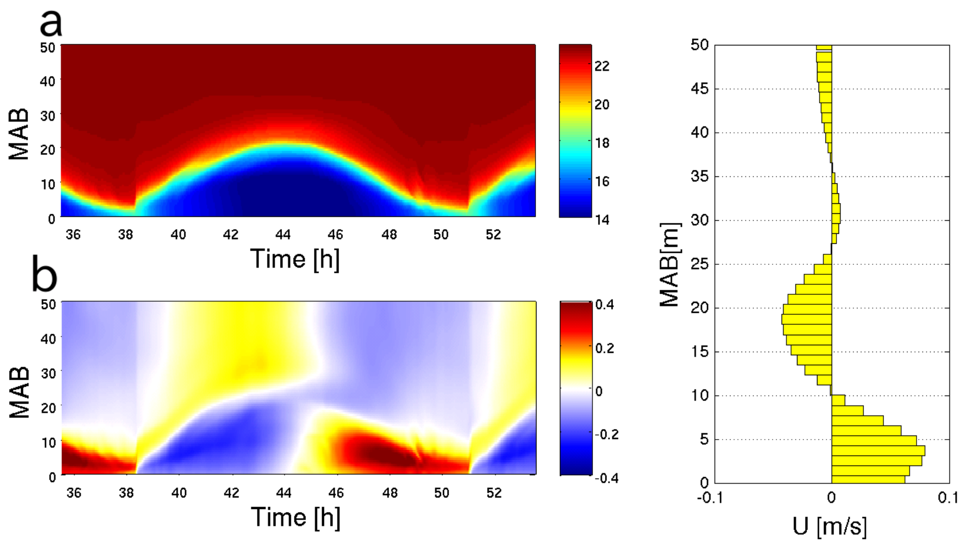

Fig. 5-7 (a) Temperature and (b) east-west current speed from the numerical simulation run#1. (c) The mean current speed over the bore wave period.

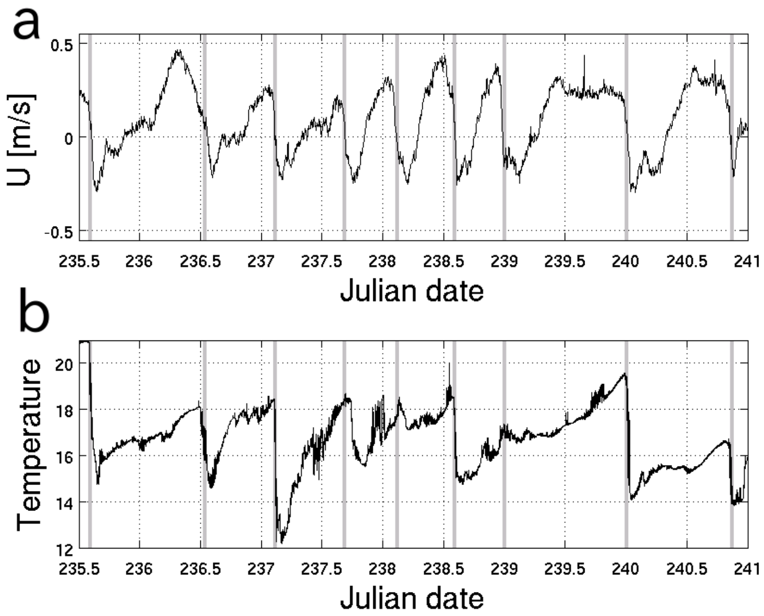

Fig. 5-8 (a) East-west current speed and (b) temperature time series observed near the bottom at Stn. 3. Thick gray vertical lines indicate the zero crossing points of current data.

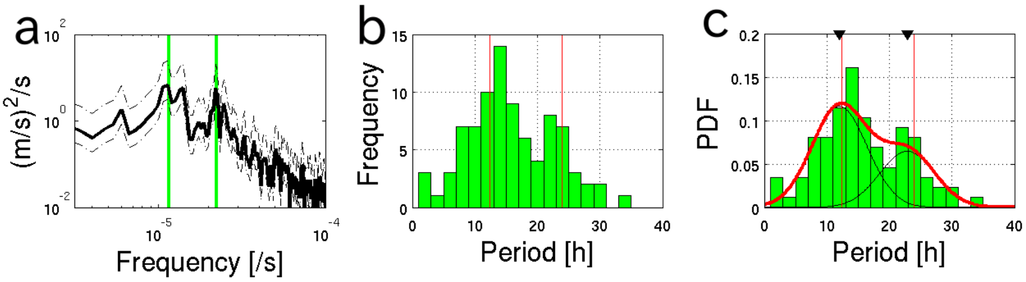

Fig. 5-9 (a) Spectrum of current data and (b, c) period of internal bores. Panel (c) shows the probability density function of the internal bore period with a bi-modal Gaussian function (red line). Chain dot lines in panel (a) show the 90% confidence interval of the spectrum. Light green (red) vertical lines indicate the semidiurnal and the diurnal frequency (period). Black inverse triangles show average values of the two components.

Crash mixing

Internal bores repeatedly run-up and recede due to the tidal forcing (e.g., *Leichter et al.*, 1996; *Walter et al.*, 2012). Observed data from Otsuchi Bay also show repeated internal bores and strong flow during the receding phase. If shoreward internal bores inflow to shallower areas repeatedly, such waves have to run into downslope receding bores.

I have observed a collision of a run-up bore and a receding bore in Otsuchi Bay. Fig. 5-10a shows the temperature distribution when the bore wave ran into the downslope receding bore on September 10, 2013. The downslope receding bore appeared near the shore side at the distance between 1000 and 4000 m, and the head of the run-up bore appeared around 5000 m from the shore. The small-scale instability-like structure appears near the head of the run-up bore (distance = 3500 – 6000). Temperature and current data obtained from two mooring stations (Stn.2 and Stn.3) indicate that the run-up bore passed through between Stn. 3 and Stn. 2 during the observation period (Fig. 5-10). The flow direction observed at Stn. 3 suddenly changed from offshoreward to toward onshoreward near the bottom during the observation period (Fig. 5-11c). Such a sudden change in flow direction may indicate that the run-up bore ran into the receding waves.

The rate of turbulent kinetic energy dissipation, ε, estimated from TurboMAP-L showed strong turbulent mixing in the interface of the internal waves, reaching 10^{-5} $\mathrm{Wkg^{-1}}$ (Fig. 5-10de). On the other hand, ε was low, 10^{-10} – 10^{-9} $\mathrm{Wkg^{-1}}$, in the inner part of the bay not influenced by the bore. The dissipation rate ε estimated from the YODA Profiler showed more details of the distribution of the mixing intensity in the shallow area (Fig. 5-12). High ε areas appeared in the bottom boundary layer (distance = 1000 – 3500 m) and the crashing area (distance = 3500 – 6000). The strong turbulent layer in the bottom boundary layer (distance = 1000 – 3500 m) can be explained by a simple law of the wall (*Dewey and Crawford,* 1988) expressed as,

$$\varepsilon = \frac{C_D^{3/2} u^3}{\kappa z} \qquad \text{(5-3)}$$

where C_D is the empirical drag coefficient 2.5×10^{-3}, κ is the von Karman constant 0.41, z is the height above the bottom and u is the velocity above the bottom. The estimated ε from Equation (5-3) was 1.6×10^{-6} – 3.9×10^{-6} $\mathrm{Wkg^{-1}}$ at 5 m above the bottom, when u is 0.3 – 0.4 $\mathrm{ms^{-1}}$, which is consistent with the observed results from the YODA Profiler. On the other hand, in the crashing area, the strong turbulent area detached from the bottom boundary and ε above the bottom was higher than ε that near the bottom (Fig. 5-10, 5-12). In addition, the strong turbulent area extended toward the sea surface. Observed strong turbulent mixing in the crashing area cannot be explained by bottom shear stress. Therefore, the crashing of the receding and the run-up bores generated strong turbulent mixing far from the bottom boundary around the crashing area. This energetic turbulent event due to crashing waves has not been observed by previous field studies, so I named this phenomenon "*crash mixing*".

Observed data from the high resolution thermistor array showed high frequency internal waves and a shear instability like feature during the crashing period on September 11 (Fig. 5-13, not same observation period as show in Fig. 5-10 and Fig. 5-11). The period and the amplitude of large amplitude high frequency waves shown in Fig. 5-13 (time 19:20 – 19:40) were approximately 5 minutes and 10 m respectively. The vertical temperature gradient decreased after the high frequency wave event (Fig. 5-13b, time > 19:30), the reduction in the stratification indicated mixing due to crash mixing. The dissipation rate may be estimated from the stratification change from following formula (*MacKinnon and Greg,* 2003),

$$\varepsilon \sim \frac{\Delta PE}{\gamma \rho \Delta t} \qquad (5\text{-}4)$$

$$PE = \frac{1}{h}\int_0^h \rho g z dz \qquad (5\text{-}5)$$

where PE is the potential energy, ρ is the density Δt is the time over the period, γ is the mixing efficiency, 0.2 (Osborn 1980), and h is the height from the bottom. The most active potential energy change appeared between 19:00 and 20:00, which giving $\Delta t = 1$ hour = 3600 s. The increase in the potential energy is approximately 20 $\mathrm{Jm^{-2}}$ during that one hour (Fig. 5-13ef). The estimated dissipation from the potential change was 2.7×10^{-5} $\mathrm{Wkg^{-1}}$. Although due to the limitation of the resolution, observed temperature data did not show the complete temperature overturning generated by shear instability, the temperature distribution showed the small scale high frequency motions likely caused by shear instability (Fig. 5-13b). Therefore, the collision of bores caused the high frequency wave motion, and the breaking of such high frequency waves may have accelerated dramatic mixing during the crash.

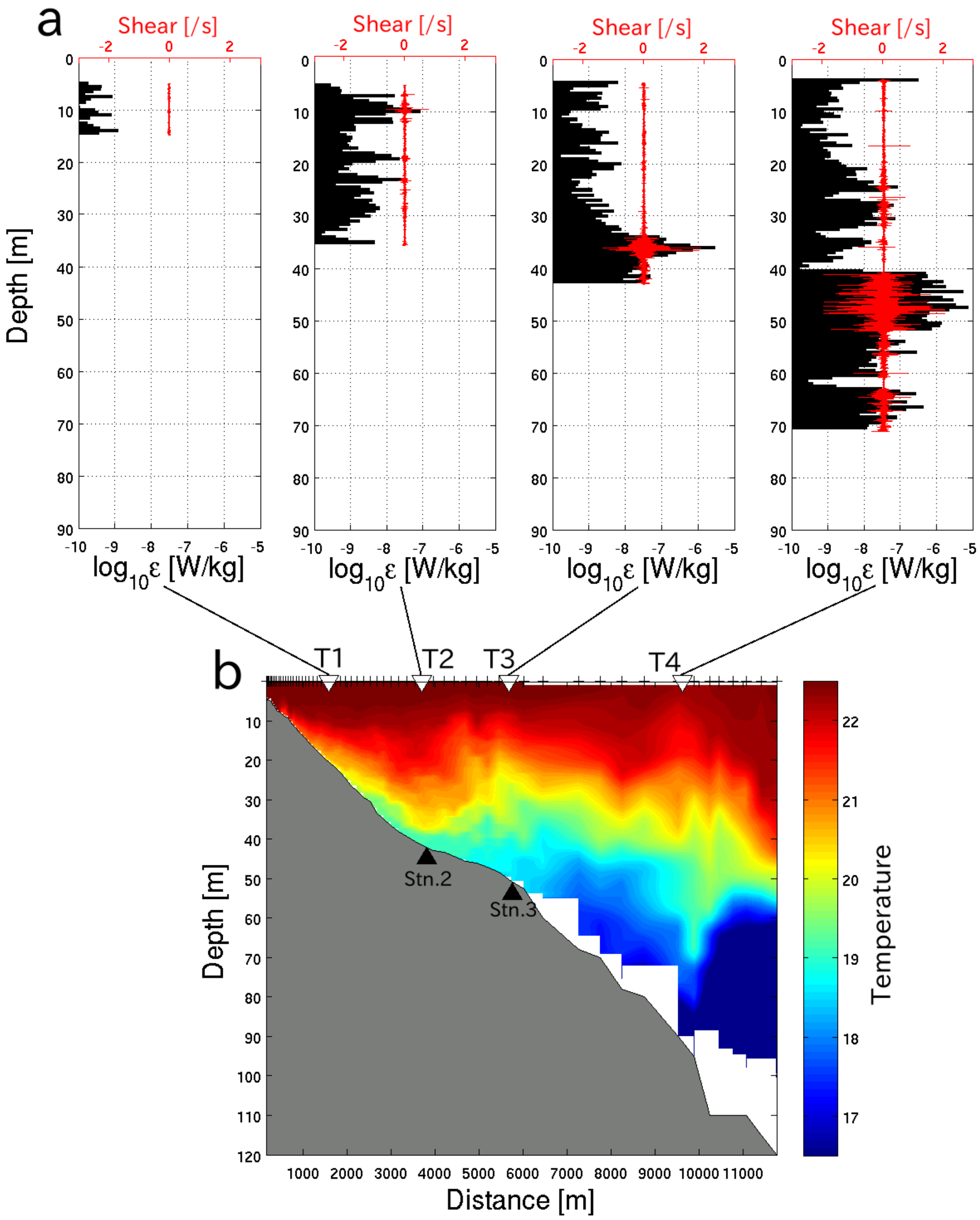

Fig. 5-10 Profiles of the shear (red lines) and ε (black bars) from TurboMAP-L, and (b) the temperature distribution from the YODA Profiler and the UCTD observations on September 9, 2013. White inverse triangle points (T1 – T4) on the upper x-axis of the panel (b) indicate the profiling points of TurboMAP-L observations shown in the panels (a). Black triangles in panel (a) indicate the locations of Stn. 2 and Stn. 3.

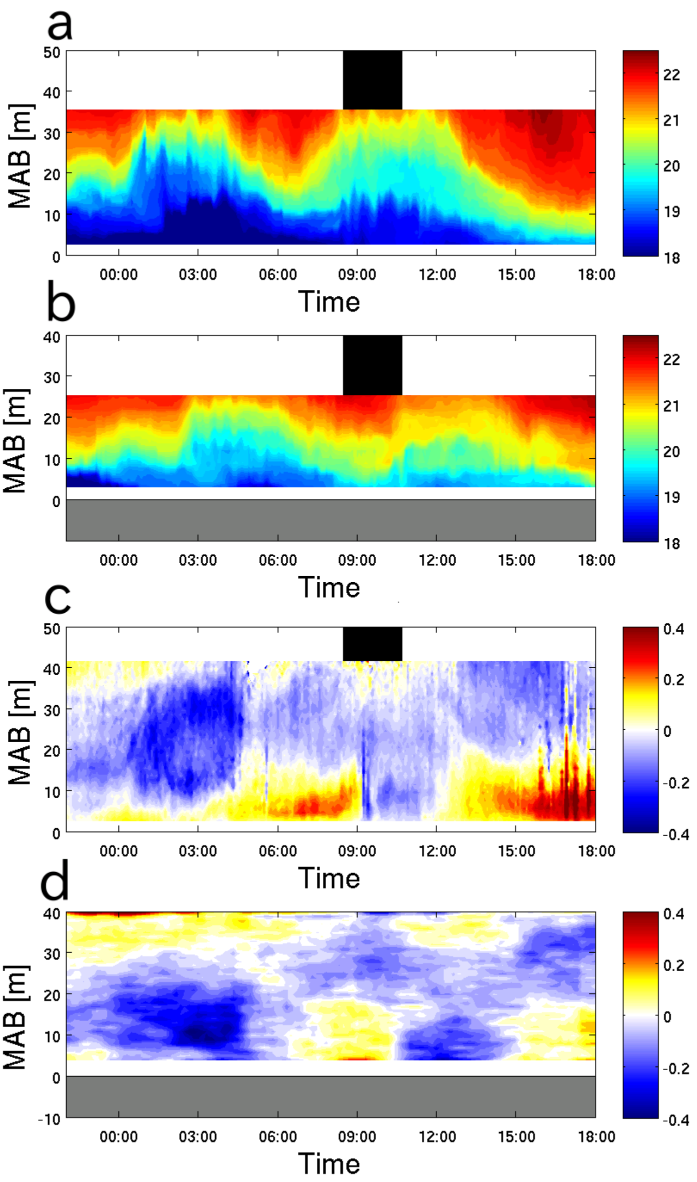

Fig. 5-11 (a, b) Temperature and (c, d) east-west current time series at (a,c) Stn. 3 and (b, d) Stn. 2. Black shaded areas in panels (a, b, c) indicate the total observation period for the surveys shown in Fig. 5-6.

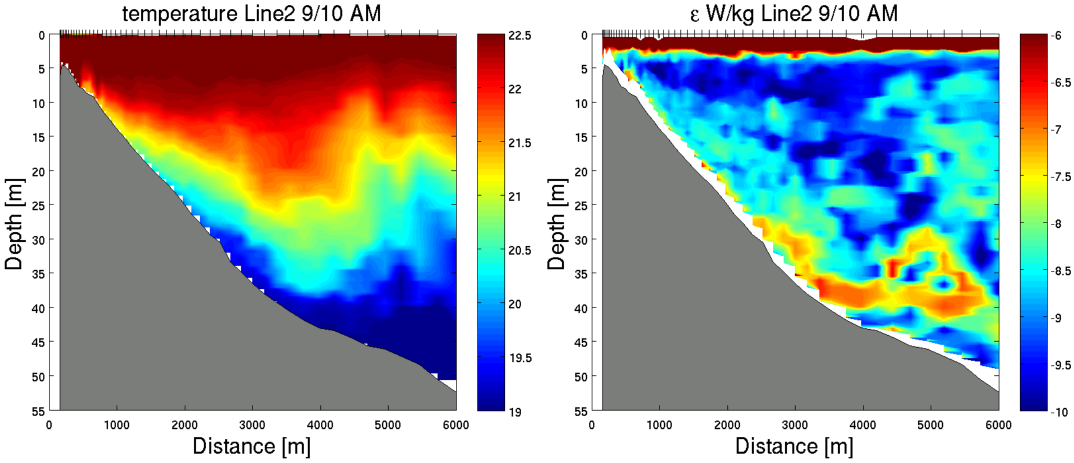

Fig. 5-12 (a) the temperature and (b) the estimated ε from the YODA Profiler on September 10, 2013. The horizontal axis range is different form Fig. 5-6a.

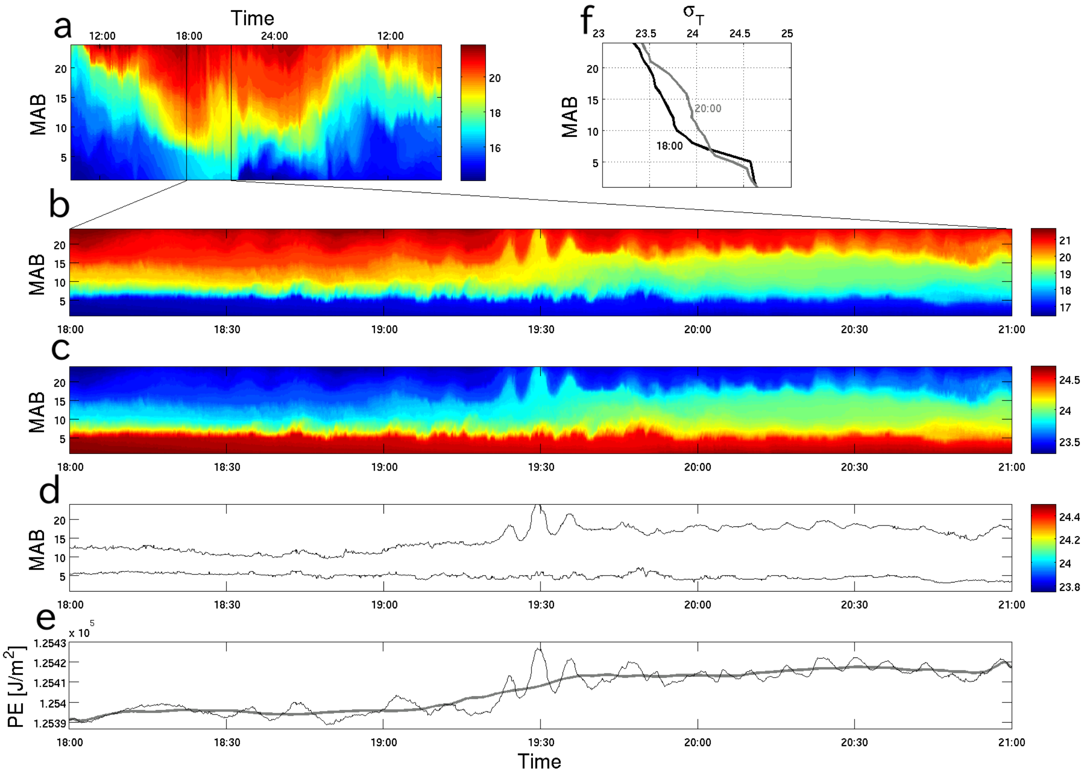

Fig. 5-13 (a) Temperature time series obtained from the high resolution thermistor array on September 11, 2013, and close-up figures of (b) the temperature, (c) the density (sigma-T), (d) isopycnal depths of 23.75 and 24.5 [σ_T], (e) the potential energy between 19:00 and 20:00, and (f) density profiles at 19:00 (black line) and 20:00 (gray line). The thick gray line shown in panel (e) indicates the run mean averaged potential energy over 5 minutes.

5. 4 Numerical results and the criteria for crashing

Numerical simulations of crash mixing

Numerical results simulated by SUNTANS showed crash mixing due to the collision of the receding wave and the run-up bore on the slope (Fig. 5-14ab, distance ~ 5000 m). The large isothermal displacement and high frequency waves were generated near the crashing area (Fig. 5-14ad). Fig. 5-14b indicates that a thin receding bore ran into the next run-up bore. The flow direction drastically changed at the crashing site (Fig. 5-14be), which is consistent with observed results (Fig. 5-11). The flow field indicated that strong convergence occurs at the crashing point. The rate of turbulent kinetic energy dissipation was parameterized by the Mellor-Yamada turbulent closure model (*Mellar and Yamada,* 1982). High dissipation rate areas appeared in the bottom boundary layer, the crashing area and the interface of the bore (Fig. 5-14c). Numerical results showed that the crash generates strong turbulent mixing in the whole water column (from the bottom to near the surface) at the crashing site. Numerical results simulated by SUNTANS are remarkably similar to the observed results. Thus, SUNTANS can produce run-up bores, receding bores and breaking due to the crash mixing.

Fig. 5-15 shows numerical results of a run-up bore wave without a receding bore, namely, the first run-up phase in the simulation. Only a run-up bore without a receding bore did not generate the high frequency motion at the head of the bore. Srong turbulent mixing appeared near the bottom below the bore ($\varepsilon > 10^{-7}\mathrm{Wkg}^{-1}$) and in the interface of the bore wave ($\varepsilon \sim 10^{-8}\ \mathrm{Wkg}^{-1}$). However, the dissipation rate did not show strong mixing at the head of the bore. Therefore, repeated run-up and receding bores led to a collision of two bores on the slope and induced a strong turbulent mixing event.

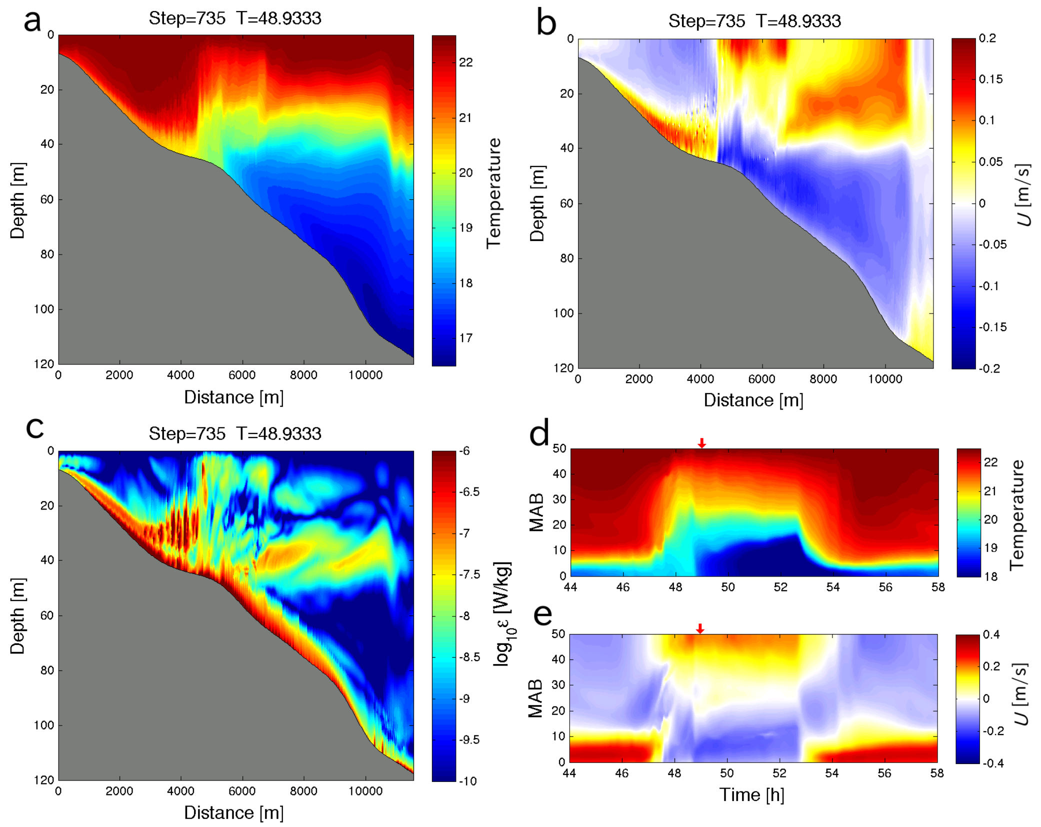

Fig. 5-14 Numerical results from SUNTANS. (a) Temperature, (b) horizontal current field and (c) dissipation rate ε Wkg^{-1}. Time series of (d) temperature and (e) the horizontal current speed at 50 m depth. In panels (b) and (e), positive (negative) is toward the offshore (onshore) area. Red arrows on the upper axis in panels (d) and (e) indicate the timing of numerical results shown in panels (a - c).

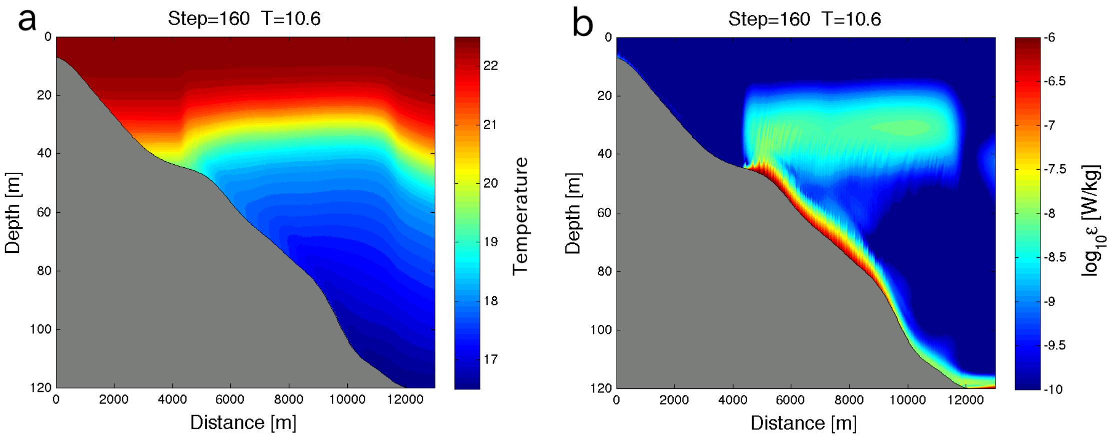

Fig. 5-15 (a) Temperature and (b) dissipation rate during the first run-up phase (without a receding bore) simulated by SUNTANS.

The criteria for crashing

The breaking type of run-up wave is classified by the Iribarren number (*Iribarren and Nogales,* 1949; *Battjes,* 1974),

$$\xi = \frac{s}{\sqrt{\frac{a}{\lambda}}} \qquad (5\text{-}6)$$

where s is the topographic slope (dz/dx), a/λ is the wave slope, a is the amplitude of the wave and λ is the length of the wave. λ and a are computed from the following two layer wave formulas,

$$\lambda = CT \qquad (5\text{-}7)$$

$$a = \frac{U_0 h_2}{2C} \qquad (5\text{-}8)$$

$$C = \sqrt{\frac{(\Delta\rho / \rho_0) g h_1 h_2}{h_1 + h_2}} \qquad (5\text{-}9)$$

where C is the wave speed, T is the period of the wave, U_0 is the velocity amplitude of the wave, h_1 and h_2 are the upper layer and the lower layer height respectively, $\Delta\varrho$ is the density difference between the two layers and g is the gravitational acceleration. *Battjes* (1974) found that the breaking type of surface gravity waves (spilling, plunging, and surging or collapsing) can be classified using the Iribarren number, as shown in Table 5-1. Four breaking types are depicted in Fig. 5-14. The crest of a plunging breaking waves is steeper than that of other types, forms curls and drops into the trough of waves (known as surf waves). *Boegman et al.* (2005) indicated that the breaking type of internal wave is also categorized by the Iribarren number, and they also pointed out that the mixing efficiency increases in the plunging breaking condition. The reflection coefficient, E_r/E_i, increases (decreases) with the increase (decrease) in the Iribarren number (*Boegman et al.,* 2005), where E_r and E_i are the reflected wave energy and the incident wave energy respectively. Thus, much of the incident wave energy is converted into turbulent kinetic energy due to the wave breaking in the low Iribarren number condition. In addition to the breaking type, the Iribarren number controls the shape of internal waves, which can be devied into two types, a canonical bore or a non-canonical bore (*Walter et al.,* 2012 and also described in chapter 4).

Table 5-1 Breaking types classified by the Iribarren number for sea surface waves.

Iribarren number	Breaking type
$\xi < 0.5$	Spilling
$0.5 < \xi < 3.3$	Plunging
$3.3 < \xi$	Surging or collapsing

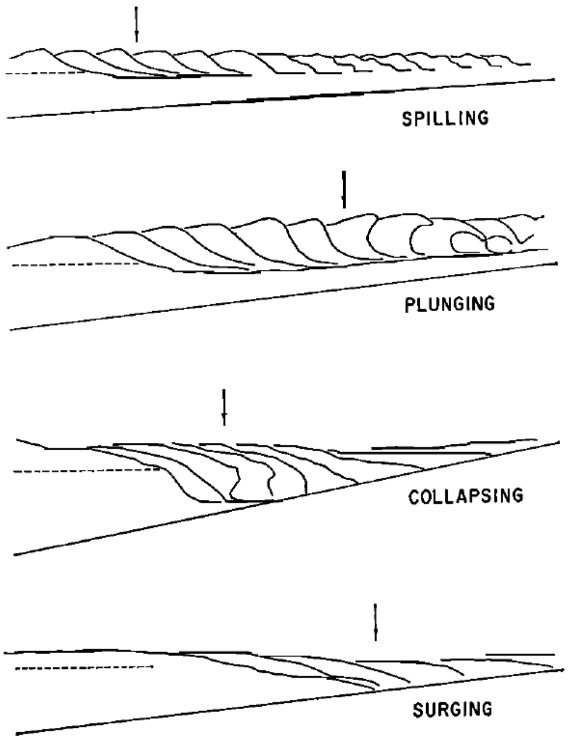

Fig. 5-16 Four breaking types, spilling, plunging, collapsing and surging (*Galvin,* 1968).

In order to investigate the behavior of internal waves and breaking under variable Iribarren number conditions, I used two gradual and steep slope conditions (run#3 and run#4) for numerical simulations. The two domains consisted of a sloping area and a 10 km of flat area with a depth of 80 m. Fig. 5-17 shows schematic images of the two domains. The ocean boundary was forced by the first mode semidiurnal internal wave.

Several parameters used in simulations are listed in Table 5-2. The wave slope in both run#3 and run#4 were the same as that in run#2 simulating Otsuchi Bay, and the topographic slope in run#3 was similar to Otsuchi Bay.

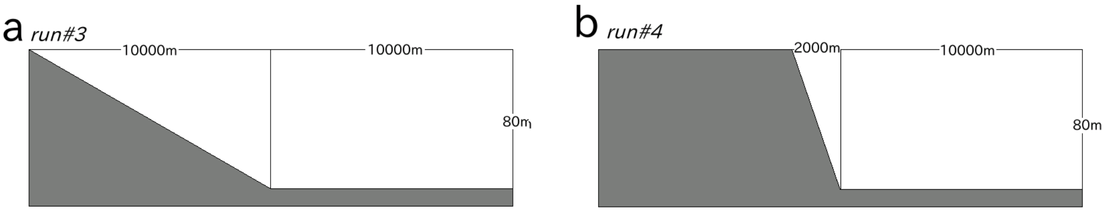

Fig. 5-17 Two domains for numerical simulations (a) run#3 and (b) run#4.

Table 5-2 Parameters used in run#3 and run#4.

run	$\Delta\varrho$	T (h)	U_0 (ms-1)	C (ms-1)	a	s	ξ	Δz	Δx	Δt
#3	0.81	12.4	0.2	0.4	10	0.008	0.34	0.53 m	20 m	1 s
#4	0.81	12.4	0.2	0.4	10	0.04	1.7	0.53 m	20 m	1 s

$\Delta\varrho$ is the density difference between the upper and the lower layers, T (h) is the period of forcing internal waves, U_0 is velocity amplitude of internal wave, a is the vertical amplitude of internal waves, s is the topographic slope, ξ is the Iribarren number, Δz and Δx are the vertical and horizontal grid spacing respectively, and Δt is the time step.

Numerical results from run#3 (low Iribarren number, gentle slope) showed that the receding wave crashed into the next bore wave at 7000 m distance (Fig. 5-18ac). The turbulent kinetic energy dissipation rate is high at the crashing point and along the sloping bottom (Fig. 5-18e). On the other hand, in the high ξ case (run#4), the receding bore disappeared before the next wave came and the crash mixing did not take place (Fig. 5-18bdf). The difference in two cases may be due to the waves run-up distance. In the low ξ case (run#3, steep slope), internal bores had to travel a 5-times longer distance across the slope than those in run#4, because the topographic slope in run#3 was 5 times less steep than that in run#4. Due to the limitation of the bores speed and the drag of the bottom, the internal bore did not completely recede back to the offshore before the next wave came in run#3. Consequently, the crash mixing event took place due to the collision of the receding bore and the next run-up bore. In addition, accelerated flows in the run-up bore caused highly non-linear motions and strong vortex motion near the bore head. Meanwhile, the internal bore did not have to travel a long distance in run#4 and the steep topographic slope may have accelerated the speed of the receding bore; the bore completely receded to the offshore before the next run-up bore came. Therefore, a low ξ condition led to crash mixing, such as that shown in Fig. 5-10. Fig. 5-19 shows behaviors of internal bores for low and high ξ conditions.

Numerical results from the two cases were also diffident in time series. Results from run#3 showed that the isothermal depth and bottom temperature rapidly changed in the run-up phase and gradually changed in the receding phase (Fig. 5-20a, Fig. 5-21a). This type bore is called a canonical bore. The vortex accompanied by the strong current, 0.2 ms^{-1}, was generated at the head of the bore in run#3. In contrast to run#3, the isothermal depth gradually decreased and rapidly went back to the bottom in run#4 (Fig. 5-20b). Bottom temperature time series showed the asymmetrical shape and the change of temperature more abruptly during the receding phase (Fig. 5-21b); this bore wave type is called a non-canonical bore. Although the vortex was generated at the bore head in run#4, the core was not accompanied by a strong current (Fig. 5-20d). The horizontal flow speed during the receding phase showed strong current near the bottom. *Walter et al.* (2012) also reported that the two internal bore types (canonical or non-caconical) are controlled by ξ. Canonical bores assume an asymmetrical saw-tooth shape, such as that shown in Fig. 5-20a, and they have been frequently found in coastal areas (e.g., *McPhee-Shaw et al.,* 2004; *Thorpe,* 1992; *Leichter et al.,* 1996; *Hosegood and van Haren,* 2004). Assuming that canonical bores indicate a low ξ condition leading to crash mixing, crash mixing may occur in coastal areas worldwide.

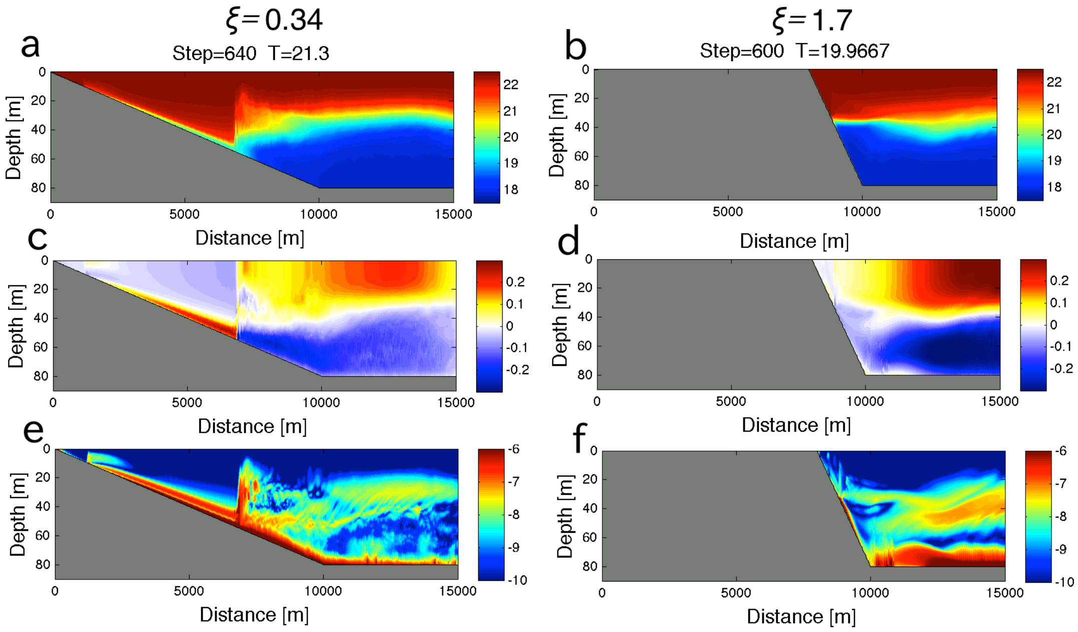

Fig. 5-18 (a, b) Temperature, (c, d) horizontal current speed and (e, f) dissipation rate in $\xi = 0.34$ (a, c, e) and 1.7 (b, d, f) cases.

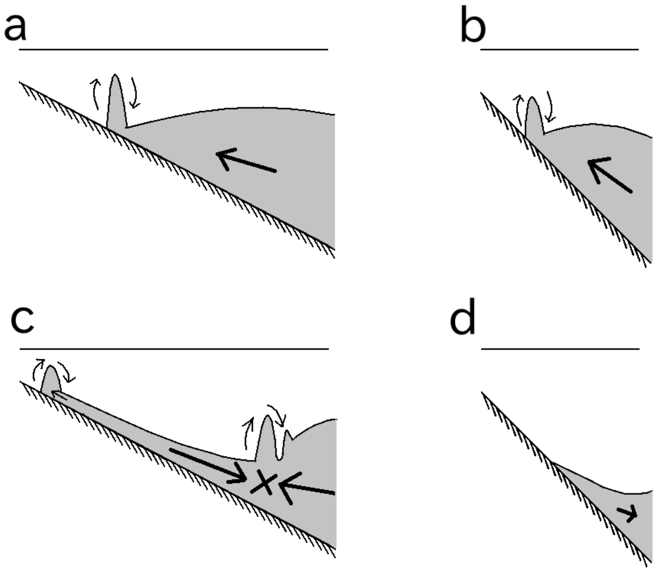

Fig. 5-19 Schematic images of (a, b) run-up and (c, d) receding bore waves in the (a, c) low and (b, d) high iribarren number conditions.

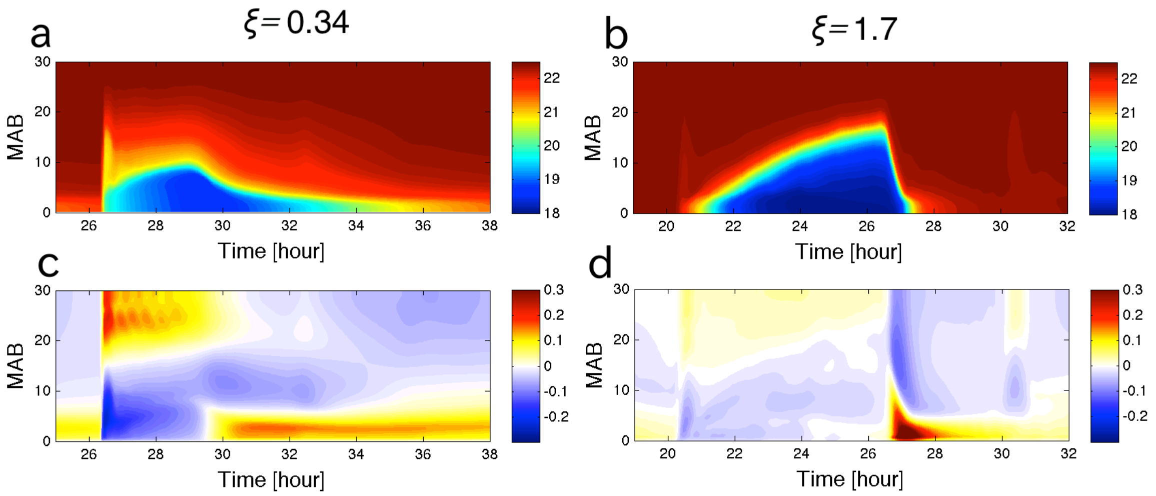

Fig. 5-20 Time series of (a, b) and (c, d) horizontal current speed at 30 m depth in ξ = 0.34 (a, c, e) and 1.7 (b, d, f) cases.

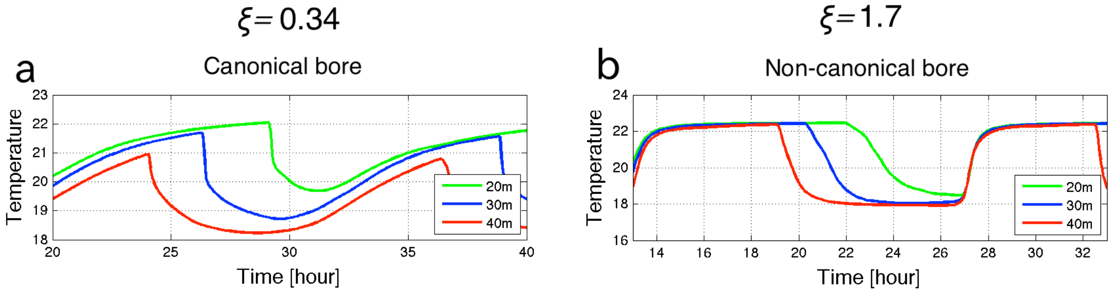

Fig. 5-21 Time series of temperature at 20 m (green), 30 m (blue) and 40 m (red) depths in ξ = 0.34 (a) and 1.7 (b) cases.

The Iribarren number is sensitive to the topographic slope. The slope angles in run#3 and run#4 were 0.46° and 2.3° respectively, both slope angles are within a typical angle range in coastal areas. A small change in the topographic slope led to two different scenarios: (1) Canonical bore generating crash mixing (Fig. 5-21a) or (2) non-canonical bore without crash mixing (Fig. 5-21b). Thus, the internal wave type and turbulent mixing due to internal wave breaking may be greatly influenced by local topographic slopes. For example, strong crash mixing was generated by the internal waves in Otsuchi Bay; however, such strong mixing may not occur in Funakoshi Bay and off Shirosaki (Fig. 5-22).

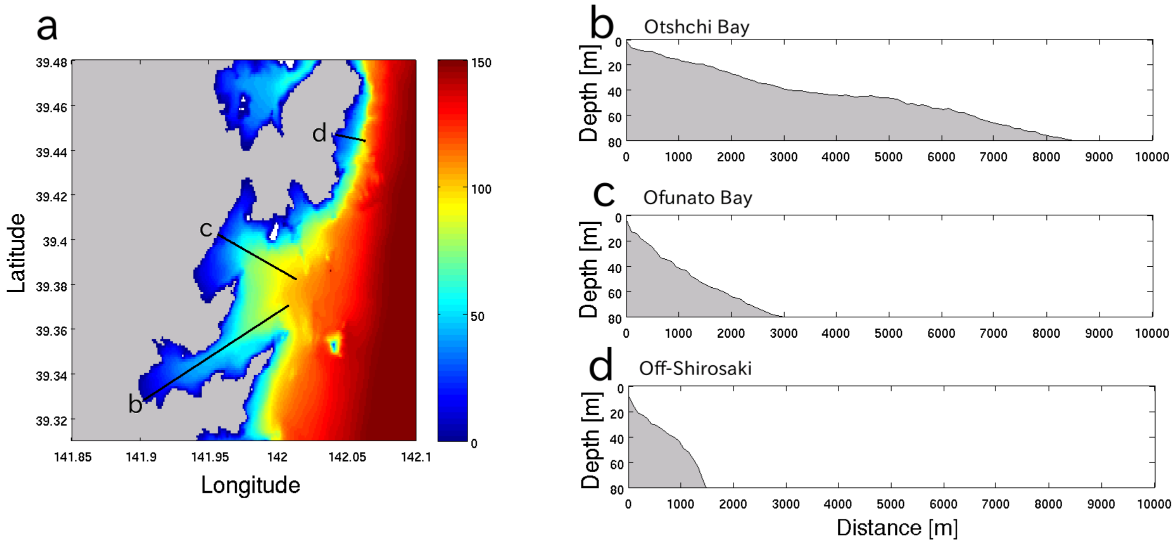

Fig. 5-22 (a) the bathymetry near Otsuchi Bay and slopes in (b) Otsuchi Bay, (c) offShirosaki and (d) Funakoshi Bay.

5. 5 Internal wave energy reflection and dissipation on the slope

Numerical simulations shown in the previous section satisfactory reproduced mixing processes along the sloping bottom caused by internal tides. However, the simulations did not show details of reflected waves from the slope due to the limitation of the scale of the numerical domain. In order to investigate the behavior of reflected internal bores, I extended the numerical domain horizontally, approximately 100 km (over 5 times longer than the wave length). To refine the grid in the slope area, the cell size was stretched in the horizontal direction; the minimum cell size in the slope area 20m and the maximum cell size off the slope was 1000 m. The vertical grid resolution was a constant size, 0.56 m, in the whole numerical domain. I used two topographic conditions for extended domains, s = 0.008 (ξ = 0.34, run#5) and s = 0.04 (ξ = 1.7, run#6). The initial condition and the boundary condition were the same as those for run#3 and #4. In addition to numerical domains with the slope, we used a non-slope domain with an 80 m depth to reproduce only incoming internal waves (run#7). Internal wave energies were released from the left boundary (opposite side to the ocean boundary) in the no-slope domain. Mixing processes along the slope reproduced by extended domains showed results almost the same as those from run#3 and #4.

Reflected waves

The extended domains well reproduced reflected internal waves from the slope. Reflected waves propagated back offshore and a standing wave-like motion occurred after the internal waves reached the slope. Results from the steep slope case (ξ = 1.7) clearly showed nodes and anti-nodes caused by standing waves (Fig. 5-23b). The isothermal displacements increased after reflections: the displacements increase by approximately 2.7% and 54.9% in the gentle and the steep slope cases, respectively. To evaluate and visualize reflected the wave from the slope, I computed isothermal displacements induced by only the reflected wave by using the following simplified formula,

$$\eta_{Ref}(t,x) = \eta - \eta_{In} \qquad (5 - 10)$$

where η_{In} is the displacement due to incoming internal waves computed from the non-slope simulation case. Fig. 5-24 shows η and η_{Ref} in all three simulation cases. Internal waves simply propagated into the slope before reflection (Fig. 5-24, Time < 60 hr). After reflection, reflected waves propagated back offshore and isothermal displacements were generated by the superposition of incoming waves and reflected waves (Fig. 5-24, Time > 60 hr). A plaid-like pattern appeared in the steep slope case, which indicates that reflected waves greatly influence offshore wave motion and cause standing wave motion. The isothermal displacement due to only reflected waves, η_{Ref}, was approximately 4 m and 10 m, respectively.

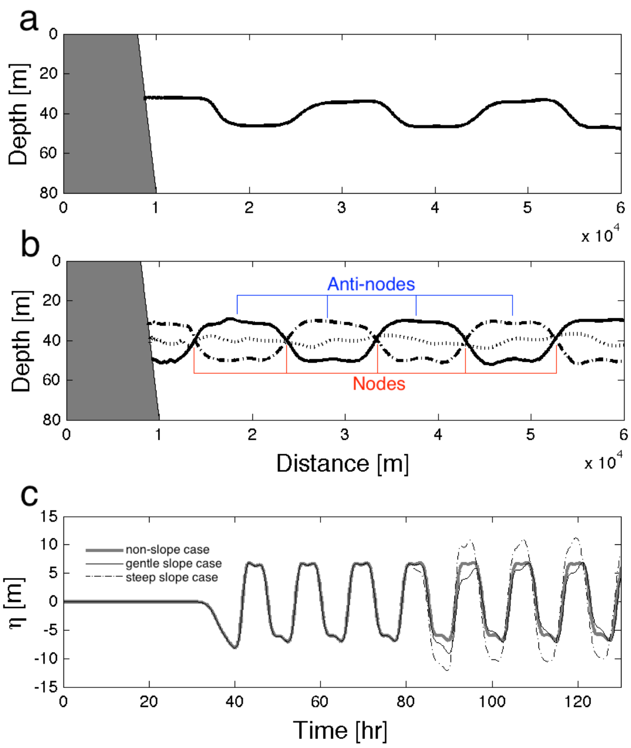

Fig. 5-23 (a, b) Isothermal depths (T = 20.1℃) in the steep slope case and (c) isothermal depth displacement at 30 km from the slope from three simulation cases. Panel (a) shows the isothermal depth before reflections and panel (c) shows isothermal depths in three different phases after reflection.

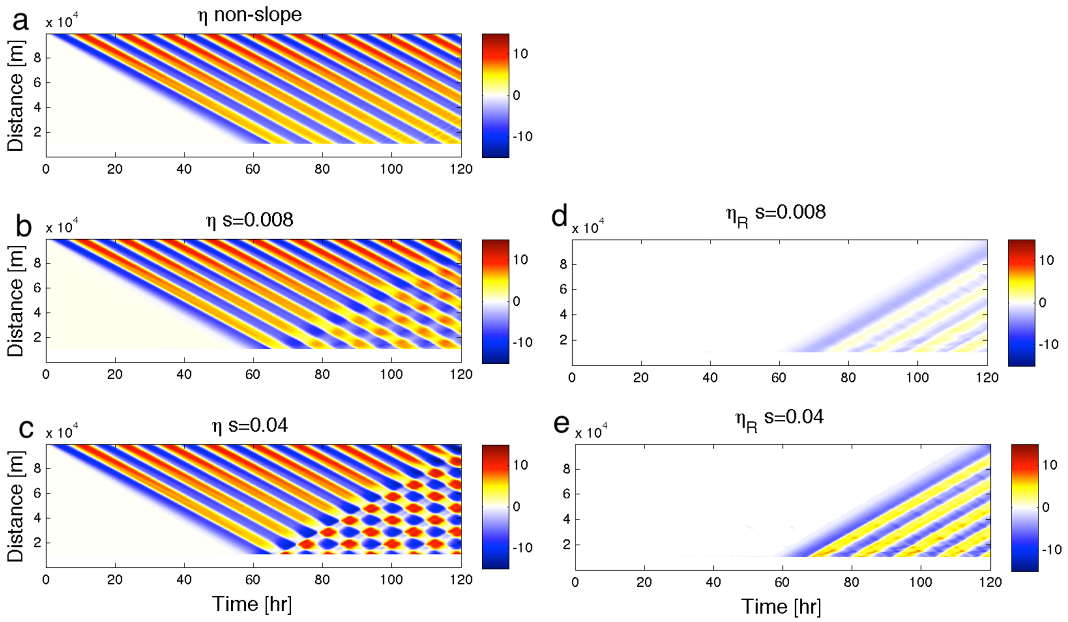

Fig. 5-24 Time series of (a, b, c) the isothermal displacement, η, and (d, e) displacement due to reflected waves, η_{Ref}, as a function of the distance from the shallow boundary.

Energy reflection and dissipation on the slope

The depth-integrated energy flux is represented as follows

$$F_E = \int_{-d}^{0} \left[u(\rho_0 q + \rho g z + p) - \mu \frac{\partial q}{\partial x} - \kappa \frac{\partial}{\partial x}(\rho g z) \right] dz \qquad (5\text{-}11)$$

where q is the kinetic energy per unit mass, $\mathbf{u}^*\mathbf{u}/2$. Assuming that the contribution of the diffusive term is negligible for the energy flux, the equation can be reduced to the following (*Venayagamoorthy and Frinegr,* 2006)

$$F_E = \int_{-d}^{0} p' u \, dz \qquad (5\text{-}12)$$

where $p' = \varrho 0q + \varrho gz + p$. Thus, the depth-integrated energy flux can be simply estimated by using the pressure perturbation, $p' = p - p_0$, where p_0 is the initial pressure condition.

The depth-integrated energy flux at 30 km from the slope in the three described cases is shown in Fig. 5-54a. The energy flux for the non-slope flat condition was stable and equable onshoreward wave energy flux in each wave period. However, the energy flux in the cases with slopes was different from that in the non-slope case after 70 hr (Fig. 25a), which indicates that reflected waves passed the point of 30 km from the slope. The difference between the non-slope and slope case was small in the gentle slope case. Meanwhile, in the steep slope case, the difference was large and the energy flux strongly fluctuated after reflected waves passed.

In order to evaluate the energy budget in the numerical domain, I computed the time-integrated energy flux in the water column as follows

$$E_T = \int_0^t F_E \, dt \qquad (5\text{-}13).$$

The energy budget in the control volume can be expressed by

$$E_i = E_r + E_t + E_d \qquad (5\text{-}13)$$

where E_i is the cumulative incident energy, E_r is the cumulative reflected energy from the slope, E_t is the cumulative transmitted energy released from the domain and E_d is the energy change due to turbulent mixing (*Venayagamoorthy and Fringer,* 2006). E_t can be assumed to be 0, since the shallow slope boundary is closed. Fig. 5-26 depicts the schematic image of the energy budget in the control volume. The cumulative incident wave energy E_i was estimated from the non-slope simulation case. Therefore, the reflected wave energy could be estimated from the difference between the time-integrated energy flux in the slope case (E_{Tslope}) and non-slope case ($E_{Tnonslope}$), which is expressed as,

$$E_r = E_{Tslope} - E_{Tnonslope} \qquad (5\text{-}14).$$

The time-integrated energy flux in these three cases showed that a small difference between the non-slope case and the gentle slope case, but the difference was much larger in the step slope case.

The reflected ratio, $R = E_r/E_i$, was 0.039 and 0.51 in the gentle slope case and the steep slope case, respectively. The relationship between the reflection ratio and the Iribarren number was compared with previous studies (Fig. 5-27, *Boegman et al.,* 2005; *Michallet and Ivey,* 1999). The previous studies estimated the relationship between the two parameters using tank experiments, and they showed that the reflection ratio increases with an increase in the Iribarren numbers. The reflection ratio ranges approximately 0.08 – 0.66 between the Iribarren number 0.2 and 2. The relationship between the reflection ratio and the Iribarren number estimated from this study was consistent with that from previous studies (Fig. 5-27). It is surprising that the results from field scale numerical simulation were consistent with those from small scale tank experiments.

Almost all of incident wave energy (96%) was used by mixing and dissipation in the slope area in the low Iribarren number case (ξ = 0.34). On the other hand, in the high Iribarren number case (ξ = 1.7), approximately half of the incident wave energy was dissipated for turbulent mixing and the other half of the energy was reflected from the slope. Therefore, the strong crash mixing in the low Iribarren number condition converted a large fraction of incoming internal wave energy into turbulent mixing. Meanwhile, much of the incident wave energy reflected on the slope and propagated back offshore in the high Iribarren number condition, which resulted in standing waves off the slope.

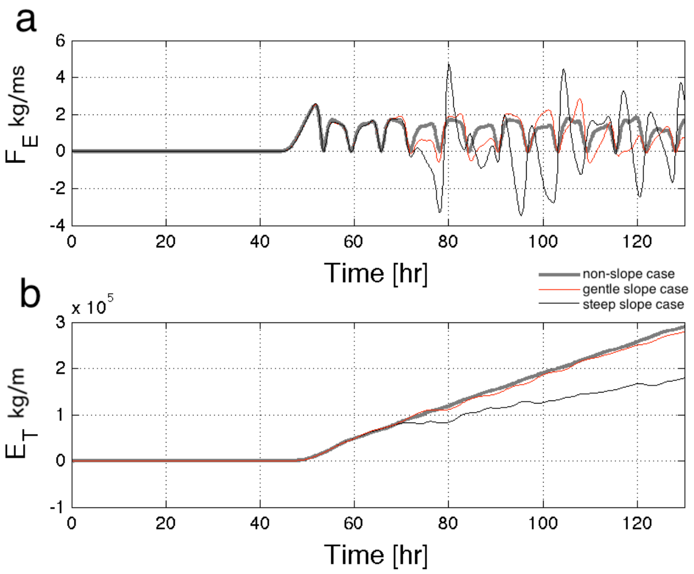

Fig. 5-25 Time series of (a) depth integrated energy flux at 30 km from the slope and (b) time integrated energy flux averaged between 20 and 30 km from the slope.

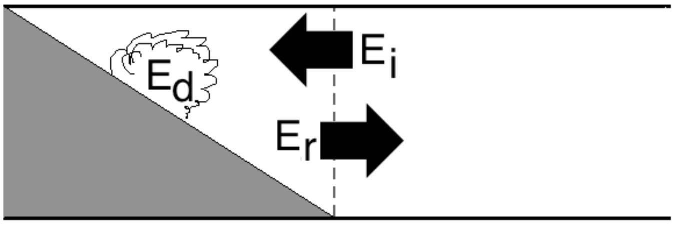

Fig. 5-26 A schematic image of the energy budget in the control volume.

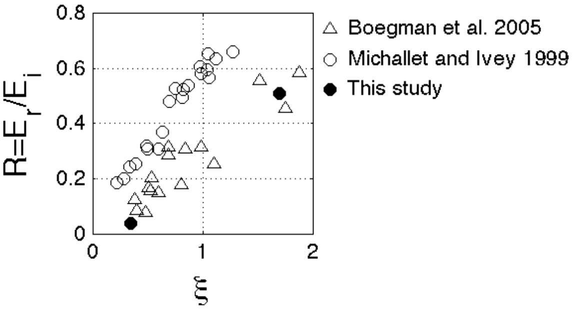

Fig. 5-27 Reflection coefficient, R, versus the Iribarren number, ξ . Triangles and white circles are taken from results producted by *Boegman et al.* (2005) and *Michallet and Ivey* 1999, and the two black circles are results from this study.

5.6 River plume mixing associated with crash mixing

Otsuchi Bay case

As described in the previous chapter, internal bores did not only cause strong turbulent mixing in bottom boundaries but also in near-surface layers. A river plume was added to the numerical simulation to investigate how the crash mixing influences the river plume mixing. The numerical domain used in this model was the same as that in run#4-2. Since the river discharge from the Unosumai River is quite low (1.8 – 8.9 in the summer season, *Anbo et al.,* 2005), I did not set a specified velocity at the boundary; the river plume outflowed into the bay as a density current in the simulation. Observed salinity in river plumes was not significantly fresh in the bay (approximately 30 psu); hence, the salinity at the shallow boundary was set at 31 psu. I compared two cases: (1) run#8 with internal tides and (2) run#9 without internal tides.

The model forced by only the low salinity outflow showed that a sharp low salinity layer had spread from the shallow boundary (Fig. 5-28). The thickness of the river plume was approximately 2 m. The average propagation speed of the river plume was approximately 0.07 ms^{-1}. The river plume was weakly mixed without internal tidal forcing. On the other hand, the model forced by internal tides showed strong vertical mixing of the river plume and shoreward high frequency internal solitary waves in the middle of the bay. The black arrows in upper panels in the Fig. 5-29 indicate the position of the solitary packets. After the run-up bore, solitary wave packets in the river plume freely propagated into the shallow area, and then breaking occurred due to the shallow slope topography. Breaking of solitary waves leads to strong diapycnal mixing in the ocean (*Moum et al.,* 2003, *Lien et al.,* 2014), and solitary waves induced by crash mixing may cause river plume mixing near the river mouth. Fig. 5-30 shows field data for salinity and temperature during the crash mixing event on September 10, 2013. A close-up of the surface salinity showed small-scale internal waves likely generated by the crash mixing (Fig. 5-30a).

Therefore, strong turbulent mixing induced by crash mixing significantly contributes to river plume mixing in the surface layer. In addition, internal bores generate high frequency solitary waves in the river plume, which also enhance river plume mixing in the bay.

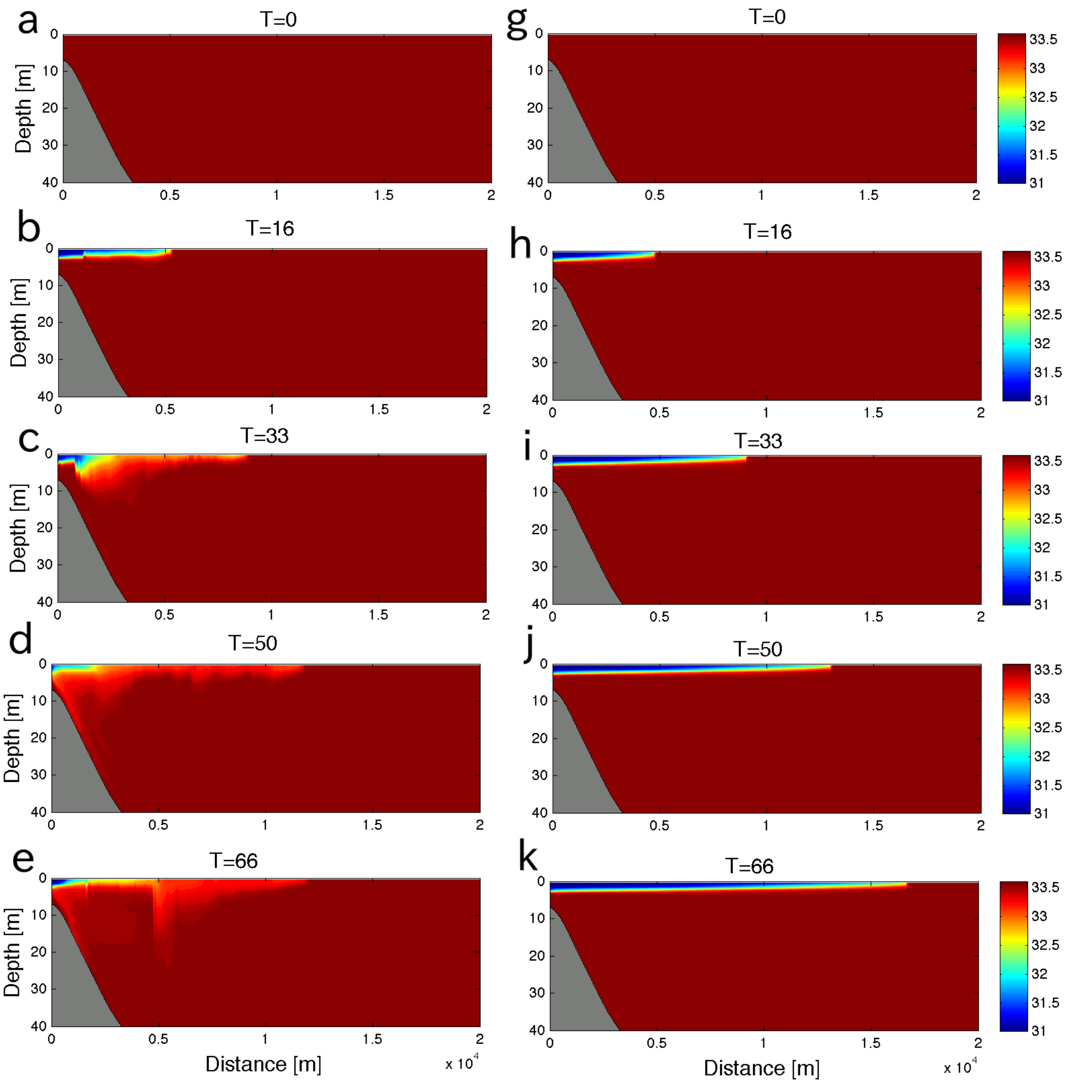

Fig. 5-28 Salinity distributions simulated by numerical simulations (a – e) forced by internal tides, and the low salinity outflow and (g – k) forced by only the low salinity outflow.

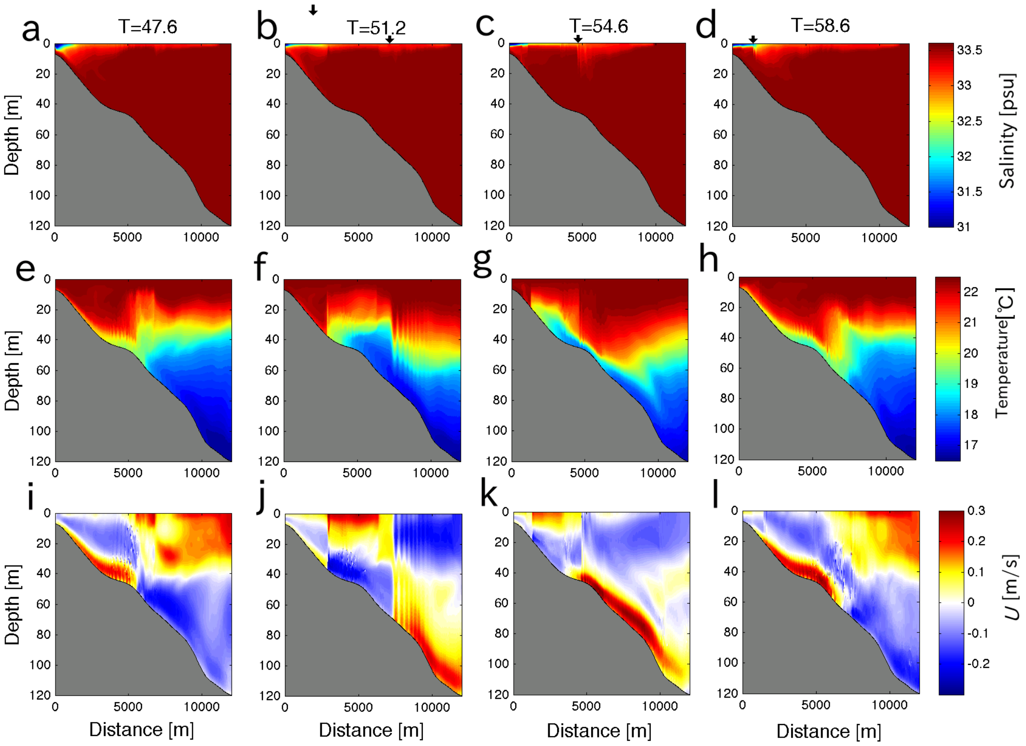

Fig. 5-29 Numerical results of river plume mixing associated with crash mixing. (a – d) salinity, (e – h) temperature and (i – l) and horizontal current at time = 47.6, 52.2, 54.6 and 58.6. Black arrows in panels (b, c, d) indicate the position of surface solitary packets generated by crash mixing.

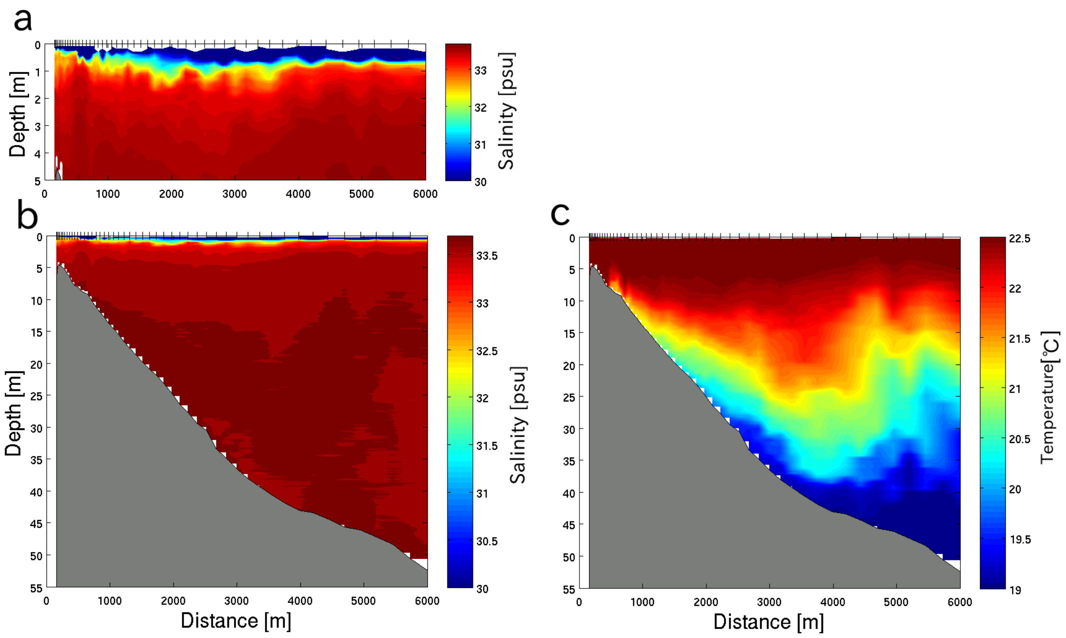

Fig. 5-30 Observed results of (a, b) salinity and (c) temperature from the YODA Profiler on September 10, 2013. Panel (a) shows a close-up of salinity distribution at depths between 0 and 5 m.

Two topographic slope cases (gentle and steep slopes)

In addition to the river plume mixing in Otsuchi Bay case, I investigated river plume mixing for two topographic condition cases. Numerical domains and topographic slope are the same as run#5 and run#6 described before. The low salinity (31) input was set at the shallow boundary as a density driven river plume (without specified velocity). Numerical results from both cases show oscillation of the river plume induced by incoming internal waves. However, the surface salinity over the slope case was much lower in the gentle slope than that in the steep slope case. The surface salinity rapidly decreased and mixed after internal bores reached the slope in the gentle slope case. Meanwhile, in the steep slope case, the low surface water remained in the surface layer for a long time.

The horizontal flow speed was much higher in the gentle slope case than in the steep slope case (Fig. 5-30de). The surface flow speed was strongly enhanced by non-linear internal bores in the gentle slope case, and the horizontal flow speed reached 0.25 ms^{-1} in the surface layer. However, internal bores did not greatly influence the horizontal current speed near the surface in the steep slope case, where the flow speed was lower than 0.1 ms^{-1}.

To evaluate mixing intensity in the river plume, I computed the river plume mixing ratio as follows,

$$R_{MIX} = \frac{S_{Surf}}{S_0} - S_{River} \tag{5-15}$$

where S_{Surf} is the surface salinity, S_0 is the mean salinity in the water column and S_{River} is the salinity of river input at the boundary. When complete vertical mixing occurs in the water column, R_{MIX} is 1,. Fig. 5-30c shows R_{MIX} at 10 km far from the shallow boundary. The river plume mixing ratio rapidly decreased after the river plume reached at a point of 10 km from the shallow boundary. Thereafter, the mixing ratio gradually increased due to incoming internal bores. The mixing ratio was stable after 130 hours in both cases (Fig. 5-30c); the mixing ratio was approximately 0.68 and 0.39 in the gentle slope case and the steep slope case, respectively.

Both numerical results from the two Iribarren number conditions (gentle slope and steep slope) showed high-frequency internal waves in the surface layer (Fig. 5-30ab). However, the direction and the horizontal scale of high frequency waves were different in these two cases. In the gentle slope case, the direction of high frequency waves was onshore (Fig. 5-31abc). Several small-scale solation packets were generated in each tidal phase and broken in the shallow region due to the topographic effect. The scale of the wave packets was approximately 100 m. In contrast to the gentle slope case, the direction of surface solitary waves was toward the offshore in the step slope case. The solitary waves were reached the front of the river plume and contributed to the horizontal expansion of the river plume offshore. The horizontal scale of the wave was a few 1000 m and was much larger than that in the gentle slope case.

The change in the Iribarren number led to two differen scenarios for river plume mixing:

1) In the low Iribarren number case, internal tide-derived crash mixing enhanced river plume mixing and caused shoreward high frequency solitary waves.
2) In the high Iribarren number case, internal tides led to weak river plume mixing and large-scale offshoreward solitary waves.

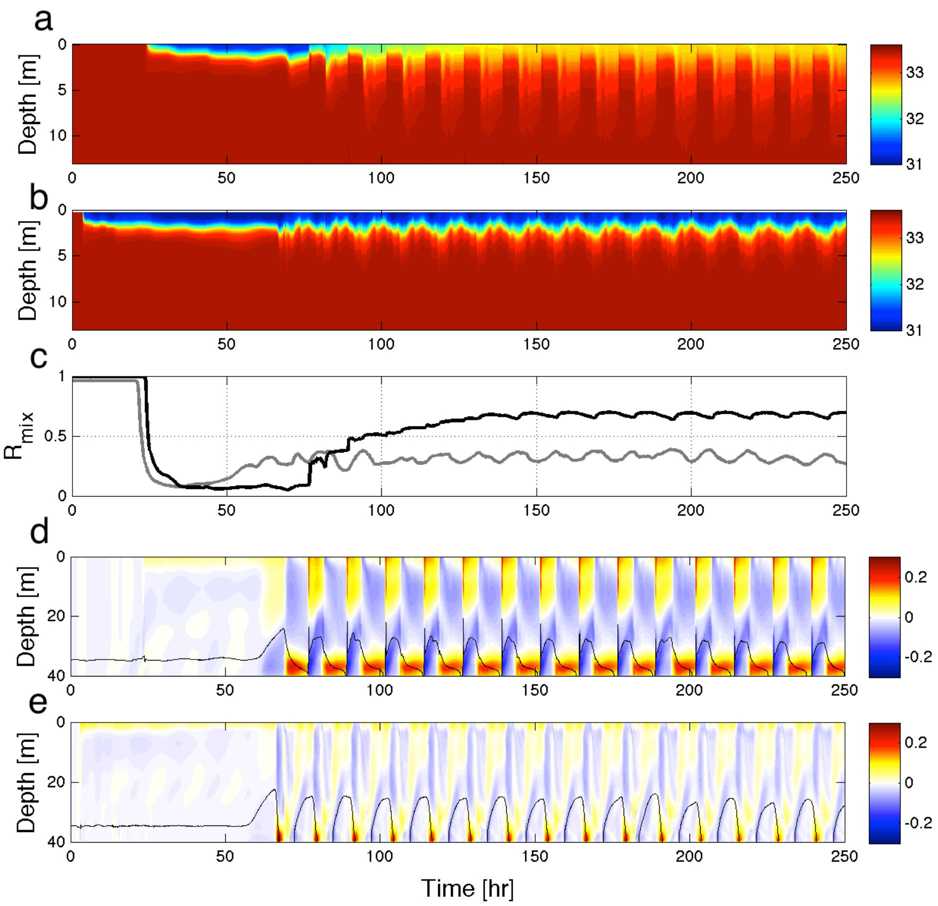

Fig. 5-30 (a, b) Time series of salinity at 40 m depth in (a) gentle slope case and (b) steep slope case. (c) River plume mixing ratio at 10 km from the shallow boundary in the gentle slope case (black line) and the steep slope case (gray line), and horizontal velocity at 40 m depth in (d) gentle slope case and (e) steep slope case. Thin black lines in panels (d, e) indicate an isothermal depth of 19°C.

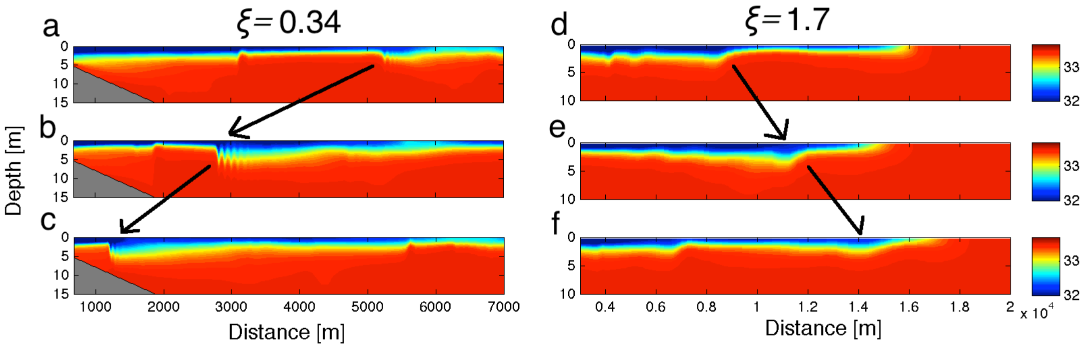

Fig. 5-31 Snapshots of the salinity distribution for ξ = 0.34 (left panels) and 1.7 (right panels) cases.

5. 7 Conclusion

I observed the collision of the receding bore and the run-up bore leading to a strong turbulent mixing event. This strong turbulent mixing event, due to the crashing waves has never been observed, so we named this phenomena "*Crash mixing*". The high turbulent kinetic energy dissipation rate near the crashing site reached 10^{-6} – 10^{-5} $\mathrm{Wkg^{-1}}$. Observed data showed a high dissipation rate area also appeared near the sea surface above the crashing site. The high-resolution thermistor array data revealed high frequency waves and shear instability motion during the crashing period.

In addition to performing field surveys, we reproduced crash mixing using a nonhydrostatic numerical model, SUNTANS. The strong turbulent mixing event at the crashing site also appeared in the model. Numerical surveys in two Iribarren number (ξ) conditions indicated that the low ξ case leads to the crash mixing. Almost all of the incident internal wave energy (96%) was dissipated due to the crash mixing in the low Iribarren number condtion. ξ also determined internal bore wave types, canonical bores and non-canonical bores. The low ξ led to canonical bores and induced crash mixing and strong breaking. I suggest that ξ is a key parameter in the investigation of the behavior of internal bores, wave breaking and local mixing events in coastal slopes.

Numerical simulation of crash mixing with the river plumes revealed that crash mixing contributes to river plume mixing significantly. The numerical results showed shoreward solitary wave packets released from the crash-mixing site. These solitary packets propagated shoreward and broke near the shallow river mouth, which caused river plume mixing near the river mouth.

Chapter 6

The generation mechanism of intermediate nepheloid layers (INLs)

6.1 Introduction

The coastal area is known as a main source of sediments, nutrients and organic materials in the ocean, and has high biological productivity (e.g, *Nakatsuka et al.,* 2004; *McPheeShaw et al.,* 2006). These materials derived from rivers temporally deposit near coastal sea beds (*Mayer et al.,* 1998), and then, the materials are resuspended and transported by tidal flows (*Ward,* 1985), geostrophic flows (*Puig et al.,* 2004), internal waves (*Cacchione et al.,* 2002), strong winds and surface waves (*Ogston et al.,* 2004; *Ross et al.,* 2009). Lateral dispersals of river-derived materials from the coastal area into offshore seas maintain ocean ecosystems (e.g., *Nakatsuka et al.,* 2004).

Internal wave are one of the most energetic phenomena in the ocean. Reflections of linear internal tides generate energy convergence and locally intensified currents along the slope where the incident wave angle matches the bottom angle (*Cacchione et al.,* 2002; *Van Gastel et al.,* 2009). The reflection of internal tides leads to shoaling internal bores/waves propagating into shallow areas. Internal bores are frequently accompanied by strong currents and sediment resuspension (*van Haren,* 2009; *Masunaga and Yamazaki* 2014). Internal bores induce a highly nonlinear vortex motion at the head of the bore accompanied by strong currents (*Venayagamoorthy and Fringer*, 2006; *van Haren,* 2009). The vortex motion generates strong sediment resuspension and is one of the keys to understanding sediment transport processes. Typically, water with highly concentrated suspended sediments (high turbidity) exists near the sea surface and in bottom boundary layers (e.g., *McPheeShaw et al.,* 2004). High turbidity surface water is typically formed by buoyant low salinity water from rivers (*Geyer et al.,* 2000), and high turbidity bottom water is created by downslope turbidity currents (*Kineke et al.,* 1996) and sediment resuspension (*Cacchione et al.,* 2002). Several field surveys reported that suspended sediments due to internal bores intrude in to interior water columns as intermediate nepheloid layers (INLs, *Moum et al.,* 2002; *McPhee-Shaw et al.,* 2004). Sediments near coastal areas consist mostly of nutrients and bioavailable nitrogen derived from rivers (*Mayer et al.,* 1998). Such materials spread toward offshore areas through INLs, which maintain ocean ecosystems (*McPhee-Shaw,* 2006). Lateral offshore mass fluxes (e.g., sediments, nutrients, iron) due to internal waves are much greater than those caused by vertical settling from the ocean surface (*Van Weering et al.,* 2001). Thus, internal waves and INLs are important processes to understand for the ocean ecosystem research.

Phillips et al. (1986) and *Garrett* (1990) suggested that offshore fluxes in the ocean interior can be explained by the buoyancy-driven “secondary” circulation (Fig. 6-1a). Turbulent mixing in the bottom boundary layer and the re-scarification processes cause this circulation. In the uniform stratification condition, the re-stratification drives the upslope flow near the bottom and the downslope flow above the upslope flow after the mixing event. If a locally maximum stratified layer exists, the secondary circulation leads to a buoyancy flux convergence at the stratification maximum depth (*Phillips et al.,* 1986; *Garrett,* 1990; *McPhee-Shaw*, 2006). The convergence results in the offshore transport of water along the isopycnal depth. This convergent flow is called a “tertiary” circulation (Fig. 6-1, *Garrett,* 1990, 1991). The tertiary circulation is generated by the nonuniform sloping bottom as well as by variable stratifications (*McPhee-Shaw,* 2006). In addition, local intensified mixing at the boundary also induces such buoyancy-driven convergence flows as shown in Fig. 6-2. *McPhee-Shaw* (2006) reported that the tertiary circulation is an important mechanism for forming INLs. *Richard et al.* (2013) showed INLs generated by breaking of solitary wave packets using numerical simulations. However, details of the generation mechanism of INLs due to internal tides/waves are not well understood.

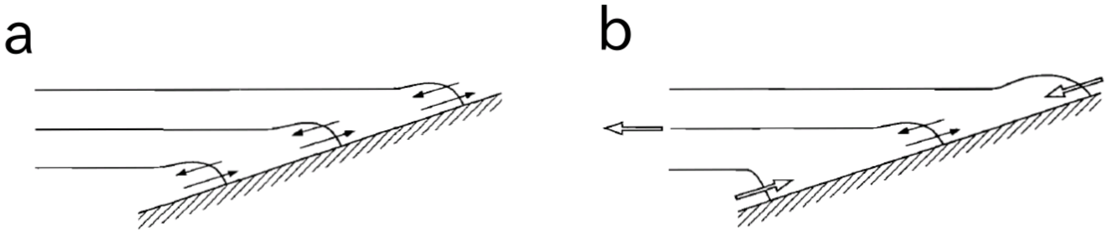

Fig. 6-1 (a) the secondary circulation and (b) the tertiary circulation depicted by *Garrett* (1991).

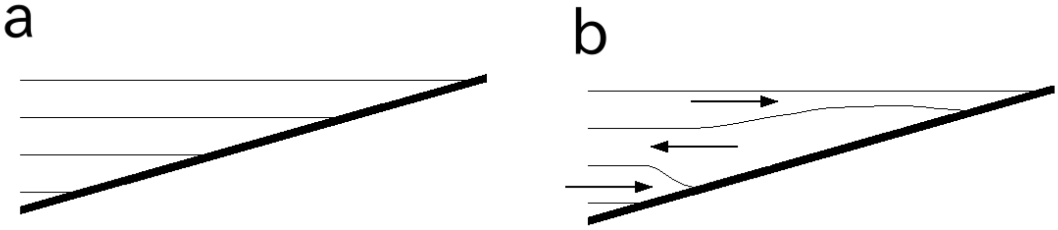

Fig. 6-2 A schematic image of the convergent flow induced by mixed fluids near the bottom boundary. Panel (a) depicts the initial or the re-stratified condition. Panel (b) depicts isopycnals when mixing occurs near the boundary. Arrows in panel (b) indicate the buoyancy-driven flow due to the re-stratification.

In order to investigate the generation mechanism of INLs, we conducted numerical surveys using a fully non-hydrostatic numerical model, Stanford Unstructured Nonhydrostatic Terrain-following Adaptive Navier-Stokes Simulator (SUNTANS, *Fringer et al.,* 2006). As described in earlier chapters, SUNTANS has the potential to reproduce internal bores in shallow coastal areas and may suit investigations into sediment resuspension due to such waves. We also investigated the behavior of internal bores and sediment resuspension in several Iribarren number conditions by changing the topographic slope.

This chapter shows the generation mechanism of INLs due to internal bores using the numerical model. The next section describes the model configuration. The third section describes how INLs are formed and the tertiary circulation generated by internal bores. The fourth section shows the behavior of internal bores and sediment resuspension under various Iribarren number conditions. The final section concludes this chapter with a summary.

6.2 Numerical setups and observastions

Numerical setups

I used numerical domains based on the Otsuchi Bay topography and several uniform sloping topographies in two-dimensional domains. The slope, dz/dx, in the Otsuchi Bay domain was set at 0.012 and 0.0066 for the shallow slope (depth 0 – 40 m) and deep slope (depth 40 – 80 m) respectively. All domains consisted of slopes and 10 km offshore flat areas as shown in Fig. 6-3. The offshore boundary was forced by the first mode semidiurnal internal wave. The velocity amplitude of the wave is listed in Table 6-1. The density difference between the upper and the lower layers, the topographic slope (dz/dx), the wave amplitude, the wave length and the Iribarren number are shown in Table 6-1.

The sediment resuspension model used in this study was developed by *Chou et al.* (2012). They have included the sediment model into SUNTANS and reproduced sediment transports due to tidal flows and wind-induced flow in San Francisco Bay. The sediment transport equation in the model is written as

$$\frac{\partial C}{\partial t}+\nabla\cdot(\mathrm{u}C)-\frac{\partial}{\partial z}\left(w_S C\right)=\nabla_H(\gamma_H\nabla_H C)+\frac{\partial}{\partial z}\left(\gamma_V\frac{\partial C}{\partial z}\right)\quad,\qquad(6\text{-}1)$$

where C is the concentration of sediments, w_S is the settling velocity of sediments, γ_H and γ_V are the horizontal and vertica eddy diffusivity respectively, and ∇_H is the horizontal gradient operator. The constant particle settling velocity, w_S, can be determined by Stokes' law

$$w_S=\frac{(\rho_S-\rho_0)gD^2}{18\mu}\,,\qquad(6\text{-}2)$$

where ρ_s is the density of particles, D is the particle diameter and μ is the dynamic viscosity of water. The bottom cell with the erosion rate can be represented as follows

$$\frac{dC}{dt}+\frac{1}{\Delta z}(w-w_sC)\Big|_{\mathrm{top}}=\frac{1}{\Delta z}(E_b-w_sC)\Big|_{\mathrm{bottom}}\,.\qquad(6\text{-}3)$$

The sediment erosion rate, E_b, is represented as

$$E_b = E_0 \exp(\alpha \Delta \tau_b^{\beta}), \qquad (6\text{-}4)$$

where E_0 is the erodibility, α and β are empirical constants, and $\Delta\tau_b$ is the excessive shear stress described as

$$\Delta\tau_b = \tau_b - \tau_{cr}, \qquad (6\text{-}5)$$

where τ_b is the bed shear stress and τ_{cr} is the critical shear stress for erosion. The bed shear stress was computed in the model from the following formula in the model

$$\tau_b = \rho C_D U^2 \qquad (6\text{-}6)$$

where C_D is the drag coefficient and U is the velocity magnitude at the bottom cell. The drag coefficient can be written as follows using the log law

$$C_D = \left(\frac{k}{\log(z/z_0)} \right)^2, \qquad (6\text{-}7)$$

where k is the von Kármán constant, 0.41, and z_0 is the bed roughness coefficient. See *Chou et al.* (2012) and *Fringer et al.* (2006) for more details about the equations used in the model.

Two particle types were simulated in the model, 10 μm and 50 μm in diameter. The sinking velocities of the two particles are estimate from Stokes' law (Equation 6-2) and were set at 8.9×10^{-5} ms^{-1} and 2.2×10^{-3} ms^{-1} for 10 μm and 50 μm respectively. The bed sedimentation ratio of two particle fractions is set at 10%. The critical bottom shear stress for the erosion of sediments was set at 0.03 Nm^{-2}. According to *Soulsby* (1997), z_0 above the silt and sand mixture condition is 5×10^{-5} m. I used this value for z_0. E_0, α and β were set at 0.1, 4.5 and 1 respectively in this study. Sediments were placed only on the sloping bottom, not placed on the flat offshore bottom.

In order to validate numerical outputs, I conducted numerical simulations based on the observations in Otsuchi Bay, Japan, and compared the numerical results with the observed results. See chapters 4 and 5 for details about the field observations.

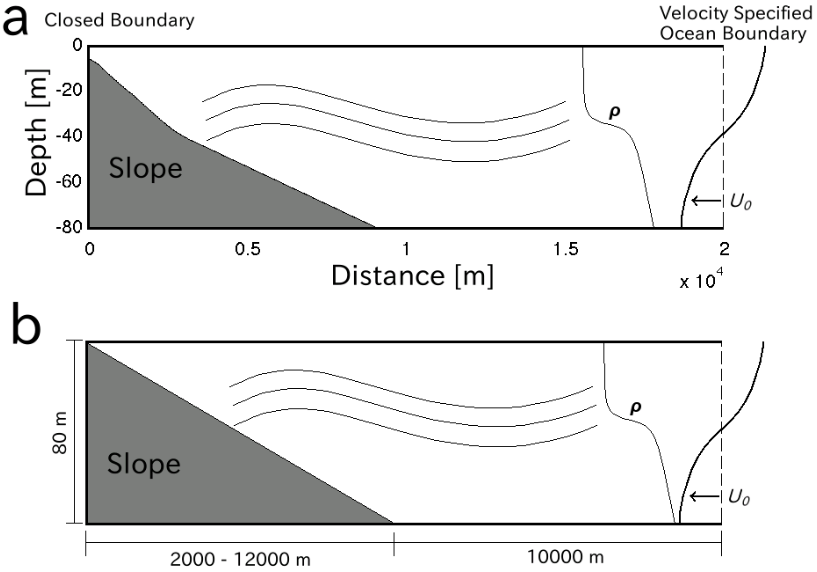

Fig. 6-3 Schematic diagrams show domains used in (a) the Otsuchi Bay case and (b) variable slope domains.

Table 6-1

run	$\Delta\varrho$	U_0 (ms^{-1})	C (ms^{-1})	a	λ (km)	s	ξ
#5-1 (Otsuchi)	2.2	0.20	0.66	6.0	30	0.012-0.0066	0.47-0.85
#5-2	2.2	0.15	0.66	4.5	30	0.04	3.2
#5-3	2.2	0.15	0.66	4.5	30	0.02	1.6
#5-4	2.2	0.15	0.66	4.5	30	0.013	1.1
#5-5	2.2	0.15	0.66	4.5	30	0.008	0.65
#5-6	2.2	0.15	0.66	4.5	30	0.005	0.41

6.3 The generation mechanism of INLs

Numerical results from the Otsuchi Bay case

Numerical results from SUNTANS showed run-up of internal bores on the slopes (Fig. 6-4). During the first run-up phase, the bore head generated weak sediment resuspension (Fig. 6-4, periods A, B and C). Suspended particles were lifted up at the bore head and were sent back to the bottom behind the head (sediments concentration is too weak to see in the figure). Strong offshoreward flow during the receding phase induced sediment resuspension along the slope after the run-up (Fig. 6-4, period D). The flow speed in the receding bore was much higher than that in the run-up bore, as described in the chapter 5. The horizontal flow speed in the receding bore reached 0.4 ms^{-1}. During the second run-up phase, the run-up bore crashed into the receding bore containing suspended particles (Fig. 6-4, period E). The crashing of these waves caused the flow convergence and the upward motion at the bore head, which resulted in strong vertical resuspension. The second bore propagated shoreward accompanied by high concentration of suspended sediments (Fig. 6-4, periods F and G). In this phase, small suspended sediments (10 μm) intruded into the interface of the internal wave, forming an INL. Although large sediments (50 μm) were suspended during the receding phase and at the head of the bore, these sediments deposited immediately and did not form any INLs (Fig. 6-5). Numerical results indicated that the INLs were generated by a sequence of several internal bores. The results also indicated that low sinking velocity particles formed INLs.

According to the numerical results, the internal bores generated an INL the following steps:

(1) The receding bore causes strong offshore ward flow leading to suspend sediments along the slope.
(2) The collision of the receding bore and the next run-up bore induces the crash mixing, leading to strong convergence and turbulent mixing at the crashing site.
(3) The upward motion due to the crash mixing lifts fine suspended sediments into the interface of the bore.
(4) The cold internal bore intrudes below the suspended sediments, forming INLs in the bay.

However, the physical processes described above do not demonstrate the lateral dispersion of suspended sediments, since suspended sediments (INL) recede back to the offshore bottom with receding bores. The latter part of this section describes the lateral dispersion of suspended sediments due to internal bores.

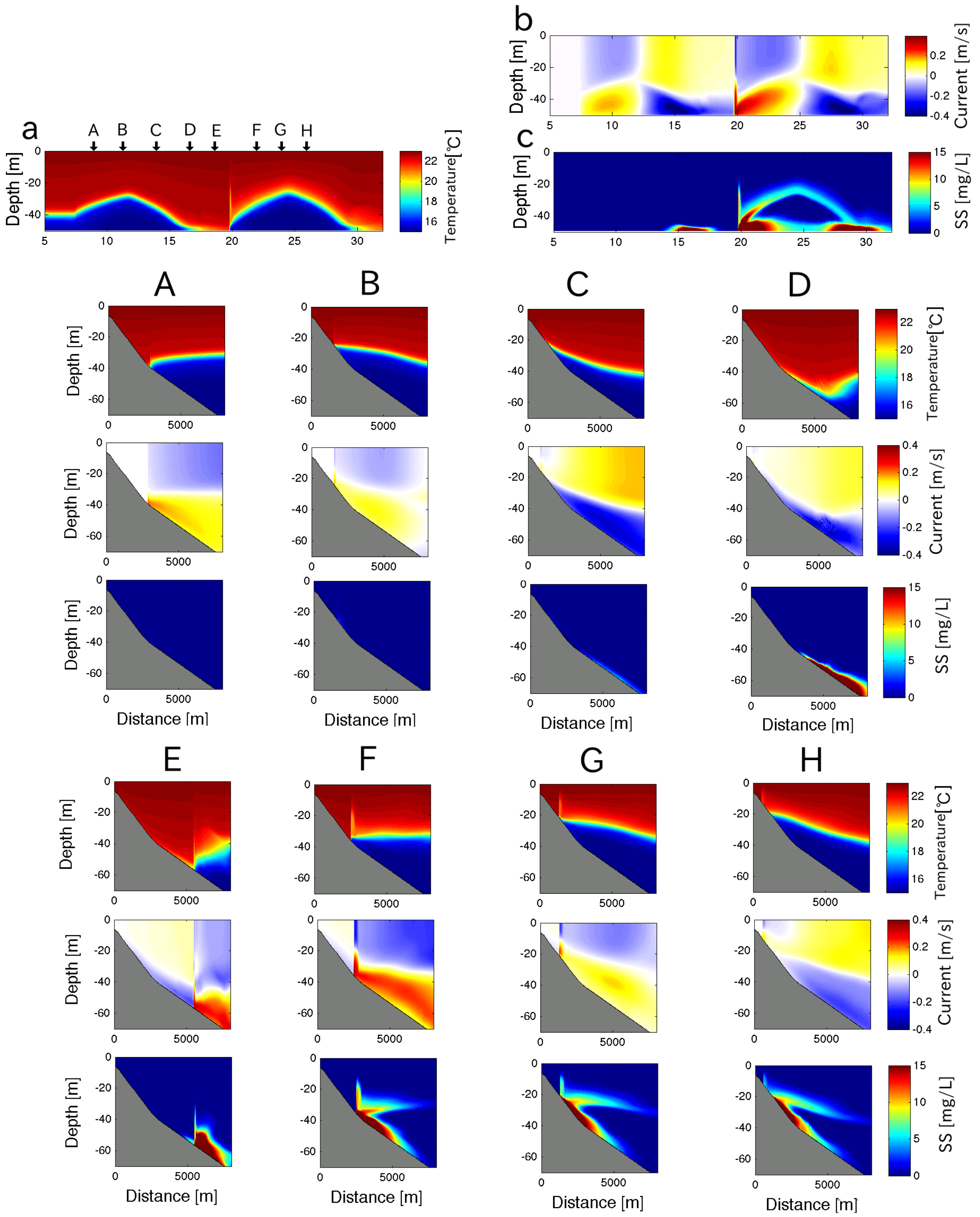

Fig. 6-4 Numerical results from Otsuchi Bay produced by the sediment model (run#5-1). (a) temperature, (b) horizontal current and (c) sediment concentration of fine particles (10 µm) time series at 50 m depth, and (A – H) vertical section results for temperature, horizontal current and sediment concentration of fine particles (10 µm) [mg/L]. Black arrows at upper x axis in panel (a) indicate the timing of vertical section snap shots (A – H). Panels (A – D) and (E – H) show the first run-up bore and the second run-up bore respectivelu.

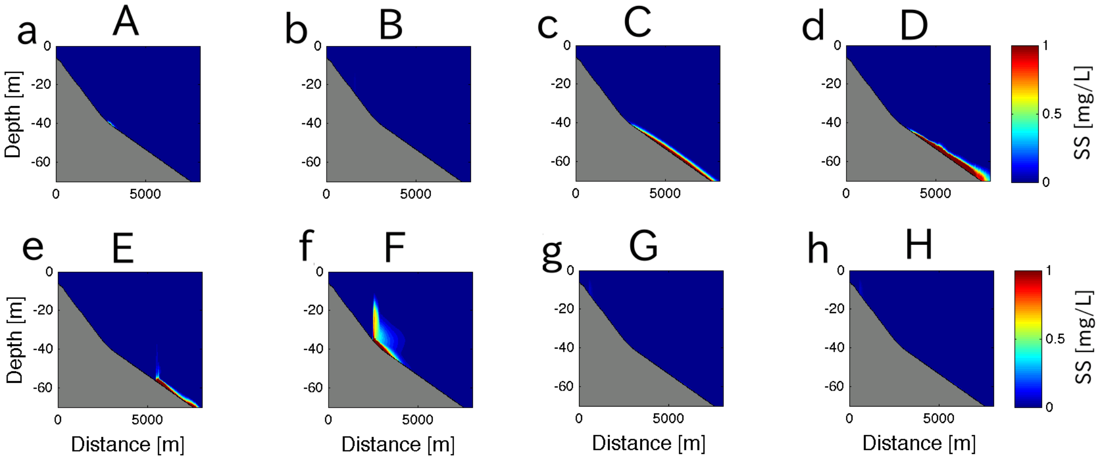

Fig. 6-5 Sediment concentration of coarse particles (50 μm). Results shown in this figure are taken from same timings as Fig. 6-4 (periods A – H).

The agreement with observations

Numerical results were compared with observed data from in situ surveys. Both the numerical results and the observation data showed that strong sediment resuspension at the head of the bore and INLs were generated (Fig. 6-6). The INL reproduced by the numerical model showed good agreement with observed data. However, the strong vertical resuspension induced by the vortex motion at the head did not appear in the observed data. This inconsistency was due to the horizontal resolution of the observation; the size of the vortex was much smaller than the horizontal resolution of the YODA Profiler survey. In addition, the size of the vortex maybe overestimated in the numerical simulation due to the numerical diffusion. The actual horizontal scale of the vortex was supposed to be a few tens of meters (see chapter 4). Fortunately, one observed result, shown in Fig. 6-6c, shows vertical resuspension of sediments likely induced by the bore head vortex (distance ~1000 m). Observed results also showed sediment resuspension in the receding bore and at the crashing site (Fig. 6-7, distance ~4000 m), which is consistent with the numerical results. Therefore, we have shown that numerical simulations performed by SUNTANS reproduce sediment resuspension and INLs generated by internal bores.

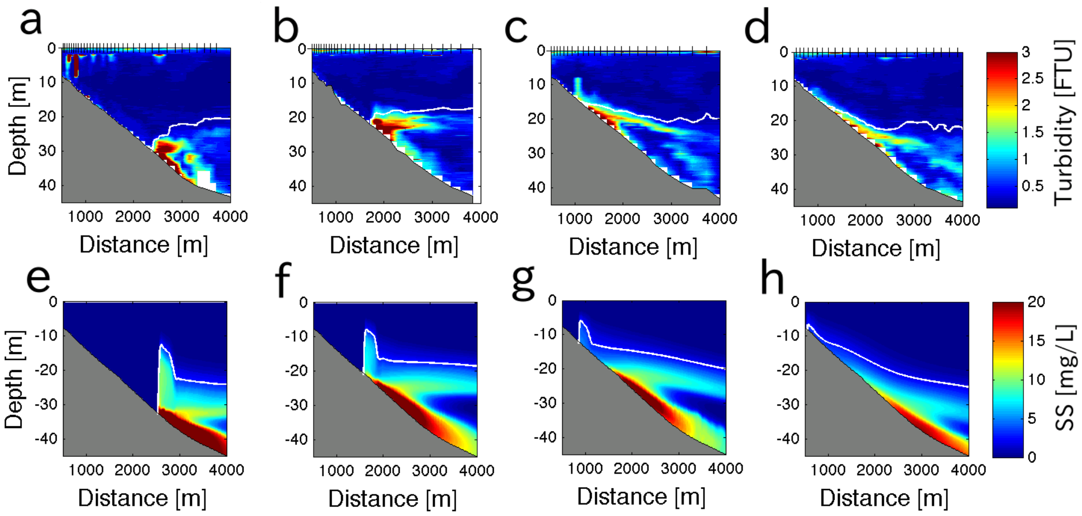

Fig. 6-6 Comparison between (a – d) observed results and (e – h) model results.

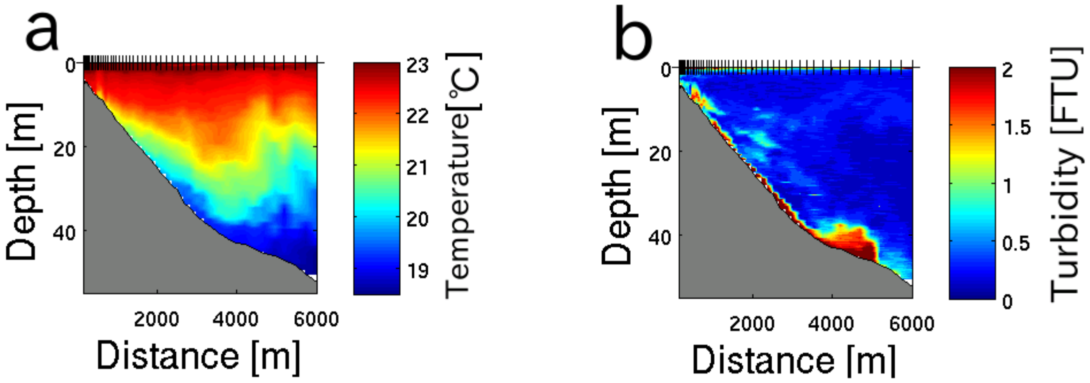

Fig. 6-7 Observed results of sediment resuspension during the crash mixing event. (a) Temperature and (b) turbidity [FTU].

The tertiary circulation

Locally intensified mixing on sloping bottoms causes unbalanced in buoyancy horizontally (Fig. 6-2). This unbalance leads to the transport of mixed water toward the offshore in order to maintain the buoyancy balance (restratification), known as the tertiary circulation (*Garrett,* 1990). The tertiary circulation transports materials from the sloping bottom to interior offshoreward (*Garrett,* 1990). As suggested by studies of the tertiary circulation, numerical results indicated growth of the INL by repeated internal bores (Fig. 6-8). Numerical results during the fifth bore phase (62.5 hours after simulation started) showed the growth of the INL spreading approximately 10 km away from the sloping bottom (Fig. 6-8). Simulated time series at 80 m depth also showed the growth of the INL in the interface of the internal waves (Fig. 6-9c). The concentration of sediments in the wave interface increased with the passage of time. The offshoreward sediment flux was much larger than the onshore ward flux in the interface. Therefore, suspended sediments were transported offshore through the INL.

The mean current speed was computed at each thermal depth. Fig. 6-10a shows the mean current speed at depth of 80 m between the third and fifth bore wave period, the mean current was plotted as a function of each initial isothermal depth. The mean current speed indicated the offshoreward flow in the middle layer (depth ~40 m) and the shoreward flow in the lower (depth > 48 m) and the upper layers (depth < 25 m). The peak of the mean flow appeared in the interface of the wave (40 m depth), and the offshoreward mean flow reached 0.05 ms^{-1}. This offshore ward flux was thought to be generated by the intensified turbulent mixing along the slope and restratification (the tertiary circulation). Therefore, numerical results indicated that internal bores propagating into shallow areas greatly contribute to offshore mass fluxes along isopycnal depths (wave interface) and the formation of INLs.

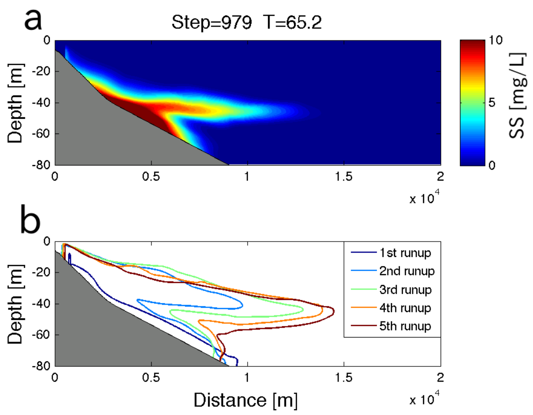

Fig. 6-8 (a) Suspended sediment distribution during the fifth run-up phase (62.5 hours after simulation started), and (b) the distribution of INLs in each run-up phase. Thick lines in panel (b) are contour lines of SS = 0.1 mg/L in the first (dark blue), second (light blue), third (light green), fourth (orange) and fifth (brown) run-up phases.

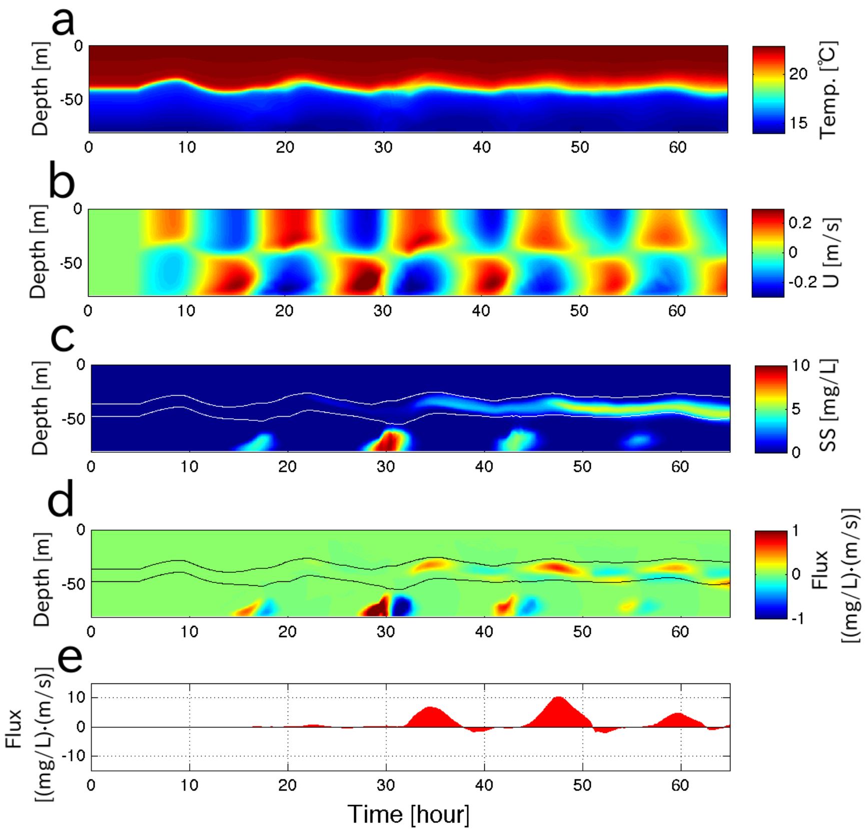

Fig. 6-9 Time series of numerical results at 80 m depth (the bottom edge of the slope). (a) Temperature, (b) horizontal current, (c) suspended sediments [mg/L], (d) flux of suspended sediments and (e) integrated flux of suspended sediments in the interface of the bore wave (temperature between 16.5 and 22.6 °C). Contour lines in panels (c) and (d) are isothermal depths of 16.5 and 22.6 °C. The positive (negative) value in panels (b, d and e) indicates the offshore ward (onshoreward) current or flux.

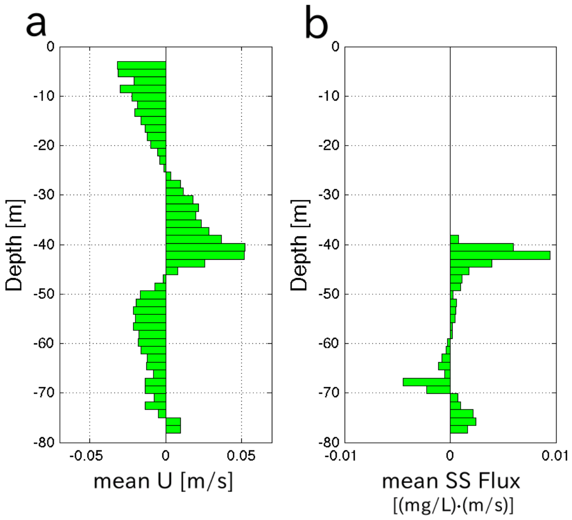

Fig. 6-10 (a) Mean current [m/s] and (b) mean sediment flux at 80 m depth (the bottom edge of the slope). The positive (negative) value in indicates the offshoreward (onshoreward) current or flux.

The mean outflow volume through the wave interface was estimated as 0.74 m^3s^{-1} per width of the channel. Although the numerical model was simplified in the two dimensional domain, the width of the bay mouth allowed to evaluate a rough outflow volume due to the tertiary circulation. Assuming the channel width is 3000 m (Otsuchi Bay case), the total outflow volume is 2.2×10^3 m^3s^{-1}. The total river discharge from the three rivers in Otsuchi Bay ranges 3 – 35 m^3s^{-1} (Anbo et al., 2005). The water transported due to the tertiary circulation is much greater than that due to the river discharge into the bay. This outflow volume due to the tertiary circulation is also greater than that of the largest river in Japan, the Shinano River (mean discharge is 5.2×10^2 m^3s^{-1}).

Field survey data over the continental shelf near the Sanriku coast were collected by the JAMSTEC group September – November, 2013. Observed data showed INLs at several points and that INLs detached from the boundary and spread into the offshore direction (Fig. 6-11). Sediment resuspension and the tertiary circulation induced by internal bores may contribute to the formation of INLs over continental shelves.

Thus, I added the following items to the steps (1) – (4), which were described at the beginning of this section:

(5) Bottom intensified turbulent mixing due to internal bores causes a tertiary circulation.

(6) The tertiary circulation transports INLs offshore over the continental shelf.

River/land-derived nutrients and sediments sink and deposit in coastal depocenters near shore areas (*Mayer et al.,* 1998). These deposited materials are resuspended and transported offshore through INLs (e.g., *McPhee-Shaw,* 2006). Lateral dispersal of sediments, nutrients and organic matters is essential for biological production and ecosystems in the ocean (*Nakatsuka et al.,* 2004; *McPhee-Shaw,* 2006).

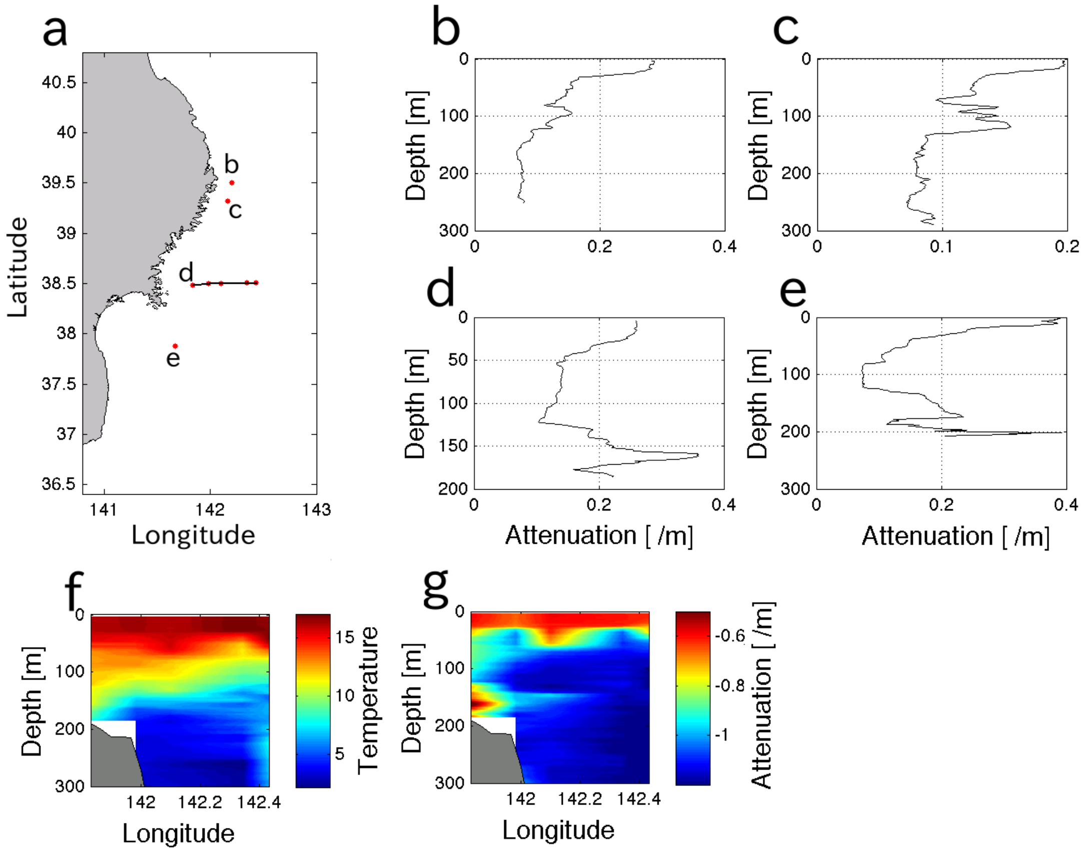

Fig. 6-11 Observed results from JAMSTEC. (a) map of the observation area, (b – e) profiles of the light attenuation [m^{-1}] at points (b) – (e) shown in the panel (a) and vertical distributions of (f) temperature and (g) light attenuation in a transect line. The black line in the panel (a) is the transect line. Data presented in this figure are provided by JAMSTEC and observed during September – November, 2013.

6.4 Sloping angles and sediment resuspension

Numerical results from variable slopes

In order to investigate the behavior of internal bores and sediment resuspension in variable topographies, I used several domains for numerical surveys (five conditions). Steep angle conditions (high Iribarren number, run#5-2, #5-3 and #5-4) produced non-canonical bores accompanied by a gradual increase in isothermal depth in run-up phases and a rapid decrease in isothermal depth in receding phases (Fig. 6-12, 6-13). On the other hand, gentle angle conditions (low Iribarren number, run#5-5 and #5-6) showed canonical bores inducing strong vortex motion (Fig. 6-12, 5-13). Results clearly indicated that the transition from canonical bores to non-canonical bores depended on the Iribarren number. The up-slope current during the run-up phases increased with a decrease in the Iribarren number (Fig. 6-12, 6-14a). Internal bores on gentle slope conditions had to run-up longer distances than those on steep slopes; therefore, gentle slope (low ξ) conditions caused strong horizontal currents in bores, which led to highly non-linear motion. The maximum upslope flow speed was inverse proportional to the Iribarren number (Fig. 6-12a). The maximum down-slope flow speed is higher in ξ = 1.6 and 1.1 cases (run#5-3 and 5-4). The highest ξ case (run# 5-2) showed weak currents in both run-up and receding phases. Two low Iribarren number cases (run#5-5 and 5-6) produced strong sediment resuspension and INLs. The internal bore in ξ = 1.1 (run#5-4) suspended sediments around the bore head vortex, but the bore did not generate a remarkable INL. Strictly speaking, ξ = 1.1 produced a weak INL, and the concentration of sediments in the INL is 10 times or more smaller than that of INLs in ξ = 0.65 and 0.45 cases. Results from the ξ = 3.6 case showed only weak sediment resuspension during the receding phase. The highest ξ (3.2) case did not produce any sediment resuspension and INLs (the bottom shear stress did not reach the critical stress). Numerical results from several slope conditions indicated that the low Iribarren number condition tends to generate strong sediment resuspension and INLs.

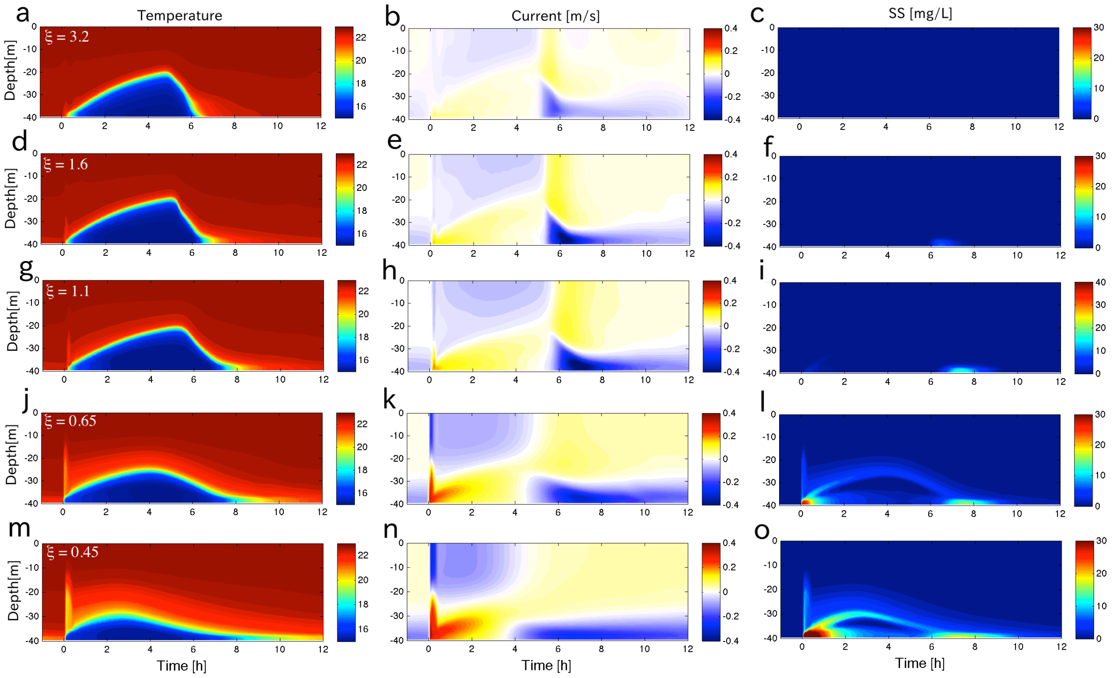

Fig. 6-12 Time series data at 40 m depth simulated in five-slope angle conditions, (a - c) *ξ* = 3.2 (run#5-2), (d - f) *ξ* = 1.6 (run#5-3), (g - h) *ξ* = 1.1 (run#5-4), (j - l) *ξ* = 0.65 (run#5-5) and (m - o) *ξ* = 0.45 (run#5-6). Left panels are temperature, middle panels are horizontal current [m/s] and right panels are suspended sediments [mg/L].

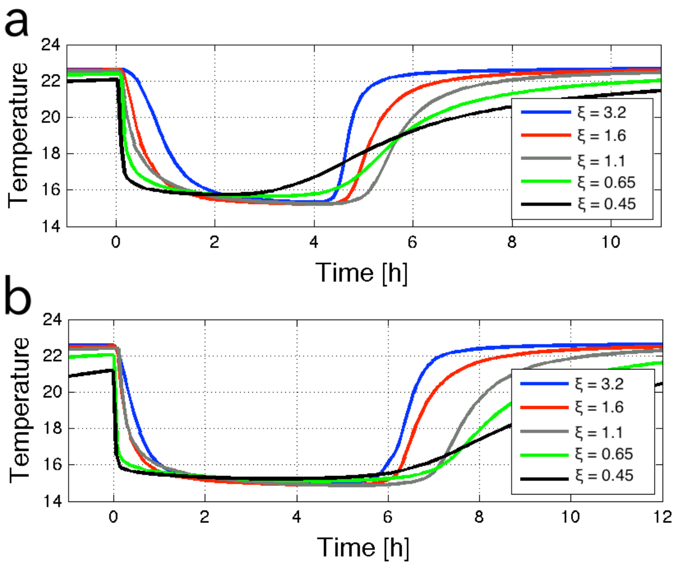

Fig. 6-13 Bottom temperature time series at (a) 30 m depth and (b) 40 m depth.

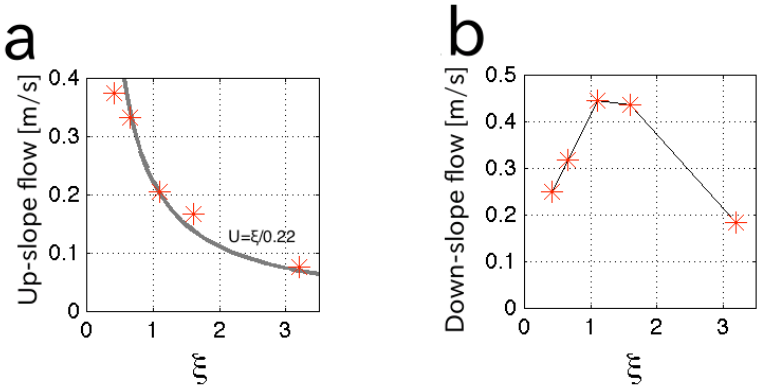

Fig. 6-14 (a) the maximum up-slope flow speed and (b) the maximum down-slope flow speed at 40 m depth in five numerical runs.

Crash mixing and sediment resuspension

Crash mixing leading to strong turbulent mixing and convergence is an important phenomenon in generating sediment resupension, as described earlier. Low ξ cases showed strong crash mixing along the slope (example is shown in Fig. 6-15 phase C, distance ~ 7000m), and the convergent flow at the crashing site lifted up suspended sediments. Intensified up-slope flows in low Iribarren cases enhanced the vortex motion at the head of bores (Fig. 6-15). The enhanced vortex motion also contributed to lift up suspended sediments. The run-up bore pushes up lifted sediments and formed the INLs (Fig. 6-15, phase D). On the other hand, high ξ cases did not lead to strong crash mixing (example is shown in Fig. 6-16). Suspended sediments were not strongly lifted up vertically, since mixing intensity and the vertical motion were weak. Therefore, crash mixing play a significant role in sediment resuspension processes and the generation of INLs. In addition, strong turbulent mixing near the slope caused by crash mixing may greatly contribute to tertiary circulation, resulting in INLs over continental shelves. The Iribarren number may be a key parameter in understanding the water exchange process between coastal waters and open ocean waters.

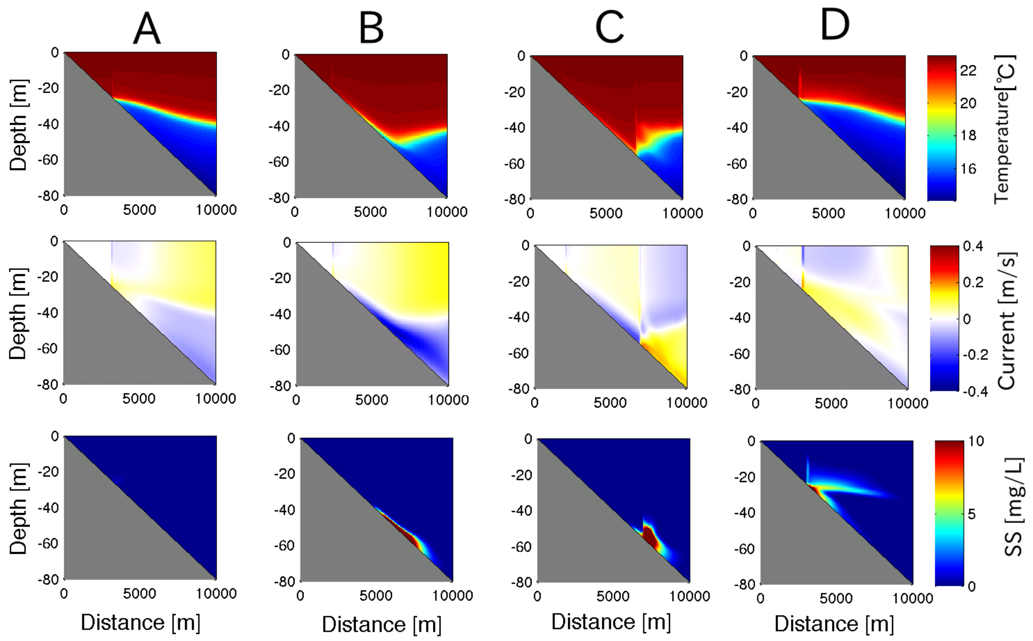

Fig. 6-15 Numerical simulation results from run#5-5 ($\xi = 0.65$).

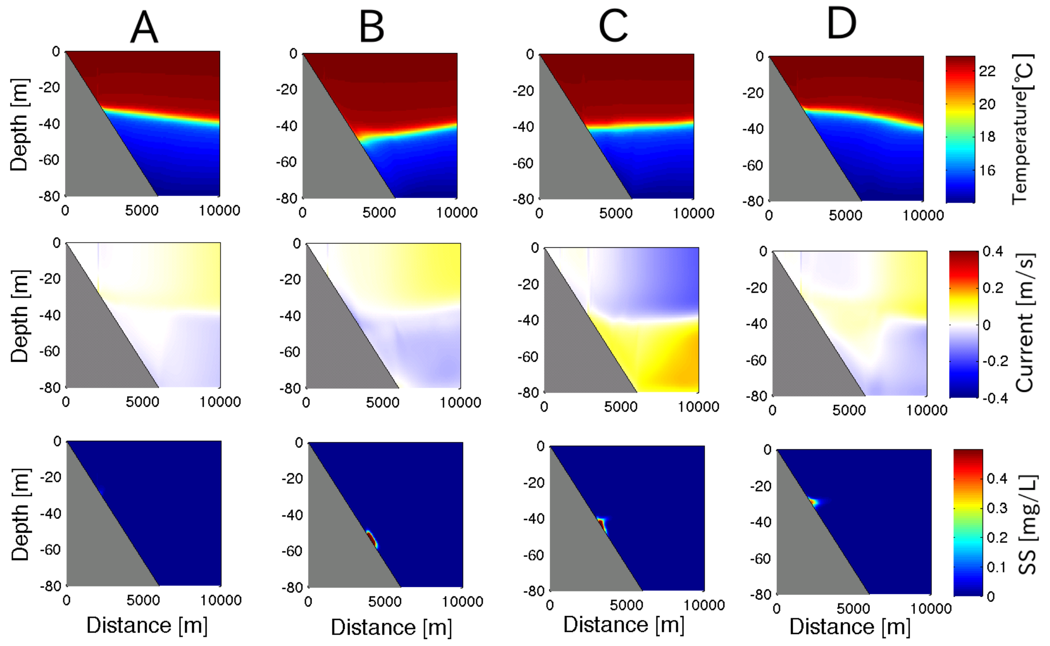

Fig. 6-16 Numerical simulation results from run#5-4 ($\xi = 1.1$).

6.5 Conclusions

Numerical simulations performed with SUNTANS showed sediment resuspension and intermediate nepheloid layers (INLs) induced by internal bores. The downslope flow during the bore receding phase caused strong bottom shear stress leading to sediment resuspension. Suspended sediments were lifted up by the upward motion due to crash mixing and the vortex motion. Run-up bores intruded below lifted up sediments and formed INLs. Internal bores enhanced turbulent mixing near the sloping bottom, leading to tertiary circulation. The tertiary circulation transported the INL to the offshore area. In our simulation case, the mean outflow speed caused by the tertiary circulation was approximately $0.05 \mathrm{ms}^{-1}$ in the interface of the internal bore. The estimated total outflow volume from Otsuchi Bay through the bore-induced tertiary circulation was much greater than the total river discharge into Otsuchi Bay. Numerical results from several variable slope conditions showed that internal bores generate strong sediment resuspension and INLs in low Iribarren number conditions (gentle slope cases). I found that crash mixing controlled by the Iribarren number plays a significant role in sediment resuspension and forming INLs. This chapter demonstrated the generation mechanism of INLs, sediment resuspension processes due to internal bores and sediment resuspension dependent on the Iribarren number.

Internal bore waves are ubiquitous features in coastal areas worldwide (e.g., *Fu and Holt,* 1982; *Helfrich and Melville,* 2006; *Bourgault et al.,* 2007; *Nam and Send,* 2011; *Walter et al.,* 2012), and coastal areas worldwide may have the potential to generate tertiary circulation and INLs. Thus, internal bore waves significantly contribute to global ocean circulation and the global scale ocean ecosystem.

Chapter 7

Conclusion and outlook

7.1 Conclusion

This study has focused on mixing processes in shallow coastal seas using a newly developed profiler (YODA Profiler) and numerical simulations (SUNTANS).

The first part of this dissertation dealt with the development of the YODA Profiler. Observed results in the Arakawa River mouth and Otsuchi Bay showed superior performance from the profiler. Observed high-resolution results indicated small-scale internal wave motion below the river plumes. Small-scale internal waves influenced the distribution of phytoplankton. The physical structure in coastal areas drastically changed within short periods. River plume structures changed with the tidal phase, and internal bores propagated into the bay within few hours. A newly developed statistical method allowed us to infer the rate of turbulent kinetic energy dissipation from vertical fluctuations of conductivity. The estimated dissipation from the YODA Profiler data showed fine features of turbulent structures in internal waves and bores.

The middle sections of this study (chapters 3 and 4) discussed internal bores propagating into a shallow bay, Otsuchi Bay, Japan. The vertical displacement of the thermocline due to internal bores reached 20 m vertically in the bay. The appearance of internal bores was intermittent and was not consistent with tidal cycles. Results indicated that internal bores generate the vortex motion accompanied by strong currents and turbulent mixing at the head of bores. Sediments were strongly suspended by the vortex motion at the head of the bore. Suspended materials intruded into the offshore area above the interface of bores, which resulted in intermediate nepheloid layers (INLs). In addition, the vortex motion largely influenced river plume mixing in the bay.

Internal bores on the shallow slope play a significant role in both the bay water and river plumes. Internal bores generate turbulent mixing not only in the bottom boundary layer but also in the surface layer.

This study discovered a new mixing process, “crash mixing”, described in Chapter 5. Although shoreward internal bores have been extensively researched by several studies (e.g., *Pineda,* 1994; *Leichter et al.*, 1996; *Walter et al.,* 2012), the behaviors of internal bores during receding phases have not been well understood. My work has found strong turbulent mixing induced by the collision of the run-up bore and the receding bore. I named the term “crash mixing” to describe this process. Strong turbulent mixing due to crash mixing expanded toward the sea surface from the bottom. The order of the rate of turbulent kinetic energy dissipation rate reached 10^{-6} – 10^{-5} $\mathrm{Wkg^{-1}}$. Numerical simulations revealed that the Iribarren number controls crash mixing slope. Low Iribarren number conditions tend to lead to strong crash mixing and the highly nonlinear motion.

The last part of the dissertation presented the generation mechanism of INLs, revealed through the use of numerical simulations. The revealed mechanism showed that crash mixing is a key process in the generation of INLs. Therefore, the Iribarren number controls the sediment resuspension caused by internal bores. Numerical results also reproduced the tertiary circulation, and the mean flow speed was toward the offshore area in the interface of the internal wave. This tertiary circulation contributes to the formation of INLs over slopes.

This study clearly demonstrated mixing processes associated with river plumes and nonlinear internal bores using the newly developed YODA Profiler and the numerical simulator SUNTANS. The schematic image of findings from this study is shown in Fig. 7-1.

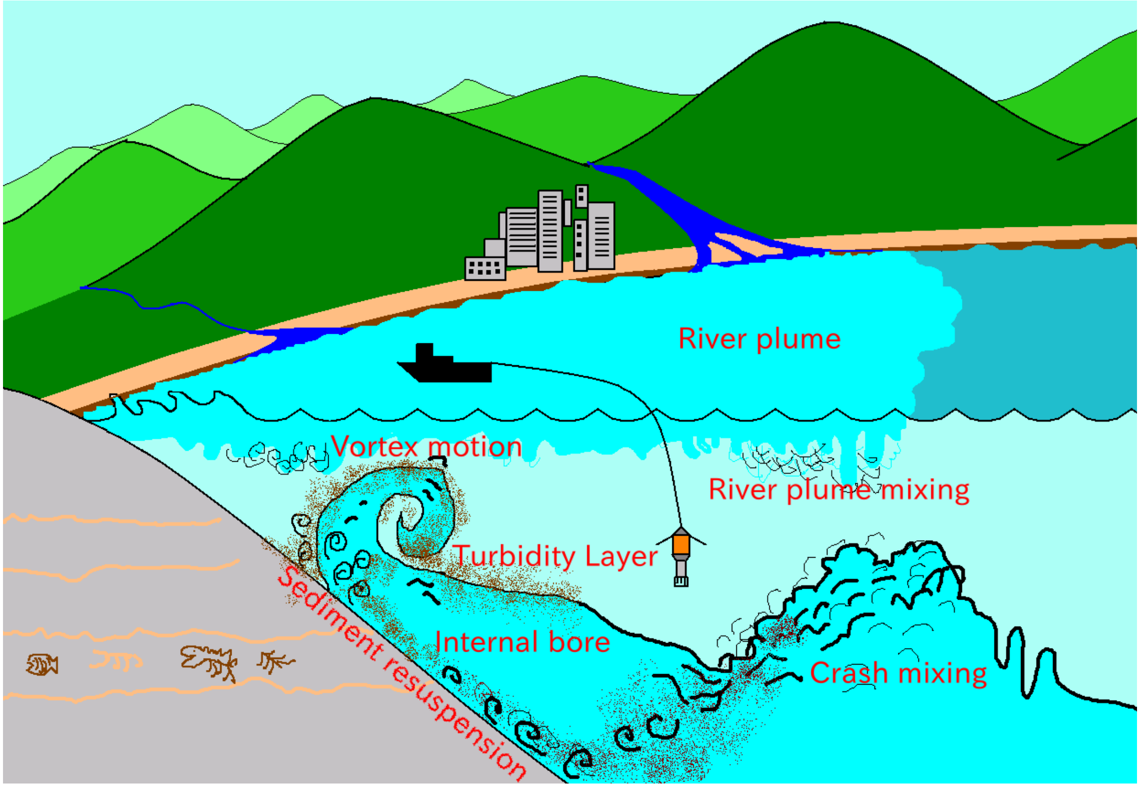

Fig. 7-1 A schematic image of findings from this study, a new observation system YODA Profiler (Chapter 2), river plume mixing de to internal tides (Chapter 3), the vortex motion and sediment resuspension induced by internal bores (Chapters 4 and 6) and crash mixing (Chapter 5).

7.2 Outlook

This dissertation has revealed details of mixing and sediment resuspesnion processes associated with internal wave/bores using a newly developed instrument. The performance of numerical simulations is improving with the remarkable growth in computer technology, however, few studies have provided direct comparisons between numerical results and observed results. Using the YODA Profiler, this work has produced high-resolution physical structures in shallow areas. Numerical simulations of internal bores performed with SUNTANS (*Fringer et al.,* 2006) showed an excellent agreement with observed results from the YODA Profiler. Such agreement between numerical simulations and observed data have never been shown in previous studies. In the future, the YODA Profiler may significantly contribute to field surveys in coastal seas. Several mechanisms have been proposed in this thesis; “the vortex at the bore head”, “crash mixing” and “the generation mechanism of INLs”. These new findings may support understanding of physical processes in coastal areas.

However, this work has left several unexplored issues. In this thesis, field surveys were only conducted in a small local bay and numerical simulations were greatly simplified in two-dimensional domains. This means that several issues were left unexplored. These remaining problems are listed below.

Three-dimensional numerical simulations

The numerical model used in this study is two-dimensional numerical model. However, three-dimensional topographic effects and the coriolis force (Earth’s rotational effect) should be consider to understand more realistic physical processes of internal bores/waves. Assuming the propagation speed of the bore is 0.1ms^{-1}, Rossby radius of deformation, C/f, is computed as 7200 m. To overcome these issues, three-dimensional domains have to be used.

The generation of internal bores

The energy source of internal bores is linear internal tides over continental shelves (e.g, *Van Gastel et al.,* 2009). Although this thesis has shown the critical generation area of internal bores by compareing the topographic slope with the incident linear internal tide angle, direct observations and numerical simulations have not shown the generation mechanism of internal bores over the continental shelf. Observations over the continental shelf are necessary to reveal the generation process of internal bores. In addition, a three dimensional large-scale numerical survey covering the continental shelf has to be used for reproducing the reflection of internal waves and the generation of internal bores. Several studies have reproduced the reflection of internal tides and the generation of internal bores over continental shelves (e.g., *Van Gastel et al.,* 2009). Recent numerical techniques have already allowed us to reproduce the generation of internal bores over the Sanriku continental shelf. An understanding of the processes behind internal bore generation will help predict the occurrence of intermittent internal bores in shallow bays.

Dispersions of INLs in the large-scale field and the impact on the global circulation

This work has suggested that internal bores contribute to lateral dispersals of sediments, nutrients and river-land derived materials. However, this study has not evaluated how much the tertiary circulation transports these materials toward the offshore and has not shown how INLs spread three dimensionally. Larger scale observations and three-dimensional numerical simulations may solve these problems.

References

Anbo, A., H. Otobe, and M. Takagi (2005), On the river water discharged into Otsuchi Bay, Report of International Coastal Marine Research Center, 30, 4–8 (in Japanese).

Antenucci, J. P., and J. Imberger (2001), On internal waves near the high-frequency limit in an enclosed basin, Journal of Geophysical Research: Oceans, 106(C10), 22465–22474.

Antonia, R.A., and C.W., Van Atta (1975), On the correlation between temperature and velocity dissipation fields in a heated turbulent jet. Journal of Fluid Mechanics, 67, 273–288.

Baker, M.A., and C.H., Gibson (1987), Sampling turbulence in the stratified ocean: statistical consequences of strong intermittency. Journal of Physical Oceanography, 17, 1817–1836.

Batties, J. A. 1974. Surf similarity, Proceedings of Coastal Engineering Conference, ASCE, 14: 466–479.

Boegman, L., J. Imberger, G. N. Ivey, and J. P. Antenucci (2003), High-frequency internal waves in large stratified lakes, Limnology and Oceanography, 48(2), 895–919.

Boegman, L., G. N., Ivey, and J., Imberger (2005), The degeneration of internal waves in lakes with sloping topography. Limnology and oceanography, 50(5), 1620-1637.

Boegman, L., and G. N. Ivey (2009), Flow separation and resuspension beneath shoaling nonlinear internal waves, Journal of Geophysical Research: Oceans, 114, C02018.

Bonnin, J., H. van Haren, P. Hosegood, and G. J. A. Brummer (2006), Burst resuspension of seabed material at the foot of the continental slope in the Rockall Channel, Marine Geology, 226, 167–184.

Bourgault, D., M. D. Blokhina, R. Mirshak, and D. E. Kelley (2007), Evolution of a shoaling internal solitary wavetrain, Geophysical Research Letters, 34, L03601, doi:10.1029/2006GL028462.

Bourgault, D., M., Morsilli, C., Richards, U., Neumeier, and D.E., Kelley (2014), Sediment resuspension and nepheloid layers induced by long internal solitary waves shoaling orthogonally on uniform slopes, Continental Shelf Research, 72, 21-33.

Broenkow, W. W., and S. J. McKain (1972), Tidal oscillations at the head of Monterey Submarine Canyon and their relation to oceanographic sampling and the circulation of water in Monterey Bay, in Moss Landing Marine Laboratories Technical Publication 72-5, Annual report, Part 6, September 1972, pp. 42, Moss Landing Marine Laboratories , Moss Landing, Calif.

Cacchione, D.A., and D.E., Drake (1986), Nepheloid layers and internal waves over continental shelves and slopes. Geo-Marine Letters, 6, 147–152.

Cacchione, D. A., L. F. Pratson, and A. S. Ogston (2002), The shaping of continental slopes by internal tides, Science, 296, 724–727.

Carter, G. S., M. C. Gregg, and R. C. Lien (2005), Internal waves, solitary-like waves, and mixing on the Monterey Bay shelf, Continental Shelf Research, 25, 1499–1520.

Chou, Y.J., R.C., Holleman, S., Lee, O.B., Fringer, M.T., Stacey, J.R., Koseff, and S.G., Monismith (2013), Three-dimensional Coupled Wind-Wave and Cohesive Sediment Transport Modeling in San Francisco Bay, *in preparation*.

Dekshenieks, M.M., P.L., Donaghay, J.M., Sullivan, J.E.B., Rines, T.R., Osborn, T.R., and M.S., Twardowski (2001), Temporal and spatial occurrence of thin phytoplankton layers in relation to physical processes. Marine Ecology Progress Series, 223, 61–71.

Dewey, R. K., and W. R. Crawford (1988), Bottom stress estimates from vertical dissipation rate profiles on the continental shelf, Journal of Physical Oceanography, 18, 1167–1177.

Dickson, R. R., and I. N McCave (1986), Nepheloid layers on the continental slope west of Porcupine Bank, Deep Sea Research, Part A, 33, 791–818.

Dillon, T.M., and D.R., Caldwell (1980), The Batchelor spectrum and dissipation in the upper ocean. Journal of Geophysical Research: Oceans, 85, 1910–1916.

Durham, W.M., and R.,Stocker (2012), Thin phytoplankton layers: characteristics, mechanisms, and consequences. Annual Review of Marine Science, 4, 177–207.

Egbert, G. D., and S. Y. Erofeeva (2002), Efficient inverse modeling of barotropic ocean tides, Journal of Atmospheric and Oceanic Technology, 19(2), 183–204.

Foloni-Neto, H., R. Lueck, Y. Mabuchi, H. Nakamura, M. Arima, and H. Yamazaki (2014), A new quasi-horizontal glider to measure biophysical microstructure, Journal of Atmospheric Oceanic Technology, submitted.

Fringer, O. B., M. Gerritsen, and R. L. Street (2006), An unstructured-grid, finite-volume, nonhydrostatic, parallel coastal ocean simulator, Ocean Modelling, 14, 139–173.

Fu, L. L., and B. Holt (1982), Seasat views oceans and sea ice with synthetic-aperture radar, NASA/JPL Publication 81–120, California Institute of Technology, Pasadena, Calif.

Gardner, W. D. (1989), Periodic resuspension in Baltimore Canyon by focusing of internal waves, Journal of Geophysical Research, 94, 18,185–18,194.

Garrett, C. (1990), The role of secondary circulation in boundary mixing. Journal of Geophysical Research 95 (C3), 3181–3188.

Garrett, C. (1991), Marginal mixing theories. Atmosphere–Ocean 29, 313–339.

Gayen, B., and S., Sarker (2011), Direct and large-eddy simulations of internal tide generation at a near-critical slope. Journal of Fluid Mechanics, 681, 48–79.

GEOHAB, 2013. Global Ecology and Oceanography of Harmful Algal Blooms, GEOHAB Core Research Project: HABs in Stratified Systems. (Eds. M.A. McManus, E. Berdalet, J. Ryan, H. Yamazaki, J.S. Jaffe, O.N. Ross, H. Burchard and F. Chavez) (Contributors: G. Basterretxea, D. Rivas, M.C. Ruiz and L. Seuront) IOC and SCOR, Paris and Newark, Delaware, USA.

Geyer, W.R., A. Lavery, M.E. Scully, and J.H., Trowbridge (2010), Mixing by shear instability at high Reynolds number. Geophysical Research Letters 37, L22607,

Gibson, C.H., and W.H., Schwarz (1963), The universal equilibrium spectra of turbulent velocity and scalar fields. Journal of Fluid Mechanics, 16, 365–384.

Gille, S.T., S.G., Llewellyn Smith, and S.M., Lee (2003), Measuring the sea breeze from QuikSCAT scatterometry, Geophysical Research Letters, 30(3).

Gloor, M., A. Wüest, and M., Münnch (1994), Benthic boundary mixing and resuspension induced by internal seiches, Hydrobiologia, 284, 59–68.

Goodman, L., and M.M., Sastre-Córdova (2011), On observing acoustic backscattering from salinity turbulence. The Journal of the Acoustical Society of America, 130, 707–715.

Hasegawa, D., H., Yamazaki, R.G., Lueck, and L., Seuront (2004), How islands stir and fertilize the upper ocean. Geophys. Res. Lett. 31, L16303.

Hasegawa, D., H. Yamazaki, T. Ishimaru, H. Nagashima and Y. Koike (2008), Apparent phytoplankton bloom due to island mass effect. Journal of Marine Systems, 69(3), 238-246.

Hanawa, K., and H. Mitsudera (1986), Variation of water system distribution in the Sanriku coastal area, Journal of the Oceanographical Society of Japan, 42, 435–446.

Helfrich, K. R. (1992), Internal solitary wave breaking and run-up on a uniform slope, Journal of Fluid Mechanics, 243, 133–154.

Helfrich, K. R., and W. K. Melville (2006), Long nonlinear internal waves, Annual Review of Fluid Mechanics, 38, 395–425.

Herman, A.W., B., Beanlands, M., Chin-Yee, A.,Furlong, J., Snow, S., Young, and T., Phillips (1998), The Moving Vessel Profiler (MVP): In-situ sampling of plankton and physical parameters at 12 kts and the integration of a new laser/optical plankton counter. Oceanology International 98 Conference Proceedings, March 1–13, 1998, Brighton, UK, 102, 123–135, Spearhead Exhibitions Ltd, ISBN 0 900254 21 1.

Heywood, K. J., A. C. N., Garabato, and D. P., Stevens (2002), High mixing rates in the abyssal Southern Ocean. Nature, 415(6875), 1011-1014.

Hosegood, P., and H. van Haren (2004), Near-bed solibores over the continental slope in the Faeroe-Shetland Channel, Deep-Sea Res. II, 51, 2943–2971.

Hosegood, P., J. Bonnin, and H. van Haren (2004), Solibore-induced sediment resuspension in the Faeroe–Shetland Channel, Geophysical Research Letters, 31, L09301.

Huthnance, J. M. (1989), Internal tides and waves near the continental shelf edge, Geophysical and Astrophysical Fluid Dynamics, 48, 81–106.

Ivey, G. N., K. B. Winters, and I. P. D. De Silva (2000), Turbulent mixing in a sloping benthic boundary layer energized by internal waves, Journal of Fluid Mechanics, 418, 59–76.

Iribarren C, R., and C., Nogales (1949), Protection des ports. XVIUfc Int. Congr. Navig. Lisbon, 31-80.

Kay, D.J., and D.A., Jay (2003), Interfacial mixing in a highly stratified estuary 1. Characteristics of mixing, Journal of Geophysical Research: Oceans (1978–2012), 108(C3).

Keister, J. E., E. D., Houde, and D.L., Breitburg (2000), Effects of bottom-layer hypoxia on abundances and depth distributions of organisms in Patuxent River, Chesapeake Bay. Marine Ecology Progress Series, 205, 43–59.

Kineke, G. C., R. W. Sternberg, J. H. Trowbridge, and W. R. Geyer (1996), Fluid-mud processes on the

Amazon continental shelf, Continental Shelf Research, 16, 667–696.

Kilcher, L. F., and J. D. Nash (2010), Structure and dynamics of the Columbia River tidal plume front, Journal of Geophysical Research: Oceans (1978–2012),115(C5).

Klymak, J. M., and J. N. Moum (2003), Internal solitary waves of elevation advancing on a shoaling shelf, Geophysical Research Letters, 30, 31–34.

Klymak, J., and M. Gregg (2004), Tidally generated turbulence over the Knight Inlet Sill. J. Phys. Oceanogr., 34, 1135–1151.

Kokubu, Y., H., Yamazaki, T., Nagai, and E. S., Gross (2013), Mixing observations at a constricted channel of a semi-closed estuary: Tokyo Bay.Continental Shelf Research, 69, 1-16.

Kourafalou, V.H., T.N., Lee, L.Y., Oey, and J.D., Wang (1996), The fate of river discharge on the continental shelf: 2. Transport of coastal low-salinity waters under realistic wind and tidal forcing, Journal of Geophysical Research: Oceans (1978–2012), 101(C2), 3435–3455.

Kundu, P. K. (1990), Fluid Dynamics, Academic Press, San Diego, Calif.

St Laurent, L. C., and A., M., Thurnherr, A. M. (2007). Intense mixing of lower thermocline water on the crest of the Mid-Atlantic Ridge. Nature, 448(7154), 680-683.

Ledwell, J.R., E.T., Montgomery, K.L., Polzin, L.C., St Laurent, R.W., Schmitt, and J.M., Toole (2000), Evidence for enhanced mixing over rough topography in the abyssal ocean. Nature 403, 179–182.

Leichter, J. J., S. R. Wing, S. L. Miller, and M. W. Denny (1996), Pulsed delivery of subthermocline water to Conch Reef (Florida Keys) by internal tidal bores, Limnology and Oceanography, 41(7), 1490–1501.

Lennert-Cody, C.E., and P.J.S., Franks (1999), Plankton patchiness in high-frequency internal waves. Marine Ecology Progress Series, 186, 59–66.

Li, M., J., Trowbridge, and R., Geyer (2008), Asymmetric tidal mixing due to the horizontal density gradient. Journal of Physical Oceanography, 38, 418–434.

Lien, R.C., F., Henyey, B., Ma, and Y.J., Yang (2014), Large-amplitude internal solitary waves observed in the northern South China Sea: properties and energetics, Journal of Physical Oceanography, 44(4), 1095–1115.

Lumpkin, R., and K., Speer, K. (2007), Global ocean meridional overturning. Journal of Physical Oceanography, 37(10).

MacDonald, D.G., and W.R., Geyer (2004), Turbulent energy production and entrainment at a highly stratified estuarine front. Journal of Geophysical Research: Oceans, 109, C05004.

MacKinnon, J. A., and M.C., Gregg (2003), Mixing on the Late-Summer New England Shelf—Solibores, Shear, and Stratification. Journal of Physical Oceanography, 33(7).

Masunaga, E., and H. Yamazaki (2014), A new tow-yo instrument to observe high-resolution coastal phenomena, Journal of Marine Systems, 129, 425–436.

Mayer, L.M., R.G., Keil, S.A., Macko, S.B., Joye, K., C Ruttenberg, and R.C., Aller (1998), Importance of suspended particulates in riverine delivery of bioavailable nitrogen to coastal zones. Global Biogeochemical Cycles 12 (4), 573–579.

McPhee-Shaw, E.E., and E., Kunze (2002), Boundary layer intrusions from a sloping bottom: A mechanism for generating intermediate nepheloid layers. Journal of Geophysical Research: Oceans, 107, 3-1–3-16.

McPhee-Shaw, E.E., R.W., Sternberg, B., and A.S., Mullenbach, Ogston (2004), Observations of intermediate nepheloid layers on the northern California margin. Continental Shelf Research 24, 693–720.

McPhee-Shaw, E. (2006), Boundary–interior exchange: reviewing the idea that internal-wave mixing enhances lateral dispersal near continental margins. Deep Sea Research Part II: Topical Studies in Oceanography, 53(1), 42–59.

Mellor, G. L., and T. Yamada (1982), Development of a turbulence closure model for geophysical fluid problems, Reviews of Geophysics, 20(4), 851–875.

Möller Jr. O.O., A.R., Piola, A.C., Freitas, and E.J.D., Campos (2008), The effects of river discharge and seasonal winds on the shelf off southeastern South America. Continental Shelf Research, 28(13), 1607–1624.

Monin, A.S., and A.M., Yaglom (1967), Statistical Fluid Mechanics, vol. 1. The MIT Press.

Moum, J. N., and W. D. Smyth (2001), Upper ocean mixing processes, Encyclopedia of Ocean Sciences, 6, 3093-3100.

Moum, J.N., D.R., Caldwell, J.D., Nash, and G.D., Gunderson (2002), Observations of boundary mixing over the continental slope. Journal of Physical Oceanography, 32, 2113–2130.

Moum, J.N., D.M., Farmer, W.D., Smyth, L., Armi, and S., Vagle (2003), Structure and generation of turbulence at interfaces strained by internal solitary waves propagating shoreward over the continental shelf. Journal of Physical Oceanography, 33, 2093–2112.

Munk, W.,and C., Wunsch (1998), Abyssal recipes II: Energetics of tidal and wind mixing, Deep-Sea Research Part I 45.12.

Nakatsuka, T., M. Toda, K. Kawamura, and M. Wakatsuchi (2004), Dissolved and particulate organic carbon in the Sea of Okhotsk: Transport from continental shelf to ocean interior, Journal of Geophysical Research: Oceans, 109, C09S14, doi:10.1029/2003JC001909.

Nakayama, K., M., Sivapalan, C., Sato, and K., Furukawa (2010), Stochastic characterization of the onset of and recovery from hypoxia in Tokyo Bay, Japan: Derived distribution analysis based on “strong wind” events. Water Resources Research, 46.

Nam, S., and U. Send (2011), Direct evidence of deep water intrusions onto the continental shelf via surging internal tides, Journal of Geophysical Research: Oceans, 116(C5), C05004.

Nash, J.D., L.F., Kilcher, and J.N., Moum (2009), Structure and composition of a strongly stratified, tidally pulsed river plume. Journal of Geophysical Research: Oceans, 114, C00B12.

Nash, J.D., and J.N., Moum (2005), River plumes as a source of large-amplitude internal waves in the coastal ocean. Nature, 437, 400–403.

Nash, J.D., and J.N., Moum (1999), Estimating salinity variance dissipation rate from conductivity microstructure measurements. Journal of Atmospheric and Oceanic Technology, 16, 263–274.

Noble, M. A., and J. P. Xu (2003), Observations of large-amplitude cross-shore internal bores near the shelf break, Santa Monica Bay, CA. Marine Environmental Research, 56, 127–149.

Ogston, A. S., J. V., Guerra, and R. W., Sternberg (2004), Interannual variability of nearbed sediment flux on the Eel River shelf, northern California. Continental Shelf Research, 24.1,117-136.

Okada, T., T., Shikata, T., Honjo (2008), Thin–layer bloom of diatoms around the mouth of the Arakawa River in Tokyo Bay. Journal of the Faculty of Agriculture, Kyushu University, 53, 73–80.

Okayasu, A., T. Shimozono, H. Yamazaki, T. Nagai, S. Sato (2013), Severe erosion of sandbar at

Unosumai River mouth, Iwate, due to 2011 Tohoku tsunami, Coastal Dynamics 2013, 1311–1320.

Okazaki, M. (1990), Internal tidal waves and internal long period waves in the Sanriku coastal seas, eastern coast of northern Japan, La mer, 28, 5–29.

Okazaki, M. (1994), The circulation of sea water and variation of the properties in some bays of Sanriku Coast, eastern coast of Northern Japan, Bulletin on Coastal Oceanography, 32, 15–28 (in Japanese).

Orton P.M., W.R., McGillis ,and C.J., Zappa (2010), Sea breeze forcing of estuary turbulence and air-water CO2 exchange, Geophysical Research Letters, 37(13).

Osborn, T.R. (1974), Vertical profiling of velocity microstructure. Journal of Physical Oceanography, 4, 109–115.

Osborn, T. R. (1980), Estimates of the local rate of vertical diffusion from dissipation measurements, Journal of Physical Oceanography, 10, 83–89.

Ostrovsky, L. A., and Y. A. Stepanyants (1989), Do internal solitons exist in the ocean?, Rev. Geophys., 27, 293– 310.

Otobe, H., H. Onishi, M. Inada, Y. Michida, and M. Terazaki (2009), Estimation of water circulation in Otsuchi Bay, Japan inferred from ADCP observation, Coastal Marine Science, 33 (1), 78–86.

Petruncio, E. T., L. K. Rosenfeld, and J. D. Paduan (1998), Observations of the internal tide in Monterey Canyon, Journal of Physical Oceanography, 28, 1873–1903.

Phillips, O.M., J.H., Shyu, and H., Salmun (1986), An experiment on boundary mixing: mean circulation and transport rates. Journal of Fluid Mechanics 173, 473–499.

Pineda, J. (1994), Internal tidal bores in the nearshore: Warm-water fronts, seaward gravity currents and the onshore transport of neustonic larvae, Journal of Marine Research, 52(3), 427–458.

Pineda, J. (1999), Circulation and larval distribution in internal tidal bore warm fronts. Limnology and Oceanography, 44, 1400–1414.

Pollard, R. (1986), Frontal surveys with a towed profiling conductivity/temperature/depth measurement package (SeaSoar). Nature, 323, 433–435.

Puig, P., A., Palanques, J. Guillén, and M. El Khatab (2004), Role of internal waves in the generation of nepheloid layers on the northwestern Alboran slope: Implications for continental margin shaping, Journal of Geophysical Research: Oceans, 109, C09011, doi:10.1029/2004JC002394.

Richards, C., D. Bourgault, P. S. Galbraith, A. Hay, and D. E. Kelley (2013), Measurements of shoaling internal waves and turbulence in an estuary, Journal of Geophysical Research: Oceans, 118(1), 273–286.

Rosenblum, L.J., and G.O., Marmorino (1990), Statistics of mixing patches observed in the Sargasso Sea. Journal of Geophysical Research: Oceans, 95, 5349–5357.

Ross, C. B., W. D. Gardner, M. J. Richardson, and V. L. Asper (2009), Currents and sediment transport in the Mississippi Canyon and effects of Hurricane Georges, Continental Shelf Research, 29(11), 1384–1396.

Rudnick, D.L., and J.,Klinke (2007), The Underway Conductivity–Temperature–Depth instrument. Journal of Atmospheric and Oceanic Technology, 24, 1910–1923.

Sharples, J., Moore, C. M., Hickman, A. E., Holligan, P. M., Tweddle, J. F., Palmer, M. R., and Simpson, J. H. (2009). Internal tidal mixing as a control on continental margin ecosystems. Geophysical Research Letters, 36(23).

Shea, R. E., and W. W. Broenkow (1982), The role of internal tides in the nutrient enrichment of Monterey Bay, California. Estuarine, Coastal and Shelf Science, 15, 57–66.

Simpson, J.H. (1997), Physical processes in the ROFI regime, Journal of Marine Systems 12, 3-15.

Simpson, J.H., E.,Williams, L.H., Brasseur, and J.M., Brubaker (2005), The impact of tidal straining on the cycle of turbulence in a partially stratified estuary, Continental Shelf Research, 25(1), 51–64.

Soulsby, R. L. (1997), Dynamics of marine sands, Thomas Telford , London, UK.

Sullivan, J.M., P.L., Donaghay, and J.E.B., Rines (2010), Coastal thin layer dynamics: Consequences to biology and optics. Continental Shelf Research, 30, 50–65.

Thorpe, S.A. (1992), Thermal fronts caused by internal gravity waves reflecting from a slope. Journal of Physical Oceanography 22, 105–108.

Thorpe, S. A. (1998), Some dynamical effects of internal waves and the sloping sides of lakes, Physical Processes in Lakes and Oceans, Coastal and Estuarine Studies, 54, 441–460.

Trowbridge, J. H. (1998), On a technique for measurement of turbulent shear stress in the presence of surface waves, Journal of Atmospheric and Oceanic Technology, 15(1), 290–298.

Van Gastel, P., G. N. Ivey, M. J. Meuleners, J. P. Antenucci, and O. Fringer (2009), The variability of the large-amplitude internal wave field on the Australian North West Shelf, Continental Shelf Research, 29(11), 1373–1383.

Van Haren, H. (2005), Details of stratification in a sloping bottom boundary layer of Great Meteor Seamount. Geophysical Research Letters, 32, L07606.

Van Haren, H. (2006), Nonlinear motions at the internal tide source, Geophysical Research Letters, 33(11), L11605.

Van Haren, H. (2009), Using high sampling-rate ADCP for observing vigorous processes above sloping [deep] ocean bottoms, Journal of Marine Systems, 77, 418–427.

Van Weering, T. C., H. C. De Stigter, W. Balzer, E. H. Epping, G. Graf, I. R. Hall, and A. Vangriesheim (2001), Benthic dynamics and carbon fluxes on the NW European continental margin, Deep Sea Research Part II: Topical Studies in Oceanography, 48(14), 3191–3221.

Venayagamoorthy, S. K., and O. B. Fringer (2006), Numerical simulations of the interaction of internal waves with a shelf break, Physics of Fluids, 18, 076603/9, doi:10.1063/1.2221863.

Vlasenko, V., and K. Hutter (2002), Numerical experiments on the breaking of solitary internal waves over a slope-shelf topography, Journal of Physical Oceanography, 32, 1779–1793.

Vlasenko, V., N. Stashchuk, and K. Hutter (2005), Baroclinic Tides: Theoretical Modelingand Observational Evidence, Cambridge University Press, Cambridge, UK.

Vlasenko, V., C. Guo, and N. Stashchuk (2012), On the mechanism of A-type and B-type internal solitary wave generation in the northern South China Sea, Deep Sea Research Part I: Oceanographic Research Papers, 69, 100–112.

Wolanski, E., and W. M. Hamner (1988), Topographically controlled fronts in the ocean and their biological influence, Science, 241, 177–181.

Wallace, B. C., and D. L. Wilkinson (1988), Run-up of internal waves on a gentle slope in a two-layered system, Journal of Fluid Mechanics, 191, 419–442.

Walsh, J. J. (1991). Importance of continental margins in the marine biogeochemical cycling of carbon and nitrogen, Nature 350, 53 – 55.

Walter, R. K., C. B. Woodson, R. S. Arthur, O. B. Fringer, and S. G. Monismith (2012), Nearshore internal bores and turbulent mixing in southern Monterey Bay, Journal of Geophysical Research: Oceans, 117(C7), C07017.

Wang, Y. H., I. H. Lee, and J. T. Liu (2008), Observation of internal tidal currents in the Kaoping Canyon off southwestern Taiwan, Estuarine, Coastal and Shelf Science, 80(1), 153–160.

Wang, Z., and L. Goodman (2009), Evolution of the spatial structure of a thin phytoplankton layer into a turbulent field, Marine Ecology Progress Series, 374, 57-74.

Ward, L. G. (1985), The influence of wind waves and tidal currents on sediment resuspension in Middle Chesapeake Bay. Geo-Marine Letters, 5(1), 71-75.

Wiberg, P. L., and C. R. Sherwood (2008), Calculating wave-generated bottom orbital velocities from surface-wave parameters, Computers & Geosciences, 34(10), 1243–1262.

Wang, B., O.B., Fringer, S.N., Giddings, and D.A., Fong (2009), High-resolution simulations of a macrotidal estuary using SUNTANS. Ocean Modelling, 26, 60–85.

Washburn, L., T.F., Duda, and D.C., Jacobs (1996), Interpreting conductivity microstructure: Estimating the temperature variance dissipation rate. Journal of Atmospheric and Oceanic Technology, 13, 1166–1188.

Wolk, F., H., Yamazaki, L., Seuront, R.G., Lueck (2002), A new free-fall profiler for measuring biophysical microstructure. Journal of Atmospheric and Oceanic Technology, 19, 780–793.

Wright, L. D., and C. A. Nittrouer (1995), Dispersal of river sediments in coastal seas: six contrasting cases, Estuaries, 18(3), 494–508.

Yanagi, T., T., Hagita, T., Saino, T., Ishimaru, and S., Noriki (1995), Transport mechanism of suspended matter above the shelf slope at the mouth of Tokyo Bay. Journal of Oceanography, 51, 459–470.

Yamazaki, H., and R., Lueck (1990), Why oceanic dissipation rates are not lognormal. Journal of Physical Oceanography, 20, 1907–1918.

Yin, K. D., R. H. Goldblatt, P. J. Harrison, M. St. John, P. J. Clifford, and R. J. Beamish (1997), Importance of wind and river discharge in influencing nutrient dynamics and phytoplankton production in summer in the central Strait of Georgia, Marine Ecology-Progress Series, 161, 173-183.